Observatoire de Neuchâtel - Université de Neuchâtel

Development of compact elastic backscatter lidars: from numerical simulations to atmospheric measurements

Thèse présentée à la Faculté des Sciences
pour l'obtention du grade de docteur ès sciences
par :

Renaud Matthey
physicien dipl. EPFZ

Acceptée le 8 juin 2000 par les membres du jury :

Prof. G. Busca	rapporteur
Dr J. Bösenberg	co-rapporteur
Prof. R. Dändliker	co-rapporteur
Dr V. Mitev	co-rapporteur
Prof. H. Richner	co-rapporteur

aux miens

à celles et ceux qui ont permis ce travail,
en particulier, V. Mitev

IMPRIMATUR POUR LA THESE

Development of compact elastic backscatter lidars: from numerical simulations to atmospheric measurements

de M. Renaud Matthey-de-l'Endroit

UNIVERSITE DE NEUCHATEL

FACULTE DES SCIENCES

La Faculté des sciences de l'Université de Neuchâtel, sur le rapport des membres du jury

MM. G. Busca (directeur de thèse), R. Dändliker, V. Mitev, H. Richner (Zürich) et J. Boesenberg (Hambourg D)

autorise l'impression de la présente thèse.

Neuchâtel, le 12 septembre 2003

Le doyen:

François Zwahlen

Resume

Lidars are optical radars that allow to sense the atmosphere remotely. They start to be considered as part of complexes of various instruments dedicated to measurements of different atmospheric parameters. Such complexes are more and more deployed on special platforms, like aircrafts, boats, space platforms, or in isolated stations. This imposes severe requirements to the instruments, particularly for reliability, long life, low power consumption, small size.

The objective of this work was to investigate two technology approaches in order to realise elastic backscatter lidars for detection of clouds and aerosol that meet these requirements. These approaches are the pseudo-random noise modulation continuous-wave (PRN-cw) and the micro-pulse techniques. The investigation was performed in two steps. First, instruments were defined by numerical simulations, and demonstrational set-ups were realised and evaluated; then, as their feasibility was proved, several compact lidars were built for practical applications based on these techniques. These instruments are described and their operations evaluated. Also discussed are their advantages and their limitations.

The PRN-cw and the micro-pulse techniques are compared to each other. The micro-pulse technique shows higher signal-to-noise ratio for equivalent instrument component characteristics. Nevertheless, the PRN-cw technique can make use of more reliable lasers and may be more adapted to some specific applications, depending on the instrument requests for cost, lifetime, eye-safety.

Résumé

Les lidars sont des radars optiques qui permettent de sonder l'atmosphère à distance. On commence à les considérer comme partie intégrante d'ensembles instrumentaux dédiés à la mesure de différents paramètres atmosphériques. De tels ensembles sont de plus en plus souvent embarqués à bord de plates-formes particulières - avions, bateaux, engins spatiaux - ou placés dans des stations isolées. Les instruments doivent donc satisfaire à de sévères critères de performance, notamment en termes de grande fiabilité, longue durée de vie, faible consommation, petite taille.

L'objectif de ce travail était d'étudier deux approches technologiques afin de développer des lidars à rétro-diffusion élastique pour la détection des nuages et des aérosols, tout en remplissant les exigences sus-mentionnées. Ces approches sont les techniques de modulation de bruit pseudo-aléatoire d'ondes continues (PRN-cw) et de micro-impulsions. Les recherches ont été effectuées en deux temps. Dans une première phase, les instruments étaient définis au moyen de simulations numériques et des dispositifs de démonstration étaient réalisés puis évalués. Ensuite, une fois leur faisabilité avérée, plusieurs lidars compacts ont été construits pour des applications pratiques, sur la base de ces deux techniques. Ces instruments sont décrits dans ce travail et leurs opérations analysées. Leurs avantages et limites sont également discutés.

Les techniques PRN-cw et de micro-impulsions sont comparées. Pour des instruments dont les composants ont des caractéristiques équivalentes, le rapport signal sur bruit est plus grand pour la technique de micro-impulsions. Néanmoins, la technique PRN-cw permet l’utilisation de lasers plus fiables et peut se montrer plus adaptée à certaines applications spécifiques, selon les contraintes de coût, de durée de vie, de sécurité oculaire, imposées à l'instrument.

Contents

Introduction

Since a long time the development of atmospheric lidars has not been driven only by the curiosity of the scientists, but by the application requirements. The lidar stopped to be only a demonstration of technical feasibility; it started to be considered as part of complex, where various instruments are dedicated to measurements of different atmospheric parameters. This is an important trend in recent atmospheric measurement campaigns and observations, including observations from special platforms (aircraft, boat, space platform, remote station). In such cases, the lidar application is not only determined by the lidar performance alone, but rather by the combination of several parameters including the lidar performances, instrument configuration, volume, mass, power consumption, reliability, its environment, the difficulty to operate it. It is obligatory to fit the lidar to the requirements of the platform and to the rest of the measurement instrumentation. In a number of measurement scenarios, the overall combination defines the constrains for the lidar use and finally the decision, shall lidar instrument be involved in the measurements or not.

These application driven developments impose more stringent requirements during the processes of realisation, operation and data presentation than to laboratory lidars. It is necessary that the lidar is user friendly, that is, operates in automatic way, keeps its alignment, is easy for control and maintenance. Reliable, long life and efficient laser sources, detectors, optics and mechanics shall be selected, as well as ways how to make from them the needed automated lidar. As the lidar application is usually specific, it is hard to find an example to copy or to follow. It is also expensive to make a number of trials with different sets of equipment. Numerical simulations help to determine the optimal combination of measurement performances and sub-systems characteristics. During missions, it is necessary to have a quick look on the data, to evaluate their quality and select them as fast as possible, because the time to take the decision for the next measurement is precious. User-friendly software greatly eases this task and the data presentation. Last but not least, applied lidars are more and more often required to be of reduced volume.

Objective of the work

The objective of this thesis is to investigate two technology approaches to realise compact elastic backscatter lidars, Pseudo-Random Noise modulation continuous-wave lidar (PRN-cw lidar) and micro-pulse lidar. PRN-cw lidars are based on cw-laser diode, while micro-pulse lidars make use of pulse laser diode or micro-chip laser. The investigation is done by numerical simulations, realisation and evaluation of demonstrational set-ups, and realisation of compact lidars for practical applications with evaluation of their operation.

The presented results for atmospheric parameters (measurements) are only as examples. With this work we do not aim at discussing directly the scientific results obtained by the developed instruments, but rather the quality of the obtained data. We limit also our investigation to elastic backscatter lidars only, at times total, at times depolarisation lidars.

Organisation of the dissertation

This work consists of three parts. The first comprises Chapters 1 and 2 and is dedicated to lidar principles and lidar numerical simulation modelling. The second part is devoted to the PRN-cw approach, while the last part presents the micro-pulse approach.

Chapter 1, *Lidar principles*, contains a brief overview of the lidar measurement technique. More detailed is the section concerning the signal and noise equations. Both pulsed and PRN-cw techniques are presented and their signal-to-noise ratios discussed and compared.

In Chapter 2, *Lidar signal numerical simulations*, we first expose the developed backscatter lidar simulation model. It is based on the equations presented in Chapter 1. Atmosphere, background radiation and topographic models are described. Based on these models, a computer program has been written, which allows to simulate the backscattered signal for a variety of elastic backscatter lidar instruments, targets and platforms.

In Chapter 3, *PRN-cw technique: requirements and demonstration*, the general instrumentation necessary to the PRN-cw technique is discussed. The principle of this technique has been checked on an optical fibre test bench. A demonstration PRN-cw lidar set-up operating in photon-counting mode and during night-time has been built. Measurements of hard targets, cloud base, and PBL aerosol obtained in this configuration are presented. Advantages and limitations of the PRN-cw technique are discussed.

Chapter 4, *A compact PRN-cw lidar*, is dedicated to the development of a transportable compact PRN-cw lidar for day-time measurements in analog mode. A PRN-cw sequence generator and an analog acquisition system have been especially designed to take full advantage of the PRN-cw technique. The measurements show that PRN-cw applications as ceilometer and range-finder are possible.

PRN-cw technique has limitations. One is the high sensitivity to background radiation. In Chapter 5, *Concepts for further development and application of PRN-cw lidars*, a demonstration version of an atomic ultra narrow-band optical filter is presented together with its application to the PRN-cw lidar technique. The idea is that, as cw-diode laser diodes are used in the PRN-cw technique, it is worth to make use of their very narrow bandwidth. In this experiment, the laser diode is locked on the atomic filter. Cw-laser diodes may also be very small, what leads to extremely compact lidar concepts. One such concept for a lidar intended for Mars planetary mission is proposed also in this chapter with numerical simulations of its performances.

Cw-laser diode are the smallest lasers but not the only small ones. Some pulse lasers are also small, like hybrid pulse diode lasers and recently appeared passive Q-switched micro-chip lasers. The development steps of a compact automated airborne lidar built around such types of lasers are exposed in Chapter 6, *A compact automated airborne lidar*.

This airborne lidar in its micro-chip laser version participated to several airborne campaigns on board a high altitude research aircraft. Measurement results from these campaigns are reported in Chapter 7, *Airborne campaigns and measurements from ground*. Clouds, polar stratospheric clouds, aerosol layers have been detected with this instrument. It also shows capabilities for unattended measurement in the low troposphere from ground.

Chapter 1

Lidar principles

Introduction

The scope of this chapter is to define the terminology in the lidar field. We will first briefly present what a lidar is, how it works (§ 1.1). It will be seen that there are several types of lidar, each of them dedicated to a particular task depending on the interaction light-atmosphere and the physical processes involved in the measurement. Section 1.2 is a short overview of the different sub-systems of a lidar. More detailed is the section dedicated to the signal and noise equations and their dependence to the measurement target and to the instrument parameters (§ 1.3). Two measurement methods are treated and compared from a theoretical point of view. They are the pulsed and PRN-cw techniques.

1.1 What is a lidar

Remote sensing allows to acquire information about an object without being physically in contact with it. Remote sensing instruments are generally divided into two categories, passive and active. Passive remote sensing instruments, like eyes, optical and microwave radiometers, measure natural radiation emanating from the object being under observation while active remote sensing instruments, like radars*, provide their own radiation source.

The lidar is an active remote sensing instrument. Its name is the acronym for "LIght Detection And Ranging". It is the optical equivalent of the radar, where a laser re-

---

* Radar means "RAdio wave Detection And Ranging".

places the radio wave emitter and a telescope the antenna. Its purpose is to determine the optical properties of the atmosphere by measuring the characteristics of the backscattered laser light. The lidar measurement technology takes advantage of the great variety of interactions of light with atmospheric gases and particles, combined with the high spectral and spatial brightness of the laser beam.

Compared to other atmospheric measurement instruments, the lidar offers several main advantages. First, as remote instrument, it does not need to be placed at the location of the item which properties shall be measured. In this sense, it is in contrast with "in-situ" instruments which operate at the location of the item, like PTU radio sondes*. The lidar may sense precise locations hard or impossible to access. It may also record their temporal evolution by measuring continuously, what is very difficult for in-situ atmospheric instruments. Another main advantage lies in the fact that the lidar may measure range-resolved profiles; it provides information from several layers at the same time. However, a lidar cannot measure all interesting features of the atmosphere and it sometimes also requires reference data. Therefore, depending on the observed atmospheric parameters, lidars, in-situ and passive remote sensing instruments are complementary.

Concerning target measurement – basically range or distance to hard target – the lidar determines the range without necessity for travelling to target or existence of a third point for triangulation.

1.1.1 Principle of a lidar

"Light scattering" by particles† designs the phenomena by which a light beam propagating in a given direction is dispersed in all directions. Each particle act as a scattering centre. For instance, without scattering, like on the Moon, the Earth sky would look black except in the Sun direction. Backscattered light refers to the part of the light which has been scattered in the direction it came from, but in opposite sense.

The laser beam of the lidar is sent into the atmosphere under the shape of pulses. A portion of the propagating light interacts with the various elements constituting the atmosphere – like molecules, particles, clouds, … – and is scattered, while the rest of the light travels further. The beam is progressively attenuated with the distance in the process of propagation. The backscatter light is collected by the telescope of the instrument, detected and converted into electrical signal. This electrical signal is then measured. Acquired data are finally stored on a mass memory and processed by a computer. The time difference between the moment the laser pulse is emitted and the reception of the light, often called "time-of-flight" is related by the known speed of the light to the range reached by the light. For instance in 1 μs the light covers 300 m, meaning that it has been backscattered at a range of 150 m. On the other side, the intensity of the signal contains information about

* Pressure-Temperature-hUmidity radio sonde.

† Here "particles" means both aerosol particles and molecules.

the scattering item, i.e. the probed atmospheric layer. The lidar signal profile is obtained by measuring – after the laser pulse was emitted – the signal at several moments, so at several ranges or altitudes.

The difference between a lidar and a range-finder is exactly at this point. A range-finder also emits a light pulse and detects the part backscattered by a solid or liquid target. However it does not measure a profile, what means several time-of-flights, like the lidar. It only measures the time spent till a signal larger than a certain value is detected.

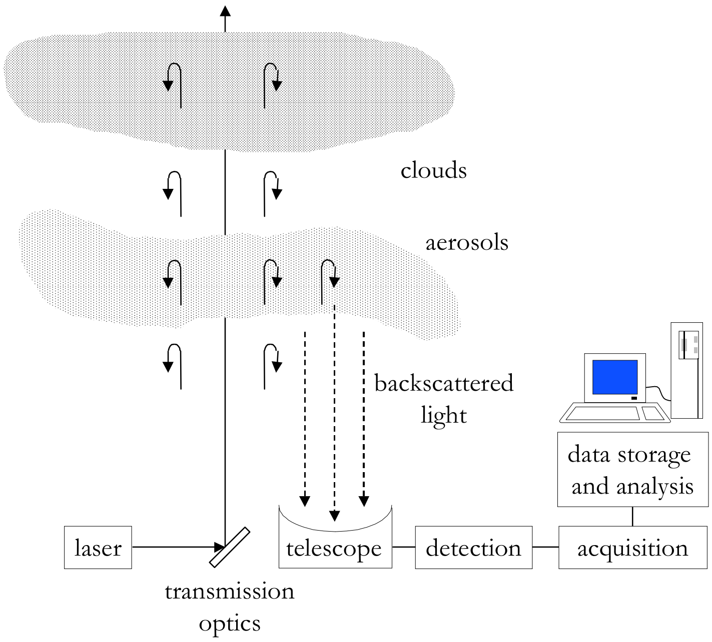

Figure 1.1. *Lidar measurement principle*

1.1.2 Types of lidars

Following about 30 years of development, a variety of lidar instrument exists. The growing use of ground-based and airborne lidars during the last years has demonstrated the maturity of this measurement technique for practical atmospheric studies. Detection of clouds, range-resolved profiles of atmospheric aerosol layers, water vapour, temperature, ozone, pollutant gases, wind velocity field, etc. are all within the scope of lidar applications.

The different lidar instruments are recognised by the different light-atmosphere interactions on which the atmospheric interrogation principle is based. Lidar based on Rayleigh and Mie scattering are the most current lidar instruments because they are relatively simple. The laser radiation is elastically scattered by atoms, molecules and particles, and there is no shift between the emitted and detected frequencies. Such lidar technique is used for instance to detect clouds and aerosol layers and to estimate the temperature in the stratosphere. Raman inelastic scattering – vibrational and rotational – is of high interest for lidar observations of molecules in the atmosphere. Raman lidar purposes are, among others, the determination of the extinction, the temperature in troposphere and low stratosphere, and, indirectly, measurements of concentration of molecular species. DIAL (DIfferential Absorption Lidar) instruments use the absorption band of a given molecule to evaluate its concentration. Two wavelengths are required for such evaluation. Wind velocity may be observed by Doppler lidar. Study of the sodium layer at very high altitude refers to resonance scattering while chlorophyll concentration of natural bodies of water is an example of application of the fluorescence lidar technique.

In the frame of this work, we restrict us only to the lidar technique based on Rayleigh and Mie scattering.

1.2 Lidar sub-system description

The goal here is not to go deep into the details, but only to provide an overview of the lidar instrument sub-systems and their function. The enumeration and the explanations are rough and incomplete. We have no ambition to list all kind of possible lidar sub-systems as the subject is very large and dedicated literature exists like [Meas84]. Our aim is to give a general idea which parts a lidar consists in and to make more comfortable the understanding of instrumentation developed in the frame of this work.

The laser occupies a central place in the lidar instrumentation. Its wavelength and bandwidth shall be properly chosen depending on the type of the observation. The power of the laser is usually chosen to be as high as possible because the higher the power, the better the quality of the signal. However, parameters like volume, weight, eye-safety, cost are often of consideration. Pulsed lasers are traditionally used. In this case, the echo to an emitted pulse from the various layers of the atmosphere shall have been recorded before the next pulse is emitted. It will been seen later, that if the amplitude of the power of a cw-laser is modulated in a precise way, it is also possible to continuously record the signal at the same time the light is emitted. In this work, we use both types of laser, pulsed and continuous-wave.

The backscattered light is collected by a telescope. It may be built of reflective (mirrors) or refractive (lenses) optics and several configurations are possible. The choice depends on the volume and the type of the lidar application. Prime focus configuration is adapted when a collecting fibre or a small detector is placed at the telescope focal point, or in its immediate vicinity. Newtonian telescope is often used. It is excellent for precise focussing and is relatively easy to align. The secondary flat mirror lets the spectral filtering sub-system to be outside the telescope. Cassegrainian telescopes are very compact with long effective focal length. However, they are also more difficult to align.

When several wavelengths are of interest – what will not be our case –, spectral filtering is obtained by dichroic beamsplitters or monochromators. Background light contaminates the optical signal of interest and diminished its quality. This background radiation is rejected (partially) by optical filters. The latter may be broad-band (e.g. band-pass filters), narrow-band (e.g. interference filters) or even ultra-narrow (e.g. multi-layer Fabry-Perot etalon). In Chapter 5, an atomic filter (FADOF) is also used in a lidar set-up. In case of aerosol particle measurement, the polarisation state of the backscattered light contains information on the shape of these particles. It is then worth to use a probing polarised beam and to separate the collected light into two orthogonal components by a proper polarisation beamsplitter. More on optics may be found in [Hech87].

Several types of detectors exist to convert light into electrical signal. Photomultiplier tubes (PMT), avalanche photodiodes (APD) are the most often used in the lidar field. Other types like CCD cameras or microchannel plates may also be found. The choice of the detector depends mostly on the sensitivity of the photocathode at the considered wavelength (we speak of "quantum efficiency" for PMT and "responsivity" for APD); but gain, bandwidth, noise level, volume, power supply voltage, dynamics are important as well. PMTs are sensitive in the UV and visible light, while APDs suit better in the IR. Detectors in the red and the IR are sometimes cooled to decrease their noise. PMTs used to be bulky and powered by high voltages. This situation is changing; very compact PMT modules exist now, which need also low voltage (they have integrated low-to-high voltage converter). As PMTs have large sensitive area, they are easy to align.

The electrical signal coming out from the detector shall then be acquired; that is its amplitude is measured in function of the time and converted into numbers for further analysis. When the optical power impinging on the detector is weak enough, the detector output current is a chain of single current pulses corresponding to single arriving photons. These pulses are then counted within successive time intervals[*]. This mode of signal acquisition is named "photon-counting" mode. By analysis of the height of the current pulses, it is possible to discriminate the pulses caused by photons from the pulses which are not generated by photons but issued by the detector itself. These latter "noise pulses" are in average smaller than the former. If the height of a pulse does not exceed a defined threshold, it is not counted. Thus the acquired signal contains only few noise. This is the main advantage of this technique. When too many photons arrive, the current pulses pile-up and it is no more possible to count them[†]. In this case, it is better to measure the current itself as it is proportional to the optical power and to convert it into digital form by an analog-to-digital converter (ADC). This mode of acquisition is named "analog" mode and suits to large optical power. However, as it is composed of more electrical circuits, it is intrinsically more noisy than the photon-counting mode[‡].

[*] It is sometimes necessary to amplify these pulses to count them. The time intervals are named "bins", "gates", "samples". All three terms are equivalent.

[†] This value depends also on the characteristic of the detector. Above 10^6-10^7 counts per second, acquisition in photon-counting mode starts to be non linear and thus no more reliable.

[‡] In order not to enter into too technical details, we renounce here to explain how to measure the current as various possibilities exist and to mention their respective advantages or drawbacks. We mentioned also only incoherent detection and omitted coherent detection (e.g. heterodyne detection) as it is not used in this work.

The recorded signal for a single laser pulse is usually noisy. In order to improve the signal-to-noise ratio, the signal is averaged on several pulses. It is also possible to take several successive data points of the measured profile and to average them ("binning" operation).

For a lidar, the geometry of the receiver optics relatively to the transmitter optics is important. Let consider the case where the laser beam is symmetrical around its propagation axis (e.g. Gaussian beam). The illuminated part of the atmosphere is then a truncated cone which depends on the divergence of the laser beam, the inclination of its propagation axis and its diameter at the level of the instrument. In the same way, the part of the atmosphere seen by the telescope is a truncated cone which is given by the field of view of the telescope, its axis and the diameter of the collecting lens*. Only targets in the intersection of both cones will be detected. This intersection depends further on the range and on the distance at the instrument level between the axes of the laser beam and the telescope. The "overlap function" at a given range is the part of the area illuminated by the laser beam and seen by the telescope at this range†. When the lidar is well aligned, the overlap function is equal to 1 at far ranges‡. At short ranges it is usually 0. The shape of the overlap function is very important for a lidar. Data measured for ranges where the overlap function is smaller than unity are either corrected or purely not taken into consideration as this correction is delicate.

1.3 Theory of lidar signal

In this section is described how the lidar signal is related to the optical properties of the atmosphere or of a hard target. First, the path to get the so-called "lidar equation" is deduced. Then, the principles of the PRN-cw method are explained. It will be seen that this method is tightly bounded to the pulsed method. Finally the signal-to-noise ratios of both kinds of measurements are discussed and compared.

1.3.1 The lidar equation

The lidar equation is for the power of the light received by the detector of the instrument. Here the lidar equation is derived for the case of elastic atmospheric backscatter only. It is assumed that the wavelength of the emitted and detected radiation is the same, λ (elastic

---

* In order not to complicate the explanations, we assume the telescope made of a single lens or mirror.

† The energy distribution of the laser beam is assumed to be uniform. If it is not the case, the overlap function is the part of the energy seen by the telescope.

‡ Full overlap at far ranges may be obtained only if the field of view (full angle) of the telescope is larger than the beam divergence (full angle). For a Gaussian beam, the divergence θ (half angle) is equal to $\lambda/\pi W_0$, where λ is the laser wavelength and W_0 the laser waist radius. At far ranges, ~86% of the energy is comprised within the cone of angle θ and ~99% within 1.5θ. In order to be safe, we consider that the field of view (full angle) shall be at least twice the divergence (full angle).

scattering from the target), and that λ is out of the absorption bands of the atmosphere. Also only the range r is taken into account, not the vector position $\mathbf{r}$, what implies uniformity of the radiation and target medium. A complete derivation is contained in [Meas84].

When a short laser pulse of wavelength λ is emitted into the atmosphere, the detected power P of the backscattered light at distance r from the instrument may be expected to be a function such as

$$P(r,\lambda) = P(r,\lambda,S,\beta,\alpha). \tag{1-1}$$

Here P depends on the instrument parameter set S, on the nature of the interaction β between the laser light and the target medium at range r and on α. α expresses the way the laser light is attenuated when propagating in the atmosphere being scattered in all directions by the atmospheric volume in the line of propagation.

Let the temporal shape of the laser pulse be approximated by a rectangular laser pulse of energy E_0, duration τ_L, emitted at time 0. If $A_L(r)$ is the area on which the laser light is distributed at range r, the laser irradiance I (in $[W/m^2]$) over $A_L(r)$ is given by

$$I(r,\lambda) = \frac{E_0 T(\lambda,r)}{\tau_L A_L(r)}, \tag{1-2}$$

$T(r, \lambda)$ represents the atmospheric transmission factor at wavelength λ from instrument position to range r. It results from the Beer-Lambert law that

$$T(r,\lambda) = \exp\left(-\int_0^r \alpha(r',\lambda)dr'\right). \tag{1-3}$$

The extinction coefficient α (in $[m^{-1}]$) and the volume backscattering coefficient β (in $[sr^{-1}m^{-1}]$) are expressed as

$$\alpha(r,\lambda) = n(r)\int d\Omega \frac{d\sigma(\lambda)}{d\Omega} \qquad \text{and} \qquad \beta(r,\lambda) = n(r)\left[\frac{d\sigma(\lambda)}{d\Omega}\right]_{\Omega=\pi}, \tag{1-4}$$

where $n(r)$ is the scatterer number density at range r and $d\sigma(\lambda)/d\Omega$ its differential scattering cross-section at wavelength λ (in $[m^2sr^{-1}]$).

In the approximation of single scattering, for the chosen shape of the laser pulse, at time t $(=r/c)$, where c is the speed of the light in the air, only the volume $V=A_L(r)\cdot c\tau_L/2$ extending from ranges $c(t-\tau_L/2)$ to ct contributes to the radiation power I_b backscattered in the acceptance solid angle $d\Omega_b(r)$ of the receiver:

$$I_b(r,\lambda) = I(r,\lambda)\beta(r,\lambda)V d\Omega_b(r) \qquad \text{with} \qquad d\Omega_b(r) = \frac{A}{r^2}, \tag{1-5}$$

where A is the effective area of the receiver lens or telescope. The range-dependant parameters have been regarded as constant since r is generally much greater than $c\tau_L/2$.

If K is a constant expressing the overall optical efficiency of the lidar transmitter and receiver sub-systems, and $\eta(\lambda)$ is the wavelength-dependent quantum efficiency of the detector, the detected signal power P is

$$P(r,\lambda) = K\eta(\lambda)O(r)I_b(r,\lambda)T(r,\lambda). \tag{1-6}$$

$O(r)$ is the overlap function corresponding to the part of the laser irradiation area $A_L(r)$ within the field of view of the receiver optics. Rewriting (1-6) with the equations (1-2) to (1-5), the "*lidar equation*" is obtained:

$$P(r,\lambda) = E_0 K\eta(\lambda)O(r)\frac{A}{r^2}\frac{c}{2}\beta(r,\lambda)\exp\left(-2\int_0^r \alpha(r',\lambda)dr'\right). \tag{1-7}$$

From the detected power, we may derive the energy received by the detector during the "integration period" τ:

$$E(r,\lambda) = E_0 K\eta(\lambda)O(r)\frac{A}{r^2}\frac{c\tau}{2}\beta(r,\lambda)\exp\left(-2\int_0^r \alpha(r',\lambda)dr'\right). \tag{1-8}$$

$E(r,\lambda)$ is the energy of the signal backscattered from the range interval $[r, r+\Delta r[$ where $\Delta r = c\tau/2$. The integration time τ, and thus Δr, is given by the lidar set-up (detector, acquisition system). Δr is called "range resolution".

1.3.2 Comments concerning the lidar equation

The lidar equation has been derived using simplifying and approximating assumptions. They are here briefly discussed. Extended forms of the equation are also presented.

In the computation of the equation (1-7) the detector response time τ_D has been neglected. This is possible only if $t >> \tau_D$. In the general case, the range resolution is limited to $c(\tau_L+\tau_D)/2$.

As the receiver optics of a lidar is usually focused at infinity, the radiation from a target plane located at short or intermediate ranges from the instrument will not be focused onto the focal plane. Instead it forms a diffuse region of illumination on this plane. The presence of a limiting aperture (diaphragm, detector of small size) in the focal plane can reduce the amount of detected power. This effect is referred to as "geometrical signal compression", and may be accounted by an upgraded overlap function called also "geometrical form factor".

The extinction coefficient α and the volume backscattering coefficient β may be considered as the sums of the contributions of molecules and aerosol particles:

$$\alpha(r,\lambda) = \alpha_{mol}(r,\lambda) + \alpha_{aer}(r,\lambda) \quad \text{and} \quad \beta(r,\lambda) = \beta_{mol}(r,\lambda) + \beta_{aer}(r,\lambda), \tag{1-9}$$

where "*mol*" and "*aer*" represent the molecular and aerosol contributions.

In case λ coincides with an absorption band of an atmospheric species, the integrand in the transmission factor expression (1-3) must be changed:

$$\alpha(r',\lambda) \longrightarrow \alpha(r',\lambda) + n(r')\sigma(\lambda) \tag{1-10}$$

where $n(r)$ is the number density of the absorbing species at range r, and $\sigma(\lambda)$ its absorption cross-section at wavelength λ.

For inelastic (Raman) scattering, the wavelength of the backscattered radiation λ_e is not the same as the wavelength of the incident radiation λ_i. In this case, β is the backscattering coefficient based on the differential cross section of the light-molecule interaction inducing the wavelength shift (cf. equation (1-4)). The extinction part of the lidar equation (1-7) is then

$$\exp\left(-\int_0^r \left(\alpha(r',\lambda_i) + \alpha(r',\lambda_e)\right)dr'\right). \tag{1-11}$$

An important difference between ground-based lidars and satellite or air-borne ones is the *surface return*. For a diffuse Lambertian extended* hard target or surface, which scattering occurs only into a single hemisphere the emitted radiance (in [$Wm^{-2}sr^{-1}$]) is [Jela92]

$$I(\vartheta) = I(\vartheta = 0)\cos\vartheta, \tag{1-12}$$

where ϑ is the angle with the surface normal vector. The total emitted radiation R (irradiance) is then

$$R = \int I(\vartheta)d\Omega = \pi I(0). \qquad \text{Thus} \qquad I(0) = \frac{R}{\pi}. \tag{1-13}$$

With this result, the lidar equation of a diffuse Lambertian extended target†, like a ground surface, is given by

$$P(r,\lambda) = \frac{E_0}{\tau_L} K\eta(\lambda) O(r_{sur}) \frac{A_t}{r_{sur}^2} \frac{a}{\pi} \exp\left\{-2\int_0^{r_{sur}} \alpha(r')dr'\right\} \quad \text{if} \quad r \in [r_{sur}, r_{sur}+c\tau_L[\,. \tag{1-14}$$

For other ranges r, $P = 0$. r_{sur} is the distance along the probing beam between the satellite- or air-borne lidar and the Earth's surface; a is the surface albedo. Following equation (1-

* Here "extended" means that the surface of the target is larger than the footprint of the laser beam. Wouldn't it be the case, that the response would depend on the scattering area and on the inverse fourth power of the range, r^{-4}.

† Also for the rest of this work, if not stated otherwise, all considered hard targets and surfaces are assumed to be lambertian.

13), this expression is valid only if the lidar looks perpendicularly to the ground surface, or target.

Instead of considering *P* as the detected electric power of the backscattered signal – power directly after the photocathode –, it is also possible to define it as the received optical power before the detector. In this case, the wavelength-dependent quantum efficiency of the detector, $\eta(\lambda)$, is removed from the lidar equation. From now on we will use this definition of *P* as optical power on the detector.

This work concerns only elastic backscatter lidars. In order to make the reading (and the writing…) easier, the wavelength parameter will be further omitted unless some confusion may arise from unclear situations.

1.3.3 Contributions to the total measured signal from ambient background and noises

The total measured signal contains the backscattered lidar signal resulting from the interaction of the laser beam with the atmosphere as only one of its components. It consists also of other contributions which are called noises, because they degrade the quality of the signal. Depending on the detection mode, analog or photon-counting, they are not always present. The most important of them ([Sale91, Jela92, Meas84]) are listed in Table 1.1.

Noise type	Ph.-count.	Analog
Noise in signal (quantum, photon noise)	x	x
Background ambient noise	x	x
Photoelectron noise	x	x
Dark (-current) noise	x	x
Gain noise		x
Thermal (Johnson) noise		x

Table 1.1. *Type of noise encountered in lidar measurement depending on the detection mode .*

The signal entering the detector (input signal) has an intrinsic photon (quantum) noise. The photoeffect converts the photons into photoelectrons. In the process, the mean signal decreases by a factor equal to the quantum efficiency of the detector. The noise decreases also but by a lesser amount than the signal. If a photodetector gain mechanism is present, it amplifies both the signal and the photoelectron noise, and introduces its own gain noise as well. Finally, circuit noise enters at the point of current collection. The background ambient noise is the noise associated with light reaching the detector from extraneous sources, i.e. from sources other than the signal of interest. The dark-current noise is generated by the photodetection device even in the absence of light.

Careful evaluation of noises is of very high importance in remote sensing. It prevents from mis-interpretation, because they may appear as to be a signal while they are actually not real. In order to understand their source and their behaviour they are discussed now.

1.3.3.1 Backscatter signal and quantum noise

Let $P_s(t)$ be the optical power of the backscatter signal impinging onto the detector (in [W]; cf. equation (1-7)). In case of photon counting detection, the number of photons $N_s(t,\tau)$ counted during the integration period τ is

$$N_s(t,\tau) = \xi_d \tau \cdot P_s(t) \qquad \text{where} \qquad \xi_d = \frac{\eta}{h\nu}. \tag{1-15}$$

The conversion factor ξ_d indicates the number of photoelectrons created per unit of optical energy for the considered detector. η is the detector quantum efficiency at the detected optical frequency ν, h the Plank constant. This equation is valid as long as the photon count rate $N_s(t,\tau)/\tau$ is smaller than the linear count rate maximum value of the detector and its following electronics.

In analog detection, the related current $i_s(t)$ (in [A]) *at the output of the detector* is

$$i_s(t) = \rho_d G_d \cdot P_s(t) \qquad \text{where} \qquad \rho_d = \frac{\eta e}{h\nu}. \tag{1-16}$$

ρ_d is the responsivity of the photodetector (in [A/W]), G_d denotes its gain* and e is the electron charge.

The photon flux associated with the optical power impinging onto the detector $P_s(t)$ is inherently uncertain due to the quantum nature of this signal. Thus a noise is generated. This noise is called *quantum* or *photon noise* because it is induced by the signal only when the signal exists. It obeys the Poisson probability distribution, under assumption that photon arrivals are statistically independent. A photon incident on the photodetector either generates a photoelectron† with probability η or fails to do so with probability 1-η. The *photoelectron noise* refers to the resulting fluctuations. Considering that the generation of photoelectron behaves in accordance with an independent random trial (Bernouilli), it may be shown that photoelectrons follow Poisson distribution [Sale91] as well.

The quantum noise is given by the root-mean-square fluctuation of the received signal $\sigma(N_s)$. For Poisson distribution, the variance fluctuation σ^2 is equal to the (mean) value of the signal itself. In case of photon-counting mode, this is written as

$$\sigma^2(N_s) = N_s. \tag{1-17a}$$

---

* Typical gain values for photomultiplier tubes are 10^5-10^6 and 30-100 for avalanche photodiodes.

† We should rather speak of “photoevent” to include both generation of photoelectrons in the case of PMT and photoelectron-hole pair in the case of APD.

In analog mode, the photon stream incident on the detector results in a stream of electrical pulses which add together to constitute the electric current $i_s(t)$. The fluctuations associated with this current and attributable to the random way in which electrons are emitted or generated in the detector form a noise named *shot noise*.

Using equations (1-15) and (1-17a)*, the current fluctuation is

$$\sigma^2(i_s) = 2eBG_d\mu i_s\,. \tag{1-17b}$$

B has been introduced as the photodetection *electrical bandwidth* and defined as $B = 1/(2\tau)$. μ is added as an *excess noise coefficient* (also called *excess noise factor*). It accounts for the *gain noise* contributions during the amplification process. The gain is not a fixed value and deterministic but fluctuates randomly. This contribution to the total noise level is important in the case of analog detection with an APD – $\mu \sim 3\text{-}7$, or more –, while a PMT has better noise performances – $\mu \cong 1$ in photon counting detection mode and less than 2 in analog detection mode.

1.3.3.2 Background radiation and background noise

The ambient background light is due to natural and artificial sources: sun, moon, lamps, etc. It consist in fact of any undesired optical radiation on the receiver. The power $b(t)$ of the received background radiation (arising from natural sources) is given as

$$b(t) = K_r S_b(\lambda)\Delta\lambda\Omega_r A \tag{1-18}$$

where K_r is a constant expressing the optical efficiency of the receiver, $S_b(\lambda)$ the spectral radiance from the sky at the instrument location and instant t (in [Wm^{-2}sr^{-1}µm^{-1}]), $\Delta\lambda$ the optical bandwidth of the receiver (in [µm]), Ω_r the receiver field of view (in [sr]) and A the effective aperture area of the receiver (in [m^2]). If θ is the full divergence of the receiver,

$$\Omega_r = \pi\left(\frac{\theta}{2}\right)^2. \tag{1-19}$$

In a similar way as for the backscatter signal but this time for the background radiation, the number of photons $N_b(t,\tau)$ detected during the integration period τ and the current i_b at the output of the photodetector are

$$N_b(t,\tau) = b(t)\xi_d\tau \qquad \text{and} \qquad i_b(t) = b(t)\rho_d G_d\,. \tag{1-20}$$

* If s is a variable that follows Poisson statistic, then $E\left[(k(s-\bar{s}))^2\right] = k^2\bar{s} = k(k\bar{s})$. N_s is such a variable. Here we have $i_s = N_s e G_d/\tau$. More precise and exact derivation of this formulae may be found in [Yari91, Sale91].

In comparison to P_s , P_b varies much less as function of the time. Of all parameters it depends on, $S_b(\lambda)$ is the one which fluctuates the most. While the duration of the atmospheric response to a single laser pulse is typically of the order of the millisecond, the sky radiance change rate will rather be of the order of the second or more. For this reason the background radiation is considered as constant during the acquisition of a single profile and its time-dependency may be neglected; it contributes as a constant offset to the total measured signal. In this sense it is of less importance.

Much more important are the fluctuations caused by the background radiation, that is the quantum or shot noise of the background radiation component. As it is an optical signal, it causes also fluctuations in the same way as the backscatter signal. These fluctuations, on analogy with equations (1-17) are given in photon-counting, respectively analog, detection mode by

$$\sigma^2(N_b) = N_b \qquad \text{and} \qquad \sigma^2(i_b) = 2eBG_d\mu i_b\,. \qquad (1\text{-}21)$$

What is usually called background noise is not the background radiation itself but the fluctuations that it induces.

1.3.3.3 Dark current and dark noise

The dark current is the leakage current produced by the photodetector when no radiation is incident upon the surface. It is mostly generated by thermal release of electrons from the semiconductor constituents of the photodetector and is consequently strongly dependent on the their temperature. This current, at the output of the photodetector and further referred to as i_d , is also associated to the term *dark counts* in photon-counting detection mode because it consists of small pulses that are distinct from each other when sufficiently rare. The dark count level, *d*, is usually provided per time unit, i.e. dark counts per second.

Let $N_d(t,\tau)$ be the number of dark counts during the integration period τ .

$$N_d(t,\tau) = d\tau \qquad (1\text{-}22)$$

As the dark current is of randomness nature, the variance of its fluctuations in photon-counting, respectively analog detection mode, are again given by

$$\sigma^2(N_d) = N_d \qquad \text{and} \qquad \sigma^2(i_d) = 2eBG_d\mu i_d\,. \qquad (1\text{-}23)$$

Here again, the dark current itself is of few importance because its change rate is much smaller than the duration of a profile and may be considered as constant, acting like an offset. Its fluctuations are of meaning; they are further simply called *dark noise*.

1.3.3.4 Thermal noise

The *thermal* or *Johnson noise* is associated with the thermal agitation of the current carriers in the load resistance R_{ld} (more precisely equivalent resistance depending on the pre-amplifier configuration) at the output circuit of the photodetector. It exists therefore only in the analog detection mode. The mean value of this thermal current i_{th} is 0 but not its fluctuations – actually referred to by the term thermal noise – which variance is given by [Yari91].

$$\sigma^2(i_{th}) = \frac{4kT_{ld}B}{R_{ld}}, \tag{1-24}$$

where k is the Boltzmann constant, T_{ld} the absolute temperature of the resistance, and B, as previously mentioned, the photodetection electrical bandwidth.

1.3.3.5 Other noises

Only the principal noises have been enumerated here. Yet other noises exist. One is due for instance to the presence of an electronic amplifier [Over95]. The associated electronic-amplifier noise is much like the thermal noise. Its variance $\sigma^2(i_{ea})$ is equal to

$$\sigma^2(i_{ea}) = \frac{4kT_{ea}B_{ea}}{R_{ea}}. \tag{1-25}$$

T_{ea} is the effective noise temperature ($T_{ea}=T(NF\text{-}1)$ where NF is the noise figure of the amplifier; its value is typically 175-190K). B_{ea} is the bandwidth of the amplifier and R_{ea} its equivalent resistance.

Electrically induced noises are another kind of noises and may be important in analog detection mode. An example is the noise induced by the high current pulses in the flash lamps of some Q-switched lasers. These current pulses may be as long as 10-100µs what corresponds to lidar ranges of 1.5-15km. The detected signal profile may be significantly affected. As these perturbations are rather constant for a given configuration of the lidar instrument – acquisition parameters included – they can be measured in absence of any optical signal and then subtracted from real profile measurements.

1.3.4 Response function

The response signal $y(t)$ received from a linearly responding system can be generally presented as a convolution of the probing signal $x(t)$ and the response function $g(t)$ of the probed medium:

$$y(t) = \int_{-\infty}^{+\infty} x(t-t')g(t')dt' + b(t) \tag{1-26}$$

In this equation, $b(t)$ represents the noise at time t.

As the atmosphere or a hard target scatters linearly in respect to the amount of incident radiation, this principle may be applied to lidar measurements. In this case, t is the response time of the probed target medium relative to the instrument, $x(t)$ the power of the probing laser pulse, $y(t)$ the optical power falling on the detector and $b(t)$ the background radiation*. The response function $g(t)$ – its unit is [s^{-1}] – is derived from the lidar equations (1-7) and (1-14):

$$g(t) = KO(r)\frac{A}{r^2}\frac{c}{2}\beta(r)\exp\left\{-2\int_0^r \alpha(r')dr'\right\} \qquad \text{with} \qquad r = \frac{ct}{2} \tag{1-27}$$

in the case of the *atmosphere*, and

$$g_{sur}(t) = KO(r_{sur})\frac{A}{r_{sur}^2}\frac{a}{\pi}\exp\left\{-2\int_0^{r_{sur}} \alpha(r')dr'\right\}\cdot\delta\left(t - 2\frac{r_{sur}}{c}\right) \tag{1-28}$$

in the case of an *extended hard target or surface*, where δ is the Dirac delta function.

To derive the lidar equation (1-7), the probing signal, i.e. the laser pulse, was assumed to be a short pulse. It may be approximated by a rectangular shape $x(t)$

$$x(t) = \frac{E_0}{\tau_L}\text{Rect}\left[\frac{t}{\tau_L}\right], \quad \text{where} \quad \text{Rect}[t] = \begin{cases} 1, & 0 \le t < 1 \\ 0, & \text{elsewhere.} \end{cases} \tag{1-29}$$

As previously defined, E_0 is the energy of the pulse and τ_L its duration. Expressed in function of $g(t)$, the backscatter signal power $P_s(t)$ falling on the detector is then

$$P_s(t) = E_0 g(t)\,. \tag{1-30}$$

Thus the response function is directly detected as the lidar response in the pulsed or "direct detection" lidar technique.

1.3.5 PRN-cw technique: probing signal, modulation, demodulation

In the PRN-cw technique, the amplitude of the emitted light is modulated according to a well defined code. The response function of the target is then recovered by taking the cross-correlation of the detected signal with this modulation code. The principles of the

---

* Only the optical power impinging onto the detector is here considered. It might also have been possible to define y as the detected photon rate at the output of the detector or the current flowing out of the detection circuit. In this case additional multiplication factors and noise components shall be introduced (cf. Section "Contributions to the total measured signal from ambient background and noises", equations (1-15) and following).

modulation and demodulation in PRN-cw lidar are presented here according to the procedure described in [Take83] and [Take86].

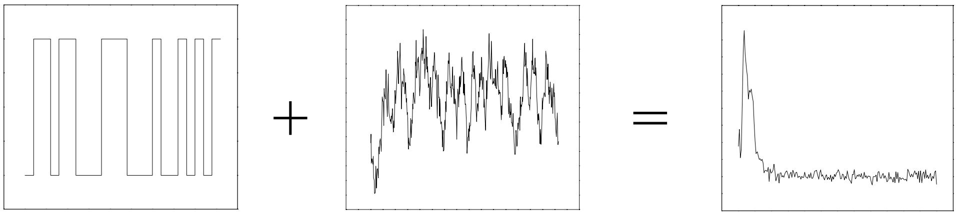

Figure 1.1. *PRN-cw lidar principle. The response function of the atmosphere is obtained by cross-correlation of the modulation code with the detected signal. The detected signal and its related response function presented here are real.*

The modulation of the transmitted probing signal with continuous-wave laser output power P_0 is assumed in the form

$$x(t) = P_0 \sum_{n=0}^{N-1} a_n \mathrm{Rect}\left[\frac{t - n\tau_c}{\tau_c}\right] \tag{1-31}$$

with the function Rect as defined in (1-29). The parameter τ_c is the unit time bin or clock-period of the modulation; it is reverse proportional to the frequency bandwidth of the amplitude modulation. a_n are elements of a sequence and equal to 1's and 0's (binary sequence).

An important requirement for the sequence a_n , n=0,1,...,N-1, is that the correlation function $\Psi_{a,a}(j)$, defined by

$$\Psi_{a,a}(j) = \sum_{n=0}^{N-1} a_n a_{n+j} \qquad (\text{modulo N}), \tag{1-32}$$

is delta-function-like. When this requirement is fulfilled, the demodulation of the detected signal is performed by cross-correlation with the original modulation sequence.

Convenient modulation codes are provided by *maximum shift register sequences*, called also *M-sequences* (the literature on this subject is large; see for instance [Araz88, Golo67, Holm82, Mink92, Skol90]). Main advantages of M-sequences are that they are generated in a simple way by a linear shift register, they can be arbitrarily long and are cyclic – what allows long measurement duration. If n is the number of stages in the shift register, the period of the M-sequence N is

$$\mathrm{N} = 2^{\mathrm{n}} - 1. \tag{1-33}$$

It consists in (N+1)/2 "ones" and (N-1)/2 "zeros". M-sequences are called *pseudo-random noise* sequences because they have similar properties like purely random sequences but yet an internal logic. The auto-correlation function of such sequences is delta-function like.

It is suitable to use for demodulation of the backscattered signal a sequence a'_n which is developed from the original M-sequence a_n using the following transformation

$$a'_n = 2a_n - 1 \qquad (a'_n = 1 \text{ or } 1). \tag{1-34}$$

The auto-correlation function $\Psi_{a',a'}(j)$ of such sequence, as defined in equation (1-32), takes then the values

$$\Psi_{a',a'}(j) = \begin{cases} N, & j = 0 \\ -1, & j \neq 0 \end{cases} \quad (\text{modulo N}). \tag{1-35}$$

It can be shown [Golo64] that this is the best possible auto-correlation function of any binary sequence of length N, in the sense of minimising $\max_{0<j<N} \Psi_{a',a'}(j)$.

The (cross-) correlation function between a'_n and a_n is $\Psi_{a,a'}(j)$:

$$\Psi_{a,a'}(j) = \sum_{n=0}^{N-1} a_n a'_{n+j} = \begin{cases} \dfrac{N+1}{2}, & j = 0 \\ 0, & j \neq 0 \end{cases} \quad (\text{modulo N}). \tag{1-36}$$

The right-hand side of Equation (1-36) is typical of the delta-function nature of pseudo-random noise correlation.

Let the return signal from the atmosphere $y(t)$, the background radiation power $b(t)$ and the atmospheric response function $g(t)$ be represented in the following series form

$$y(t) = \sum_{n=0}^{N-1} y_n \text{Rect}\left[\frac{t - n\tau_c}{\tau_c}\right], \qquad b(t) = \sum_{n=0}^{N-1} b_n \text{Rect}\left[\frac{t - n\tau_c}{\tau_c}\right],$$

$$G(t) = \tau_c g(t) = \sum_{n=0}^{N-1} \tau_c g_n \text{Rect}\left[\frac{t - n\tau_c}{\tau_c}\right]. \tag{1-37}$$

y_n, b_n, g_n are the values of the functions $y(t)$, $b(t)$, $g(t)$ taken at time $t = n\tau_c$. The function $G(t)$ is non-dimensional. Following the definition of $\text{Rect}[t]$, the elements y_n, b_n and $G_n = \tau_c \cdot g_n$ are circular (modulo N). Using equation (1-37), equation (1-26) simplifies to the form

$$y_n = P_0 \sum_{j=0}^{N-1} a_{n-j} G_j + b_n \,, \tag{1-38}$$

or $$y_n = \tilde{y}_n + b_n \qquad \text{where} \qquad \tilde{y}_n = P_0 \sum_{j=0}^{N-1} a_{n-j} G_j \,.$$

When the transmission of the probing signal is repeated over L sequences of the same kind, the resulting signal, averaged over L sequence, is

$$\bar{y}_n = \frac{1}{L} \sum_{k=1}^{L} y_{n+(k-1)N} \,. \tag{1-39}$$

Time average values normalised to one sequence are denoted by a " $-$ ". We define as $\bar{S}_i$ the cross-correlation function of the averaged signal $\bar{y}_n$ and the sequence a'_n,

$$\bar{S}_i = \sum_{n=0}^{N-1} \bar{y}_n a'_{n-i} \,. \tag{1-40}$$

By using the expressions of the equations (1-36) to (1-39) in (1-40), the cross-correlation in the time cell i of the probed profile is obtained:

$$\bar{S}_i = P_0 \frac{N+1}{2} \bar{G}_i + \bar{b} \qquad \text{where} \qquad \bar{b} = \sum_{n=0}^{N-1} \bar{b}_n a'_{n-i} \,. \tag{1-41}$$

$\bar{b}$ is the mean background radiation value and is equal to the ensemble average of the $\bar{b}_i$'s. It acts as an offset that may be subtracted. $\bar{S}_i$ is the equivalent PRN-cw optical signal power in front of the detector. As $\bar{G}_i = \tau_c \bar{g}_i$ and $E_0 = P_0 \tau_c$,

$$\bar{S}_i = \underbrace{E_0 \frac{N+1}{2} \bar{g}_i}_{signal} + \underbrace{\bar{b}}_{\substack{background\\radiation}} \,. \tag{1-42}$$

Comparing (1-42) with (1-30), it comes out that in the PRN-cw technique, *the cross-correlated signal is $(N+1)/2$ times larger than the same signal measured for a single pulse of the same energy*; this is because $(N+1)/2$ pulses are emitted during a sequence instead of a single one. It is a very nice result; the signal did increase by a factor of N ! However, as it will be seen later in the section dedicated to the signal-to-noise ratio evaluation (cf. page 24) that the noise also becomes larger.

After subtraction of $\bar{b}$, as $\bar{S}_i$ is proportional to $\bar{g}_i$, further parameters of the backscattering layers can be derived (cf. equations (1-27), (1-28) and (1-37)).

What happens if we integrate the cross-correlated profile, that is if we sum $\bar{S}_i$ overall i ? In the resulting sum of the right member of equation (1-40), the sums over i and n may be swapped. Recording that there is one more 1 than 0, resp. -1, in the sequence a_n, resp. a'_n the sum over the a'_n is 1. Remained then only the sum of $\bar{y}_n$ over n. Thus the integral of the cross-correlated signal is equal to the integral of the acquired signal.

The (cross-) correlation mathematical operation imposed the following:

- The number of acquisition samples shall be equal to the length of the sequence.
- The sequence elements and the sampling time intervals shall all be of equal duration.
- The sequence and the signal acquisition shall develop exactly the same way: passing from one sequence element to the next means passing from one acquisition sample to the next. Sequence modulation and acquisition procedure shall be synchronised.
- When a sequence finishes, the next must start without delay; there should be not interruption or deadtime between them.

These requests should be particularly respected during a real measurement because signal averaging is usually performed. Shouldn't they that unexpected results may arise.

The length of the sequence has to be chosen taking into account the range to be covered in the atmosphere. The sequence must be long enough to allow unambiguous range determination. In fact, the mathematical operation modulo is not respected by the light: when a slight amount of light reaches the distance $\mathrm{N}\cdot c\tau_c/2$, it does not restart from 0; it follows its path forwards to upper layers. The atmosphere may be imagined cut in $\mathrm{N}\cdot c\tau_c/2$-meter thick layers which add themselves one to the other: the response from sample i is actually the summed response from samples $i+(i+\mathrm{N})+\ldots+(i+\mathrm{kN})+\ldots$ to previous emitted sequences. Thus the sequence length should be long enough for the contributions from the upper layers (k>0) to be negligible in respect of the first layer (k=0). We call the minimal range fulfilling this requirement the "*critical distance*".

It may be argued that the principle of the PRN-cw technique has been proven on a very simplified case: only the received optical power falling on the detector – but still not converted into electrical signal – has been considered and in presence of the background radiation only. Actually the signal should first be detected, then likely amplified, and other sources of noise might be present. However, if the detection, amplification and acquisition stages are linear, the upper demonstration of the principle will not change. As result, only multiplication factors and other noise components added to $b(t)$ will finally have been introduced in equation (1-41). For instance, in photon-counting detection mode, the number of equivalent PRN-cw detected backscattered photons is

$$\overline{N}_{s,cw}(i) = \frac{N+1}{2}\xi_d \tau_c^2 P_0 \overline{g}_i \,, \tag{1-43}$$

while the equivalent PRN-cw current in analog mode is given by

$$\bar{i}_{s,cw}(j) = \frac{N+1}{2} \rho_d G_d \tau_c P_0 \bar{g}_j .^{*} \qquad (1\text{-}44)$$

It is worth to compare these equations with their corresponding pulsed lidar equivalents (1-15) and (1-16). Remembering that in the pulsed case $P_s(t) = E_0 g(t)$, we see that they are identical up to a factor $(N+1)/2$. However, in the above equations, $(N+1)/2\,\tau_c P_0$ is the energy emitted during one sequence. It follows that if for both types of lidar the emitted energy per second is the same, the cross-correlated number of detected photons (resp. current) in the PRN-cw mode is equal to the number of direct detected photons (resp. current) in the pulsed mode .

1.3.6 Signal-to-noise ratios

In this section the signal-to-noise ratio (SNR) of a lidar measurement is presented and discussed for both analog and photon-counting detection modes and for both pulsed and PRN-cw techniques. The SNR is defined in the usual way by

$$SNR = \frac{S}{\sqrt{\sum_{noises\ k} \sigma_k^2}} , \qquad (1\text{-}45)$$

where S is the backscatter signal only[†]; the σ_k's are the standard deviations of the noises. The denominator is the total noise standard deviation and may be expressed this way because all sources of noise are independent from each other. In order to improve the quality of the measurement and hence the SNR, the lidar signal is usually averaged over L successive laser pulses or sequences. The SNR is then

$$SNR = \sqrt{L} \cdot \frac{S}{\sqrt{\sum_{noises\ k} \sigma_k^2}} . \qquad (1\text{-}46)$$

1.3.6.1 Pulsed SNR

Following this definition of the SNR and referring to section 1.3.3 for the values of the signal and noises in the case of a pulsed lidar, we get for photon-counting and analog detection modes

---

[*] For analog detection mode, index i is changed to j in order not to be confused with the current variable.

[†] It is assumed that offsets due to background radiation or dark current and electrically induced noises can be subtracted from the total measured signal.

$$SNR_{pulsed}^{phc}(i) = \sqrt{L}\,\frac{\overline{N}_s(i)}{\sqrt{\overline{N}_s(i) + \overline{N}_b + \overline{N}_d}} \tag{1-47}$$

and

$$SNR_{pulsed}^{analog}(j) = \sqrt{L}\,\frac{\bar{i}_s(j)}{\sqrt{\dfrac{4kT_{ld}B}{R_{ld}} + 2eBG_d\mu\left(\bar{i}_s + \bar{i}_b + \bar{i}_d\right)}}\,. \tag{1-48}$$

Signals and noises may be measured and the signal-to-noise ratios evaluated. The estimation of the analog signal-to-noise ratio requests a signal current value measured in DC because the fluctuations stemmed from the total number of photoelectrons and not from their AC-component only.

It is also very interesting to examine how signal-to-noise ratios depend on the instrument parameters. It is done hereafter for the photon-counting case only, as it is also valid for the analog case. Referring again to equations of section 1.3.3, it may be written

$$SNR_{pulsed}^{phc}(i) = \sqrt{L}\,\frac{\xi_d \tau E_0 \bar{g}_i}{\sqrt{\tau\left(\xi_d E_0 \bar{g}_i + \xi_d \bar{b} + \bar{d}\right)}} \tag{1-49}$$

The number L of laser pulses is linked to the total integration time T through the relation $L=Tf_s$, where f_s is the laser shot repetition rate. If $P_0=E_0 f_s$ is the mean power of the laser, the SNR is

$$SNR_{pulsed}^{phc}(i) = \sqrt{T\tau}\,\frac{\xi_d P_0 \bar{g}_i}{\sqrt{\xi_d P_0 \bar{g}_i + f_s\left(\xi_d \bar{b} + \bar{d}\right)}} \tag{1-50}$$

This equation is important because it describes in details how and on which parameters depends the quality of a measurement. Showing explicitly the instruments parameters contained in $\bar{g}_i$ and $\bar{b}$ (cf. equations (1-27) and (1-18)) and omitting atmospheric attenuation, the signal-to-noise ratio may be expressed as

$$SNR_{pulsed}^{phc} \sim \sqrt{T\tau}\,\frac{\xi_d P_0 A O(r)}{\sqrt{\xi_d P_0 A + f_s\left(\xi_d \Delta\lambda \theta^2 A + \bar{d}\right)}}\,. \tag{1-51}$$

The instrument parameter dependency is presented in this last equation. Conception of traditional pulsed lidars in the frame of this work was based on this equation and lidar signal numerical simulations.

1.3.6.2 PRN-cw SNR

To evaluate the SNR of a PRN-cw measurement, we have to evaluate the variance V_i for the cross-correlated (demodulated) signal at location i, derived from the lidar signal y_n, accumulated over the time duration of one sequence. In order not to complicate the formulas by too many terms, we consider again only the optical power – backscatter signal and background radiation – impinging onto the detector. From equation (1-40), we obtain

$$V_i = E\left[\left(s_i - \bar{s}_i\right)^2\right] = E\left[\left(\sum_{n=0}^{N-1} a'_{n-i}\left(y_n - \bar{y}_n\right)\right)^2\right]. \tag{1-52}$$

The received signal and the background being statistically independent from each other, it may be written

$$V_i = E\left[\left(\sum_{n=0}^{N-1} a'_{n-i}\left(\tilde{y}_n - \bar{\tilde{y}}_n\right)\right)^2\right] + E\left[\left(\sum_{n=0}^{N-1} a'_{n-i}\left(b_n - \bar{b}_n\right)\right)^2\right]. \tag{1-53}$$

Considering the properties of the PRN sequence a', the development of the squares of the sums results in

$$V_i = \sum_{n=0}^{N-1} E\left[\left(\tilde{y}_n - \bar{\tilde{y}}_n\right)^2\right] + \sum_{n=0}^{N-1} E\left[\left(b_n - \bar{b}_n\right)^2\right]. \tag{1-54}$$

As light detection and conversion into electrical current follows Poisson statistics*,

$$E\left[\left(\tilde{y}_n - \bar{\tilde{y}}_n\right)^2\right] = \frac{1}{\xi_d \tau_c}\bar{\tilde{y}}_n \qquad \text{and} \qquad E\left[\left(b_n - \bar{b}_n\right)^2\right] = \frac{1}{\xi_d \tau_c}\bar{b}_n \ , \tag{1-55}$$

where ξ_d is the conversion coefficient from the received optical power into number of photoelectrons per unit of time as defined in equation (1-15). τ_c is the integration time and is equal to the clock-period of the modulation in the PRN-cw technique. From equations (1-38) and (1-41), we may write for the variance

$$\begin{aligned} V_i &= \frac{1}{\xi_d \tau_c}\left\{\sum_{n=0}^{N-1}\bar{\tilde{y}}_n + \sum_{n=0}^{N-1}\bar{b}_n\right\} = \frac{1}{\xi_d \tau_c}\left\{\sum_{n=0}^{N-1}\left(P_0 \sum_{i=0}^{N-1} a_{n-i}\overline{G}_i\right) + N\bar{b}\right\} = \\ &= \frac{1}{\xi_d \tau_c}\left\{\frac{N+1}{2} P_0 \sum_{n=0}^{N-1}\overline{G}_n + N\bar{b}\right\} \end{aligned} \tag{1-56}$$

or

* Cf. note * on page 16.

$$V_i = \frac{N}{\xi_d \tau_c}\left\{\frac{N+1}{2}P_0\tau_c\bar{g} + \bar{b}\right\} \qquad \text{where} \qquad \bar{g} = \frac{1}{N}\sum_{n=0}^{N-1}\bar{g}_n \ . \tag{1-57}$$

$\bar{g}$ represents the mean atmospheric response. An important feature is that V_i is independent of any index so that *the cross-correlate noise is range-independent for a PRN-cw lidar* what is not the case in pulsed lidar.

This formula can be explained intuitively. In order to compute the atmospheric response function we needed to sum – during the cross-correlation process – over all samples of the recorded signal. Thus the cross-correlated variance is the sum of the individual variances of the N recorded samples as they are independent from each other. The factor $(N+1)/2$ is explained by the fact that the signal of a single sample consists of all $(N+1)/2$ small pulses of a sequence backscattered by the mean atmospheric response value.

Variance V_i is the variance of the optical power impinging onto the detector. In photon-counting detection mode , the variance of the number of detected photons is obtained by replacing the factor $1/\xi_d\tau_c$ by $\xi_d\tau_c$. In this case, V_i , as sum of the individual variances, is equal to the total number of measured photons. In fact $N\cdot\xi_d\tau_c(N+1)/2P_0\tau_c\bar{g}$ is the total number of detected backscattered photons and $N\cdot\xi_d\tau_c\bar{b}$ the total number of detected background noise photons – the factor N refers to the single elements of the sequence while the remaining parts are the detected photons for a single element (bin) of duration τ_c.

As the cross-correlate noise is range-independent for a PRN-cw lidar and is equal to the total detected signal, small atmospheric response may be lost in the noise, particularly if a strong response – like the one of a hard target – is also present.

In a general form, we may write for photon-counting mode

$$SNR_{cw}^{phc}(i) = \sqrt{L}\,\frac{\overline{N}_{s,cw}(i)}{\sqrt{N\left(\overline{N}_s + \overline{N}_b + \overline{N}_d\right)}}, \tag{1-58}$$

where $\overline{N}_s$ is the mean value of the detected backscattered photon number and $\overline{N}_{s,cw}(i)$ the cross-correlated backscattered photon number for sample *i*. In analog mode, in a similar way,

$$SNR_{cw}^{analog}(j) = \sqrt{L}\,\frac{\bar{i}_{s,cw}(j)}{\sqrt{N\left(\frac{4kT_{ld}B}{R_{ld}} + 2eBG_d\mu\left(\bar{i}_s + \bar{i}_b + \bar{i}_d\right)\right)}}, \tag{1-59}$$

where $\bar{i}_s$ is the mean measured signal current* and $\bar{i}_{s,cw}(j)$ the cross-correlated signal current for sample *j*.

From equations (1-43) and (1-46) and taking into account the dark noise, the signal-to-noise ratio of the PRN-cw signal averaged on L sequences in photon-counting detection mode is

$$SNR_{cw}^{phc}(i) = \sqrt{L}\,\frac{\xi_d \tau_c^2 P_0 \dfrac{N+1}{2}\bar{g}_i}{\sqrt{N\tau_c\left\{\xi_d \tau_c P_0 \dfrac{N+1}{2}\bar{g} + \xi_d \bar{b} + \bar{d}\right\}}}\,. \tag{1-60}$$

The number L of sequences is linked to the total integration time T through the relation $T = LN\tau_c$. Assuming the sequence length $N >> 1$†, we obtain

$$SNR_{cw}^{phc}(i) = \sqrt{T\tau_c}\,\frac{\xi_d \dfrac{P_0}{2}\bar{g}_i}{\sqrt{\xi_d \dfrac{P_0}{2} N\,\bar{g} + f_{cw}\left(\xi_d \bar{b} + \bar{d}\right)}}\,, \tag{1-61}$$

with $f_{cw} = 1/\tau_c$, the modulation frequency of the cw laser light.

For real PRN-cw measurements, it will be noticed later (cf. Chapter 3) that cross-correlated photon numbers are sometimes negative. This is artefact due to the cross-correlation using 1's and –1's sequence and does not have any real physical meaning. It happens when the noise fluctuations are larger than the sum of the cross-correlated signal itself and the mean noise value (cf. Equation (1-42)), i.e. when the SNR is smaller than 1.

1.3.6.3 PRN-cw SNR dependence on sequence length

The unique dependency on N in the previous equation is in the expression $N\bar{g}$. As N must have be chosen to cover the "critical distance",

$$\exists N_* < N-1 \,|\, \sum_{n=0}^{N_*-1} \bar{g}_n >> \sum_{n=N_*}^{N-1} \bar{g}_n\,. \tag{1-62}$$

Signals coming from long ranges are negligible in confrontation to the ones from near ranges. Therefore *the PRN-cw SNR does not depend on the length of the sequence.*

---

* Here again, the estimation of the signal-to-noise ratio requests a signal current value measured in DC because the fluctuations stemmed from the total number of photoelectrons and not from their AC-component only.

† This is usually the case as N should be long enough for the sequence to cover the "critical distance" (cf. p. 23). N is typically ≥ 511 (8-bit sequence or more).

1.3.6.4 PRN-cw and pulsed SNR comparison

Having computed the signal-to-noise ratio for both types of lidar, it is now possible to compare them. Let's do it for the photon-counting case. We see that the SNR ratios, given by equations (1-50) and (1-61), are very similar in form. If all measurement parameters are the same for both systems,

$$\frac{SNR_{pulsed}}{SNR_{cw}}(i) = \frac{P_{0,pulsed}}{P_{0,cw}/2} \cdot \frac{\sqrt{\xi_d \frac{P_{0,cw}}{2} N\,\bar{g} + f_{cw}\left(\xi_d \bar{b} + \bar{d}\right)}}{\sqrt{\xi_d P_{0,pulsed}\bar{g}_i + f_s\left(\xi_d \bar{b} + \bar{d}\right)}}. \tag{1-63}$$

where $P_{0,\,pulsed}$ and $P_{0,\,cw}$ are the mean power of the pulse and cw lasers. The dark count level is assumed to be much smaller than the background noise value, what is usually the case. Then

$$\frac{SNR_{pulsed}}{SNR_{cw}}(i) = \frac{P_{0,pulsed}}{P_{0,cw}/2} \cdot \frac{\sqrt{\frac{P_{0,cw}}{2} N\,\bar{g} + f_{cw}\bar{b}}}{\sqrt{P_{0,pulsed}\bar{g}_i + f_s\bar{b}}}. \tag{1-64}$$

When the powers $P_{0,\,pulsed}$ and $P_{0,\,cw}$ are of comparable value, this ratio is then bigger than 1. From a theoretical point of view, for equivalent instrument component characteristics the pulsed method always yields better results than the PRN-cw one. This is due to the fact that in the pulsed method the error on the signal at a given height is due only to the fluctuations of the signal at this range or height; on the contrary, in the PRN-cw method, as all samples are needed to reconstruct the atmospheric signal at a given range or height, the fluctuations of all samples add to each other. More, as $f_{cw} >> f_s$, the PRN-cw signal is much more sensitive to the background radiation. This is because the ratio backscattered photons-to-background noise photons is much smaller in the PRN-cw case.

However the power of the laser is one parameter of a lidar; one very important, but one among others. For some applications, the environment in which a lidar instrument shall work imposes strong constrains that must be observed: small volume availability, limited weight and power consumption, long-term reliability , eye-safety, laser life-time, … Diode lasers might then be preferable or the only possibility (cf. Chapter 5, section 5.2). They usually show narrower wavelength bandwidth, what allows the use of optical filters with narrower bandwidth as well, like illustrated in Chapter 5, section 5.1.

If only a cw-laser diode is available, shall it be used in PRN-cw or in pulsed mode ? If P_0 is the power of the cw-laser diode, the mean used power in pulsed mode is P_0/N because the pulse repetition rate f_s is equal to f_{cw}/N. N is the minimal sequence length possible to cover the "critical distance"*. In this case, equation (1-64) simplifies to

* The "critical distance" is a concept valid for both types of lidar. In PRN-cw mode, it may happen that a n-bit sequence is just too short to cover the critical distance, so that an at least (n+1)-bit sequence should be used. In the pulsed case, the pulse repetition rate may be chosen to cover precisely the "critical distance".

$$\frac{SNR_{pulsed}}{SNR_{cw}}(i) = \sqrt{2} \cdot \frac{\sqrt{P_0\,\bar{g} + \frac{2 f_{cw}}{N}\bar{b}}}{\sqrt{P_0 \bar{g}_i + f_{cw}\bar{b}}} . \tag{1-65}$$

For night-time, assuming $\bar{b} \approx 0$, stronger backscattering layers ($\bar{g}_i > 2\bar{g}$) are better detected in PRN-cw mode than in pulsed mode. The situation is reversed for weaker backscattering layers ($\bar{g}_i < 2\bar{g}$). If some background light is present, like during day-time, PRN-cw measurement mode is even more preferable. Of course, all this has a sense only if the individual signal-to-noise ratios SNR_{pulsed} and SNR_{cw} are larger than 1 for the considered layers. In resume, PRN-cw modulation of a cw-laser diode provides in most cases better results than pulsing a cw-diode laser.

A pulsed laser diode used in a pulsed lidar has an emitting area larger by two orders of magnitude than the cw one for comparable mean power. Respectively, the transmitting optics has two orders of magnitude larger dimensions.

1.3.7 Depolarisation lidar

Not all particles present in the atmosphere are spherical. Spherical and non-spherical particles may however be distinguished between them because non-spherical particles change the polarisation of the probing laser light. If a laser with linear polarised light is used and the backscattered light detected in two polarisation plans, one parallel to the polarisation of the transmitted beam ("parallel polarisation", or "p-polarisation") and the other perpendicular to it ("perpendicular polarisation", or "s-polarisation"*), the depolarisation degree of the particles may be determined. So depolarisation elastic backscatter lidar measurements provide precious indications for the presence of non-spherical aerosol particles.

Two definitions exist for the depolarisation ratio, the volume and the aerosol depolarisation ratios [Cair99]. The volume depolarisation ratio does not separate the contributions from the molecular atmosphere and the aerosol particles. It is defined by †

$$\delta_{vol} = \frac{\beta_{mol}^{\perp} + \beta_{aer}^{\perp}}{\beta_{mol}^{//} + \beta_{aer}^{//}} , \tag{1-66}$$

and, assuming that the extinction of the light is independent from its polarisation, is obtained directly from the raw measured signals $P^{\perp}$ and $P^{//}$:

$$\delta_{vol} = K_d \frac{P^{\perp}}{P^{//}} . \tag{1-67}$$

Without making an important error – a factor of 2 at maximum – we set the pulse repetition rate to be equal to the shortest possible sequence repetition rate.

* The term "s-polarisation" stemmed from German: "senkrecht Polarisation".

† We consider as obvious that the depolarisation ratio depends on the altitude or range, all layers having their own properties. This is the reason why a "z"- or "r"-variable is not mentioned.

The constant K_d , called "calibration constant", corrects for the difference of efficiency of both detection channels; it is the ratio of the "p-polarisation" channel to the "s-polarisation" channel overall efficiencies. It may be obtained by rotating the polarisation of the emitted light by 45°, using a λ/4-plate for instance. This way the backscattered light intensity is equally divided between the two polarisation plans. Comparing the amount of totally unpolarised background radiation* detected by both polarisation channels is another method to determine the calibration constant. The volume depolarisation ratio is also sometimes defined as

$$\delta_{vol}^{tot} = \frac{\beta_{mol}^{\perp} + \beta_{aer}^{\perp}}{(\beta_{mol}^{//} + \beta_{aer}^{//}) + (\beta_{mol}^{\perp} + \beta_{aer}^{\perp})} = \frac{K_d P^{\perp}}{P^{//} + K_d P^{\perp}} \qquad (1\text{-}68)$$

In this case, δ_{vol}^{tot} cannot be bigger then 1 (=100%).

The main drawback of the volume depolarisation ratio is that it is difficult to compare data of various lidars together. In fact, the molecular part of the depolarised signal depends on the bandwidth of the optical filtering process. Besides elastic scattering of light by molecules, Raman rotational scattering shall also be taken into consideration. Pure Raman rotational lines are on both sides of the elastic line and close to it. If the optical filtering process may reject all rotation lines, the depolarisation ratio of the elastic line only is 0.365% [Wede97], while if it cannot, the depolarisation ratio is 1.44%.

In order to be able to compare data obtained by different lidar instruments, it is better to use the aerosol depolarisation ratio

$$\delta_{aer} = \frac{\beta_{aer}^{\perp}}{\beta_{aer}^{//}} \qquad \text{or} \qquad \delta_{aer}^{tot} = \frac{\beta_{aer}^{\perp}}{\beta_{aer}^{//} + \beta_{aer}^{\perp}} \qquad (1\text{-}69).$$

To compute the aerosol depolarisation ratio, the molecular depolarisation ratio shall be known as well as the scattering ratios for both p- and s-polarised signals shall be computed by inverting the lidar equation. In the frame of this work, we rather consider the volume depolarisation ratio as it may be directly computed from the measured signals.

Conclusion

The aim of this first chapter was to expose the principles of lidar remote sensing. Both pulsed and PRN-cw lidar techniques were described. A special emphasis was laid on the signal, noise and signal-to-noise equations. We did it so because, in the perspective of numerically simulating and building compact lidars, it is worth to understand how important is each instrument parameter. Compactness means less powerful instrument; but in com-

* Such atmospheric optical conditions happen when the sky is fully covered by dark-grey dense clouds. Solar light reaching the ground is usually partially polarised. The presence of thick clouds makes the light unpolarised.

pensation more attention shall be brought to its conception. In the next chapter, we will described the model and computer software we developed to simulate elastic backscatter lidar signals for both pulsed and PRN-cw techniques. Equations exposed in this chapter are the bases of this model.

Chapter 2

Lidar signal numerical simulations

Introduction

Nowadays, laser, detector and acquisition system technologies allow a lidar demonstration to be built relatively easily. What is not so simple is the realisation of a lidar instrument which shall possess optimal capabilities for detection of specified atmospheric parameter(s) and, at the same time, shall fit to given design requirements – volume, mass, power consumption, etc. One way to achieve this is a chain of trials and errors, what is rather expensive. Another way is to base the first iteration of the realisation on the results from a realistic numerical model. This is the method used here.

Numerical simulations of lidar signals make possible to investigate how a lidar is affected by atmospheric and its sub-systems parameters, without spending months and money in building a real lidar. The operation and performances of a PRN-cw lidar are not straightforward understandable. Simulations help to evaluate them and find the advantages and drawbacks of this technique. Conceiving a lidar that shall run in demanding environmental conditions instead of in a comfortable place like a laboratory asks for well balanced solutions and compromises. For instance the instrument shall be small and request a laser of little volume. If such a laser exists, is it powerful enough to detect a given atmospheric phenomena still with a reasonable signal-to-noise ratio ? Is it enough to increase the area of the telescope to compensate the weaker power ? Simulations really help to appreciate the performances and limits of an instrument and are a profitable tool in the perspective of developing compact instruments.

In this chapter we expose our backscatter lidar simulation model (§ 2.1). The parameters of the lidar instrument considered for the simulations are first enumerated, as well as the platform from where the instrument measures. Then are described the models for the atmosphere, the background radiation and for a topographic terrain. The goal of the model is to present design considerations in realistic and characteristic situations. In the next section, the computer program based on the simulation model is presented. Its inputs are the atmospheric and topographic models, the instrument parameters and its platform. Its outputs are the simulated lidar signal profile and signal-to-noise ratio. Only total atmospheric elastic backscatter lidars and target range-finders are concerned. They may use either pulsed or PRN-cw technique and photon-counting or analog detection mode.

2.1 Simulation model

2.1.1 Device parameters

Hereafter are listed all device parameters which are taken into account for the simulations. They are divided in four main groups: transmission, reception, detection and acquisition parameters.

Emission

- Wavelength
- Optical power [laser optical mean power]
- Beam diameter [after beam expansion]
- Axis-to-axis distance [distance between the laser beam axis and the telescope field of view axis]
- Axis-axis angle [angle between the laser beam axis and the telescope field of view axis]
- Modulation frequency [determines the resolution in PRN-cw technique; by convention it is also the bin duration for the pulsed technique]
- Modulation efficiency [is related to the modulation depth of the laser beam in case of PRN-cw lidar; unmodulated light injected into the atmosphere will act as a background noise component]
- Transmission [total efficiency of the transmission optics]
- Laser repetition rate [for pulsed lidars only: pulse repetition rate]
- Sequence length [in the PRN-cw technique, number *n* of bits in the sequence, the actual sequence length is 2^n-1]

Reception

- Primary mirror diameter
- Secondary mirror diameter [if present]
- Full telescope divergence [full angle field of view]
- Filter bandwidth [full width at half maximum]
- Filter transmission
- Transmission [total efficiency of the receiver optics, filter excepted]

Detection

- Detection mode [photon-counting or analog*]
- Detector quantum efficiency
- Detector gain
- Detector dark current [dark counts per second in case of photon-counting detection mode]
- Detector excess noise factor [analog detection mode only]
- Detector window transmission [if present]
- Load resistance [analog detection mode only]
- Load resistance temperature [analog detection mode only]

Acquisition

- Accumulation time [measurement duration, integration time]

2.1.2 Platforms

There are three platform considered in the model. The *ground-based* instruments are probing vertically, towards zenith. The *airborne* instruments are treated as having fixed direction of probing, either nadir- or zenith-looking and fixed altitude. The velocity of the platform is not considered; it is assumed that the instruments probe horizontally homogeneous atmosphere. The *satellite-borne* lidars are nadir-looking instruments only. The same considerations as for the airborne are valid for the altitude and speed of the satellite. No scanning is considered for any platform.

---

* In analog detection mode, the electrical bandwidth is set equal to the frequency modulation (or sampling rate) divided by 2.

2.1.3 Atmospheric model

As atmospheric model we understand here a model for atmospheric backscatter and extinction for horizontally homogenous atmosphere. The model used in this study for the atmospheric features causing scattering and extinction follows mainly the models recommended for the ATLID Program from ESA/ESTEC [Este91 and Este92]*. We will first describe how these optical parameters are handled and then how the various components or layers of the atmosphere are modelled.

In the lidar equation (1.7), the atmospheric contribution is expressed by the volume backscattering coefficient and the extinction coefficient. We shall model their profile. As they usually consist in several components (cf. equation (1.9)), we call them "total" and represent them as

$$\begin{aligned}\beta_{tot}(r) &= \beta_{mol}(r)+\beta_{PBL}(r)+\beta_{ta}(r)+\beta_{cum}(r)+\beta_{cir}(r)+\beta_{sc}(r)\\ \alpha_{tot}(r) &= \alpha_{mol}(r)+\alpha_{PBL}(r)+\alpha_{ta}(r)+\alpha_{cum}(r)+\alpha_{cir}(r)+\alpha_{sc}(r)\end{aligned} \qquad (2\text{-}1)$$

Subscripts *mol*, *PBL*, *ta*, *sc*, *cum*, and *cir* refer resp. to atmospheric molecular component, aerosol in the planetary boundary layer, tropospheric aerosol, cumulus cloud, cirrus cloud, stratospheric cloud.

Two parameters relevant to the model are used: *SR* or "scattering ratio", and *EBR* or "extinction-to-backscatter ratio". They are determined in the commonly accepted manner

$$SR_x(r)=\frac{\beta_x(r)+\beta_{mol}(r)}{\beta_{mol}(r)} \qquad \text{and} \qquad EBR_x(r)=\alpha_x(r)/\beta_x(r), \qquad (2\text{-}2)$$

where x stands for the layer, cloud or aerosol. These parameters are the optical values introduced in our model at λ=532 nm. This is the wavelength used in the above quoted models†. The extinction profile α_x of each layer is obtained directly from the corresponding backscattering coefficient profile β_x and the EBR_x value.

The optical parameters, being introduced for 532 nm, are determined for the actual wavelength in the following way. For the molecular atmosphere, in accordance to the well-known Rayleigh λ^{-4}-dependency, the backscattering value is given by

$$\beta_{mol}(\lambda,r)=\beta_{mol}(532,r)\cdot\left(\frac{532}{\lambda}\right)^4, \qquad (2\text{-}3)$$

where λ is expressed in [nm]. $\beta_{mol}(532,r)$ (in [$sr^{-1}m^{-1}$]) is computed by multiplying the mo-

* We consider yet a small differences: altitude distributions of clouds of all kinds are Gaussian instead of rectangular. We omitted stratospheric aerosols, which were not of principle importance for us. They may however be easily implemented in the model. In the actual state of the model, they may still be described, as clouds are, by a Gaussian distribution.

† 532 nm corresponds to the wavelength of the second harmonics of a Nd-YAG laser. This type of laser is commonly used in the lidar field.

lecular atmosphere density [m^{-3}] by the mean backscattering cross-section per unit solid-angle for a single molecule at λ=532 nm, 6.2259·$10^{-32}$$m^2$/sr [Meas84, p.42]. For clouds and aerosols, the equivalent conversion of the scattering ratio is

$$SR_x(\lambda)-1=\left(SR_x(532)-1\right)\cdot\left(\frac{\lambda}{532}\right)^{4+SRE_x}, \tag{2-4}$$

where SRE_x is the scattering ratio exponent wavelength dependency of layer x . It is an input parameter in the computer program. As it is assumed that α_x has the same wave-

Atmospheric layer	Base and top [km]		β	α	*EBR*	*SR*	SRE
PBL: summer, day	0	1.5	$1.0\cdot10^{-5}$	$3.3\cdot10^{-4}$	33	7	-1
summer, night	0	0.5	$5.0\cdot10^{-6}$	$1.7\cdot10^{-4}$	33	4	-1
winter	0	0.2	$2.3\cdot10^{-5}$	$7.8\cdot10^{-4}$	33	15	-1
Tropospheric aerosols	PBL top	10	$4\cdot10^{-6}$	$1.6\cdot10^{-4}$	40	4	-1
Polar stratospheric cloud	13	21	$8\cdot10^{-7}$	$1.6\cdot10^{-5}$	20	5	-1
Fair-weather cumulus	0.75	1	$6\cdot10^{-4}$	0.012	20	400	0
Stratus	0.2	0.7	$5\cdot10^{-3}$	0.09	18	3000	0
Cumulo-nimbus	2	4	$1\cdot10^{-2}$	0.18	18	8500	0
Alto-stratus	4	4.5	$1\cdot10^{-3}$	0.018	18	1000	0
Cirrus	8.5	9.5	$1.4\cdot10^{-5}$	$2\cdot10^{-4}$	14	25	0

Table 2.1: *Generally used values for aerosol and cloud optical parameters at 532nm (from [Este91 and Este92]). The computer program allows other values to be introduced. β is the volume backscattering coefficient in [$sr^{-1}m^{-1}$], α the extinction coefficient in [m^{-1}], EBR the extinction-to-backscattering ratio α/β in [sr], SR the scattering ratio peak value, and SRE the scattering ratio exponent wavelength dependency.*

length dependency as β_x, EBR_x does not vary with the wavelength. For the molecular atmosphere, we take

$$EBR_{mol}=\frac{8\pi}{3}. \tag{2-5}$$

The parameter values generally used for the different typical layers are given in Table 2.1. However other values may also be introduced in the computer model.

Molecular atmosphere

The atmospheric molecular density is taken from the US76 standard model atmosphere [Usst76]. A linear interpolation is applied between the given altitudes. As mentioned above, multiplying the profile density by the mean backscattering cross-section per unit solid-angle for a single molecule results in the volume backscattering coefficient. Multiplying again this profile by the extinction-to-backscattering ratio of equation (2-5) results that time in the extinction profile.

Planetary boundary layer

The model optical properties of planetary boundary layer (PBL) aerosol are derived from the standard ESA model [Este92]. We consider only one kind of aerosol presents in the PBL. The aerosol altitude distribution is a rectangular one, i.e. its basic value is characterised by a constant backscatter coefficient β_{PBL}^{main} – and a constant extinction-to-backscatter ratio – between the PBL base $r_{PBL,base}$ and top $r_{PBL,top}$ heights,

$$\beta_{PBL}^{main} = SR_{PBL} \cdot \beta_{mol}(r_{PBL,base}) \,. \tag{2-6}$$

Then one or two optional sub-layers (i=1,2) are added. For convenience they are modelled as sine function variations – in function of the altitude r – of the main layer:

$$\beta_{PBL}^{tot}(r) = \beta_{PBL}^{main} \cdot (1 + A_1(r) + A_2(r)) \tag{2-7}$$

with $A_i(r) = S_i \cdot A_i^{\%} \cdot \sin(k_i r)$ and $k_i = \pi \cdot \dfrac{r_i^{top} - r}{r_i^{top} - r_i^{base}}$. (2-8)

S_i is the variation of the sign of the i-sub-layer (1 for positive, -1 for negative) and $A_i^{\%}$ is amplitude variation (positive) in percent. The base r_i^{base} and top r_i^{top} heights of the sub-layers are independent from the base and top heights of the PBL. The extinction coefficient profile is again obtained by multiplying the backscattering coefficient profile by the EBR_{PBL} value.

Such model allows the simulation of the vertical profile of the basckscatter coefficient if temperature inversions occur in the PBL. In urban and industrial areas temperature inversions in the PBL prevent the transportation of the pollution by the wind out of the urban or the industrial area and increase the possibility for smog. In this way, their detection is one of the primary tasks for PBL lidars. That is the reason to include the case of temperature (i.e. aerosol) inversions in polluted urban PBL.

Tropospheric aerosol

The contribution of the tropospheric aerosol layer is described by an exponentially decreasing function between its base $r_{ta,base}$ and top $r_{ta,top}$ heights,

$\beta_{ta}(r) = \beta_{ta,0} e^{-\frac{r}{r_{ta,0}}}$, and $\beta_{ta,0} = SR_{ta} \cdot \beta_{mol}(r_{ta,base})$. (2-9)

The value $r_{ta,0}$ is set equal to 1500 meters. The base of the layer is usually above the top of the PBL, and its top is below the height of the tropopause. The extinction coefficient profile is computed like for the PBL case.

Clouds

Clouds of all types are modelled by Gaussian distributions. They are preferred to rectangular ones because cloud edges are less sharp defined. They each are defined by three parameters: their central – peak – altitude $r_{x,0}$, their width Δ_x and their scattering ratio SR_x at $r_{x,0}$. These parameters are inputs in the computer software. Their basis and top altitudes are given by $r_{x,0}$ and Δ_x : $r_{x,base} = r_{x,0} - \Delta_x / 2$ and $r_{x,top} = r_{x,0} + \Delta_x / 2$. The volume backscattering coefficient of the layer x is

$$\beta_{x,0} = SR_x \cdot \beta_{mol}(r_{x,0}) . \tag{2-10}$$

The backscattering coefficient profile $\beta_x(r)$ in interval $r_{x,base} \le r \le r_{x,top}$ is then given by

$$\beta_x(r) = \frac{\beta_{x,0}}{1 - e^{-2}} \left(e^{-\frac{1}{2}\left(\frac{r - r_{x,0}}{\Delta_x / 4}\right)^2} - e^{-2} \right) \tag{2-11}$$

The profile is maximal in $r_{x,0}$ with a value of $\beta_{x,0}$ and equal to 0 at $r_{x,base}$ and $r_{x,top}$. The extinction coefficient profile is computed in the same way as for the PBL case.

2.1.4 Background radiation model

Beside the instrument parameters, the necessary atmospheric parameter to compute the background noise radiation falling on the detector is the spectral radiance $S_b(\lambda)$ from the sky at the instrument location (cf. Chapter 1, Section 1.3.3).

The exact calculation of the background radiation may be done using the MODTRAN code [Afrl]. The exact calculation of the background radiation in lidar numerical simulations lead in many cases to unnecessary increase of the computation time with a small advantage in the determination of the lidar output. For this purpose our approach is to replace the necessity for exact MODTRAN calculations for the practical simulation with a simplified evaluation of the background radiation.

In the case of nadir probing lidar (satellite-borne and air-borne) we consider a surface (ground, cloud top, etc.) as the only source of optical background. We consider also this surface illuminated by the direct solar radiation:

$$S_{b,nadir}(\lambda) = S_0(\lambda)(\cos\varphi + n_s) \cdot a / \pi \cdot \exp\left(-2k \cdot \delta_{atm}(\lambda)\right) \tag{2-12}$$

$S_0(\lambda)$ is the solar irradiance at wavelength λ above the atmosphere, φ is the solar zenith angle, *a* is the illuminated ground surface albedo and $\delta_{atm}(\lambda)$ the atmosphere optical depth at wavelength λ. The factor n_s is the ratio between night-time spectral radiance and day-time spectral radiance. It is set equal to 10^{-6} (full moon situation, [Wald93]; for night-time condition, we take φ=90°). *k* is introduced as an empirical correction factor for the atmosphere optical depth*.

Computed this way, the nadir-looking lidar value for the optical background is with an overestimate with respect to the MODTRAN values. This overestimate depends very slightly on the solar zenith angle [Wald93, Gate66]. We may expect that for practical considerations the lidar performances are determined with slight underestimation.

For the case of lidar probing at zenith, we take a similar formulae as above, but with a proportionality factor *B*, which may be empirically determined from the results in [Wald93]:

$$S_{b,zenith}(\lambda) = S_0(\lambda)(\cos\varphi + n_s)\cdot B/2\pi \cdot \exp(-\delta_{atm}). \qquad (2\text{-}13)$$

B is the ratio between the diffuse sky light and the global radiation, both at ground level. It depends on the wavelength and the solar zenith angle†. It takes into account the fact that during a measurement, the background radiation reaching the collecting telescope of the lidar is the sky light and not the direct sun light. In this case also, our simplified model values are obtained with slight overestimate as compared to the precise model, and the lidar performances are determined with slight underestimate. This overestimate increases with the altitude of the airborne platform for airborne lidar.

This background radiation model is simple, particularly in the case of zenith-looking instrument: the state of the atmosphere is entirely contained in the term δ_{atm} , the presence of clouds and their albedo are not taken into account, the angular dependency of the sun is reduced to a simple cosine dependency. However the background radiance spreads over the necessary multitude of situations. Therefore developing a precise model for it is a complex task and was out of the scope of this work. It is also not really necessary. In fact our model is sufficient to provide an approximate value of $S_b(\lambda)$. It allows also to use values from the literature or from much better models ([Afrl], [Wald93]) and to introduce them in the equation, adapting the parameters. For instance, if the value of the spectral radiance at see level shall be computed for a sky completely covered by clouds and that this value may be found in an article, one may set $S_0(\lambda)$ equal to this value and δ_{atm}=0. As example for the development of a compact elastic depolarisation instrument (cf. Chapter 6), we compared our simulations with the ones of our partner from IROE-CNR‡; no significant differences were found for the instrument capabilities.

---

* We usually consider the platform for nadir-looking lidar at altitudes higher than the tropopause and set *k* equal to 1. This way, the optical depth is multiplied by a factor of 2 corresponding to the round-trip of the light through the whole atmosphere. Setting *k* to 0.5 would illustrate the situation where the instrument is just some meters above the ground, still looking nadir. For a high altitude cloud like a cirrus, *k* is equal to 0 as the solar light has almost not been attenuated by the atmosphere.

† When the sun is around the zenith, *B* is about 5.3% for 532 nm and 10% for 780 nm.

‡ Instituto di ricerca sulle onde elettromagnetiche – Consiglio nazionale delle ricerche, Florence, Italy: Simulations by Mr M. Morandi, with MODTRAN calculations for background radiation. Private communication.

2.1.5 Topographic surface model

For the cases of satellite- and air-borne lidars, a topographic surface model has been developed in order to get an impression of what the return from the Earth surface might be and of the noise induced in the atmospheric signal. This model is based on a function describing discrete surface distribution. This function is normalised to 1. It presents the altitude distribution of the area into the lidar field of view. Each surface level has also its own albedo (Lambertian reflection is considered; if for a given level there are two different albedi, its corresponding surface can be divided in two sub-surfaces). From these topographic values the equivalent optical coefficients α and β as functions of the altitude are computed and can be then considered as atmospheric layers and introduced in the "lidar" equation. One condition is that the laser beam must be fully extincted by these "topographic" layers.

2.1.6 Comments on the model

The model allows to simulate a multitude of elastic backscatter lidar instrument and atmospheric configurations. It is also possible to combine the existing possibilities to create new ones. Horizontal probing for instance was initially not implemented. Yet it may be modelled by the PBL which has constant backscattering coefficient, independently from the altitude. Setting the base height to 0, i.e. at the instrument location, and the top height as far as wished or needed, horizontal slant-path conditions are created. Of course, the molecular atmosphere component is still present, but as it decreases quickly with the altitude, i.e. with the range in this case, it introduces only a small error for realistic ranges. The PBL remains the same, as it is a constant computed for altitude 0.

In the same way, horizontal hard-target measurement simulation may be obtained by a nadir-looking instrument and the topographic model: the object is at location of the topographic surface and the instrument at the altitude of the flying platform. It is assumed that the illuminating laser area is fully contained by the target surface. PBL aerosol defined as described in the previous paragraph may also be used.

Simulation of lidar measurements on other planet is also possible. The planet molecular atmosphere is modelled by artificially positioning the lidar at Earth altitudes, which correspond to the surface pressure of the planet. The rest of the planet atmosphere is simulated by a proper choice of parameters of the atmospheric layers, PBL, clouds, etc. Such examples will be show in Section 5.2 related to a Mars instrument concept.

The model concerns only total elastic backscatter lidars. Nevertheless, it is possible to simulate a depolarisation elastic backscatter lidar in two stages: one simulation run for each polarisation. If the depolarisation of the molecular atmosphere is negligible or is not the point of interest, the depolarised signal may be approximated by adapting only the scattering ratio of the various layers. On the contrary, if the molecular atmosphere depolarisation is of interest, the power of the laser shall be multiplied by the depolarisation ratio of the molecular atmosphere; on its side, the scattering ratio of the various layers shall be first multiplied by the inverse of the molecular atmosphere depolarisation ratio in order to compensate for the lower laser power and then adapted for the depolarisation of the layer itself.

Emission		
Wavelength	[nm]	780
Power	[W]	0.1
Full divergency	[mrad]	0.08
Beam diameter	[cm]	4
Axe-to-axe dist.	[cm]	12
Axe-axe angle	[mrad]	0
Modulator eff.	[%]	99
Modulator freq.	[MHz]	10
Opt. transmission	[%]	*80

Receiving optics		
Primary mirror diameter	[cm]	*10
Secondary mirror diameter	[cm]	0
Full divergency	[mrad]	0.2
Transmission	[%]	100
Filter bandwidth	[nm]	.2
Filter transmission	[%]	100

Figure 2.1. *Examples of panels for instrumental parameter input: emission and reception optics.*

Clouds and aerosols layers (@ 532 nm)

Layer	Base [m]	Top [m]	S.ratio	Ext/back	Exponent
Aero.trop.	*0	2000	2	40	-1
	Peak alt.[m]	Width [m]	S.ratio	Ext/back	Exponent
Cumulus	4000	500	1	20	-1
Cirrus 1	7000	1000	1	19	0
Cirrus 2	8000	1000	15	22	0
Cirrus 3	11000	1000	1	25	0
Aero.strat.	17000	4000	4	20	-1
PSC	22000	1000	1	20	-1

Planetary Boundary Layer (@ 532 nm)

Layer	Base [m]	Top [m]	S.ratio	Ext/back	Exponent
Main	0	2000	5	33	-1
	Base [m]	Top[m]	Peak [%]	Sign	Exponent
1st corr	500	600	0	-	-1
2nd corr	900	1000	0	*+	-1

Figure 2.2. *Examples of panels for atmospheric parameter input: planetary boundary layer, clouds and aerosols. The signification of the various parameters is explained in Section 2.1.3, "Atmospheric model".*

2.2 Computer program

2.2.1 Program overview and flow-chart

The program is intended to perform lidar simulations for ground-based, air-borne and satellite-borne platforms. Required *inputs* are the main sensitive device parameters (emission, reception, detection, acquisition), the aerosol and cloud layers, the background conditions, and the geometry of the system. Photon-counting or analog detection mode is considered. All input parameters appear on the screen under panel form, like in Figures 2.1 and 2.2. Their values may be changed if necessary and are saved into files in order to be displayed again during the next simulation. The *outputs* of the program are the PRN-cw and pulsed signatures at the same time, as well as the evaluation of their respective signal-to-noise ratios. All inputs and outputs may be saved into an ASCII file for further use.

The computer program runs under DOS – or in a DOS emulated window like under Microsoft Windows – and has been written in QuickBasic 4.5. This language is nowadays obsolete, and newer languages would offer faster computational time and better user interface, especially for the graphics. However, the translation would not change the simulation model itself and the results would be the same.

During the execution of the program, various graphs are displayed, like, as illustrated in Figure 2.3, the volume backscattering coefficient and the scattering ratio altitude profiles, the time evolution of the number of photons reaching the photodetector, the detected signals, the final results, the signal-to-noise ratios.

The program flow-chart is presented in Figure 2.4. It enumerates the main successive computation steps of the program. The graph appearances are omitted.

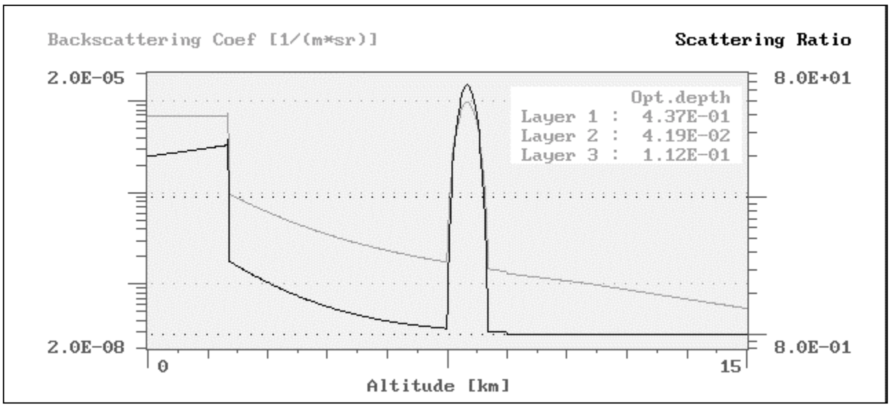

Figure 2.3. *Illustration of a modelled backscattering coefficient and its corresponding scattering ratio as they are displayed by the simulation software for a wavelength of 780 nm. Apart the molecular atmosphere three layers are present: the PBL up to 2 km altitude with SR of 7 at 532 nm, a tropospheric aerosol up to the tropopause at 9 km with SR of 4 at 532 nm, and a 1 km-thick cirrus centred at 8 km with SR of 15 at 532 nm.*

2.2.2 Transmitted powers, signal and noise calculation, retrieved response profile

The program is intended to simulate at the same time the lidar signatures for both PRN-cw and pulsed techniques, in order to ease their comparison. All instrument and atmospheric parameters are similar. The spatial resolution is determined by the modulation frequency of the PRN-cw technique. For instance, a 10 MHz modulation corresponds to a 15-meter resolution. For the comparison, it is important that the transmitted mean powers are similar. In the PRN-cw technique, as the duty cycle is 50 %*, half of the nominal cw-laser

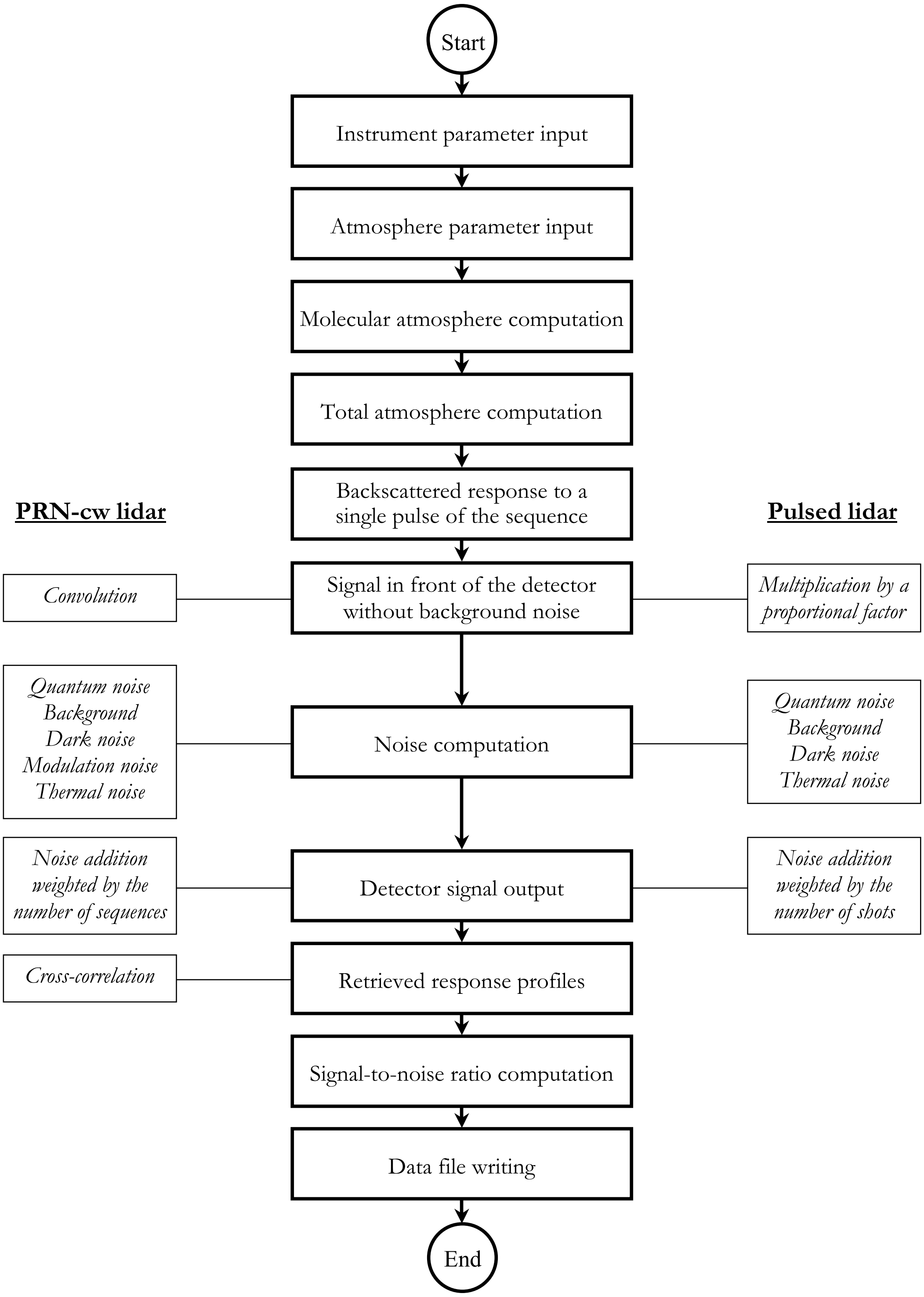

Figure 2.4. *Flow-chart of the lidar signal simulation computer program. PRN-cw and pulsed lidar signals are simulated in parallel for the same instrument and atmospheric parameters to allow direct comparison of both techniques. Simulated profiles and corresponding signal-to-noise ratio as well as all parameters are eventually saved in an ASCII file.*

* In a M-sequence, there is one more “1” than “0” only, whatever is its length.

power and introduced as parameter in the simulation program is sent into the atmosphere. The equivalent mean power emitted by the pulsed laser is set by convention to be half of the nominal power*.

In order to know the backscattered signal falling on the photodetector in the PRN-cw case, it is necessary to compute the response of the atmosphere to a single pulse of the PRN-sequence, which energy is the power of the laser divided by the modulation frequency. This step is performed using the lidar equation, taking particularly into account the overlap function. The backscattered signal in front of the photodetector – without the background noise – is then given by the sum of each individual layer weighted by the sequence code – what corresponds to a convolution, as seen in Chapter 1. To get the signal in the pulsed case, it is necessary to multiply the response signal to a probing single pulse of the PRN-sequence by the ratio of the energies of both kind of pulses: energy of a single shot of the pulsed lidar divided by the energy of a single pulse of the PRN-sequence. The energy of a single shot of the pulsed lidar is taken as half the nominal mean laser power (as explained previously) divided by its pulse repetition rate.

In accordance with the theory explained in Chapter 1, the quantum noise, assumed to follow Poisson statistics, is the square-root of the backscattered signal incident on the photodetector, while the background noise is the square-root of the background radiation incident on the photodetector. Since the efficiency of the modulation of the cw-laser beam may not be 100%, the light sent into the atmosphere may have a DC-component. If this is the case, a continuous backscattered offset signal is created. We treat it independently from the background radiation but in the same way. It results as well in an optical shot noise that we call “modulation noise”. For simulation in photon counting detection mode, the thermal noise is not considered.

The signal at the output of the photodetector is the sum of the backscattered signal, the mean background radiation value and the mean modulation DC-component. To this value is added, through a random multiplication factor and a weighting factor, the square-root of the sum of the variances of the different noises. The random multiplication factor is randomly chosen in the interval $[-1;+1]$ to create the effect of fluctuation. The weighting factor is the square-root of the total number of sequences in the PRN-cw case or total number of shots in the pulsed case. It describes the effect of accumulation or time-average. The total number of pulses, resp. sequences, is computed from the accumulation time and the pulse repetition rate, resp. sequence length. In the pulsed case the final profile is the signal at the photodetector output itself, while in the PRN-cw case the cross-correlation between the PRN-sequence code and this signal is to be computed.

* For instance if a mean power of 500 mW is entered in the simulation program, backscattered signals are computed both for an injected power into the atmosphere of 250 mW. It might also have been possible to consider that the power input parameter is the actual nominal value for the pulsed laser too, i.e. 500 mW.

2.3 Verifications of the simulation model and program

The simulation program was first checked. We did it for the case of a pulsed lidar because this technique is more straightforward and simple. The method was to verify each step of the algorithm, one by one for very simple atmospheric measurement parameters, like molecular atmosphere only. We compared the obtained results with "hand made" calculations. Then we controlled the dependency on the instrument parameters and finally implemented the noises and the average on the number of shots.

The PRN-CW lidar model was checked by comparing its signature with the one for pulsed lidar: in absence of any kind of noise, quantum noise included – only the return signal is so considered –, the total number of photons backscattered by a layer should be the same for both types of lidars (cf. Chapter 1, last paragraph before Section 1.3.6).

The atmospheric model algorithm – wavelength dependency, correctness of the atmospheric response – could be checked numerically. This was not the case of the validity of the atmospheric and topographic models; they required comparisons between simulations and real signals. This stage was performed with measurement obtained by a PRN-cw total elastic backscatter lidar developed at the Observatoire de Neuchâtel. Some examples of comparisons will be presented in Chapter 3 which is devoted to this instrument. They reveal a good agreement between the measured signals and the signals simulated with relevant atmospheric parameter values and the main characteristics of the instrument. They allow to validate the model.

Conclusion

A backscatter lidar simulation model and its related computer software have been developed. This tool allows to simulate lidar signals for various total elastic backscattering instruments and atmospheric or topographic targets. The platform for the instruments may be the ground (zenith-looking), an aircraft (zenith- and nadir-looking) or a satellite (nadir-looking). Both pulsed and PRN-cw techniques are considered, while the detection may be either in analog or photo-counting mode. Other situations, like horizontal probing, depolarisation instruments, hard targets, may also be modelled by combining the existing possibilities of the developed simulation tool. In the next chapters, several different lidar instruments will be presented which conception was based on the elaborated lidar signal simulation software.

Chapter 3

PRN-cw technique: requirements and demonstration

Introduction

The theoretical aspect of the PRN-cw lidar technique was presented in Chapter 1. Here we will focus on the experimental aspect of this technique. After explanations why diode lasers may be attractive as lidar light sources and why to use the PRN-cw technique (§ 3.1), the instrumentation requirements to apply such a technique are discussed (§ 3.2). A two-optical fibre test-bench will allow us to check the data acquisition and processing procedures. It will also reveal experimentally whether the lidar signal is really independent from the sequence length and what happens when the acquisition system is not synchronised with the modulation of the laser beam (§ 3.3). Based on the simulation program, a total elastic backscatter lidar has been realised. The transmitted light is in the near infrared and the detection is in photon-counting mode. A description and typical measurements achieved with this instrument, like topographic target return, cloud base return and aerosol in the PBL are presented in section § 3.4. Based on the measurements and the gained experience, limitations and advantages of the PRN-cw technique are then discussed (§ 3.5). Finally, a comparison between real and simulated signals validates the numerical model proposed in the previous chapter (§ 3.6).

3.1 Diode lasers and PRN-cw technique

Pulsed lidar technology is well developed and is being used with great success in various fields like in atmospheric research, topographic studies research, satellite tracking, etc. In Chapter 1, we have seen that, theoretically, the performances, in term of signal-to-noise ratio, are worse in the case of PRN-cw lidars than in the case of pulsed lidars, if the mean emitted powers are of comparable value. Therefore, why would it be preferable to use PRN-cw lidars in some situations ?

In many measurement scenarios starts to appear a conflict between the aims and the limitations of the pulsed lidar technology, particularly in terms of size and weight, electric power efficiency, eye-safety requirements, optical stress and life-time of components. These limitations are due to the use of pulsed lasers as light sources. One convenient way to avoid such conflict is to go to continuous-wave (cw) diode lasers. They are small and light – one can speak in cubic centimetres and grams instead of litres and kilos. They offer a much higher electrical-to-optical power conversion factor – several tens of percents instead of maximum some percents. This makes them candidate for airborne, satellite and spacecraft mission, or for harsh ground-based environmental conditions. Their low peak power offers two significant advantages. It makes a lidar easier to be eye-safe than if it was built around a pulsed laser, what is an advantage for application in populated areas or in airports. It also ensures laser diodes long life-time and less stress on the optics. Another reason to consider cw-laser diodes is their narrower laser bandwidth. In cw-mode it is orders of magnitude less than in the case of pulsed operation. In many measurement scenarios, like ultra-narrow band filter elastic lidar measurement, incoherent Doppler wind lidar, H_2O-vapour DIAL, the transmitted laser bandwidth is one critical parameter for the quality of the measurement results. Using laser diodes locked on atomic lines makes them very stable in frequency what is advantageous. They are also fast and may be modulated.

The AlGaAs laser technology is developing fast. This lead recently to laser diodes with the highest cw emitted power per unit volume of active media and with the highest electric plug-in efficiency, as well as with excellent coherence. For commercially available MOPA structures and emitters (master oscillator-power amplifier), it may reach more than 1 W. Their spectral region, 640-690 and 770-1000 nm, is well suited for atmospheric applications. It contains several spectral windows with high atmospheric transparency to H_2O, which makes it readily applicable for elastic backscatter lidar measurements. Due to the possibility to lock the extremely narrow-band AlGaAs laser wavelength to external standards (like Rb or Cs absorption lines) in these spectral windows, it makes possible in a future development incoherent Doppler wind measurements. Their spectral region contains also several bands of H_2O-vapour absorption, making possible H_2O-vapour DIAL applications. It should be also noted that robust and compact photodetectors sensitive in the spectral region of AlGaAs lasers emission now exist, like quenched and Geiger mode avalanche photodiodes.

As seen, for applications where strong constrains are imposed to the system, the lidar PRN-cw concept becomes a good candidate for atmospheric remote sensing*. This fact was recognised before the start of developing a PRN-cw instrument at the Observatory of Neuchâtel in 1994. Several previous lidar systems already used PRN-code modulation to obtain range-resolved signal with low peak power lasers. The first reported PRN experiment is dated 1983, by Takeuchi et al. [Take83]. They used externally modulated Argon laser at 514.5nm to measure the lidar return from a smoke plume at 1km distance. In 1986, Takeuchi et al. [Take86] demonstrated a PRN aerosol lidar using a 30mW AlGaAs laser diode transmitter. This system detected returns from aerosol, snow, smoke and cloud field during night-time. In 1988, Norman and Gardner [Norm88] proposed a PRN technique for performing satellite laser ranging. In 1992, Abshire et al. reported night-time measurement to tree canopies using a PRN modulated AlGaAs laser [Absh92]. In 1993, Abshire and Rall reported night-time measurement to cirrus at 13.5km and terrestrial targets at 13km [Absh93].

One might claim that a laser diode does not need to be PRN modulated. As pulsed lidar SNR is better then PRN-cw SNR, the diode might also be pulsed modulated, emitting only a small pulse instead of a full sequence. As demonstrated in § 1.3.6.4, the PRN-cw modulation, with a 50 %-duty cycle, shows very frequently better results than the pulsed modulation. The only case it does not is during night-time measurement for ranges where the response function is smaller than the mean response function, and as far as the SNR is bigger than 1 ! Pulsed laser diodes require also bulky optics due to the larger size of their emitting area.

3.2 Instrumentation requirements for PRN-cw technique

Pulsed and PRN-cw lidars do not differ from each other in their principle structure. For both systems, the laser light is transmitted through a transmission optics package toward the target. The backscattered light is collected by the reception optics and then spectrally filtered to select only the appropriate wavelength and reject the background noise component. A photodetector converts the light into electrical signal which is then memorised. In the PRN-cw technique, four sub-systems must be added: the sequence generation, the light modulation unit, the clock synchronisation unit and the cross-correlator. The basic block-diagram of a PRN-cw lidar is illustrated in Figure 3.1.

* In Chapter 7 will be presented a compact lidar instrument built around a micro-chip laser. This kind of laser appeared very recently on the market. The are pulsed, passively Q-switched. Small, light, they are real rivals to diode lasers in lidar field applications. However, as pulsed lasers, they still have high peak power and broader bandwidth than diode laser.

3.2.1 Code generation

Maximal-length sequences (also called *M-sequences*) are usually the type of code used in the PRN-cw lidar technique. As seen, an important requirement is that the sequences shall roll on without any pause between them (cf. § 1.3.5). If the modulo operation contained in the theory is not respected, an error will arise from the cross-correlation. M-sequences are easily generated by linear feedback shift register set-ups that may be implemented on an electronic board. Another way is to use an arbitrary waveform generator where the sequences are stored. In both cases, the sequences are injected in the modulation unit at a rate controlled by the clock unit.

3.2.2 Light modulation

There are two possible methods for the modulation of the transmitted optical power. The first is the direct internal modulation of the diode laser current. It is effective but can not be fit to the wavelength stabilisation; it will have as a result wavelength jumps and the bandwidth will effectively increase. This will make not possible the use of ultra-narrow-band filter. Additional disadvantage for atmospheric measurements is that some parts of

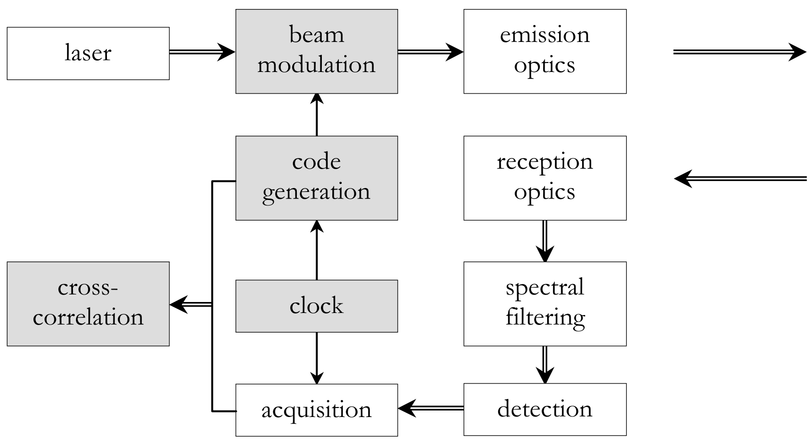

Figure 3.1. *Basic block-diagram of a PRN-cw total elastic backscatter lidar. Elements in grey are those specially requested by the PRN-cw technique, while the other elements are also shared by the pulsed technique.*

the badly controlled transmitted spectrum may coincide with water vapour absorption lines. The second modulation method is to use an external devices like an acousto-optical (AO) or electro-optical modulator (EO). AO modulators are faster than EO ones and require less driving voltage, but they are less efficient. They are not as fast as direct current modulation, but sufficiently enough for range resolutions of about 15-150 m. Their advantage is that they insure wavelength stabilised output radiation.

For both direct internal and external modulation processes, a small amount of unmodulated light may still be left and emitted as probing signal; it is determined by the achieved modulation depth. This offset component shall be as small as possible because it creates a constant backscatter signal noise and decreases the performances of the system.

3.2.3 Clock synchronisation and acquisition system

The PRN-cw principle of modulation and demodulation requires the acquisition system to fulfil strict synchronisation conditions. The number of samples (named also bins) shall be equal to the length of the sequence. In the pulsed technique, this is not critical, because the time between two successive pulses does not need to be totally filled by samples.

The sampling rate shall be equal to the light modulation frequency* in order to prevent a degradation of the SNR by a "*contamination*" effect. This effect will be demonstrated later in section 3.3.2. This means that the clock of the modulation unit and the clock of the acquisition system shall be synchronised for the time of measurement. Also for the same reason, there should be no deadtime between two successive sweeps of the acquisition system. If any deadtime exists, for each two sequences only one shall be acquired in order to always have the first sequence element corresponding with the first bin of the acquisition system. In this case, the effective measurement time will be twice longer to reach the same result.

3.2.4 Cross-correlation unit

As the PRN code is known and the acquired signal is converted by ADC or detected in photon numbers, the cross-correlation is performed by software by a processor, like the central unit of a computer (CPU) or a dedicated DSP (digital signal processor).

The purpose of the acquisition system is to record data for further data processing, like time averaging for SNR improvement. Depending on the goal of the measurement, this unit may be absent and the detected signal directly hardware cross-correlated with the code, like for instance in cw-radar. If the resulting signal needs to be recorded, it can further be converted into numbers. In this case, the acquisition system and the cross-correlator order is inverted. As it asks for demanding electronics, a comparison between these two possibilities has not been done in this work. It may happen that for analog detection mode systems, the noise influence changes if the order is reversed.

As each cross-correlated data is the result of the addition of N multiplications between an element of the code and an acquired data, N being the length of the code, the total number of operations, and consequently the computation time necessary to obtain the cross-correlation signal, is proportional to N^2. It is therefore convenient to choose a sequence as short as possible, but sufficiently long enough to cover what we called the "critical distance" (cf. 1.3.5), i.e. the maximum range unambiguously measured.

* It may also be a multiple of it, but in this case, a binning operation is necessary before performing the cross-correlation. Binning means to sum or average several successive bins in order to get a single value. For instance, binning two successive samples together make the range resolution to decrease by a factor of two.

3.3 PRN-cw technique demonstration with a two-optical fibre test bench

A bench consisting of two optical fibres of different length has been set-up for indoor functional tests independent of the conditions for atmospheric probing. The fibres, used in parallel and acting as delay lines, simulate the atmosphere round-trip of the laser light. It is as if the light was backscattered by a hard target placed at half the length of the fibres.

The block-diagram of the delay line experiment is illustrated in Figure 3.2. The procedure is to inject the modulated laser beam into the two fibres simultaneously (by scattering the beam through translucent paper, without collimating lens). Then the light is guided by the fibres to the photodetector. The signal is recorded by the acquisition system and the

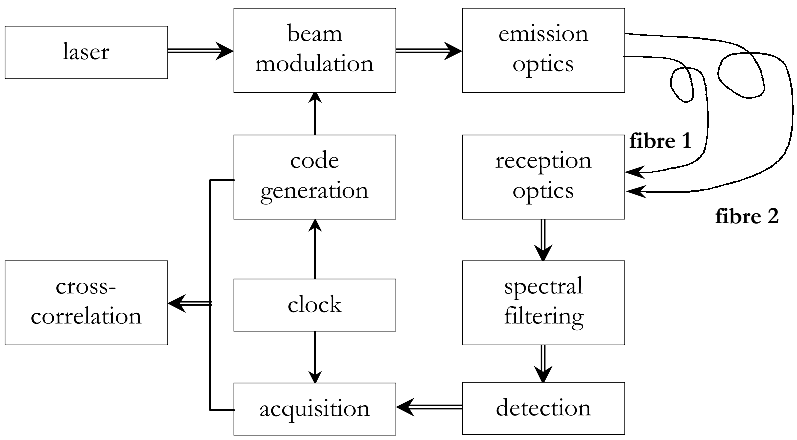

Figure 3.2. *Block-diagram of the delay line experiment. The two fibres simulate each a 100 %-reflecting hard target situated at half their length.*

cross-correlation performed by a computer. This set-up – except the two-fibre delay line – has been used exactly in this configuration for real measurements. The two only differences are that the transmission optics sends the light into the atmosphere and is adapted in consequence, and that the reception optics is built around a telescope and adapted in consequence too. We renounce then to describe it here in order to concentrate on the principle demonstration results; the detailed description will be addressed later in this chapter, in Section 3.4 dedicated to the actual lidar instrument. It is enough to mention now that that photon-counting detection mode is used and that the signal is recorded by a multichannel scaler.

This delay line experiment provided the possibility to test the modulation, detection and acquisition sub-systems of the instrument and to evaluate their functionality with real optical signals. Were tested in particular the sequence generation, the response of the modulation unit to the sequences and the amplitude of the modulated laser beam in function of the modulation frequency, the optical power detection and the data acquisition system, and the demodulation operation.

3.3.1 Example of measurement

An example of PRN measurement with the delay line is shown in Figure 3.3. The modulation code was a 10-bit M-sequence consisting so in 1023 ($=2^{10}$-1) bins. The frequency modulation was 10 MHz corresponding to a bin duration – also called dwell time or time - resolution – of 100 ns and determining a range-resolution of 15 m (round trip at light

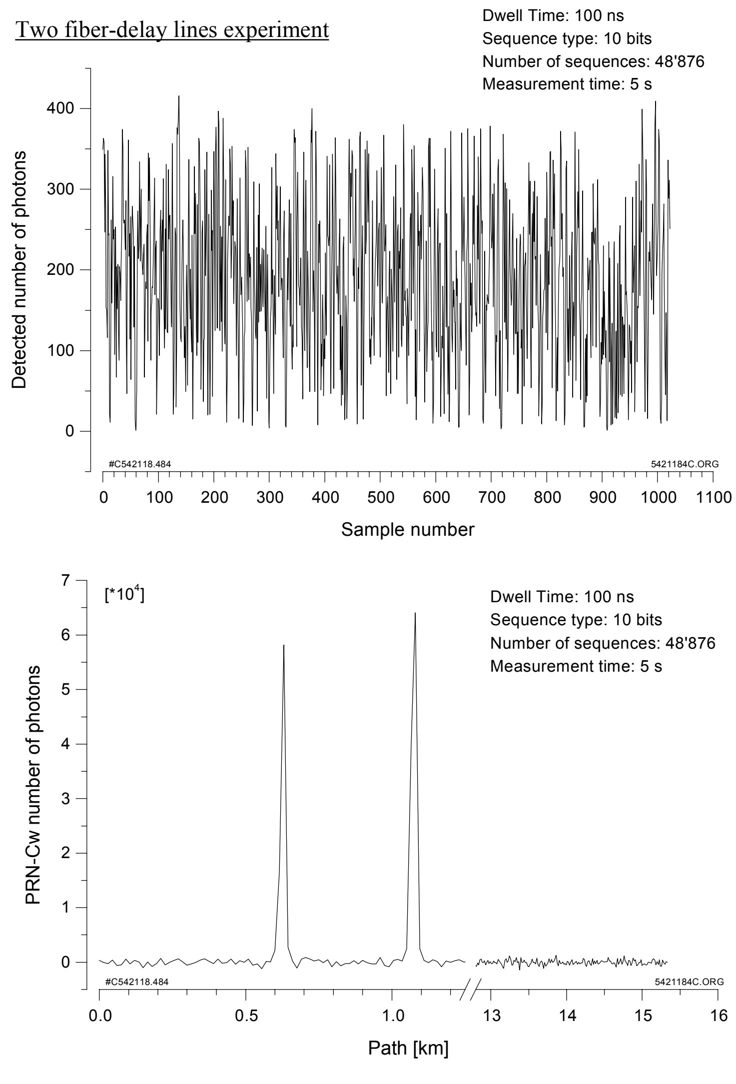

Figure 3.3. *Typical example of measurement with the two-fibre delay line experiment. The laser beam was modulated at 10 MHz following a 10-bit M-sequence and injected into two fibres in parallel. The upper plot is the signal recorded by the multichannel scaler. The signal issued from the cross-correlation between the sequence and the measured signal is drawn in the lower plot and clearly illustrates the two hard targets simulated by the fibres.*

speed in 100 ns). The signal was accumulated during 5 s, time necessary for the sequence to be repeated 48'876 times without interruption. The upper plot shows the measured signal; it is the accumulated number of photons detected in function of the sample – or bin – number, that is in function of the time as each bin has the same duration of 100 ns. In total

$1.908{\cdot}10^5$ photons were detected (that is a total optical energy of 0.05 pJ), or, expressed in term of average values 3.9 counts per sequence or 185.5 counts per bin. The number of counts per sequence and per bin is $3.816{\cdot}10^{-3}$ and corresponds to a mean photon arrival rate of 38.16 kHz. Obviously this detected signal does not speak a lot and is difficult to interpret. The situation is much simplified in the lower plot where the cross-correlation between the 10-bit M-sequence and the total acquired signal is reported. The obtained number of photons is called "PRN-cw number of photons" or "cross-correlated photon number". The two peaks at 630 m and 1080 m correspond to the two fibres acting as hard targets. The x-axis has been broken in order to show clearly the position of the targets and the maximal range covered by the sequence, 15.35 km (=1023·15 m).

The fibres were certified to be 729 m and 1327 m long by the manufacturer and should correspond to hard targets situated at 364.5 m and 663.5 m. The discrepancy with the actual measured peak values comes from the fact that the fibre refraction index and the mode dispersion shall be taken into account as shall be further set-up delays introduced by electrical BNC cables, the modulation unit, the detector, etc. As the fibre length difference Δl is known (=598 m) and the time delay Δt between the two fibres is given by the measurement (=300 ns), the (group) refraction index n of the fibres is calculated by the speed of the light c and the relation $n=c\Delta t/\Delta l$: n=1.504. Due to n the fibre targets peaks shall be actually found at 548 m and 998 m. The remaining range offset of 82 m is due to the above mentioned set-up delay.

It may be noticed that cross-correlated photon numbers are sometimes negative. This is artefact due to the cross-correlation using 1's and –1's sequence and does not have any real physical meaning. It happens when the noise fluctuations are larger than the cross-correlated signal itself, i.e. when the SNR is smaller than 1.

In accordance to the theory, the calculated sum of the accumulated cross-correlated counts is also $1.908{\cdot}10^5$ as for the direct recorded signal. The square-root of this value, 436.8, shall be equal to the fluctuations on the cross-correlated signal, whatever point is considered. From the lower plot we see that the fluctuations are constant. The standard deviation of the cross-correlated signal computed on the interval from range 1.5 km to the last point at 15.35 km is equal to 424.7 and is thus in excellent agreement with the above mentioned value. In conclusion we may say that actual measurements obey the theory and that our set-up works correctly.

The cross-correlated peak value of the second hard target is 64'087 counts and would correspond to a mean photon arrival rate of 13.1 MHz in the pulsed technique with a laser pulse repetition rate equal to the sequence repetition rate (about 10 kHz). Compared to the value of 38.16 kHz in the PRN-cw technique, it may be deduced that in the PRN-cw technique, photon-counting detection mode suffers much less from non linear effects due to pulse pile-up than in the pulsed technique*.

* In order to be able to separate between counts, a minimum separation time - called deadtime - between two pulses is required for them to be distinguished. Pulses pile-up when they are not distinguishable and they overlap. This causes a nonlinear response. For a given number of photons, the larger the deadtime, the more important the nonlinear effect. Also, for a given deadtime, the larger the number of photons, the more important the nonlinear effect.

3.3.2 Clock synchronisation and SNR

Ideally, as assumed in the theory, the PRN-cw lidar is piloted by a single clock: the PRN-cw sequence generator and the acquisition system are fully synchronised*. What may happen when each device possesses its own clock and they are desynchronised ? Is there any degradation of the SNR ?

To answer these questions, we proceeded the following way. Using a counter, we measured the internal clock rate of the acquisition system. Then we phase-locked the sequence generator to a precise external reference clock. We varied finally the rate of the latter. Figure 3.4 shows the SNR of the peak of the shorter fibre as a function of the difference between the generator clock (more precisely the external reference) and the scaler one. A 9-bit M-sequence (511 bins) was used and the scaler sampling rate fixed at 10MHz. Each

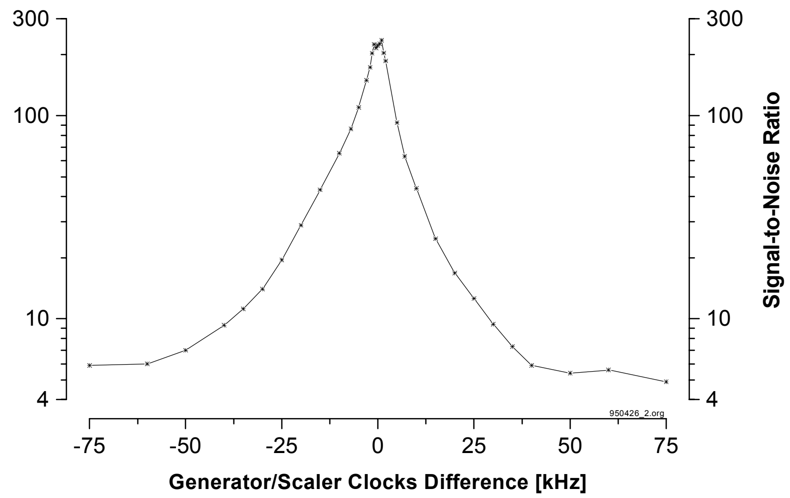

Figure 3.4. *Effect of the imperfect clock synchronisation between the PRN-cw generator and the acquisition system. The SNR ratio of the shorter fibre peak is plotted versus the difference of the individual clocks. The sampling rate of the acquisition system was fixed at 10 Mhz and the sequence generator clock varied. The SNR decreases drastically if both clock are not synchronised.*

measure lasted 10 s and consisted in $2 \cdot 10^5$ sequences. Even if the clocks were not synchronised, each scan of the multichannel scaler was triggered by the generator and began when the next sequence started: the start of a scan was always synchronised with the beginning of the sequence, but the sequence modulation frequency (the duration of a single sequence element) was varied and might be different from the sampling rate (the time resolution).

For differences within [-1.5 kHz, 1.5 kHz], the SNR changes by less than 10 %. For larger differences it is drastically degraded. When the clocks are not synchronised, a “contamination” or “decorrelation” effect occurs. It stems from the fact that photons are not counted in the channel they should with perfect synchronisation and the cross-correlation is then strongly affected. The effect would be even stronger if each scan was not triggered

* More precisely, it is the output signal from the PRN-cw sequence generator which drives the modulation unit that shall be synchronised with the acquisition system.

by the next sequence but only once at the beginning of the measurement, because the channel discrepancy grows with the time. The effect depends also on the scaler clock rate and the length of the sequence; the longer the sequence and/or the higher the scaler clock rate, the more important the effect. The conclusion is that both the multichannel scaler and the PRN-cw generator must be driven by the same clock. It could be an external clock or one driving the other one.

3.3.3 Sequence length dependency

Tests were also carried out in the delay line configuration in order to determine how the cross-correlated signal depends on the length of the sequence. Two series of tests were performed during which the sequence length was varied. Each measurement lasted 5 s, the sampling rate was 10 MHz. In the first series, the PRN-cw generator and the multichannel scaler were not synchronised and ran each free while in the second series, they were synchronised.

Figure 3.5 shows the cross-correlated signal in the case of not synchronised PRN-cw generator and acquisition system for 7, 8, 10 and 12-bit sequences (127, 255, 1023, 4095 samples). Here again, however, for each measurement the start of a scan was always synchronised with the beginning of the sequence and not only once at the beginning of the

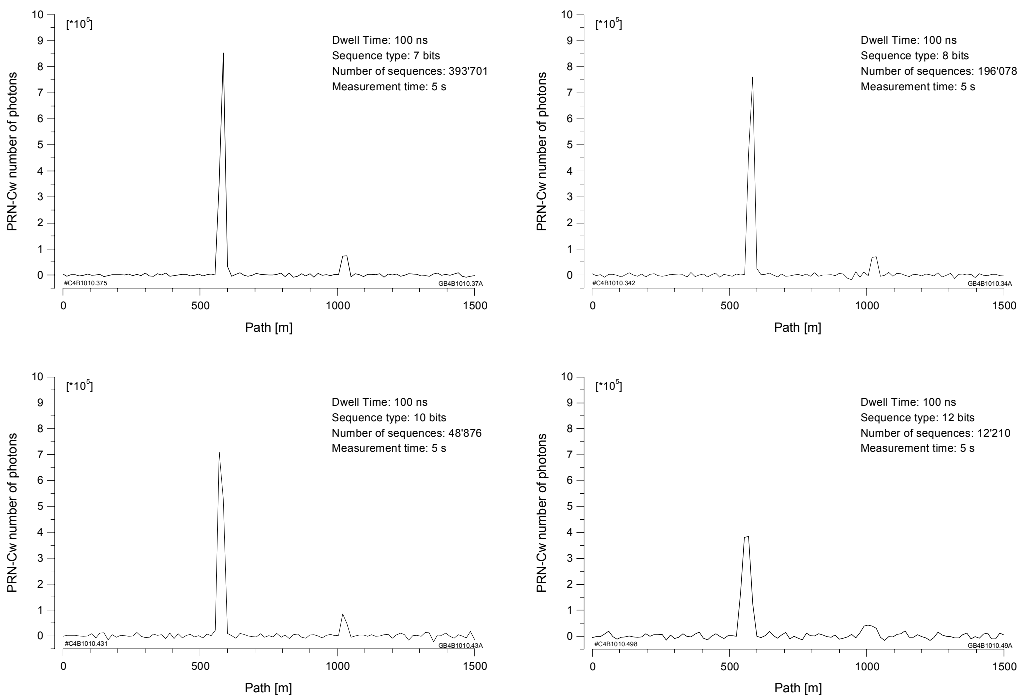

Figure 3.5. *Effect of the sequence length on the cross-correlated signal when the clocks of the PRN-cw generator and the acquisition system are not synchronised and run free. Both the modulation frequency and the sampling rate were at 10 MHz and each measurement lasted 5 s. The sequence length is 127 (upper right plot), 255 (upper left), 1023 (lower left), and 4095 (lower right). Peaks become smaller and smaller, broader and broader and the noise increases more and more as function of the sequence length.*

measurement. The longer the sequence, the smaller the peak values, the broader their shape, the larger the noise fluctuations. This is the result of the decorrelation effect which becomes more and more marked when longer and longer sequences are used.

Figure 3.6 shows the cross-correlated signal when the PRN-cw generator and the acquisition system are synchronised again for 7, 8, 10 and 12-bit sequences. We see that the shapes and the values of the peaks remain constant; the same holds for the noise fluctuations. Only the range covered by the sequence varies.

In conclusion, when the two clocks are synchronised, the sequence length has no influence on the cross-correlated signal and the SNR. The way photons are emitted (sequence length dependency) does not matter, while their number does (acquisition time dependency).

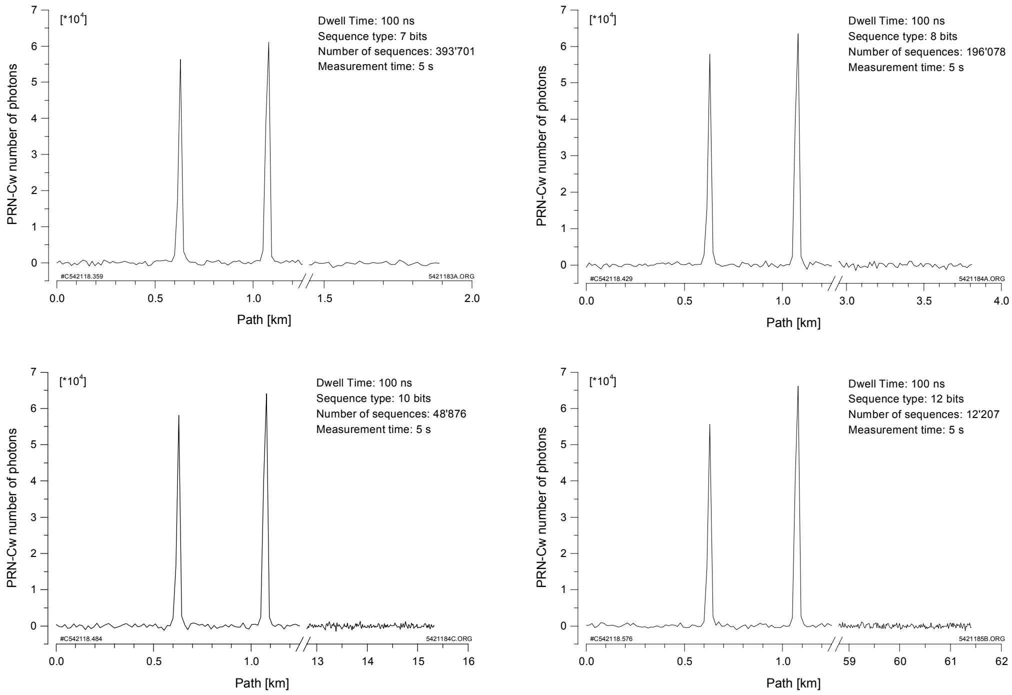

Figure 3.6. *Effect of the sequence length on the cross-correlated signal when the clocks of the PRN-cw generator and the acquisition system are synchronised, at 10 MHz. Each measurement lasted 5 s. The sequence length is 127 (upper right plot), 255 (upper left), 1023 (lower left), and 4095 (lower right). The shape of the cross-correlated signal remains clearly the same and no degradation occurs.*

3.4 A demonstration total elastic backscatter PRN-cw lidar

Our idea was to build a demonstration total elastic backscatter PRN-cw lidar to detect cloud base, topographic targets, and aerosol in the PBL during night-time. The desired performances are enumerated in Table 3.1. The configuration should be flexible enough to be easily adaptable to different objectives and instrumental test. Such a test was the two-optical fibre bench which allowed the development of know-how for PRN-cw laser modulation, detection, acquisition and demodulation of range-resolved backscattered signal, by hardware simulation of hard-targets. The instrument should probe in various directions: towards zenith for atmospheric measurements and horizontally for topographic target measurement. The instrument should also be adapted to the laboratory premises. Following from this, we decided to mount the transmitting and receiving optics on a steering platform connected to the rest of the instrumentation by two fibres, one transmitting the modulated beam to the platform (called the "transmitter fibre") and one transmitting the collected backscattered signal from the platform to the photodetector (called the "receiver fibre"). In this way, stable pointing to a chosen direction was ensured as well as assembly simplification and hardware control. The lidar was also assembled at the maximum from commercially available elements. The conception of the instrument was helped by the simulation software.

	Performances		
Mode of operation	Range [m] min.-max.	Range resolution [m] min.-max.	Integration time [s] min.-max.
Cloud base detection	500 – 1500	15 - 30	5 - 20
Surface return detection	500 – 3500	15 - 30	5 - 15
Aerosol layer detection	500 – 1500	30 - 60	30 - 300

Table 3.1. *Night-time desired performances for the demonstration total elastic backscatter PRN-cw lidar.*

3.4.1 System consideration and lidar description

In this section we will explain how we operated the selection of the main elements constituting the instrument and we will enumerate their essential characteristics. The lidar block-diagram is shown in Figure 3.7, and the instrument specifications are resumed in Table 3.2.

Laser source and optical filter

Three consideration guided the choice of the cw-laser diode: the wavelength, the wavelength bandwidth and the power. The choice of the wavelength is closely related to the envisaged optical filter. As mentioned previously, locking laser diodes on atomic lines makes them very stable in frequency and makes possible the use of very narrow filters for enhanced background noise rejection. That is why we chose 780 nm as it corresponds to an atomic vapour line of Rb where possibility of ultra narrow-band atomic vapour filter operation exists. It coincides also with an H_2O-vapour absorption spectrum mini-window, i.e., all of its isotopic and fine structure components are far enough from H_2O-vapour absorption lines. Windows in the H_2O-vapour absorption spectrum are also found around other appropriate strong atomic vapour lines, notably the Rb 796.7 nm and Cs 852 nm absorption lines. It would make possible the application of the same technique for diode laser wavelength stabilisation as for 780 nm. The laser diodes at these wavelengths also have higher cw output power. However we preferred the 780 nm concept, because it suited better optical detector performances: photomultiplier tubes with GaAs photocathode are more and sufficiently sensitive for this wavelength (quantum efficiency > 10 %).

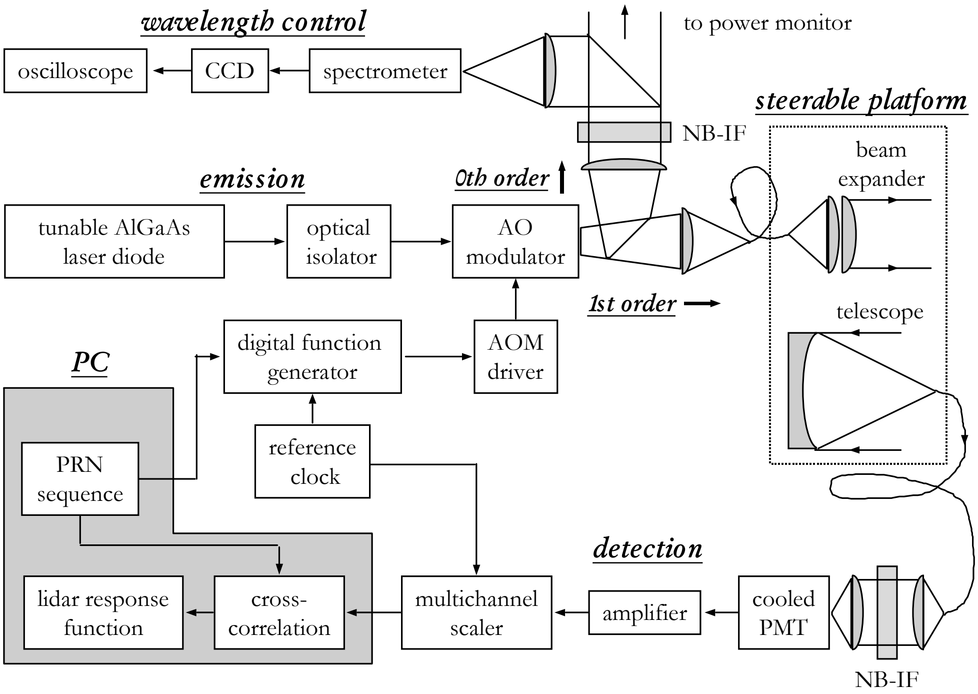

Figure 3.7. *Block-diagram of the demonstration total elastic backscatter PRN-cw lidar*

At 780 nm, some tens of mW are required to achieve the desired performances. At this wavelength, single mode AlGaAs cw-laser diodes with such output power were supplied by several firms – Spectra Diode Lab (SDL), Sharp, Mitsubishi. In a first step, we opted for and used a SDL-5412-H1 AlGaAs laser diode (further referred to as "normal" laser diode), which was specified as a single longitudinal and transversal mode laser with output power of 100 mW at 780 nm. It was then replaced by a SDL-8630 diode laser of MOPA type (MOPA, master oscillator-power amplifier, further referred to as "MOPA" laser diode) with a specified maximal nominal output power of 600 mW.

For the part of the work described here the laser diodes were not locked on a reference atomic line; yet, such operation has also been achieved and is reported in Chapter 5. The SDL-5412-H1 AlGaAs was used in stand alone configuration* with output power of 67 mW while the MOPA output power was adjusted to 220 mW.

* The SDL-5412-H1 AlGaAs laser diode was designed for extended cavity configuration operation and came with an anti-reflection coated front facet. However, that time, SDL stopped temporarily the production of

As only night-time measurement was envisaged, the optical filter bandwidth had to be chosen large enough to account for laser diode mode jumping as they were not locked. With the normal laser diode, we used a filter with 2 nm FWHM for accounting 200 GHz mode jump. For the MOPA laser diode, specified with bandwidth of 20 GHz, we used a 0.2 nm narrow-band interference filter centred at 780.1 nm. A second filter, identical to the one in the receiver chain, was used for the laser wavelength control. The wavelength of the laser was tuned around 780 nm till it coincided with the central wavelength of the filter. A grating spectrometer and a CCD camera were install to detected eventual changes of the laser bandwidth and its central wavelength.

Once the wavelength had been finely tuned, no problem of de-tuning has ever been faced. Mode jumping occurred but inside the optical filter bandwidth. The laser intensity stability was characterised to be better than 1 % over periods typical of one sequence duration, i.e. time scale of 10^{-5} s. Over long term periods typical of the measurement integration time, i.e. 100-1000 s, the stability was again better than 1 %. These measurements were made in cw mode.

Light modulation

For the laser beam modulation we chose the combination of an arbitrary waveform generator driving an amplitude modulator. This combination had to produced PRN-cw sequences with pulses as narrow as 100 nm to achieved 15 m range-resolution. The sequences were generated by a computer program, what allowed flexible and convenient way to vary the sequence parameters, like length and pulse duration. They were then transmitted via GPIB interface to the arbitrary waveform generator, a Tabor Electronics, Model 8553, arbitrary/function generator. This instrument stored the sequence in its memory and, when triggered, output the sequences with rate up to 50 Msps (mega-samples per seconds). This instrument provided rise- and fall-time of 7 ns; its bandwidth was thus well in accordance with the minimal range-resolution of 15 m (10 MHz) to be achieved. Of prime importance for PRN-cw measurement because of the modulo operation of the theory, this generator showed absolutely no deadtime between two successive sequences. A PLL is integrated in this device so that it can be locked to an external clock.

The amplitude modulator of the laser radiation was an acousto-optic modulator (AOM) from Crystal technology, model 3200-124, along with the AOM driver, model 1200-10 (operating frequency: 200 MHz). The PRN-cw sequence was sent to the digital input of the AOM driver and in this way the laser beam was modulated following PRN sequence patterns. The first order diffracted beam was used for the lidar measurements. This combination allowed to achieve pulsed modulation up to 10 MHz as desired*.

---

such high power diodes at 780 nm and no spares were available. The stand alone mode was retained as higher output power could more easily be obtained without risking to damage the laser. Using the diode in stand alone configuration was less risky but had the drawback that undesirable mode hops occurred and broadened the wavelength bandwidth of the laser.

* An electro-optic modulator from Isomet, model 1206C, and its driver, model 223A-1, was also tested. It couldn't reach convenient modulation at 10 MHz and it was renounced to it.

An optical isolator was placed between the laser diode and the AOM in order to prevent reflected light from the AOM crystal from damaging the laser diode.

Transmitting and receiving optical subsystems

The output beam after the AOM was fed by a lens into the transmitter multimode optical fibre (gradient index, 50 μm core diameter). The other end of the fibre was fixed at the focal point of a doublet lens, which served as beam expander – 4-cm diameter. The divergence of the output beam was about 0.4 mrad. The efficiency of the overall transmitter system – from the optical isolator to the beam expander lens including the AOM – was estimated to 18 %. The mean modulated laser power at the output of the beam expander was 11-12 mW for the "normal" laser diode and 38-40 mW for the MOPA diode laser.

The receiver was a Newtonian telescope with primary mirror only. This mirror was supplied by Edmund Scientific Company, model G32056. It was a F/5 parabolic mirror of 200 mm diameter, with a precision of $\lambda/8$ at 780 nm. Due to its gold coating it had an increased reflection in the near IR region – about 98 %. To transmit the collected backscattered radiation to the detector, one end of a step-index fibre of 600 μm-core diameter was positioned at the focal point of the mirror. In this configuration, the telescope field of view was 0.6 mrad. The efficiency of the overall receiver system – from the receiver mirror to the PMT, including the interference filter – was estimated to about 35 %.

The transmitting beam expander and the receiving telescope were fixed on a common platform for convenient pointing.

Detection and acquisition system

As photomultipliers (PMTs) show higher gain and are easier to align than avalanche photodiodes, we opted for a large bandwidth, GaAs photocathode PMT from Hamamatsu, model R-943-02. This PMT has quantum efficiency more than 10 % at 780 nm and is designed for photon-counting. It was placed in a housing and cooled at –20 °C in order to limit the dark noise as low as 20-50 counts per second.

In front of the PMT photocathode, we positioned an optical system consisting of two lenses and the narrow-band interference filter. The receiver fibre end was positioned in the focus of the first lens in order to collimate the beam. The second lens only concentrated the light, without focussing it, into a spot smaller than the sensitive area of the photocathode. Doing so prevented the photocathode from being damaged by high photon fluxes. The interference filter was in the collimated beam between the two lenses.

The single photoelectron pulses from the PMT were amplified 200 times by a fast amplifier and sent into a multichannel scaler from EG&G, model Turbo-MCS™. The Turbo-MCS™ features relevant for our experiment were: dwell time per channel selectable in a range from 5 ns to 65535 s – from this option we used 100 ns to 1 μs –, external clock input possible for minimal dwell time of 200 ns corresponding to 30 m range-resolution,

Instrument	Parameter	Specification
Laser	wavelength cw power SDL-5412-H1 (normal) cw power SDL-8630 (MOPA)	780 nm 67 mW 220 mW
PRN-code	clock time, min. clock time, max. deadtime between sequences sequence length	0.1 μs (15 m resolution) 1 μs (150 m resolution) 0 s 8-14 bit
Cw laser beam modulation	pulse duration rise and fall times	0.1 μs – 1 μs <10 ns
Transmitting telescope	beam diameter output beam divergence overall transmission efficiency	40 mm ~0.4 mrad 18 % (see § on transmitter)
Receiving telescope	type primary mirror diameter focal length field of view overall transmission efficiency	Newtonian 200 mm 1000 mm ~0.6 mrad ~35 % (see § on receiver)
Optical filter	central wavelength bandwidth, transmission transmission (@ max.)	780.1 nm 3 nm/45% (norm. diode conf.) 0.2 nm/35 % (MOPA conf.) ~45 %
Detector	Type mode of operation quantum efficiency (@ 780 nm) bandwidth rise and fall times dark current	photomultiplier tube photo counting >10 % >100 Mhz <5 ns <50 count/s
Data acquisition system	type count rate (max.) single channel duration number of channels deadtime between scans	multichannel scaler 150 Mhz 0.1 μs – 1 μs $\leq 2^{14}$ 0 s
Steering	horizontal plane vertical plane	0 – 360° 0 – 90°

Table 3.2. *Specifications of the demonstration total elastic backscatter PRN-cw lidar*

number of bins per scan up to 16384 channels – 60 km range with 15 m resolution requires 4000 channels –, memory capacity of 24 bits/channel – more than $16 \cdot 10^9$ counts per channel –, 150 MHz input rate, no deadtime between channels, and no deadtime between two successive scans for dwell time of more than 100 ns. This last performance was of prime importance as it allowed data accumulation with a continuously repeated sequence.

A single computer controlled the lidar instrument and experiment. It generated the sequences, controlled the Turbo-MCS™ and performed the computation of the cross-correlation.

3.4.2 Pulsed and PRN-cw response from a hard target

As a system function test, the response of a hard target has been measured during night-time successively for both operation modes. The instrument pointed to a tower 4075 m far away from the instrument (cf. photography of Figure 3.9). The conditions of measurement were exactly the same, 30 m resolution, 100 s measurement duration. The pulse repetition

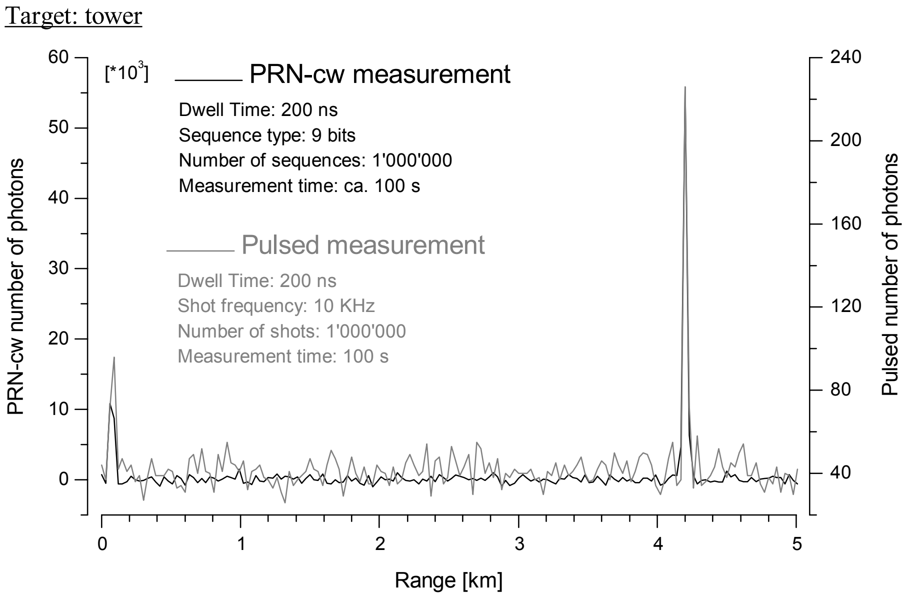

Figure 3.8. *Night-time accumulated return signals from a hard target – a tower. The darker line represents the cross-correlated signal obtained by PRN-cw modulation of the laser diode beam and the lighter line the signal obtained by pulsed modulation at a repetition rate equal to the inverse of the duration of a single sequence. Normal laser diode was used here.*

rate was set at the sequence repetition rate – that is 10 kHz as the duration of a single sequence was 0.1 ms. The results are presented in Figure 3.8, where are plotted the accumulated numbers of detected photons. The only data processing was the computation of the cross-correlated signal in the PRN-cw measurement.

We see that the tower was detected exactly at the same range, 4200m*. In the pulsed case, the mean background noise value is 41 counts while the peak value corresponding to

* The range offset due to the overall instrumental delay for the demonstration lidar was measured to be 850 ns equivalent to 128 m. This offset shall be systematically subtracted from the measured range to get the actual range. This explains why the tower was measured at 4200 m instead of 4075 m. This range offset is larger than the one of the two-fibre delay line test bench because of the additional presence of the transmitter

the tower is 185, after subtraction of the background value*. In the PRN-cw case, the mean noise value is 37 and is, as expected, of the same magnitude as the pulse case; the similarly corrected PRN-cw peak is 55'728. As a 9-bit sequence consisting in 511 bins was used, this signal should be 256 times larger than the signal in the pulse case ([511+1]/2). The actual ratio of the peaks is 301. This is slightly more than expected, but considering the errors on the signals (fluctuations), this value fits to the theory.

This example of comparison between PRN-cw and pulsed real measurements shows that the demonstration PRN-cw lidar is working and in accordance to the theory.

3.4.3 Examples of measurements

In this section we present examples of signal obtained by the PRN-cw demonstration total elastic backscatter lidar for several types of target. They include hard targets, cloud base, aerosol in the PBL. The goal is to show some potentialities of the PRN-cw technique ap-

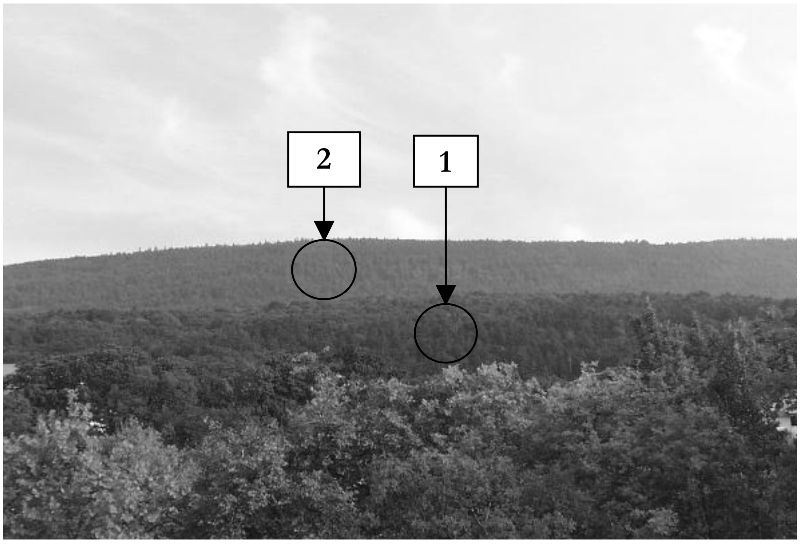

Figure 3.8. *Target areas on the slope of the Mountain Chaumont, north of the Observatory of Neuchâtel as seen from the cupola. Targets 1 and 2 are about 600-700 m, respectively 2-2.5 km far from the lidar instrument depending on the pointed area.*

plied to lidar. All measurements were performed during night-time with the normal laser diode unless other indications are mentioned. Only raw (cross-correlated) data are plotted; they have not been filtered. As explained in the foot note on page 54, an offset of 128 m has to be subtracted from the range indicated in the plots to get the actual distance.

The hard targets pointed most often with this lidar and other instruments reported later in this work are presented in Figures 3.8 and 3.9. The Observatory of Neuchâtel is situated at an altitude of 487 m altitude. 500 m on south is the lake of Neuchâtel at altitude

---

and receiver fibre in the lidar set-up. When speaking about ranges further in this chapter, we will refer to ranges without considering this offset. It is a systematic error of few importance in our case as we will only illustrate the possibility of this lidar by presenting raw signal examples. In case of range-correction (R^2-correction), this offset shall be accounted.

* The background noise mean value is computed as the mean value of the channels corresponding to ranges larger than the distance to the tower, [4.5 km, 15 km]. 15 km is the upper limit of the range interval covered by a 10 kHz sequence or pulsed repetition rate.

of 430 m. It is about 6 km width. On north a mountain chain, Chaumont, runs alongside the lake. The rim is at 1'000 m altitude. On east, there is the lake in the immediate vicinity and a plain with smoothed hills some kilometres farther. On west is the city, direction where we never shot. The observations are usually performed from the cupola located on

Figure 3.9. *Target area at the opposite shore of the lake of Neuchâtel. east of the Observatory of Neuchâtel. Target 3 is a tower at 4070 m distance from the cupola.*

the roof of the Observatory. All directions on a full 360°-circle may be pointed. Target 1 probing area requires a elevation angle of 5-10° degrees and target 2 area 15-20° degrees. Horizontal slant path are used for target 3.

Topographic ranging

Figure 3.10 present the cross-correlation function of the lidar return from the nearby Mountain Chaumont (target 2), with an almost grazing incidence to the slope. The presented measurements are with a 8-bit sequence, a range resolution of 15 m and an integration time varying from 51.1 s to 5.11 ms and performed with the normal laser diode. As it may be expected the maximum of the signal decreases in the same proportion as the integration time. The SNR degrades gradually from about 135 to 1.6*. With high integration time we may see the low level response of the ground below the tree canopies; it is the sec-

* As PRN-cw fluctuations mainly follow Poisson statistics – they linearly result from the fluctuations of the acquired signal which is dominated by optical noises – they tend to Gaussian statistics with σ as standard deviation. The confidence level for 2σ is 95.4%. In the PRN-cw technique, the noise is constant for any point of the cross-correlated profile. As the length of the sequence has to be chosen to include the critical distance, there is always a range interval where the signal is lost in the noise. On this interval the fluctuations oscillate around the mean noise value. For numerical statistics we define the noise level as equal to 2σ. For empirical noise level estimation, such a definition corresponds to the difference between the mean noise value and a estimation of the peak value of the fluctuations above (or below) this mean noise value. We speak about estimation because taking the absolute maximum peak value into consideration would correspond to a confidence level of 3σ (99.7%) or more. It would give thus too much weight to very few data which are exceptional. 2σ fits better to empirical estimation. When speaking about SNR in PRN-cw photon-counting mode, we will refer to this definition of the noise.

ond peak. For much short integration time, this peak is buried in the noise fluctuations. For 51.1 ms, the signal is still good with a SNR of about 6. Such a low integration time makes realistic the possibility to use a PRN-cw lidar for topographic mapping with sufficiently

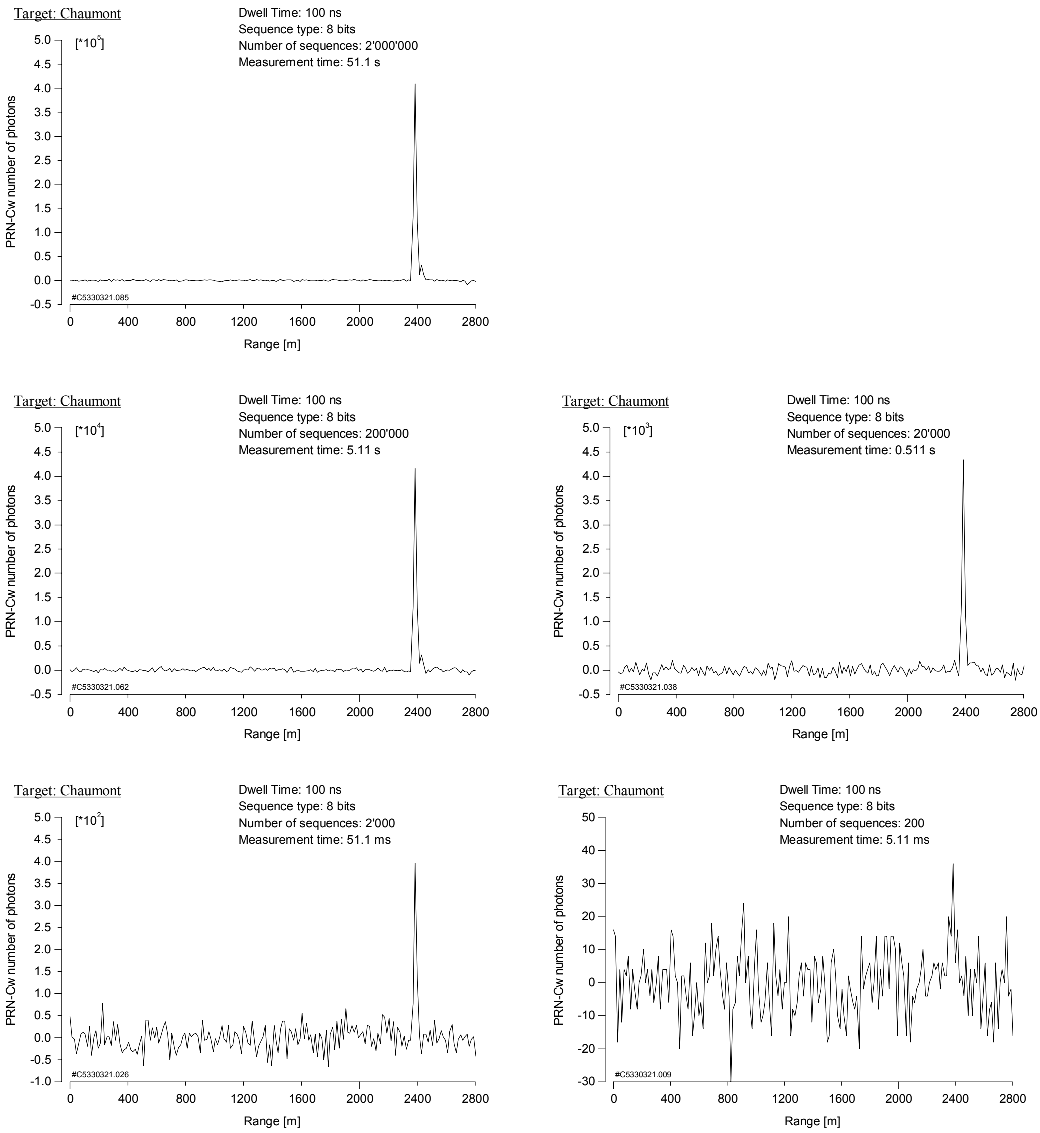

Figure 3.10. *Lidar signal from Mountain Chaumont (target 2). The measurement time varies from 51.1 s to 5.11 ms, while the resolution was fixed at 15 m. Even for very short duration the target is still detected. For higher duration, as the SNR increases, we may note a double echo: the first is the tree canopies return, the second the ground return.*

horizontal resolution from airborne platform. It corresponds to a distance of 5 m when flying at 360 km/h.

Another example of topographic measurements is presented in Figure 3.11. It is a long range lidar measurement in the horizontal direction obtained with the MOPA diode laser. The target was a mountain slope at about 45 km from the lidar. For this measurement, the dwell time was set to 1 μs equivalent to 150 m. The left plot shows the cross-correlated lidar signal over the total range covered by the sequence, while the right plot is the zoomed lidar response from the mountain slope. The SNR for the topographic target is circa 7. When probing in the horizontal path, the laser beam suffers from a 5 times approximately larger extinction coefficient than when probing the whole atmosphere vertically*.

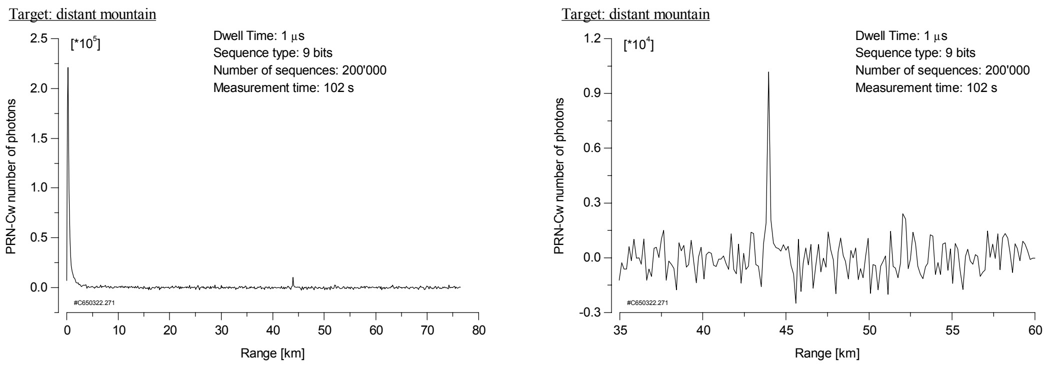

Figure 3.11. *Long range topographic measurement with MOPA laser diode. The lidar pointed horizontally to a distant mountain. The resolution was 150 m and the integration time 102 s. Notice the peak at 44 km with SNR of 7, and immediately after the flat plateau, evidence of a slope.*

Cloud base monitoring

Of interest for meteorology is the altitude of the cloud base. Figure 3.12 demonstrates that it is possible to determine this value with a PRN-cw lidar. It presents a time series of short measurements. They were performed each with 3.06 s integration time and 30 m resolution. The cloud base is double and oscillates in the interval 1.7-2.1 km, as if two layers were present. The change of the cloud base pattern is fast as the time interval between two successive measurements is 17 s in average. This example demonstrates that monitoring routinely the cloud base during night-time is possible. Similar task but for day-time was not achieved by this instrument but is yet feasible by PRN-cw technique, as it will be reported in the next chapter.

* A value of 8.5 km is assumed for the thickness of the molecular atmosphere reduced at see level normal conditions.

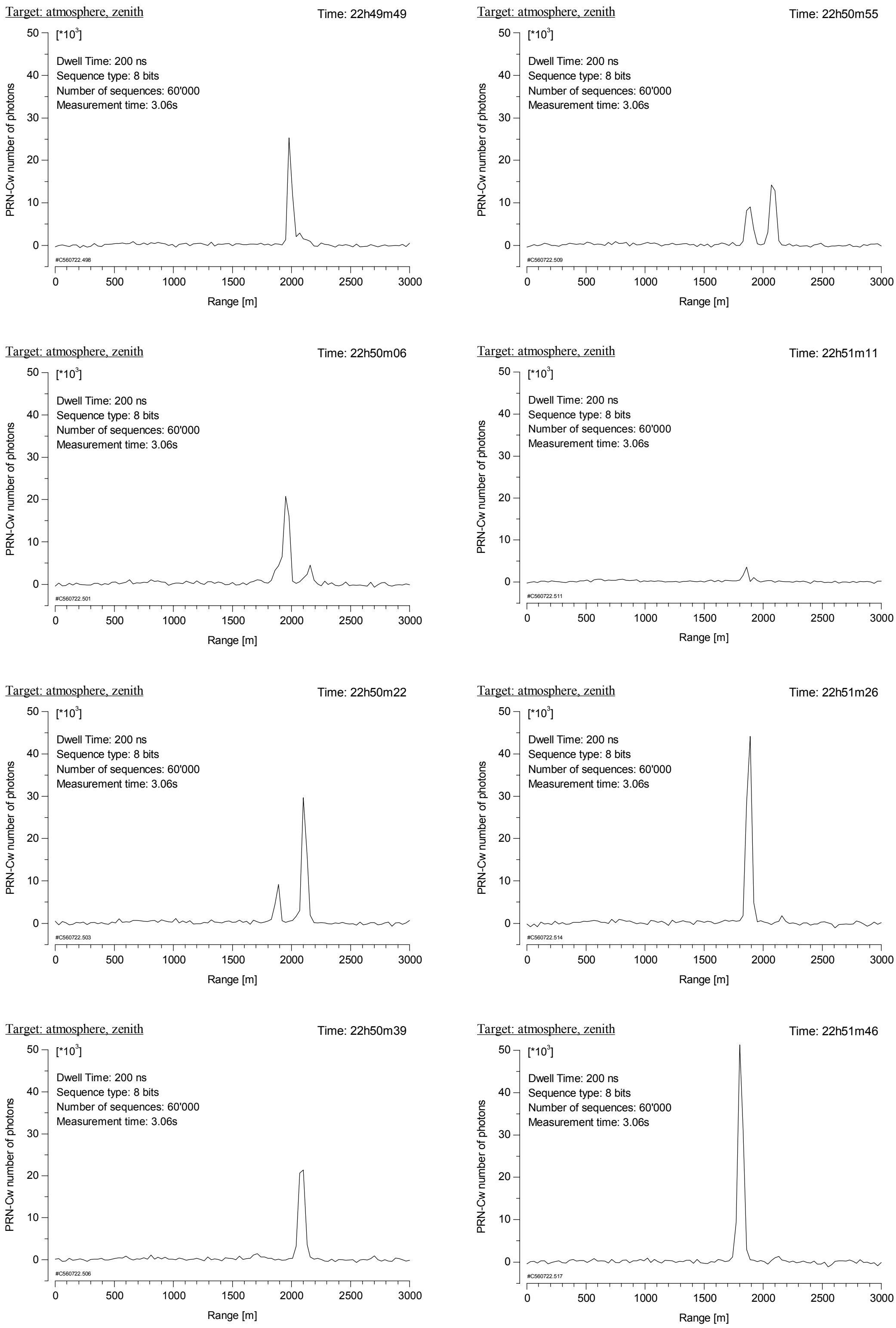

Figure 3.12. *Time series of cloud base measurements with short interval between two successive measurements – in average 17 s. The resolution was 30m and the integration time 3.06 s for each acquisition.*

PBL aerosol detection

Lidar returns of cloudless sky were also recorded that show aerosol content in the planetary boundary layer. They requires longer integration time, typically several hundreds of seconds, and lower range resolution, usually 150 m. In Figure 3.13 two examples illustrate such type of measurements. The structure in the PBL is well expressed, and the top of the PBL is clearly visible. The overlap function of the instrument is zero below ~500 m, what means that backscattered signal from below this distance cannot be detected. The small initial peak in the left plot is so no real signal; it is due to scattered light in the laboratory.

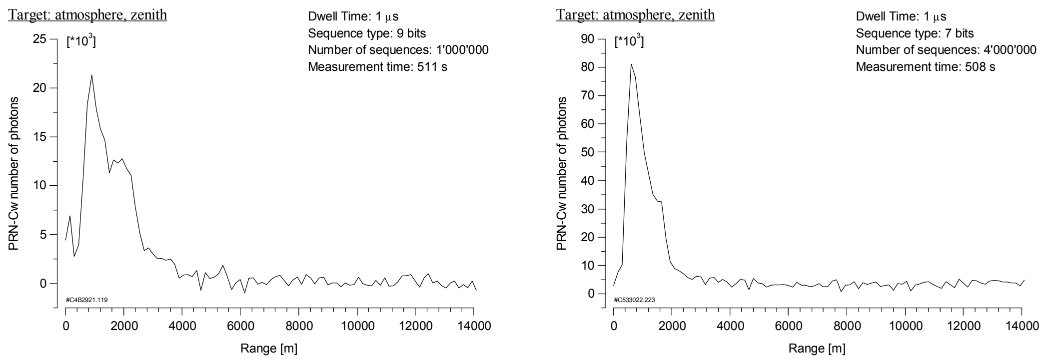

Figure 3.13. *Atmospheric lidar return from cloudless sky with range resolution of 150 m and integration time of about 500 s. The top and the structure of the planetary boundary layer are well seen. These two measurements were not performed during the same month a fortiori the same evening.*

3.4.4 Comparison between calculated and obtained performances

The calculated performances for the demonstration instrument were enumerated in Table 3.1. If we compared them with the obtained results, we see that the objectives for cloud base and topographic modes of operation have been largely fulfilled. Concerning the aerosol layer detection, measurements with longer integration times and lower range resolution than the calculated parameters have been obtained. Passing from 500 s integration time to 300 s, 1.67 times less counts would be detected and the noise fluctuation amplitude would be smaller by the square-root of this value, 1.3. Increasing the resolution from 150 m to 60 m, that is by a factor of 2.5, means dividing proportionally the number of accumulated counts per bin. In total, the SNR would diminish by a factor of 2 (square-root of 1.67*2.5). If we look at the obtained PBL profiles, we see that the structure and the top of the PBL would still be detected. We conclude that the calculated performances have been achieved.

3.5 Limitations and advantages of the PRN-cw technique

As already exposed, the fluctuations are constant over the full cross-correlated profile and proportional to the square-root of the integrated detected signal. This induces two main limitations to the PRN-cw technique.

As in the pulsed technique, the background noise degrades the quality of PRN-cw measurements and limit the use of a PRN-cw instrument. But a PRN-cw lidar is even more sensitive to background radiation – in fact to all sources of noise – than a pulsed lidar because of the reason explained here above. In the latter technique, for each bin, the background noise is square-root proportional to the background radiation detected by one bin only. In the PRN-cw technique the background noise in a single bin is given by the total amount of background radiation detected during the whole measurement. This is the main limitation of the PRN-cw technique.

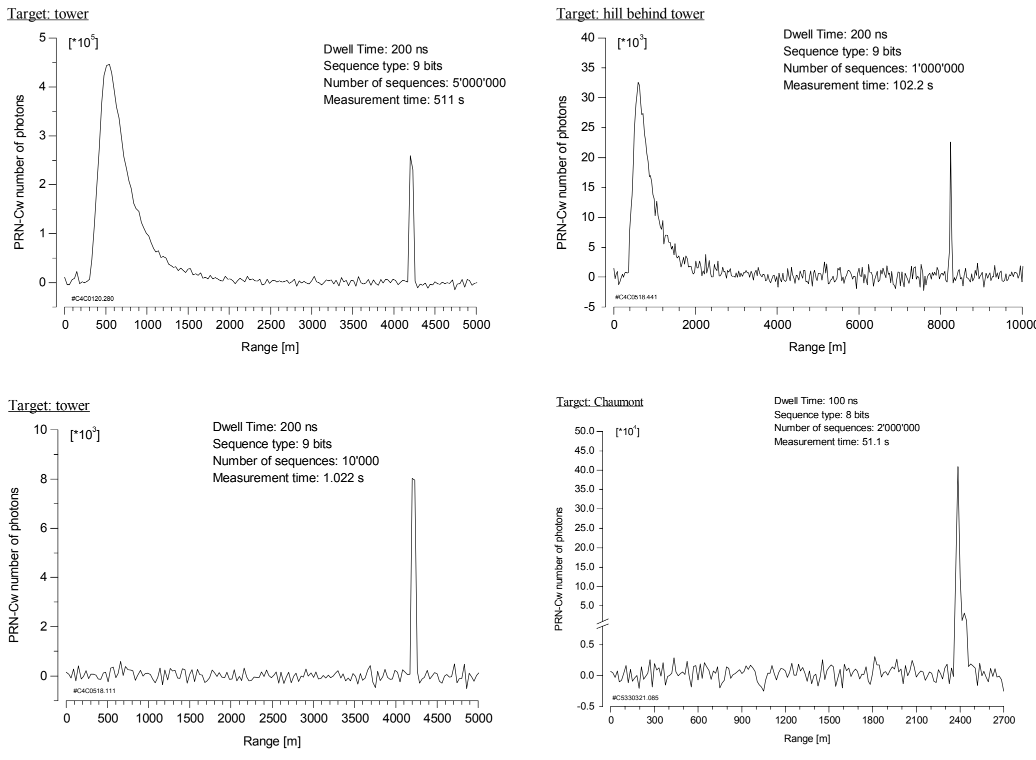

Figure 3.14. *Lidar signals from various hard targets. A too strong return function like from a hard target may prevent the detection of much weaker responding target like from the atmosphere. The too large noise level is induced by the high shot noise related to the strong event which spreads over the whole measurement interval. For detailed explanations of the plots, see the text.*

The second important limitation is related to the difference in the signal dynamics. Weak responses in confrontation to large ones can be lost. Figure 3.14 illustrates this effect. The signal of the upper left plot was obtained by probing at the tower during a hazy evening. The humidity in the air (fine water droplets) increases the backscattered signal and the beam is faster extincted: the humid atmosphere is clearly seen, while the signal from the tower is in the same order of magnitude. The signal shown in the lower left plot is a similar measurement, but done another day in dryer conditions. The molecular or aerosol atmospheric return is not visible. The measurement duration is short and thus the SNR is in all cases lower. However if the conditions were the same as for the upper left plot, something would have appeared anyhow; what is actually not the case.

The importance of the noise is confirmed by the upper right plot where is reported a measurement made half an hour later than the one of the lower left panel. The atmospheric conditions were the same. We changed the pointing direction in order to avoid the tower, and shot at the hill twice further behind the tower. Due to the increased range and likely lower albedo (ground, trees have smaller albedo than buildings when hit perpendicularly to their surface) the response function was weaker by 40 times. The induced noise fluctuations were then relatively lower and allowed to detect the atmospheric response. In the lower right plot, the noise induced by the return from Mountain Chaumont also prevented to detect the atmospheric backscatter signal from the closer ranges (the y-axis contains a break to emphasise the low signal values). In conclusion, the PRN-cw technique is not suited to measure simultaneously response functions of highly different dynamics.

Besides the practical advantages related to the use of a laser diode and already discussed previously in this chapter, there are also “plus” offered by the PRN-cw technique from the detection point of view. Pulsed lidar signals usually show high signal level variations along the profile, what requires a high dynamic range detector. In the PRN-cw technique the total backscattered power impinging onto the detector is spread over the full sequence and requires less dynamic range detector.

For equivalent mean laser power, the maximal arrival photon rate onto the detector is much lower in the PRN-cw technique than in the pulsed technique as it was demonstrated in Section 3.3.1, page 53. In photon-counting detection mode, this is a two-fold advantage. Non linear response of the detector due to pile-up effect is much less probable; and detectors with long relaxation time like quenched avalanche photodiodes may be used. Counting units require also less number of bits for the accumulation and may be slower in counting as the photon pulse arrival rate is smaller.

3.6 Measurement simulations

Comparisons between simulations and signals obtained from the demonstration total elastic backscatter lidar were performed. The main characteristics of the instrument in its configuration with standalone diode laser were used as inputs for the simulation model. Hereafter three examples of such comparisons are presented. They are all night-time measurements and simulations. Figure 3.15 illustrates the case of a topographic target, a tower located at about 4 km far away from the instrument. The range resolution is 15 m and the integration time 0.2 s. Figure 3.16 presents the case where the atmospheric return near the

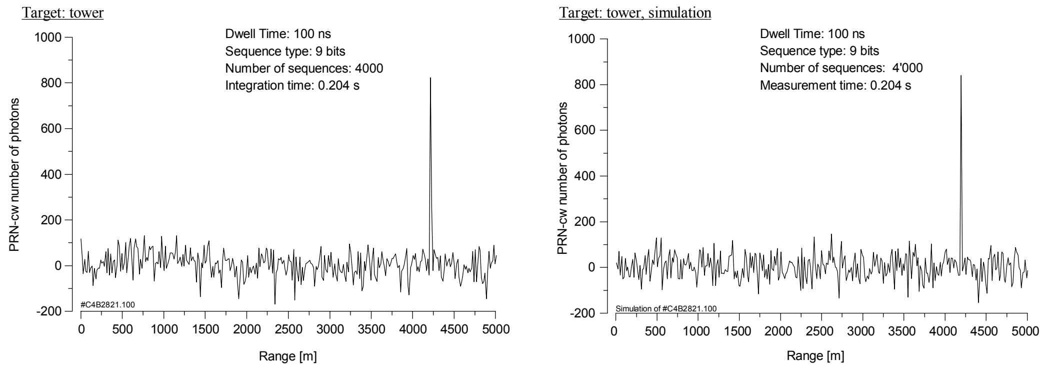

Figure 3.15. *Lidar response from a 4-km distant tower as measured (left pane), and as simulated (right pane), for a 0.2-s integration time and 15-m range resolution.*

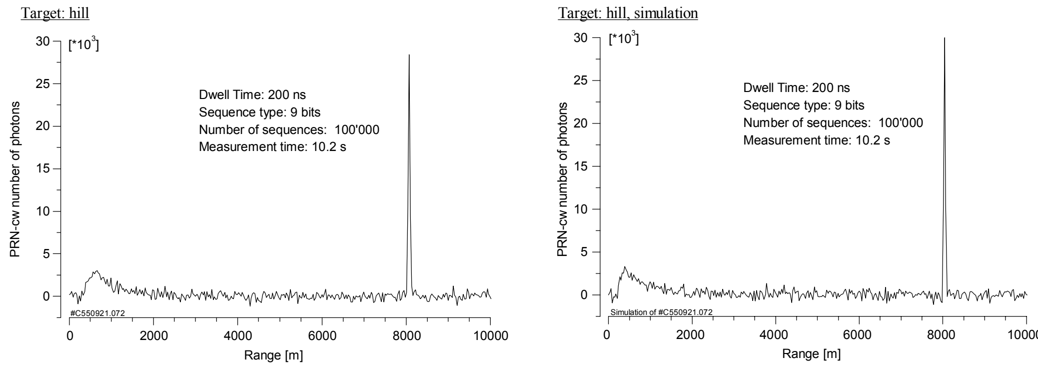

Figure 3.16. *Lidar response from a 8-km distant hill as measured (left pane), and as simulated (right pane). The integration of 10.2 s was long enough for the return from the atmosphere to emerge from the fluctuations induced by the hard target detection.*

instrument starts to be detected while a topographic target is pointed. Here the resolution has been decreased to 30 m and the integration time increased to 10.2 s. As third case, Figure 3.17 is an atmospheric example and shows the detection of the cloud base with 15 m range resolution and 2.55 s integration time. The scattering ratio is also plotted for 780 nm. The initial input cloud peak scattering ratio value was 4250 at 532 nm. Clearly visible is the full extinction of the beam few hundreds of meters after the cloud base.

The result of a simulation depends not only on the instrument parameters but also on the parameters of the atmospheric and target models (albedi, backscattering and extinction ratios, etc.). These are less obvious to evaluate because it is not possible to measure them, like the former. To get a simulated signal resembling the measured signal, several combinations of parameters have to be tested. At the end there are usually few possible combinations for reaching a good result, not only at a single distance from the instrument but over the whole probed path. Our final combination results in atmospheric and target parameter values that are in agreement with [Este91 and Este92] and that are reasonable and plausible in comparison with the weather conditions at the times of the measurements. Or, expressed in another way, the model, with use of appropriate values from [Este91 and Este92], allows to simulate signals resembling measured ones. Thus, these comparisons reveal a good agreement between measured and with relevant parameter values simulated signals, and validate the model.

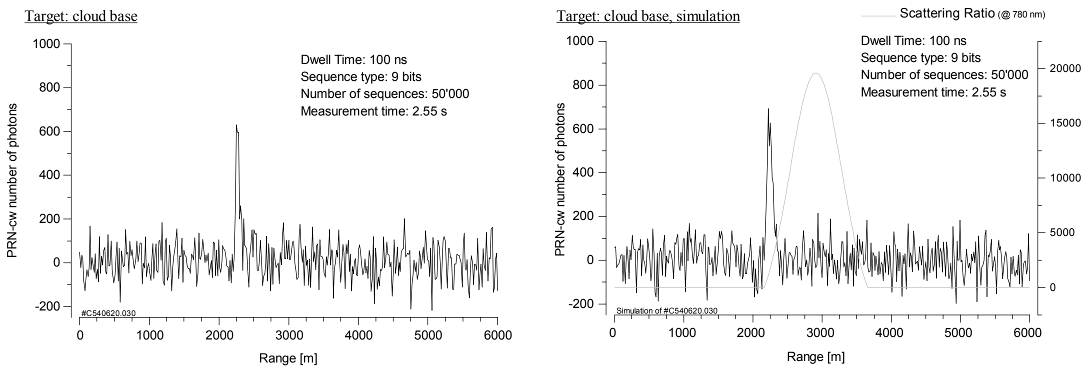

Figure 3.17. *Cloud base detection as measured (left pane), and as simulated (right pane). The integration time was 2.5 s and the range resolution 15 m.*

Conclusion

It has been demonstrated here that an atmospheric backscatter lidar based on the PRN-cw technique and a diode laser is feasible. The method has been proven in several application modes for night-time operation. In topographic mode, the very good results obtained offer a potential for airborne topographic mapping, field where eye-safety is of particular importance. For cloud measurements, the investigated technique has revealed powerful, especially for applications such as ceilometer. As shown, measurements of multiple layer clouds in dynamic atmosphere were possible with good time and spatial resolution. The instrument also demonstrated its capability of sensing aerosol. The planetary boundary layer has been detected but with longer integration time. The good results obtained for topographic and cloud base range determination suggest that day-time operation for these applications should be feasible too. This will be described in Chapter 4. This technique, whereas not as powerful as the pulsed one, may be useful for simple tasks, like cloud-based monitoring, or applications where eye-safety is requested, or for planetary space mission. As illustration, a concept of a PRN-cw lidar as part of a payload for a Mars expedition will be exposed in Chapter 5 too.

Limitations and advantages of the PRN-cw technique have been discussed. This technique offers several instrumentation advantages, but the price to pay is the increased sensitivity to noises and particularly to the most important of them, the background noise. However, due to the continuous-wave feature of the laser light, a solution exists to improve the background noise rejection and will be presented in Chapter 5.

Finally, real PRN-cw measurements allowed to validate the computer model that was discussed in Chapter 2 and by means of which the demonstration PRN-cw lidar was conceived.

Chapter 4

A compact PRN-cw lidar

Introduction

In previous Chapter 3, the PRN-cw technique has been investigated and validated. Knowledge has been acquired on the probing beam amplitude modulation and the detected signal demodulation as well as on the requirements for the various components of the instrument and on the evaluation of measurement capabilities of a total elastic PRN-cw lidar. These aspects have been studied on a lidar demonstration set-up working in photon-counting detection mode during night-time only, and which volume and configuration have not received a special attention. Base on this knowledge, we developed and present here a compact and transportable lidar of the same total elastic backscatter PRN-cw type, able to measure during day-time also. The realised instrument is built around a powerful laser diode, with light modulation by direct driving of its current, and uses a solid-state detector with analog detection.

The concept of the instrument, its purpose, operation requirements and set-up, will be explained in Section 4.1. How the components were chosen and the sub-system parts designed will be the subject of matter of Section 4.2. In the PRN-cw technique, the electronics package is the core of the instrument. Transmitted light modulation, acquisition system, clock synchronisation, laser diode control are discussed in this section. The performances of the instrument are reported in Section 4.3. The capabilities and limitations of the instrument are finally discussed in Section 4.4.

4.1 Concept of the compact PRN-cw backscatter lidar

4.1.1 Objectives

The objectives of this development are to show the technical possibility for realisation of a compact transportable PRN-cw total backscatter lidar, to demonstrate the detection capabilities for different kind of targets, and finally to demonstrate that day-time operation and detection are possible

We decided to built a compact total elastic PRN-cw lidar called ABB – for Advanced Bread-Board – around a high power laser diode and a solid state detector – avalanche photodiode or APD. We aimed at topographic and cloud-base detection both night- and day-time, with integration time of a few seconds. The instrument should be lightweight for convenient transportation and outdoor operation of the optical package. It should be also reliable enough for stand-alone and unattended operation. Eye-safety immediately at the output of the light transmitter was not so primordial; a distance of 100 m appears still sufficient for the tasks assigned to the instrument.

A flexible design both of the instrument architecture and of the sub-systems should allow easy integration and replacement of components. It should also be adapted to convenient implementation of changes and future upgrading as well as fast implementation of the PRN-cw principle in other configuration of lidar backscatter instruments. This means for instance that the transmitter and receiver parts might be changed but the rest of the instrument – code generation, acquisition system, procedure of measurement, etc – would remain the same.

4.1.2 Lidar set-up

To fulfil the above requirements, ABB was designed to consist of three separate packages: the computer with the electronics package, the optical package and the power supply unit. Figure 4.1 shows the realised instrument and its three packages.

The computer with the electronics package contains the PRN modulation waveform generator as a computer board – called simply PRN-cw board –, the analog data acquisition board, and the software for piloting the ABB operation. The PRN and the data acquisition boards are designed and manufactured as PC boards and plugged in the PC. We have two realisations of the computer system. The first realisation is based on desktop PC. The second and final realisation is based on an industrial PC which provides robust platform for operation and convenient slots. For data storage and presentation, it is connected to a laptop PC. This second configuration is further referred to as PC only. A PC software program establishes the inputs for the parameters of the measurement: the M-sequence length, the modulation frequency, the integration time, the number of measurements to be done, the pause duration between two successive measurements. The same software presents the output of the detected lidar response signal.

The optical package contains the diode laser, the diode driver and temperature stabilisation unit, the APD and APD preamplifier, the beam transmitting and receiving optics. The structure of the optical package is a single solid frame with the proper adjustment possibilities for the optical components, the APD and the laser diode. The laser diode is of a fibre optics pigtail configuration and is mounted in the same physical unit as the its driver, while the temperature stabilisation electronics is a separate unit. The fibre pigtail is connected and aligned to the transmitter optics in the focal plane of the latter to achieve minimum transmitting beam divergence. The information about the laser diode temperature,

Figure 4.1. *View of the compact PRN-cw total backscatter lidar (ABB). Counter-clockwise from right up: the optical package, the optical fibre link, the computer with the PRN generator and the acquisition boards, the DC power supply unit. The desktop computer has been replaced by an industrial computer connected to a laptop in the final configuration.*

the output power – state, power level, modulation – is sent to the PC via an optron coupled interface. The PRN waveform, generated by the PRN board, is sent to the laser diode driver through fibre optics link, thus avoiding galvanic connections. The backscatter radiation from the target or the atmosphere is collected by the receiving optics and concentrated on the photosensitive surface of the APD. The pre-amplifier is positioned very close to the APD. The amplified electric signal is then sent by a co-axial cable to the data acquisition board in the PC. The electrical and optical fibre connections from the PC and the power supply unit to the optical package are combined in a single cable bundle. The optical package operates outdoor mounted on an appropriate base while the PC and the power supply unit are indoor on a table or a desk.

The power supply unit contains DC voltage power supplies for the laser diode driver and the temperature stabilisation unit and for the APD and its pre-amplifier. The electric power supply is 230 V/50 Hz.

The block-diagram of the instrument and a view of the optical package are shown in Figure 4.2, while Table 4.1 presents the main parameters and characteristics of the ABB instrument and its sub-systems.

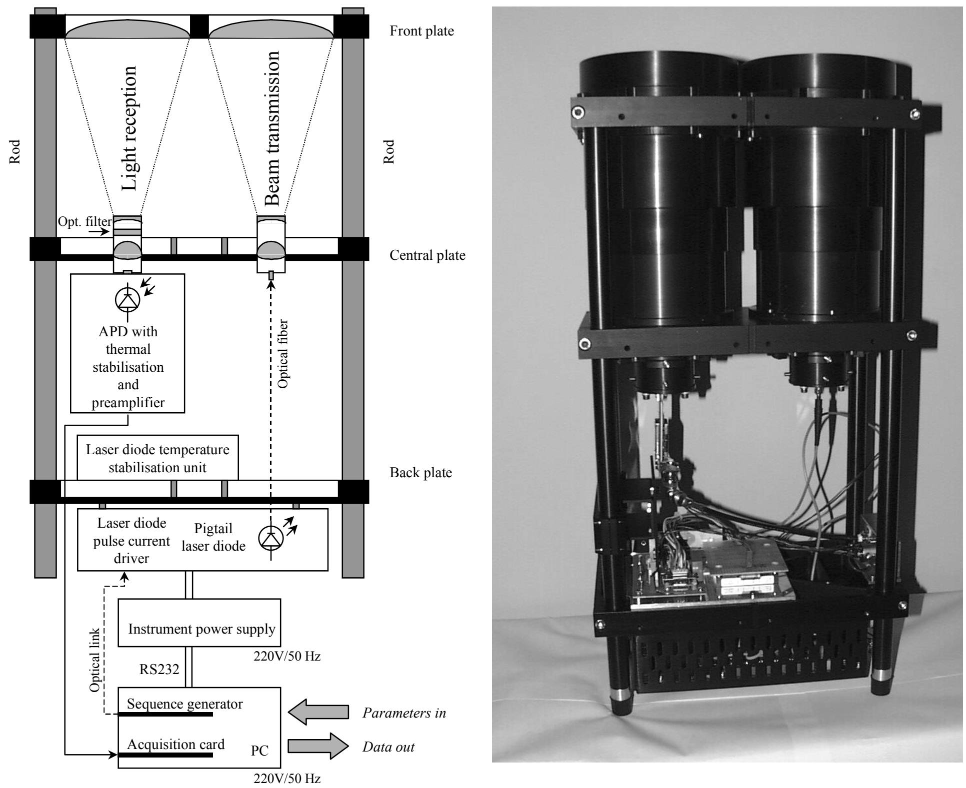

Figure 4.2. *Block diagram of the ABB instrument and view of the optical package looking up with side covers removed. The two tubes contain the transmitter and receiver optics. The optical package has dimensions 51x32x17cm* ^{3}*, a volume of 28 litres and a weight of 15 kg.*

Laser diode	
Type	SDL-2371-P2
Configuration	pig-tail optical fibre output, fibre core ∅ 0.1mm
Wavelength	800nm @ 35°C
Bandwidth (FWHM)	1.8nm ± 0.1nm
Operating mean power (50% duty cycle)	385mW ± 5% @ 35°C
Rise/fall times	11ns/14ns
Modulation depth (extinction ratio)	evaluated <1000:1 @ 20MHZ

Table 4.1. *Specifications of the ABB instrument and its sub-systems – cont. on next page.*

PRN modulation board	
Modulation frequency	1, 5, 10 and 20MHz
PRN sequence length	from 2 to 14 bit
Signal outputs	TTL and optical
Signal output options	PRN, clock, synchronisation pulses
Synchronisation output	TTL, 10MHz
External synchronisation input	TTL, 10MHz
Computer environment	PC, ISA bus
Parameter setting	by software

Transmitter and receiver	
Transmission and receiver telescope type	Galilean refractor
Transmission and receiver telescope aperture	134mm diameter
Transmitted beam divergence (full angle)	0.9mrad ± 10%
Receiver field of view (full angle)	4.2mrad ± 10%
Interference filter CWL	800nm
Interference filter FWHM	5nm
Interference filter transmission	67% @ CWL
Eye-safety minimal distance (1s exposition)	38m
Eye-safety minimal distance (10s exposition)	87m

Detection	
Type	APD HAMAMATSU C5331-02
Effective area	0.5 mm diameter
Sensitivity @ 800nm	0.5 A/W (specified at gain 1)
Frequency band	4KHz to 100MHz (specified)
Gain	20-60 (specified)
Output impedance	50Ω
NEP	typ. 0.3pW/Hz$^{1/2}$ @ 800nm

Data acquisition board	
Data acquisition type	12-bit transient ADC
Sampling rate / range resolution	10MHz / 15m
Amplitude range	±3V
Gain	variable, up to 100
Coupling	DC or AC (by jumper)
Number of samples / number of cycles	Up to 2^{15} / from single cycle up to 2^{20}
Dead-time between sweeps	0
Synchronisation output and input	TTL, 10MHz
Input impedance / trigger input impedance	50Ω / 1kΩ
Computer Environment	PC, ISA bus
Parameter setting	by software

Mechanical and power characteristics	
Dimensions (optical package)	51x32x17cm^3
Weight (optical package)	14.8kg
Consumption (optical package)	40W
Consumption (electronic package)	35W

Table 4.1. *Specifications of the ABB instrument and its sub-systems – end.*

The minimal distance at which the eye may be directly exposed to the laser radiation depends on the beam area at the output of the transmission telescope and on the time of exposition, among other parameters. This explains why a so large output lens was used. Following the IEC 60825-1 standard [Iecs93] – the standard for safety of laser products published by the International Electrotechnical Commission –, the minimal distance from which the eye may be exposed to the laser beam radiation without being hurt is in the case of ABB 38 m, resp. 87 m, for an exposition of 1 s, resp. 10 s. In consequence, ABB is not fully eye-safe at any distance, but its performance may already be qualified of good.

4.2 Description of the sub-systems

Here we discuss in detail on which criteria we operated the choice of the components and how the sub-systems have been designed.

4.2.1 Laser diode and driver

The key component of a lidar, pulsed or PRN-cw, is the laser. For us, the criteria determining the choice of the laser diode are its wavelength and the one of the interference filter, its power and its modulation, its beam quality and its package.

The laser central wavelength λ_L shall be close to the maximum of the low-noise detector quantum efficiency wavelength dependence function and shall coincide with the central wavelength of the interference filter transmission λ_F .The laser diode bandwidth $\delta\lambda_L$ shall be 2 to 2.5 times smaller than the interference filter transmission bandwidth $\delta\lambda_F$. The filter was purchased after λ_L and $\delta\lambda_L$ had been measured.

High optical power is an obvious requirement for the diode laser. As ABB has to operate with a stand-alone laser diode, its optical output is directly modulated by the driving current. An important parameter in this case is the modulation bandwidth of the cw laser. The necessary high optical power shall be provided with the optimal modulation depth and efficiency, what is the task of the laser diode driver.

The laser beam divergence and the size of the laser front facet usually determine the size of the transmitting optics necessary to obtain the required transmitted beam divergence – in absence of aberrations and distortions. A special case is the optical fibre pigtailed configuration. In this case the requirement for the laser output power is transferred to requirement for the power at the end of the fibre. The requirements for the laser diode beam divergence and front facet size is transferred to requirement for the numerical aperture and core diameter of the fibre. These parameters are discussed further in connection to the critical optical components.

For high power laser diode, due to the driving current, the temperature drift may move the laser diode central wavelength at the wings or even out of the transmission curve of the interference filter. A thermo-electric cooler (TEC) and a thermistor are necessary for this purpose and the best solution is to have them integrated in the laser diode package. The laser diode output power shall be also monitored during the measurement and this require a monitor photodiode. For some laser diode, the monitoring photodiode is integrated in the laser diode package.

We opted for a laser diode from Spectra Diode Lab – SDL-2372-P3 [Sdlc96]. This diode is a fibre optics pigtail package with integrated TEC and monitoring photodiode. The output power delivered from the fibre end is 1.2 W. At 35°C the central wavelength is 800 nm and the diode bandwidth – FWHM – is about 2 nm. The temperature drift of the central wavelength is 0.27-0.3 nm/°C and the temperature was stabilised within 0.5°C in order to stabilise λ_L within 0.15 nm. The pigtail diode laser package gives the possibility to minimise the length of the electrical connection and by this to make possible fast modulation of the driving current. At the same time it provides an output radiation with axial symmetry. The fibre has a core diameter of 100 μm and a numerical aperture of 0.4.

As already mentioned, the light modulation code, sequences or single pulses, is generated by the PRN board. It is then transmitted to the laser diode driver unit by optical fibre connection. The laser diode driver unit receives this code and modulates the amplitude of the laser diode beam power following it. This modulation is achieved by driving the laser diode current. The driver stands as near as possible from the laser source to reach as large bandwidth as possible and to limit the current losses. It has been developed by the firm Oerlikon-Contraves, Zürich, Switzerland.

The driver is not an ideal current source driver. A saturated voltage switch causes a current to flow in a series resistor with the laser diode. This approach has the disadvantage to increase the rise-time of the current. It has however the advantage to limit the maximum current by the voltage and the resistor, making initialisation and error condition handling easier. The high power driver is performed by putting in parallel a large number of low current drivers. The developed driver may ensure pulse repetition rate up to 20 MHz with a bandwidth of 100 MHz. The extinction ratio between the ON and OFF states – i.e. the 1 and 0 states of a code – is specified better than 1000:1. The drive current is about 1.4 A in the OFF state and 4.3 A in the ON state. A calibration cycle determines the exact values. A safety loop has been implemented in case of problem with the diode laser.

4.2.2 Photodetector and pre-amplifier

The optical detector is another critical component for the lidar power balance. As day-time operation should be possible with ABB and as the filter has 4-5 nm bandwidth, what makes it rather broad, analog APD's have been considered. Photomultiplier tubes would have been saturated during day-time and could have been damaged.

At the laser wavelength, the detector shall have high responsivity, i.e. high electrical output from the received optical backscattered power, but low noise-equivalent power – NEP – or dark current. A convenient way to decrease the dark current is the cooling of the photo-diode and definite advantages are offered by APD with integrated TEC. As the offset level due to the background radiation is very different during night and day-time, the detector shall show high-dynamic range. The detector bandwidth shall be larger than the modulation frequency and the time-resolution of the data acquisition system. The choice of the sensitive photodetector area is based on the trade-off between the dark current, the response time and the possibility to accommodate to large aperture receiver (cf. below). Finally, typical configuration for low-level signal detection is a photodetector with closely packed pre-amplifier unit to avoid undesired noise contribution from long cable.

Our preferable choice was for an analog APD from EG&G Optoelectronics-Canada, model C30902S-TC. This APD is cooled by a TEC integrated in the APD package. The APD output signal shall however be amplified. Unfortunately is was not possible to use such a detector and we opted for a Hamamatsu APD module, C5331-02. It shows lower performances but has built-in pre-amplifier.

4.2.3 Transmitter and receiver

The transmitting optics has to collect the output radiation from the fibre end in the pigtailed laser diode package and to form a beam with the required divergence, while the receiving optics has to collect the backscattered light from the target or from the atmosphere and to concentrate it on the sensitive area of the APD.

Transmitter

In the approximation of geometrical optics and with no aberrations in the optical system, the full angle divergence of the transmitted beam θ_T is determined by the expression

$$\theta_T = d_L / f_T \tag{4-1}$$

where f_T is the transmitter optics effective focal length. For a stand-alone laser diode, d_L is the size of the laser diode front facet, while in the case of a fibre optics pigtail configuration, d_L is the fibre core diameter. Direct coupling of a typical high-power laser diode requires optics to equalise the divergences of the two planes of the laser diode junction. In the case of a pigtail configuration, due to the mode mixing in the optical fibre, the beam at the output of the fibre has round shape with equalised divergence. This is the reason why we selected a pigtail fibre laser diode.

In order to collect the emitted laser diode power from the fibre output, the numerical aperture of the optical system, NA, shall match the numerical aperture of the fibre, NA_f that is to say, $NA_f \leq NA$. The telescope clear aperture diameter d_T is linked to NA by the relation

$$d_T = 2 \cdot NA \cdot f_T . \tag{4-2}$$

Thus the fibre core diameter is given by

$$d_L = \theta_T \cdot d_T / 2NA_f \,. \tag{4-3}$$

From performed simulation, a divergence of 0.8 mrad was desired. Two possibilities for the optical fibre pigtailed configuration existed: a fibre with core diameter of 100 μm and NA_f of 0.4, or a fibre with core diameter of 200 μm and NA_f of 0.5. The first solution was chosen because it corresponded to a smaller telescope clear aperture diameter d_T , 100 mm instead of 250 mm, and in consequence to a much more compact optical head package.

In order for the laser radiation from the fibre output to be emitted with the specified beam divergence, a single aspheric – convex – lens ensures the collection of the optical power from the fibre with minimum loss, and a 4-times beam expander after the aspheric lens allows to obtain the proper divergence. The beam expander is of Galilean type – a plano-convex lens followed by a plano-concave lens –, as it is more compact. The exact references of the used lenses may be found in Table 4.2. All lenses are anti-reflection coated.

Lens type & catalogue number	Focal length [mm]	Diameter [mm]	f-number
plano-convex 01 LPX 289	250 @ 546.1nm	145	1.72
plano-concave 01 LPK 027	-64.5 @ 546.1nm	40.0	-1.60
aspheric-convex 01LAG 009	29.5 @ n.a.	40.0	0.74

Table 4.2. *Lenses for the transmitting and receiving telescope. All lenses are from Melles Griot.*

Receiver

The collected optical backscatter power is proportional to the collecting lens area and the collected optical power shall be concentrated on the sensitive area of the photodetector. The diameter $d(r)$ of the transmitted beam at range r from the lidar is determined, in axial symmetry and geometrical optics considerations, as

$$d(r) = r \cdot \theta_T \,. \tag{4-4}$$

The backscatter optical power from the illuminated target is concentrated on the sensitive detector area by the receiver optics. Let d_{spot} be the size of the produced spot. This parameter is related to the receiver optics parameters in the following way:

$$d_{spot} = d(r) \cdot f_R / r = \theta_T \cdot f_R \,, \qquad \text{or} \qquad d_{spot} = d_L \cdot f_R / f_T \,, \tag{4-5}$$

with f_R being receiver effective focal length. This relation is transformed to a requirement for the diameter of the sensitive area of the detector d_{det}

$$d_{det} = d_L \cdot f_R / f_T \,. \tag{4-6}$$

From these last equations and from the lidar equation (cf. Chapter 1), the requirements for the receiver optics may be formulated. To collect a high level of optical backscattered power from the target, a receiver optics with large area is necessary. At the same time we have to fulfil the requirement for a small focal length, in order to concentrate the collected optical backscatter power on the small sensitive surface of the APD. All this cannot be achieved by a single lens or mirror with high numerical aperture. We chose here the same combination of a Galilean telescope with a single aspheric lens. The interference filter is positioned in the parallel beam after the plano-concave lens of the telescope. The aspheric lens with high numerical aperture provides concentration of the optical power in a small spot. To ensure less sensitivity to small instabilities of the ABB during the measurements, the APD has larger diameter of the sensitive area than this spot (1.5 to 2 times). Using the same lenses in the same configuration with an APD of 0.5 mm diameter sensitive area, determines a telescope field of view of 4 mrad*.

Interference filter

The central wavelength of the laser was measured at 800nm at a temperature of 35°C, with a FWHM 0f 1.8 nm. To accommodate to these specifications, an interference filter centred at 800 nm, with FWHM of 5 nm and 67% transmission at 800 nm was selected. The out-of-band blocking is smaller than 10^{-4}.

Mechanical design

The requirements for the mechanical supports are a handy access to the optical components and units for replacement and maintenance, convenient alignment possibilities and stability for the optical components. To answer to these requirements we realised the mechanical configuration of the optical package as a rigid cage formed by three machined All plates – specified as "front", "central" and "back" – held by four Al-rods at their corners. The front plate supports the two plano-convex lenses which are the front lenses of the transmitter and receiver telescopes. The central plate supports the adjustable mechanical components holding the transmitting end of the laser diode pigtail fibre and the APD. The one for the receiver part also supports the interference filter. The back plate provides the support for the laser diode driver with the laser diode in it and for the laser diode temperature stabilisation unit.

* The system was initially planned for an APD from EG&G. The diameter of the sensitive area would have been in this case 0.2 mm. The field of view would have decreased then to about 2 mrad and the lidar would have been four times less sensitive to background noise radiation.

4.2.4 Electronics package

While the optical elements existed and were found on the market, the electronics for the transportable ABB lidar was more specific and requested precise functionalities. It had to be developed. It is divided in several subsystems, the PRN modulation board, the data acquisition board, the laser diode driver, the detector electronics, the temperature control circuits and the power supply unit. A block diagram showing all these sub-systems is given in Figure 4.3.

The PRN modulation and data acquisition boards are in the PC, interfaced via standard ISA bus. They are controlled by software. Interconnection between them are done with standard coaxial cables. Inside the optical package, the laser driver and the detector electronics are separated; galvanic isolation is required to avoid cross-talk and other ground loop problems. The PRN modulation signal is therefore transmitted via high speed fibre optics digital link, and commands are fed through opto-couplers.

PRN sequence generator

The PRN generator stands as a board with ISA bus, which can be used in IBM PC or compatible. This board generates PRN sequences and sends them through optical link to the laser diode driver. The functionality of the PRN generator is implemented in PLDs (Programmable Logic Device). This provides flexibility of development in a minimum size. It allows also modifications of the logic of the board without important hardware changes.

The main part of the PRN board is the sequence generator. By software it simulates hardware linear shift-registers with proper feedback connections to generate M-sequences. These are configurable by software. Their length may vary from 2 to 15 bits. The clock frequency is 20, 10, 5, 1 MHz and corresponds to 7.5, 15, 30 and 150 m range resolution.

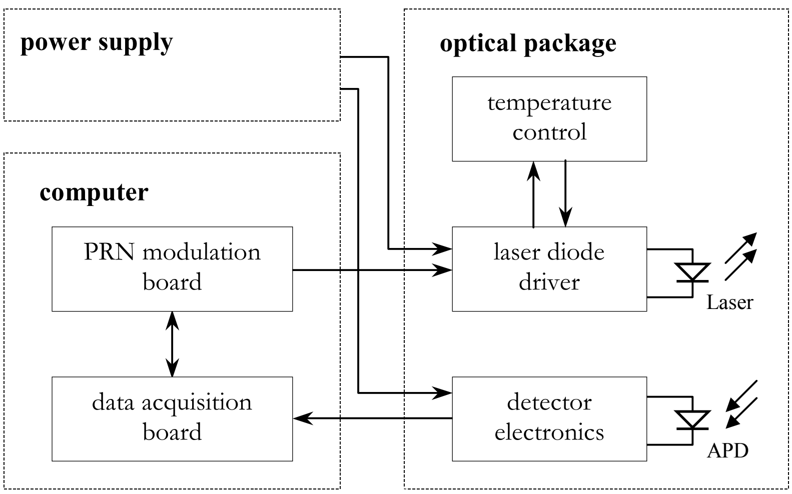

Figure 4.3. *Block diagram of the electronics of the transportable day-time total elastic backscatter PRN-cw lidar.*

In order to insure optimal SNR (cf. Chapter 3) the beam modulation shall be synchronised with the data acquisition system; they shall be run by the same clock. Therefore the PRN board can be locked on an external 10 MHz clock or generates its own synchronisation.

The configuration of each parameter of the PRN board is done by software only and no external inputs are needed, except the 10 MHz for external synchronisation if required. The outputs of the board are the PRN sequences, the sequence trigger, the clock selected for the PRN generator and the 10 MHz synchronisation. All these outputs are TTL. The sequences are also available through optical interface. This possibility is used to transmit the pulse modulation to the laser diode current driver. It is also worth to mention that not only PRN sequences are generated by the PRN board. Single pulses of 50, 100 and 1000 ns duration may also be output. The possible pulse repetition rates correspond to the sequence repetition rates.

Acquisition system

As ABB should be able to operate during day-time, analog detection mode was considered, and the acquisition system is based on an ADC – analog-to-digital converter. Three strong requests were addressed to the acquisition system. First, it had to ensure a range resolution of 15 m, equivalent to 10 Msps, with a 12-bit amplitude resolution. Then, it should be a transient recorder able to work in standalone mode, what means to average by hardware the incoming signal in real time on the spot. Finally, in order for the measurement integration time to be equal to the effective time requested for the measurement – that is to say a 24-hour integration measurement needs one single day and not more –, there should be no dead-time between two successive sweeps in the acquisition system, like there should be no dead-time between two successive sequences generated by the PRN board. We did not find any instrument on the market complying with these requirements at the same time so we decided to developed them[*]. As we wanted the modulation waveform generation and data acquisition system to be built as a single compact hardware package for easy transportation, the acquisition system was develop as PC board as well.

The developed acquisition board is an averaging data acquisition system that digitises, with a resolution of 12 bits, a repetitive incoming signal and accumulates it. The board runs at a sampling rate of 10 MHz. The on-board memory size is 32 k per 32 bits. This allows to record up to 2^{15} samples, i.e. 15-bit sequences, and to accumulate 2^{20} successive sequences with no dead-time between them – at 10 MHz sampling rate, the maximal integration time is then 3430 s or about 57 minutes. A cycle counter ensures that the right number of cycles – sequences – for averaging is respected. Continuous sampling and triggered sampling are available. The sampling can be synchronised with an external 10 MHz

[*] That time, some transient recorders existed, but they needed recovery time at the end of a sweep before starting the next one. Some were not transient recorders but had very large memory. However it was never sufficient; working at 10 Msps means 10 Mbytes memory and software data averaging each second, what takes time. At the moment of writing this document, such an acquisition system device was still not found.

reference signal. Also, the board can synchronise another device such as the PRN generator.

The incoming signal is either AC or DC coupled – choice by a jumper. The signal is then amplified up to 100 times by a variable gain amplifier and a DC offset may be added or removed from the signal, before it is digitised*. To respect the Nyquist theorem, a passive anti-alias filter at frequency of 5 MHz from the firm Mini-Circuit – model BLP-5 – is placed in front of the analog input.

Five BNC connectors are provided for the external interface: the analog input, the 10 MHz synchronisation input, the 10 MHz synchronisation output, the trigger input and the trigger output. The configuration of each parameter of the acquisition board is done by software.

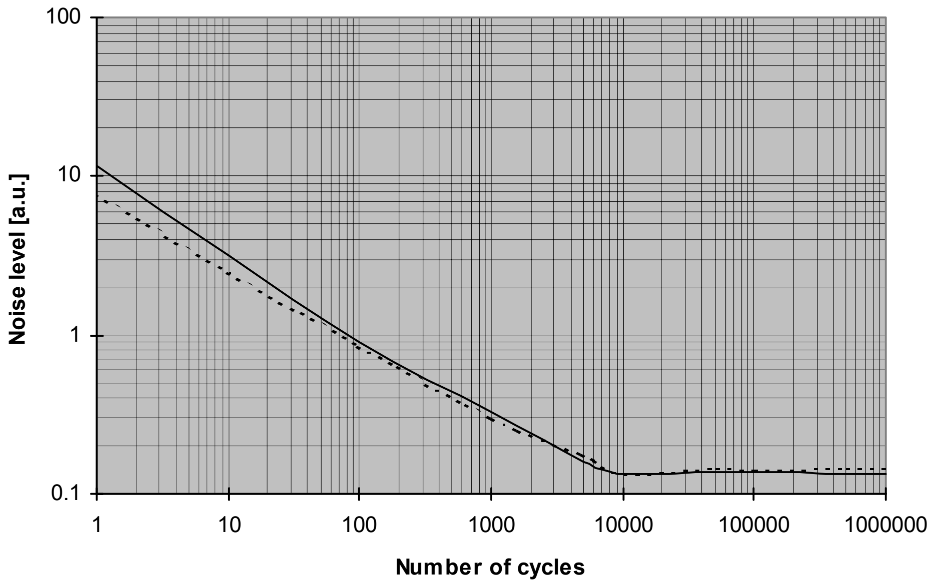

Figure 4.4. *Typical data acquisition noise dependence on the number of accumulated cycles. All other parameters are kept constant. The dash line is the noise of the acquisition board only while the solid line is the noise of the APD as measured by the acquisition board.*

The dependence of the noise on the number of accumulated cycles is shown in Figure 4.4. A set of constant parameters is chosen (sample number, gain, offset, etc.) and then only the number of cycles is varied. The dash line is the noise of the board only when the analog input is grounded. The solid line is the noise of the APD as recorded by the acquisition board. The noise is deduced from the direct measured signal and not from any cross-correlation operation. This measurement shows that the averaging effect follows well the power law till approximately 10'000 cycles. After a transition interval, it stabilises to an almost constant level. Since the PRN generation and the acquisition boards are synchronised in such a way, so one cycle on the acquisition board is equivalent to one sequence,

* The ADC component of the acquisition system works in a fixed window, which lower and higher voltages are 0 and +2 V. It is therefore necessary to centre the incoming signal between these two rails. This is done by adjusting the gain and the offset.

there is a number of sequences above which a coherent noise starts to be higher than the noise from the detector. This noise is due to the amplification and DC offset adjustment stages of the acquisition system. As observed from actual measurements, for a same integration time, measurements with longer sequences show higher SNR.

A software for general control of the whole instrument has been written. Its first task is to ensure full control of the instrument, uninterrupted operation over long periods and flexible parameter settings. It lets the user to introduce parameters like the number of successive measurements, the integration time of each single measurement, the sequence length, the range resolution*, the gain and the offset to be applied on the detected signal, etc. It monitors the laser temperature as well. Its second task is to compute the cross-correlation and to display graphically the measured response function profile.

4.3 Performances of the lidar

Hereafter, examples of measurement are shown to demonstrate the performances and capacities of the instrument. These are test and demonstration results only; there is no detailed discussion of the measurements from the point of view of atmospheric research, because such were not the purpose.

The result of each measurement is the cross-correlation function of the lidar response and the initial PRN sequence. The only additional processing operation is the subtraction of the global offset resulting from the background radiation and the offset introduced by the acquisition system†. The value of the cross-correlation function is given in relative units. Two signals may only be directly compared if they were issued from the same measurement process during which no change of parameters occurred. Otherwise, SNR's have to be compared, because the measurement parameters may be different. The SNR is computed following the definition given in Chapter 3 (§ 3.4.3) for photon-counting detection mode. Briefly resumed, the noise is taken as 2σ of the noise statistics and the signal value is obtained by subtracting the mean noise value from the cross-correlated signal.

Topographic target, cloud and aerosol layer cross-correlation functions are illustrated for night- and day-time. The detection of clouds is understood as the detection of cloud base. Topographic target measurements are done horizontally or close to it, while cloud measurements are done vertically. For all measurements the range offset is 120 m and has to be subtracted from the ranges read from the graphs. The range resolution is 15 m unless otherwise indicated. The targets are the same as those presented as images in Chapter 3.

* The acquisition board always samples data at 10 MHz. If a range resolution of 30 m resp. 150 m is chosen, i.e. 5 MHz resp. 1 MHz sampling rate, each 2 resp. 10 samples are averaged to provide a single data.

† Not subtracting this global offset would not have been of indication for the background radiation as the whole detected signal is prepared before being digitised – cf. foot-note on page 76.

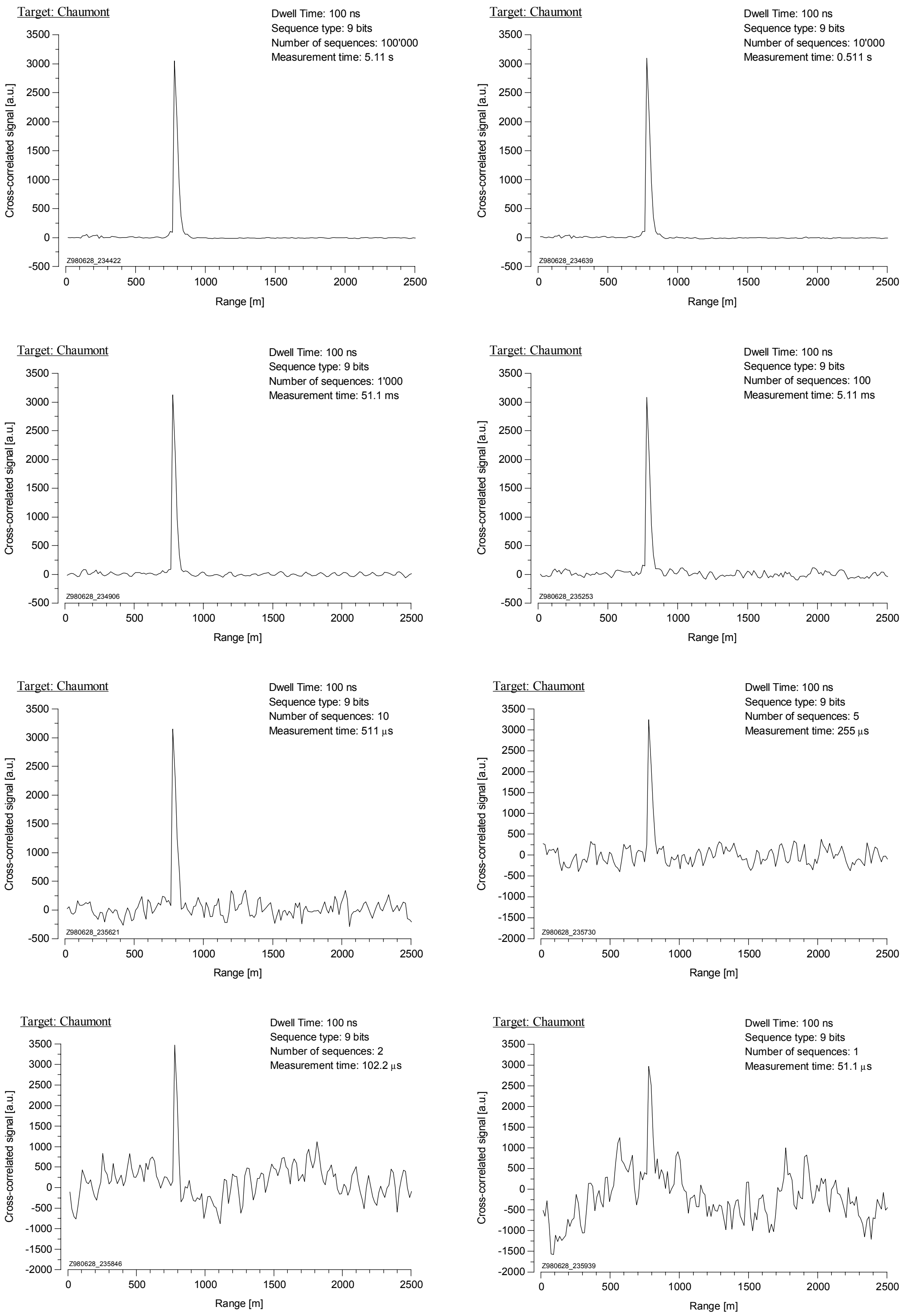

Figure 4.5. *Night-time topographic target lidar response. The target is Mountain Chaumont (target 1) The measurement time varies from 5.11 s to 51.1 µs, while the resolution is fixed at 15 m. The shorter the integration time, the worse the SNR. But even for a very short integration time, as a single sequence duration, the target is still detected with a SNR of 2.8.*

4.3.1 Topographic measurements

Figure 4.5 presents a set of measurements with the same modulation frequency, 10 MHz, the same sequence length, 511, and variable integration times (i.e. numbers of sequences), from 5.11 s to 51.1 μs, when probing the same topographic target, Chaumont (target 1). The SNR of the target for these measurements as a function on the number of the sequences is reported in Figure 4.6. From the set of results we may see that for very short integration time, that is for very few sequences, the target is detected. Even for a single sequence, the SNR is about 2.8.

The SNR of the target is proportional to the square-root of the integration time or number of sequences. We may notice from the related figure a discrepancy from this rule for large numbers of sequences. This is explainable by the effect of the coherent noise from the front-end electronics as already described. Filtering the raw data with an appropriate numerical filter may improve the situation. This is in our future plans for improvement of the data acquisition.

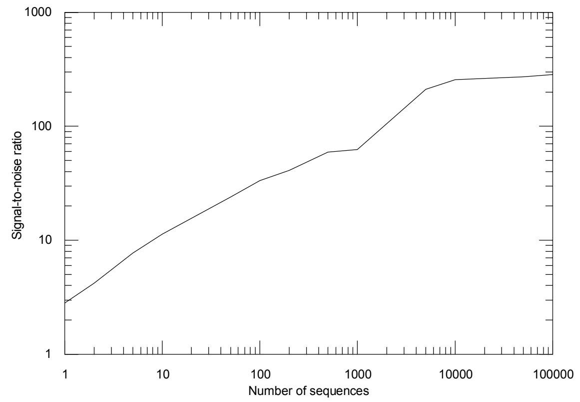

Figure 4.6. *Dependence of the SNR for the measurements of the same target response on the number of the sequences (all other parameters are the same). For large numbers the dependence becomes saturated because of a coherent noise in the acquisition board.*

Day-time measurements with the ABB for topographic targets are demonstrated in Figure 4.7. As expected the quality of the signal is degraded as compared to night-time measurements. Nevertheless SNR of 3.3 is obtained in 51.1 ms – 8.1 for 1.02 s. As the tar-

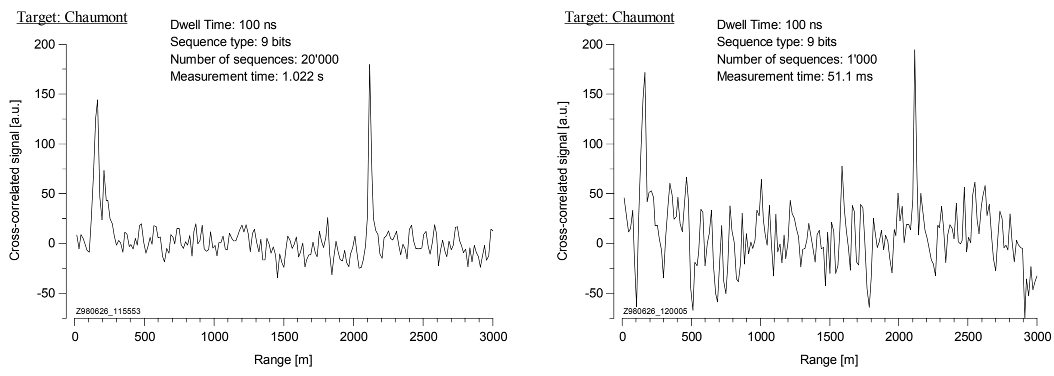

Figure 4.7. *Day-time measurements for two different integration times of the same topographic target. The target is Mountain Chaumont (target 2) and its actual range to the instrument is 1'995 m. The time of measurement was noon, end of June.*

get is much further than in the night-time case – factor of 4 – the target response is small enough for the molecular atmosphere in the near-field to emerge from the noise. Day-time measurements from Mountain Chaumont, target 1 at 660 m, were also done, but are not illustrated here. We obtained a SNR of 6.3 for an integration time of 51.1 ms and 17.5 for 0.51 s. The corresponding night-time SNR's – cf. Figure 4.6 – were 62.6 and 256.4.

4.3.2 Cloud base detection

One of the purpose of the instrument ABB was to demonstrate that day-time cloud base measurements are possible with a compact PRN-cw lidar. Some examples of such measurements are shown here. Figure 4.8 presents cross-correlation functions from successive

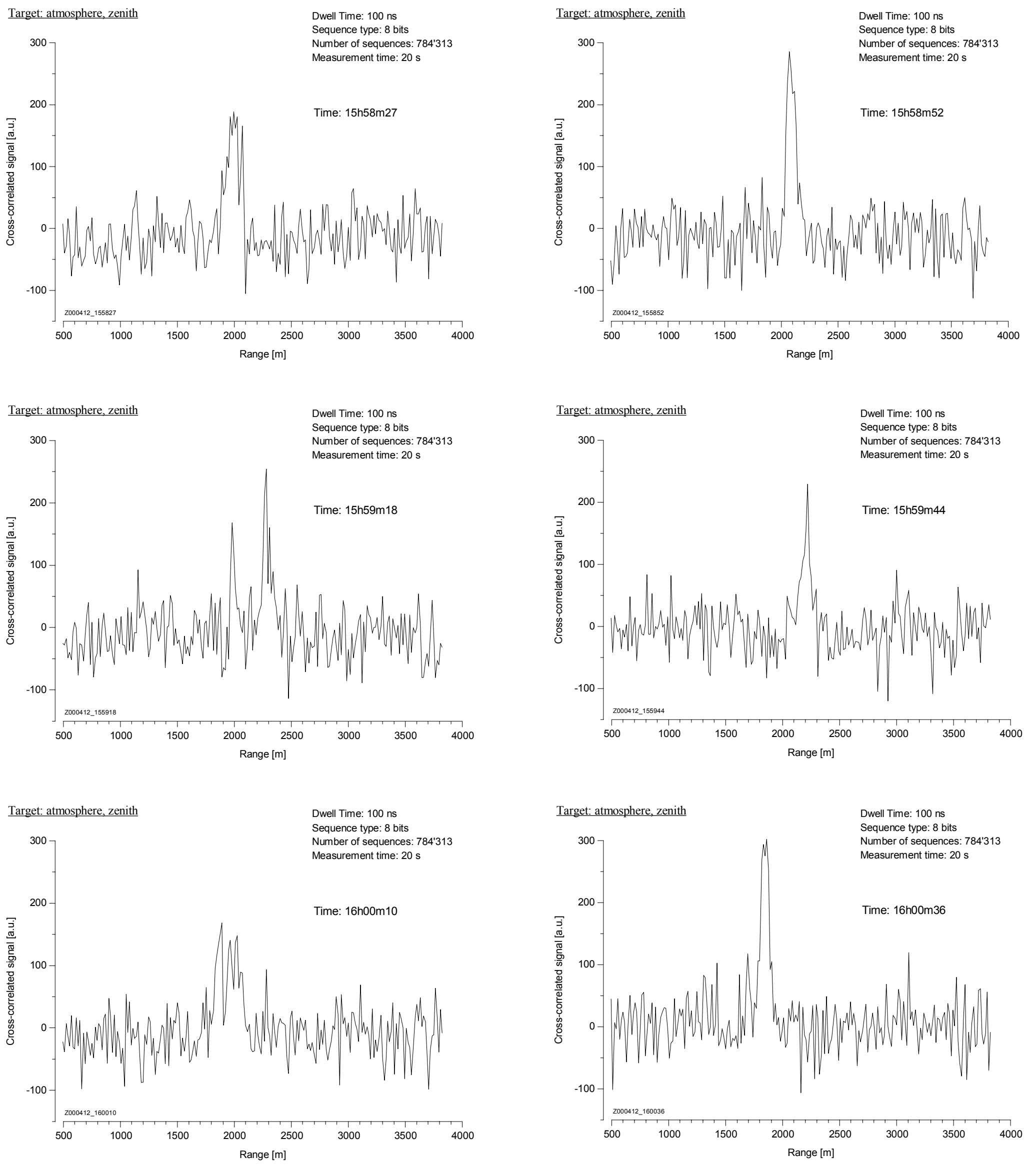

Figure 4.8. *Time series of day-time cloud base measurement. The resolution was 15 m and the integration time 20 s for each acquisition. The measurement time is indicated for each plot. About 6 s separate two measurements. That afternoon, the cloud layer was optically thin.*

observations with 15 m range resolution of the cloud field, each lasting 20 s. Dead-time between two measurements is 6 s, what corresponds in the present configuration of the software to the time necessary for downloading the data, cross-correlating the data and starting the next acquisition. The variation of magnitude of the peak may be associated with the variation of the cloud backscattering coefficient.

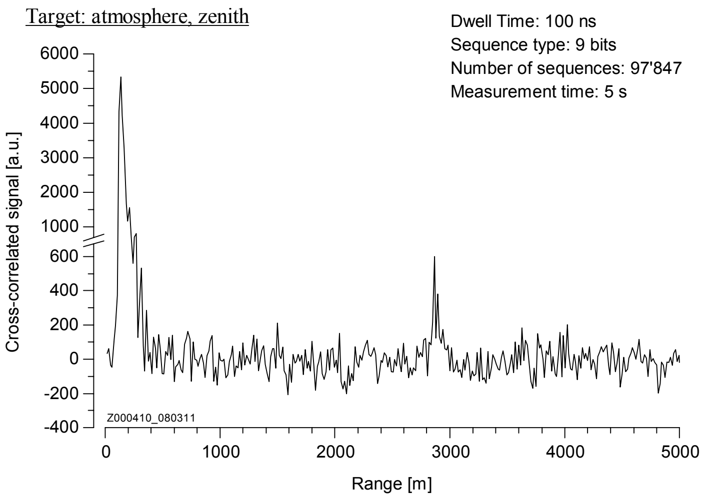

Figure 4.9. *Example of cloud base measurements with the instrument pointing to zenith during morning time. The range resolution is 15 m and the integration time, 5 s.*

Depending on the characteristics of the cloud and the level of the background radiation, shorter duration of observation are possible. For instance, in Figure 4.9, the integration time is 5 s, with a range resolution of 15 m. As expected the quality of the data is improved when the range resolution is decreased as illustrated by Figure 4.10. The left curve shows the lidar return for a range resolution of 15 m while the right curve is for 30 m resolution. All other parameters are similar and the measurements were performed just one after the other, at noon.

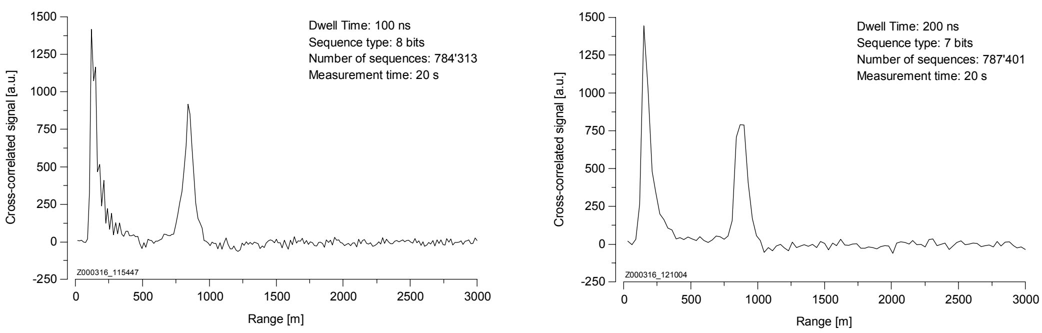

Figure 4.10. *Measurements of cloud base with the instrument pointing to zenith at midday. They were done one after the other. The only difference is the change of resolution, 15 m for the left plot, 30 m for the right plot. The sequence length has been adapted to have the same integration time and about the same number of sequences.*

Finally Figure 4.10 presents the case of observation of patchy cloudy sky with two layers of clouds, one below the other when a rain started. The left pane presents the signal when the rain was just about starting (a few drops) and the right pane presents the signal from already started rain. The measurement was done from below a cover at 45 degrees from the zenith. This observation was done during day-time. When raining, the signal backscattered from the atmosphere is stronger what is clearly visible comparing both signals. The beam is also more extinguished as it may be seen from the shape of the curve slope in interval 300-700 m.

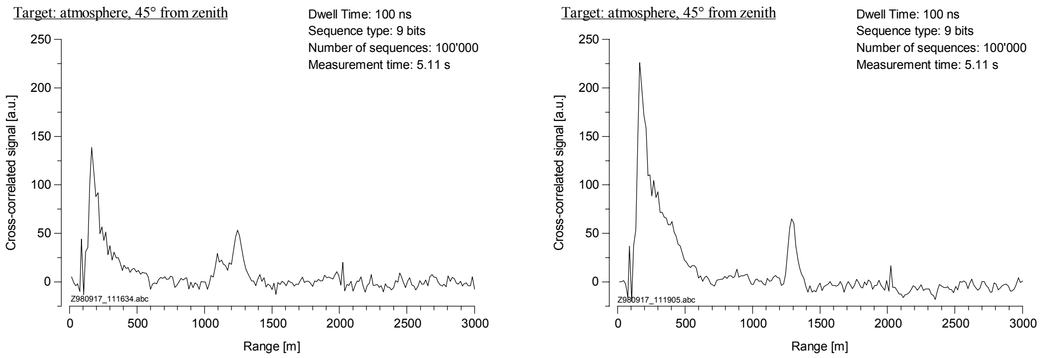

Figure 4.10. *Day-time measurement at 45° to zenith of low clouds in layers. The cloud base appear at range 1160 m from and altitude 820 above the instrument. The left signal was measured just before a rain started; the right signal was measured when it was raining.*

4.4 Discussion of the instrument performances

The compact PRN-cw lidar (ABB) is aimed at demonstration of PRN-cw lidar operation during night- and day-time. The result is positive. Fast detection of hard target is demonstrated for both night- and day-time with range resolution of 15 m, i.e., the one provided by the PRN modulation and data acquisition. The limit of integration time for such detection, depending on the range, may be as short as one sequence only.

Day-time detection of the cloud-base is demonstrated, as well as the capability to follow the changes of the layered structure of the low and medium altitude clouds. This is achieved within integration time of a few seconds or tens of seconds with altitude resolution up to 15 m. The best results were obtained however with 30 m resolution what is still sufficient as precision. Dense aerosols like rain, fog and haze are also detectable at near ranges from the instruments.

There is one technical limitation of the instrument in its present configuration This limitation concerns the acquisition system. The one developed for ABB works well in its logical and digital functions, that is no dead-time between two sweeps, 10 Msps sampling rate, cycle counter, 12-bit resolution. On the other hand, it is too noisy in its analog part and should be improved to take advantage of the full potential of the instrument. The accumulated coherent noise exceeds the shot noise (both dark and from the ambient background) at sequence numbers above 10^4-10^5. In consequence, after some seconds of measurement the SNR does not improve much any more. This limit of the integration time is not due to the PRN-cw operation principle but to the used technical realisation of the data acquisition card. The PC environment was initially chosen for the comfort of the digital part development of the electronics. Yet it is not a quiet environment for analog detection. A stand-alone acquisition system would likely be more adapted to the situation.

The sensitivity of the SNR on the ambient optical background has been evidenced from the results obtained from topographic targets during night- and day-time. The interference filter is with FWHM 5nm while narrower filters are usually used for day-time operation. As the bandwidth of the laser is 1.8 nm FWHM, there is no margin for the replacement of the filter. A possible improvement may come from a decrease of the transmitted beam divergence by using a receiver with a smaller field of view or a detector of smaller sensitive area. Presently the transmitter divergence is 0.9 mrad while the field of view is 4.2 mrad. A value of 1.8mrad would decrease the detected background radiation by a factor of 5.44 and improve for a same integration time the SNR by 2.3 in case the measurement is limited by the optical background noise. Decreasing the field of view has the inconvenience to increase the range of full overlap from 100 m now to 400 m in case of 1.8 mrad. Using a combination of narrower laser and interference filter is possible, but it would be better to re-develop a new optical package as the laser is the main part of a lidar, particularly when it is compact.

Conclusion

In this chapter we demonstrated that it is possible to develop a compact, transportable and eye-safe - at some tens of meters – lidar based on the PRN-cw technique for day-time measurements, with practical detection range of some kilometres. The realised instrument confirms that PRN-cw lidars are efficient for detection of hard target, cloud base and dense aerosol layers. This instrument is only a prototype and as such is not perfect. But it suggests that compact lidars with simple measurement objectives are useful and feasible. Based on these results, we may consider fast detection PRN-cw range-finder sensor with possible applications for scanning range-finding, topographic mapping, altimetry, target imaging. PRN-cw sensor for a ceilometer is another possible application. A very compact instrument might be even planned for a planetary mission, as it will be discussed in Chapter 5.

Several technical developments have been achieved. A high power laser diode is used which beam is modulated directly by the current injected in the laser diode. The light source and its driver are integrated in a compact and mechanically stable optical package. For the electronics, a fully synchronised and with no dead-time coupled PRN generator and analog data acquisition system has been developed. However, the analog part of the acquisition system has coherent noise and should be improved for better performances of the whole instrument, especially when long integration times are necessary. The present experience and the one from the previous photon-counting demonstration instrument show that the PRN-cw acquisition system is one of the most critical area in the PRN-cw lidar technique.

The instrument is able to measure during day-time, but it is still sensitive to the background radiation. Day-time SNR is degraded in confrontation to its night-time values. Apart from decrease of the field of view, the approach is to use more narrow-band laser and optical filter. Using a narrow-band interference filter may give improvement by a factor of 25 – 5 nm in the present design compared to 0.2 nm if a narrow-band laser is employed. Additional decrease of the optical bandwidth – up to additional 3 orders of magnitude – may be provided by combination of an atomic filter called FADOF and a diode laser which wavelength is actively locked to the FADOF central wavelength. Such an experiment is described in Chapter 5.

Chapter 5

Concepts for further development and application of PRN-cw lidars

Introduction

Cw-diode lasers allow the development of PRN-cw lidars with narrow-band stabilised wavelength. Their wavelength may be tuned to the vicinity of the transitions of atomic vapours in the near IR region. Such atomic vapours are convenient media to observe resonance Faraday rotation effect and to realise ultra narrow-band Faraday Anomalous Dispersion Optical Filters (FADOF). The diode laser wavelength may be tuned to the central wavelength of such filter. In Section 5.1 we describe an exploratory development of FADOF and PRN-cw lidar based on the combination of ultra narrow-band diode laser and FADOF. Day-time measurements done with this lidar in photon-counting mode are shown.

Cw-diode lasers allow also the development of very compact backscatter PRN-cw lidars with high reliability in harsh environment and with low power consumption. Those are the usual requirements for space-borne instruments and we expect the advantages of PRN lidars to be best demonstrated in such applications. In Section 5.2 we present the concept for a backscatter lidar for operation on Mars surface from a lander. We also present the numerical simulations of the performances of such lidar. This concept was the base for one proposal for lidar measurements of aerosol and clouds in Mars atmosphere presented to ESA Mars Express announcement of opportunity*.

5.1 FADOF: an appropriate optical filter for PRN-cw lidar

One of the principle problem of PRN-cw lidars is their higher sensitivity to the optical background as compared to the direct detection lidars. This limits their use basically to night-time operation with exceptions presented in Chapter 4. The reason is that the noise variance at whatever cross-correlated data is equal to the total accumulated signal (cf. Chapter 1, § 1.3.6.2). It is therefore necessary to decrease as much as possible any source of noise and particularly the background noise, for it is the main noise during day-time, independently from the signal quantum noise. A perspective way to solve this problem is the use of a narrow-band laser locked to an ultra narrow-band optical filter like Faraday Anomalous Dispersion Optical Filters (FADOF). Another advantage of FADOF compared to narrow-band interference filters and Fabry-Perot etalons is its large field of view what makes it not critical for alignment.

FADOF's are ultra narrow-band atomic line filters based on a vapour cell, such as Potassium (K), Rubidium (Rb), Cesium (Cs), and Sodium(Na) [Dick91, Mend91, Yinb92, Yinb94]. They are already considered for extensive application in the free-space optical communications [Chen94, Kore96]. Example for such considerations is the new satellite optical communication system SRTV-2 lasercom, developed for NASA/JPL [Kore97]. A FADOF, based on Na vapour [Chen93], was also successfully used in the lidar field for measurements of the mesopause temperature and wind profiles at the Na layer [Chen96]. In these two particular applications, FADOF allowed background light rejection with an efficiency of two orders of magnitude higher than with narrow-band interference filters.

The capability of the PRN-cw lidar to make use of coherent AlGaAs cw diode lasers operating in the near IR region, provides the opportunity to lock the transmitted wavelength at the absorption lines of either Rb or Cs vapour and to use a FADOF as background noise rejection filter. Hereafter we report such an experiment with a Rb vapour FADOF at 780 nm and demonstrate day-time PRN-cw backscatter lidar measurements based on this set-up.

* There were two alternative proposals for Mars Express landing mission: one was for atmospheric studies (Netlander) and one was to search for the presence of biologically active molecules on the surface (Beagle). The final selection of ESA was for Beagle.

5.1.1 Rubidium FADOF

The FADOF is an atomic vapour subjected to a strong magnetic field (~ 100 G). The vapour is contained in a glass cell, placed between two crossed polarisers [Yehp82], as illustrated in Figure 5.1. The light passing through the first polariser is blocked by the second polariser, except if its polarisation changes in the cell. This is the case when the light wave-

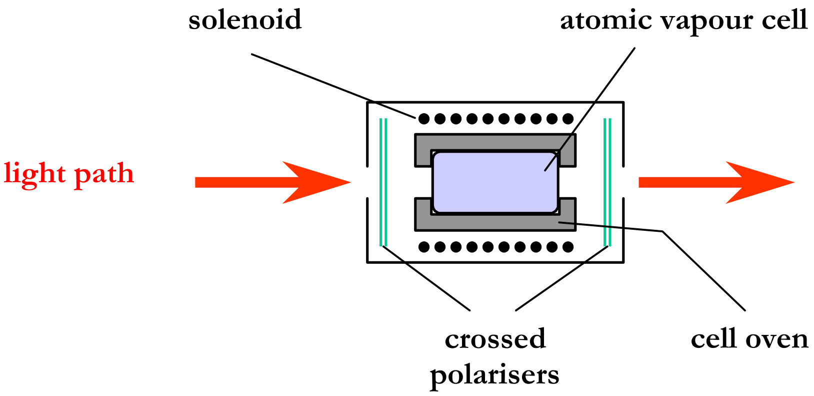

Figure 5.1. *Principle of Faraday anomalous dispersion filter (FADOF).*

length is near an atomic resonance of the vapour, due to the combination of the Faraday anomalous dispersion effect and the magnetic field. The spectral region of wavelengths where this phenomenon occurs is as narrow as the atomic absorption lines are, that is only a few GHz. Typically a FADOF shows 0.7-3 GHz bandwidth, a near unity peak transmis-

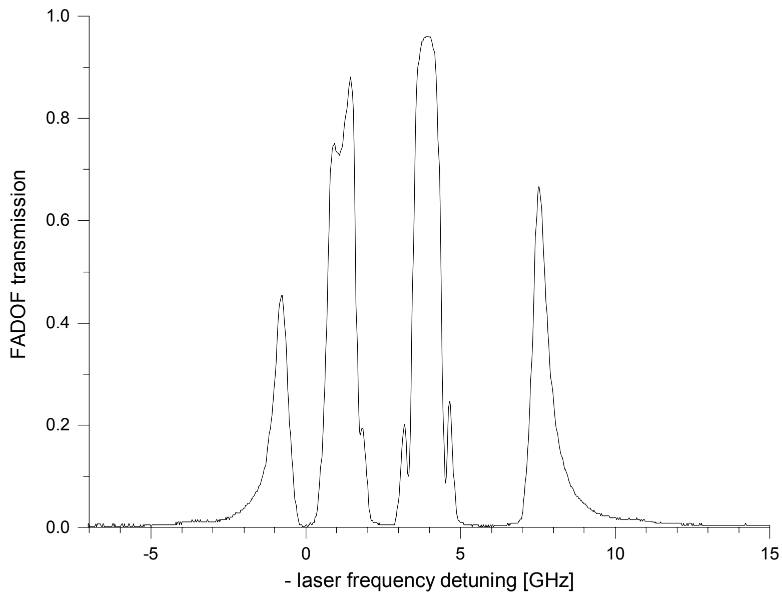

Figure 5.2. *Rubidium FADOF experimental transmission curve. The equivalent bandwidth is 2.9 GHz, or 5.8 nm at 780 nm if expressed in wavelength bandwidth. The four lines are due to the hyperfine structure of the Rubidium.*

sion, 50-60 dB noise rejection, response time smaller than 1 ns. In addition, and unlike narrow-band interference filters, it has a wide field of view making the lidar alignment less critical. Due to these properties, FADOF is really adapted to lidar instruments.

For PRN-cw lidar demonstration, a compact Rb FADOF operating at 780 nm has been built. The Rb vapour is contained in a cylindrical cell of 15-mm diameter and 25-mm length. The cell is placed in a temperature controlled oven stabilised at 100°C in order for the Rb to stay in gas-phase. The oven is placed in a coaxial solenoid, capable of producing a longitudinal magnetic field up to 200 G. The total package is a 5 cm long cylinder having a diameter of 3.5 cm. Figure 5.2 shows the transmission curve of this FADOF. At its maximum, the transmission, without the Fresnel losses on the glass surfaces, is above 95%. The equivalent transmission bandwidth is 2.9 GHz, equal to 5.8 pm at 780 nm. This value is 50 times lower than the width achievable with narrow-band interference filters.

5.1.2 MOPA laser diode system

Application of FADOF to PRN-cw backscatter lidar requires a narrow-band tuneable laser diode, which is stabilised in the spectral region where FADOF is transparent. The Observatory of Neuchâtel has accumulated experience in stabilising laser diodes on Rb (780 and 795 nm) and Cs (852 nm) atomic lines for atomic frequency standards [Mile95, Leco00] and interferometers [Obne94]. The requirements on the laser stability for these applications ranged from a minimum of $\delta\nu \leq 1$ MHz, to a maximum of $\delta\nu \leq 10$ kHz. They are therefore stronger than for lidar applications, where the only requirement is that the laser frequency is within the receiver's filter bandwidth ($\delta\nu \leq 5$ nm for broad-band interference filter, $\delta\nu \leq 0.2$ nm for narrow-band interference filter and $\delta\nu \leq 1$ GHz with FADOF.

Our laser system is shown in Figure 5.3. The modulated laser beam is generated in a MOPA (Master Oscillator Power Amplifier) configuration*. The

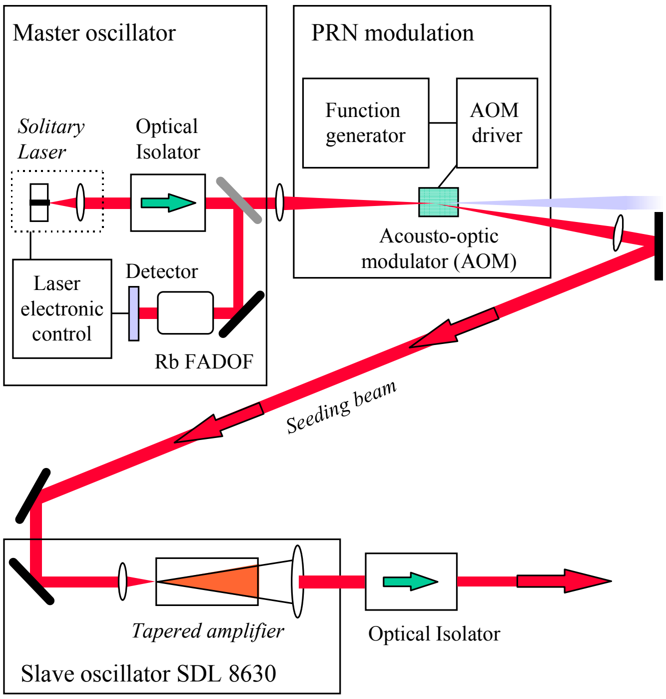

Figure 5.3. *MOPA laser diode system.*

* We remember that in Chapter 3, a commercial laser diode of MOPA type was also used (SDL-8630). It was consisting in a tapered laser amplifier in a extended cavity and a grating to tune the wavelength. Here the original extended cavity is removed and only the amplification part of the MOPA is used.

Master Oscillator (MO) is a Fabry-Perot laser diode of 50 MHz line-width and 10 mW power, tuned to the D_2 Rb line at 780 nm. The transmitted beam wavelength is matched with the central wavelength of FADOF in the reception by using another identical FADOF to control the laser frequency. The MO is employed to seed a Tapered laser Amplifier (TA) [Marq96], that becomes the "slave". With proper spatial mode matching between the MO beam and the beam emitted by the back facet of the TA, and with MO power >3 mW, the slave emits a beam which has the spectral properties of the MO, but with a much higher power. With this scheme, we obtained more than 0.5 W in cw-mode as

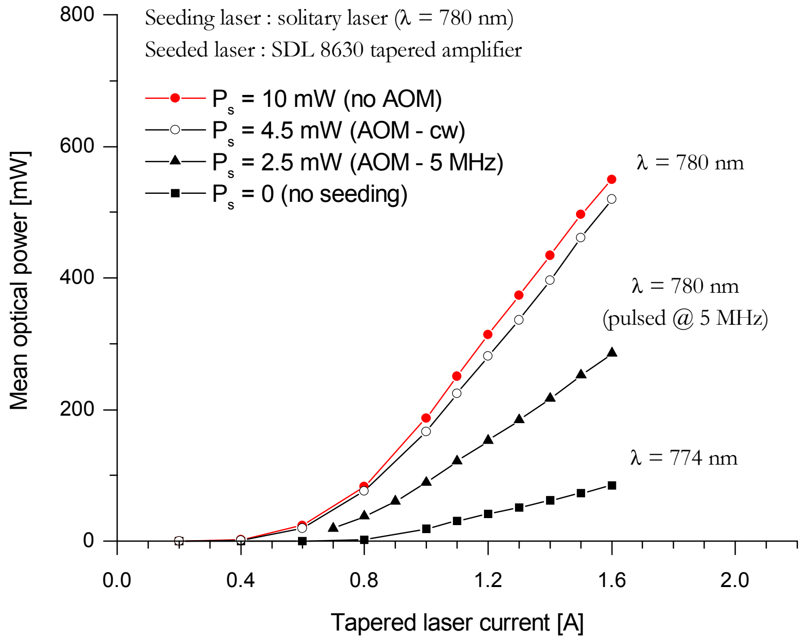

Figure 5.4. *Output power of the tapered laser diode (TA) in the MOPA configuration.* P_s *is the power of the seeding beam. The maximal allowed current for the TA is 2.2 A.*

reported in Figure 5.4. In standalone mode, i.e. without being seeded, the slave amplifier emits at 774nm and with much lower power than when seeded. PRN-cw modulation is performed with an Acousto-Optical Modulator (AOM), the same as in Chapter 3, between the MO and the slave. The loss due to the AOM is of no importance for the slave operation in cw-mode. When a modulation is present, the mean power depends on its duty-cycle sequence and the modulation frequency. For a PRN-cw sequence – which duty-cycle is 50% – and a modulation frequency of 5 MHz, half of the unmodulated power is reached. At higher modulation frequency, the AOM starts to become less efficient and to distort the wave-form. Nevertheless, the TA output beam is still modulated.

5.1.3 PRN-cw lidar demonstration set-up

The set-up for the demonstration of PRN-cw lidar measurements with diode laser MOPA and FADOF is illustrated by the picture in Figure 5.5 and its block diagram is shown in

Figure 5.6. It is based on the set-up we used previously for the PRN-cw lidar experiment in photon-counting mode and exposed in Chapter 3. The two main differences are the optical filter and the telescope diameter. The detection, acquisition and data processing systems are the same. The modulated laser beam from the MOPA laser diode system is sent to the atmosphere or to a target after a beam expansion. The backscattered light is collected by a lens with diameter of 20 mm. The receiver optics includes a diaphragm, a collimating lens,

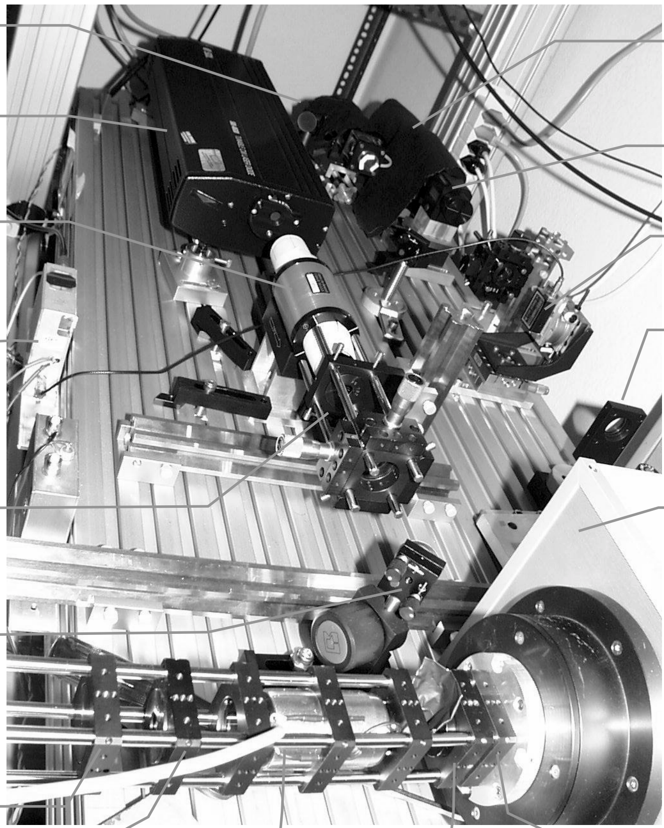

Figure 5.5. *Picture of the FADOF PRN-cw experiment set-up. The narrow-band interference filter and the collecting lens at the reception are not visible and would be on the left lower part of the image. During the measurements, an aluminium foil wrapped the whole reception optical bench to avoid stray light.*

the Rb FADOF and a field lens. Two interference filters more are used, which transmission peak is centred on the measured wavelength, 780 nm. A 0.2-nm narrow-band filter is placed before the FADOF as security to insure proper background rejection from other spectral windows. A second broad-band filter of 6-nm bandwidth is placed in front of the PMT to protect it during the set-up assembly and adjustment. The divergence of the laser beam is 4 mrad while the field of view of the receiver optics is 10 mrad. The latter value and hence the background radiation falling on the detector is high for a lidar. However, as the distance between the axes of the transmitter and the receiver is 150mm, it enables a full overlapping at 45-50 m. The detection of the backscatter signal is performed by a cooled PMT (Hamamatsu R943-02) in photon-counting mode. The data acquisition is performed by a multichannel scaler. The FADOF PRN-cw lidar demonstration is assembled on small optical bench in the laboratory. The transmitted beam and the receiver field of view are pointed towards the atmosphere in horizontal or in vertical direction by a system of two plane mirrors. A PC is providing the experiment piloting, by generating the PRN sequence and the cross-correlation of the acquired signal with the original sequence.

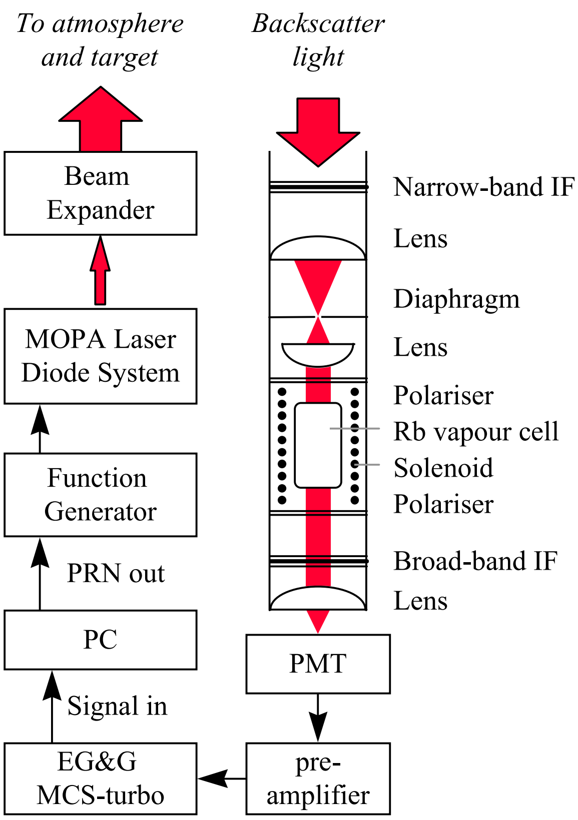

Figure 5.6. *Set-up of the demonstration FADOF PRN-cw lidar experiment.*

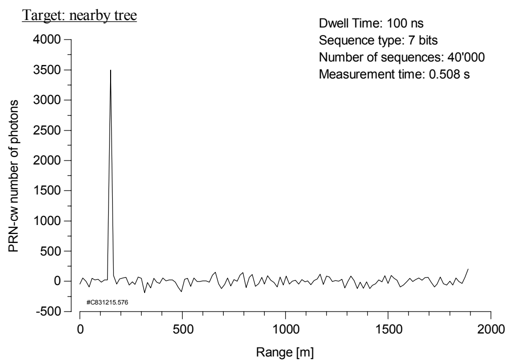

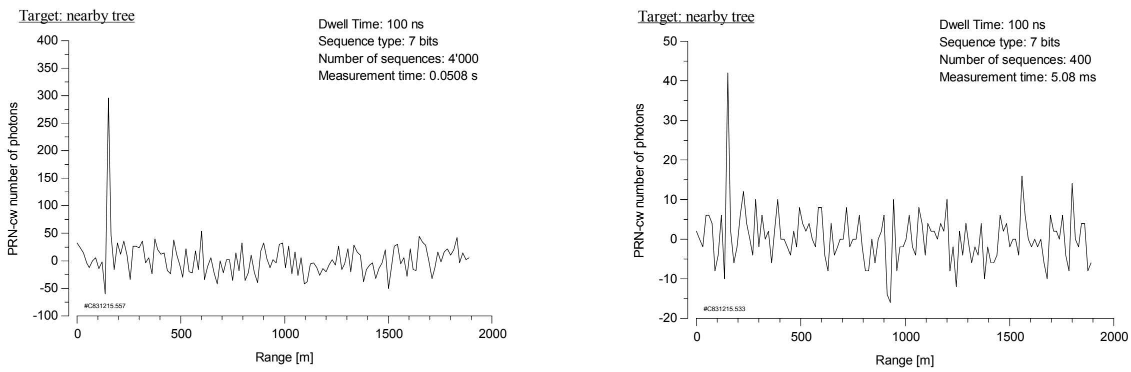

Figure 5.7. *Day-time lidar signal from a nearby tree with FADOF filter. The lidar pointed horizontally. The measurement time varied from 0.5 s to 5 ms, while the resolution was fixed at 15 m. Although the tree is close to the instrument, it would not have been possible to detect it in 50 ms integration time with a 6 nm-bandwidth interference filter.*

5.1.4 Results

Three examples of day-time FADOF PRN-cw lidar operation performed in this set-up configuration are presented: detection of the signal from a close hard target – a tree –, from a distant hard target – a mountain – and from a cloud base. For all measurements the mean transmitted power was 350 mW. We point out that the receiver had 20 mm-diameter aperture. The cross-correlated lidar signal from a nearby tree is presented in Figure 5.7. The PRN sequence is 7 bit, the time bin is 100 ns, what establishes a range resolution of 15 m. The integration time was successively 0.5 s, 50 ms and 5 ms, what corresponds to 40'000, 4'000 and 400 sequences. As we see, with 5 ms integration time the SNR for the tree is still

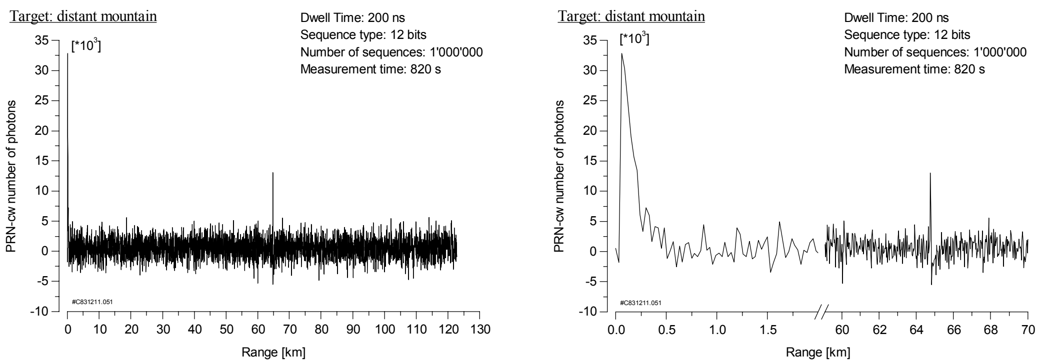

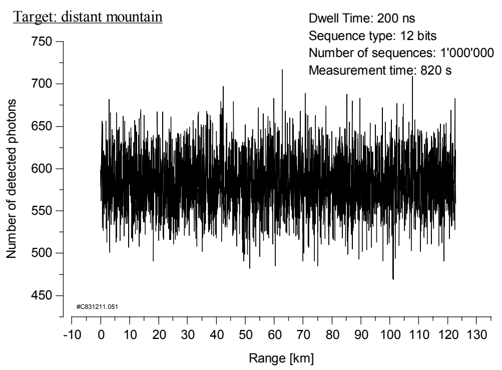

Figure 5.8. *Day-time long range topographic measurement with FADOF filter. The resolution was 30 m and the integration time 820 s. On the upper left is plotted the whole cross-correlated signal while on its right, the range near the instrument and the region of the mountain are zoomed. The peak is located at 64.77 km and has SNR of 4. The lower left plot is the directed acquired signal.*

in the order of 3. If we had used a simple interference filter of 6 nm bandwidth, that is 1'000 times larger than our FADOF, the tree would not have been detected for 50 ms integration time*.

Another example of day-time measurement is the detection of a mountain at far distance. It is illustrated in Figure 5.8. The lidar pointed horizontally to a mountain in south direction. The resolution was 30 m and the integration time 820 s, that is slightly less than a

* From the measurement with 0.5 s integration time, the tree signal is at 3500 counts, while the number of background counts is 370 (total detected signal minus tree signal). For 1'000 larger filter (6nm) and 10 times less integration time (50 ms), we would collect 350 signal counts and 37'000 background counts for a total of 37'350 counts. The noise fluctuations at one-sigma is then the square-root of this value, 193. As explained we work with a two-sigma confidence level, 386. The SNR is thus 370/386 and less than 1. With these figures it is also possible to calculate the minimum integration time that would have been necessary to get a SNR of 1. It is 61 ms.

quarter of hour. The mountain was detected at 64.77 km from the Observatory of Neuchâtel with a SNR of 4. The measurement took place by clear weather, at local noon – 11h UTC –, in early spring time – March 1998. In probing horizontally till the mountain, the beam was much more attenuated as the integrated value of the extinction coefficient from the lidar instrument to the mountain was 7.5 times more than the integrated value over the whole atmosphere.

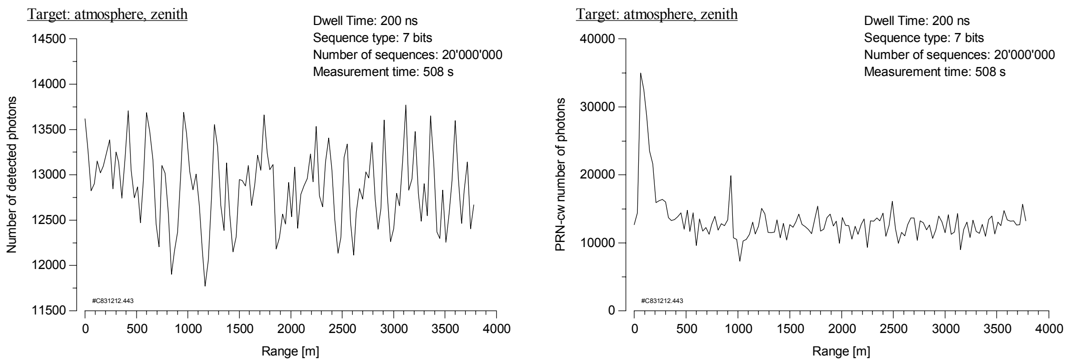

Figure 5.9. *Day-time cloud base detection with FADOF filter. The resolution was 30m and the integration time 508s. On the left is plotted the acquired signal, on the right, the cross-correlated signal. A cloud with base at about 1km is detected. The atmospheric response is seen at short distance above the instrument.*

Finally, Figure 5.9 is an illustration of a cloud base measurement. The PRN-cw sequence is again 7 bits with bin duration of 200 ns what establishes a range resolution of 30 m. The integration time is 508 s. Like for the distant mountain example and as shown by the detected signal plotted in the left pane, the background radiation mean level is higher than the level of the signal. Compared with the acquired signal of the mountain example, the cloud base signal has an higher offset for an integration time of the same order of magnitude, although it was measured the same day, also at noon. The reason is the higher number of sequences needed due to the shorter length of a single sequence, 127 bins instead of 4'095. However, the number of background photons detected per second is 2'600 for the horizontal mountain probing and 2'930 for the zenith cloud probing. This result is in accordance with pointing direction. Looking at both acquired signals, the mountain one might give the impression that it is more noisy. This is only an illusion due to the number of bin per sequence again. There are much more data points in the mountain plot than in the cloud one.

5.1.5 Conclusion

The possibility for day-time PRN-cw backscatter lidar operation with ultra narrow-band FADOF and narrow-band diode laser locked on this filter was demonstrated. The results are satisfactory for very fast detection of hard target, when the mean background level is decreased to values comparable with the mean value of the target response. In the opposite case – atmospheric and cloud response – longer integration time is required to account still higher background light level.

The rejection of the background with FADOF depends on the optical quality of the windows and the performance of the used polarisers. This demonstration set-up is far from optimal. Sheet polarisers are used, what is not enough to obtain higher out-of-band rejection. The cell windows are not of high quality and not anti-reflection coated. Use of higher quality components will bring additional background rejection. The bandwidth of the filter could be further reduced by adding a “Zeeman cell” – Rb cell in a high magnetic field of ~1000 G – after the FADOF [Yinb94].

5.2 Example of PRN-cw lidar concept: mission to Mars

Space-borne instruments are required to work in very harsh environment, to be highly reliable, compact and light, and to show low power consumption. Cw-laser diodes are light sources which fulfil these requirements and some of them are already even space-qualified. As they may use such kind of laser, PRN-cw lidars are appropriate candidates for space lidar applications. Sounding the atmosphere of a planet with an orbital-based elastic backscatter PRN-cw instrument will not be advised as the signal backscattered by the surface of the planet will likely mask weaker signals from the atmosphere (cf. Section 3.5 in Chapter 3). This limitation does not exist for ground-based PRN-cw lidar. This is the reason why we proposed to ESA (European Space Agency) in early 1998 a concept for a total elastic backscatter PRN-cw lidar dedicated to probe the Mars atmosphere from the Mars surface. This proposal was in reply to the ESA announcement of opportunity “Mars Express – A European Orbiter and Lander Mission to Investigate the Interior, Surface and Atmosphere of Mars” of 3rd December 1997 and planned for June 2003. The lidar was part of a lander dedicated to atmospheric studies and composed of several complementary instruments. Unfortunately this type of lander has been cancelled in its whole from the mission program. We think that the lidar concept submitted to ESA is still good and present it here. Objectives are described and instrument capabilities demonstrated by numerical simulations.

5.2.1 Objectives for aerosol lidar operating from Mars surface

Aerosol particles in the Mars atmosphere originate from soil material and/or water ice, and as it is suspected, also from carbon dioxide ice. They have substantial contribution in the atmosphere heat balance, and from this point of view are important inputs in climatological models and Mars atmospheric dynamics [Zure92]. Several important phenomena affect the aerosol distribution in the Martian lower atmosphere. Among them are water vapour exchange between the surface and the atmosphere, water transport in the atmosphere [Zure92], dust storm development, lifting and sedimentation [Kief92].

Information about aerosol distribution and scattering properties is already obtained by passive instruments: limb scanning orbiting instrument [Blam91], lander and orbiter imaging data [Poll77, Brig77]. The already carried studies revealed existence of high altitude aerosol layers, diurnal and day-per-day variation of the optical thickness of the atmosphere, mean size and shape of the aerosol particles. There are however very few data on the vertical structure and stratification of the aerosol in the layer of the Mars atmosphere close to the surface. The passive instruments – both lander and orbital-based – have limits to access the altitude distribution of the aerosol in the lowermost part of the atmosphere; they are also constrained during night-time, when it is the most advantageous period for lidar observations. That is why, in the recently planned Mars lander missions, aerosol backscatter lidars operating from the surface of the planet are considered as part of the scientific payload [Absh94, Bukh98]*.

We propose the use of an ultra-compact PRN-cw total backscatter lidar for determination of the altitude-resolved profile of the optical parameters of the layers of the Mars atmosphere close to the surface and in particular the PBL. The instrument shall measure at zenith from the lander as illustrated in Figure 5.10. This is why we call it Mars Lander Lidar (MLL). The instrument shall allow measurement till altitudes of a few kilometres with altitude resolution of 15 m, 30 m and 150 m if necessary. It will work night-time only†. Since the Martian atmosphere is very rare, with density at ground level equal to the Earth atmosphere at 33 km altitude, the contribution of the molecular component to the backscatter signal will be negligible and the principle contributor to the backscatter signal will be the aerosol component. Here follows a brief account of atmospheric phenomena located close to the surface of the planet which may be addressed by elastic backscatter lidar measurements:

I. Information how the dust is elevated from the surface in the atmosphere may be provided. When such measurements are done with simultaneous monitoring of the meteorological parameters they may give inputs to understand the meteorological phenomena associated with dust storms [Kahn92].

II. Observations during large dust events may provide answers to the questions "is there a distinctive boundary between the dust cloud and the atmospheric surface layer" and "what is the elevation of the base of the dust cloud".

III. Observations of local and regional dust events and addressing the same questions as above shall be also included. For instance, observation of local "dust devils" is with low probability, due to the small size of the latter – 200 to 600 m [Zure92]. The appearance of such events in the narrow field of the lidar is unlikely; nevertheless, such observation shall be not ruled out.

IV. Altitude variation of the atmospheric backscatter coefficient may be indicated. In a number of cases this may be a direct check for the existing mod-

* A Russian compact lidar was on board the NASA Mars surveyor program lander. The lander was launched in 1999 and unfortunately lost at the beginning of year 2000.

† During day-time it might operate in passive mode as photometer for observation of the variation of the sky radiance. In this case, the laser is off.

els. An example is the hypothesis for the "late night early morning haze". The appearance and variation of the altitude during the night of such haze layer may be assessed. This kind of evidence, combined with monitoring of the meteorological parameters, may provide inputs for the surface-atmosphere water exchange [Flas76].

V. From the lidar measurements there may be indications of presence or passage of low clouds. The cloud-base altitude and its variation may be determined. Combined with wind measurement, this may provide indication of transport phenomenon [Jame90].

VI. Vertical backscatter profiles may indicate the height of the night-time, early morning and evening PBL. Such measurements will be complementary to observations of day-time convective PBL by orbiting* cameras [Zure92, Kahn84].

It is important to note that, in most of the cases envisaged above, the lidar data will make the best impact if and when combined with the data from the meteorological instruments, like wind, temperature, pressure, water vapour, and optical depth from passive measurements of lander-based instruments as well as with the orbiter camera. The simultaneous measurements of the total optical depth and the low-altitude range-resolved atmospheric backscatter may discriminate low clouds or aerosol layers from high-altitude ones. In investigation of dust events, the backscatter lidar profiling from the lander is complementary to the orbiter imaging and optical depth measurements from the lander.

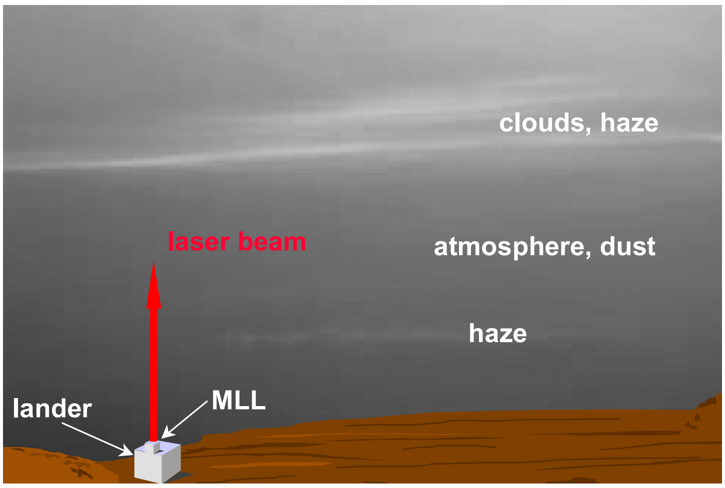

Figure 5.10. *The MLL is mounted on the top of a lander and looking at zenith. In this picture has been integrated the image of the sky recorded by Mars Pathfinder (NASA Sol 39, 05:13 local solar time).*

* An orbiter was also part of the initial ESA mission program.

5.2.2 Instrument concept

Operation mode

MLL is a stand-alone instrument installed on the upper part of the lander. Its block-diagram is presented in Figure 5.11. The command to switch the lidar on comes from the CPU synchronised with the diurnal cycle of the lander instrument operation. The lidar operation is during the night. A total of five to seven measurements are planned during the night, each having 1000 s integration time. The measurements are separated by pauses of about 60-90 minutes. After having received the command to start the measurement, the lidar electronics is warmed to the operating temperature and is switched on when the

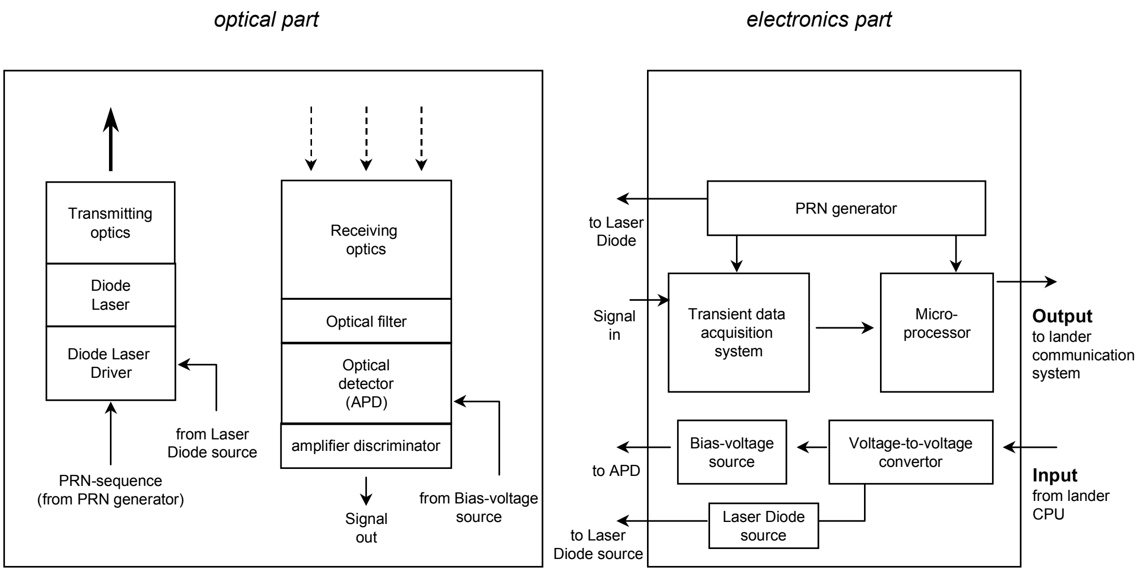

Figure 5.11. *MLL block-diagram.*

proper temperature is reached. The PRN-cw waveform generator sends the PRN-cw waveform to the laser diode driver and synchronisation pulses to the data acquisition circuit. The laser diode driver supplies the diode laser with current-driving pulses following the PRN pattern and the laser diode starts to emit radiation, power modulated following the driver. The radiation is scattered back by the atmospheric aerosol – dust, cloud, fog particles – and collected by the receiver. The received signal is filtered from the ambient optical background and is detected by the detector, an APD, in photon-counting mode. The signal – in number of photon counts – is acquired by a multichannel scaler in accordance with the time of arrival after the synchronisation pulse send from the PRN generator. Both the waveform generator and the acquisition system are synchronised and locked on a common clock, as required by the PRN-cw technique. The operation, i.e. the laser transmission and signal collection, continues for the envisaged integration time.

After the expiration of the integration time, the accumulated signal, which is already in digital form, is sent for data processing to the Earth. The cross-correlation is calculated on Earth. After the pause, which duration depends on the cycle of operation of the other instruments present on the lander and the available lander power, the next measurement starts. The aim is to distribute the planned five to seven individual measurement during the night in such way to cover the significant variation of the atmospheric backscatter in the lower part of the atmosphere during the night, sunset and sunrise.

Concept for mechanical design

The concept for the mechanical design of Mars lander lidar includes two options. In the first option, the instrument is realised in a single package, while in the second it consists in two separate packages. The single package instrument is presented in Figure 5.12. The laser, the detector and all electronics components are in a box, which is used as base-plate for the optical part. This optical part consists of the transmitter and the receiver. The transmitter is realised as a single aspheric lens. The diode laser and the lens are fixed on the upper wall of the electronics box and base-plate part. The receiver is realised as a Cassegrain telescope. Its primary mirror is part of the upper plate of the electronics box. This solution saves mass and increases the mechanical stability. All reflective optical components, the mechanical support and the walls of the electronics box shall be manufactured from beryllium. This will ensure the necessary stiffness, the minimum mass and, at the same time, will help to minimise the influence of the thermal load. The instrument is mounted on

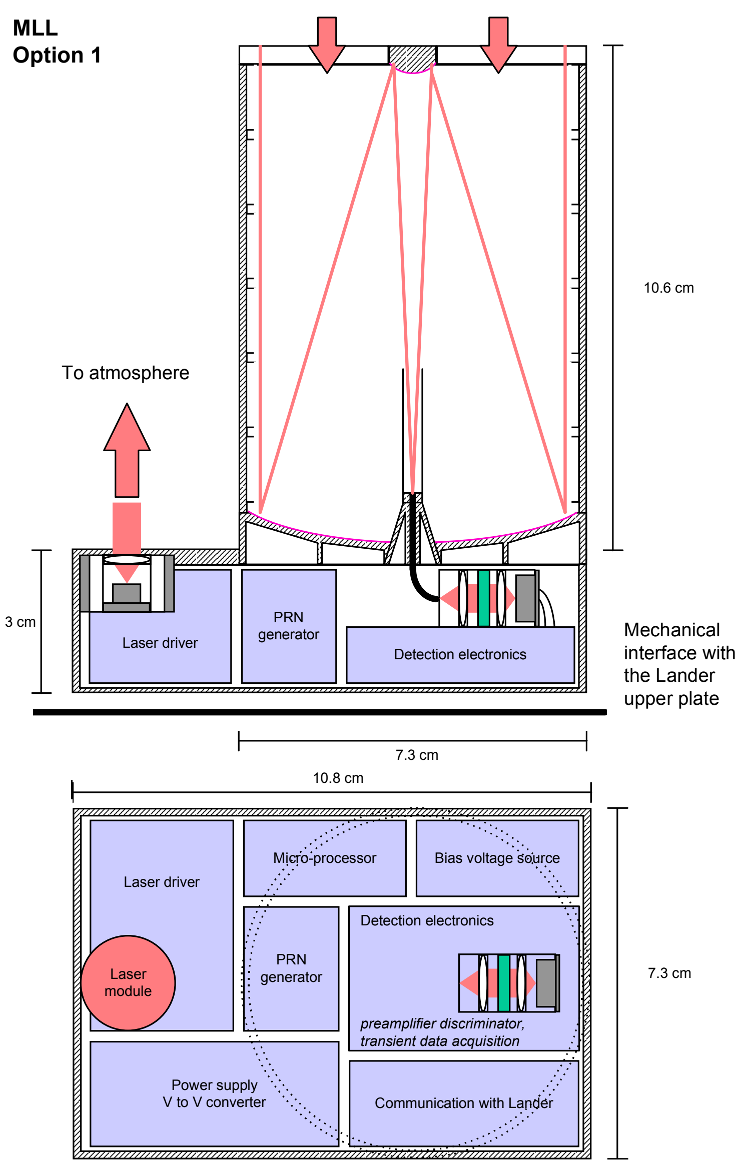

Figure 5.12. *View of the single package instrument option.*

the top of the lander. The mechanical interface is at the bottom plate or at the side panels of the electronic box, depending on the convenience of the upper panel of the lander.

The instrument consisting of two-separate package instrument is presented in Figure 5.13. The laser, the detector and all electronics components are in the electronics package, while the optical package consists of the transmitter and the receiver. The electronics package may be positioned in a closed volume of the lander together with electronics packages from other instruments or from the lander system. By this, the radiation and thermal protection will be shared, resulting in a lower mass and power consumption – less power for warming the electronics components will be required. The optical package is positioned again on the top of the lander, pointing towards zenith. The connection between the two packages is by optical fibres, one for the transmitter and one for the receiver. The transmitter will be realised as a single aspheric lens with fibre end at the focal plane. Since the fibre

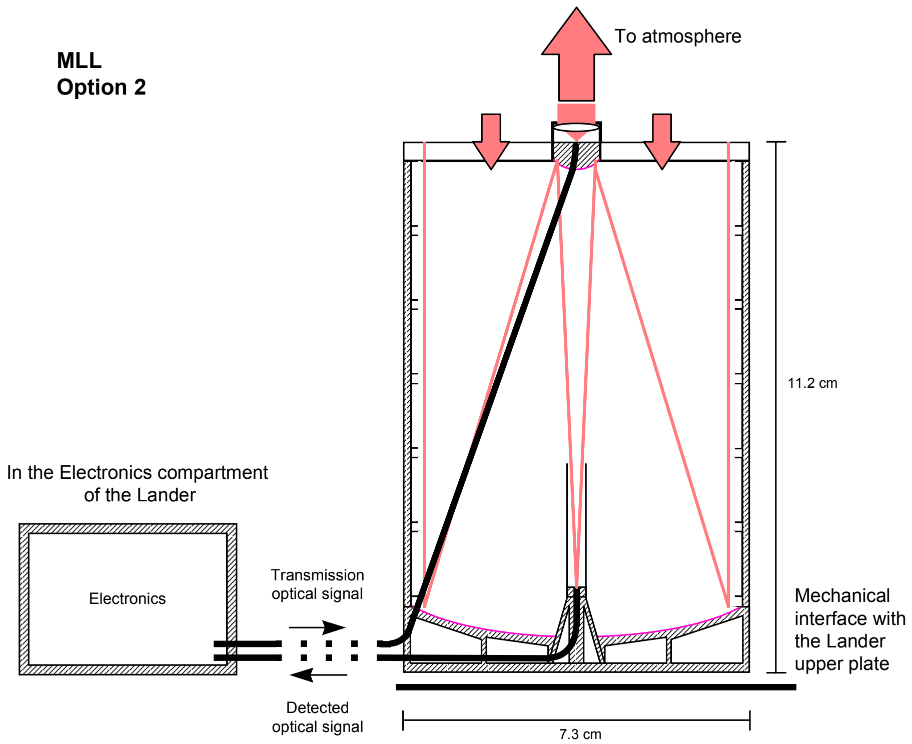

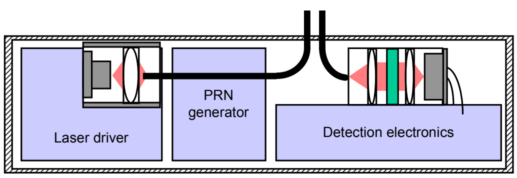

Figure 5.13. *View of the two-package instrument option. Left, the electronics package; above the optical package. Both packages are connected through two optical fibres.*

end is assumed to be twice the larger size of the laser diode emitting facet, the transmitter lens shall have longer focal length and larger diameter. This brings however negligible increase of the mass, because the lasing area is very small (cf. further). The receiver is realised again as a Cassegrain telescope. All reflective optical components, the mechanical support and the optical unit walls shall be manufactured from beryllium. This configuration offers more flexibility for integration in the lander than the single-package configuration.

The two alternative configurations have approximately the same mass which is estimated at 420 g, or slightly less for the separate package option. They have the same laser power, receiver diameter, etc.; so in the evaluation of the performances of the instrument we will not consider them as different. The final choice of the layout has to be done following the requirements for positioning of the other instruments on the lander, as well as the convenience following from the layout of the lander.

Operational environment

Temperature

The operating temperature for lidar operation of MLL, determining by the electronics, is specified to be about -45°C. Since the lidar operation will be during night-time, temperature stabilisation by heating only is required. The optics in option 1 and the optical package in option 2 can operate at the ambient Mars surface temperature.

Electrical power consumption

The power consumption for operation in active mode is expected to be approximately 2.2 W. It gives total consumption per night in the order of 4.0-4.4 Wh. The heating and data transmission power is not included. Option 2 is expected to operate with less heating power.

Communication

The data volume per single lidar measurement is about 13 kbit, not compressed. The maximum data volume per night is 7x13 kbit. The data for the auxiliary day time operation depends on the measurement cycle and is evaluated to 200 kbit, not compressed. Total for diurnal cycle is below 300 kbit. The nature of the signal detection and the household parameters control will allow the data to be sent to the lander data storage unit in digital form.

5.2.3 Instrument specifications

The specifications of the sub-systems of the proposed lidar are listed in Table 5.1. Space-qualified cw laser exist with spatial coherence, low size of the emitting facet, operating wavelength in the region around 850 nm and maximal cw-average power of 150 mW [Sdlc97, Crai94]. Such laser has also high-frequency modulation capability and in this way can provide a convenient source for an extremely compact PRN-cw lidar. Its efficiency is about 30%. Due to the lower size of the emitting facet, 1 μm x 3 μm, a small-size single lens can achieve the necessary divergence for the transmission. This is a basic advantage compared to the approach to use pulsed hybrid laser diode. The emitting facet of the latter, for mean quasi-cw power of about 20 mW, is 1 µm x 254 µm. This would require large-size optics to achieve the appropriate divergence.

APD's of SLIK™ type are compact detectors with high quantum efficiency in the region of 850nm and operate in photon-counting mode [Eggc97]. They are available in space-qualified realisation and in the very compact package TO-5. A photon-counting APD combines sensitivity and detection efficiency of a photon-counting PMT with robust design and long life.

Sub-system	Parameter	Specification
Laser diode	type	SDL 5421
	wavelength	850nm (approximately)
	bandwidth	2nm (specified)
	cw power	150mW (specified)
	modulation depth	better than 99.9%
Modulation	PRN sequence length	10-bit (1023 bins)
	frequency	10MHz
Transmission telescope	type	single aspheric lens
	effective beam aperture ∅	6mm
	transmitted beam divergence	0.5mrad (full angle)
Receiving telescope	type	Cassegrain, beryllium optics
	primary mirror aperture ∅	70mm
	focal length number	f:3
	secondary mirror aperture ∅	10mm
	field of view	1.5mrad (full angle)
	receiver filter bandwidth	5nm
	full overlap distance	55m
Detector	type	EG&G APD SLIK™
	mode of operation	photon-counting
	effective area, ∅	200µm
	quantum efficiency (@ 850 nm)	25% (specified)
	dark noise	70-100count/s (specified)
Data acquisition system	type	multichannel scaler
	single channel duration	0.1µs
	range resolution	15m and multiples
	number of channels	1023
	integration time	1000s
	number of measurements/night	5-7

Table 5.1. *Specified and planned target parameters of the sub-systems for MLL.*

Using high-density programmable logic devices has many advantages. The design is simplified by the advanced logic design and the simulation software packages. Complex functionality, like PRN code generator, acquisition sequences and multiscaler, as well as interface logic, can be implemented in a single device, reducing the number of parts and the PCB size and complexity.

5.2.4 Performance simulations

The performance simulations of the proposed instrument are derivative from the computer model of the PRN lidar described in Chapter 2. For the purpose of the present performance simulations, the instrument input part of the model do not need any modifications. On the other hand it is necessary to elaborate a preliminary model for the Martian optical atmosphere.

Atmospheric model

The performance simulations require model values for the molecular and aerosol backscatter components. The model for the Rayleigh backscattering coefficient is following the model for the Mars molecular atmosphere from [Moro91]. For the aerosol component the following typical layers are considered:

- Layer type 1. Mineral dust with optical depth of 0.214, distributed homogeneously, step-wise, from the planet surface to 10 km altitude.
- Layer type 2. Mineral dust with optical depth of 2.17, distributed homogeneously, step-wise, from the planet ground to 10 km altitude.
- Layer type 3. Cloud containing ice particles, with optical depth 0.465, Gaussian altitude distribution with thickness of 0.5 km, with maximum at various altitudes above the planet surface:

type 3a	0.5 km
type 3b	1.0 km
type 3c	2.0 km
type 3d	3.0 km
type 3e	8.0 km

For layers 1 and 2, the volume backscattering coefficient and the extinction-to-backscatter ratio are taken as for PBL aerosol of mineral origin in the Earth atmosphere. For all layers of type 3, these characteristics are taken as for ice-crystal cirrus clouds also in the Earth atmosphere. Such approximation is consistent with the findings and the assumptions for particle microphysics parameters in the Martian atmosphere [Murp93, Hunt79, Thor77]. In this way we may use, after their evaluations, the respective scattering ratios R for the layers in the Martian atmosphere, in the same way as for the Earth atmosphere*:

$$R(h) = (\beta_{aer}(h) + \beta_{mol}(h)) / \beta_{mol}(h), \tag{5-1}$$

where β_{mol} and β_{aer} are the molecular and aerosol volume backscatter coefficients and h the altitude above the surface. The optical depth of the layers is chosen with respect to the values of the optical depth and its variation as evaluated from Viking Lander and Mars Pathfinder cameras [Smit97, Poll77, Poll95]. The optical depth τ over the altitude interval $[H_1, H_2]$ is defined as

$$\tau = \int_{H_1}^{H_2} \alpha(h) dh = \int_{H_1}^{H_2} [\alpha_{mol}(h) + \alpha_{aer}(h)] dh, \tag{5-2}$$

where α_{mol} and α_{aer} are the molecular and aerosol extinction coefficients. These coefficients are derived from the assumed scattering ratios and the backscatter-to-extinction ratios (cf. Chapter 2). Our procedure to determine the values of the scattering ratio as inputs to our model is actually reverse. We start from a range of values for the scattering ratio and we chose the one which gives optical depth consistent with the above quoted measurements.

The estimated values for R and τ may be related to the particle number density for dust and fog in the Martian atmosphere [Poll77]. Extrapolation of values for the lidar scattering ratio as related to the particle number density in the Earth stratosphere when the stratosphere is loaded both with sulphuric acid aerosol and silicate particles short time after major volcanic events like El Chichon in 1982 and Pinatubo in 1991 [Thom87, Rose83, Desh94, Vaug94] gives results consistent to the particle number density for Martian atmosphere. The parameters of the cloud layers type 3 are consistent with [Colb89, Flas76]. The difference is that we assume less optical depth and, for some of the cases, higher altitude.

Figures	Resolution	Combination of aerosol layers
5.14-I	30 m	type 1
5.14-II	30 m	types 1+3a
5.14-III	30 m	types 1+3b
5.14-IV	30 m	types 1+3c
5.14-V	150 m	types 1+3e

Figures	Resolution	Combination of aerosol layers
5.15-I	30 m	type 2
5.15-II	30 m	types 2+3a
5.15-III	30 m	types 2+3b
5.15-IV	30 m	types 2+3c
5.15-V	150 m	types 2+3d

Table 5.2. *Parameters for the computer simulations of MLL measurement performances presented in Figures 5.12-5.20. The instrument specifications used as inputs in the model are the ones enumerated in Table 5.1, unless stated otherwise. Integration time for all measurement simulations is 1000 s. The detector dark noise is taken as 70 counts/s.*

* In our model we have as input parameter the scattering ratio R, which is defined as the ratio of the total volume backscatter coefficient – as sum of the molecular and aerosol components – to the molecular component (cf. Chapter 2).

Simulation results

Some aerosol layer combinations chosen for the computer performance simulations are given in Table 5.2. The corresponding simulation results are given in Figures 5.14 and 5.15, where are plotted the recovered cross-correlated signals and the signal-to-noise ratios.

Comparing Figures 5.14-I and 5.15-I, we may see that the cross-correlated signal level is demonstrating dependence on the model backscattering coefficient, that is on the scattering ratio that follows from the model optical density of the layer with the same altitude

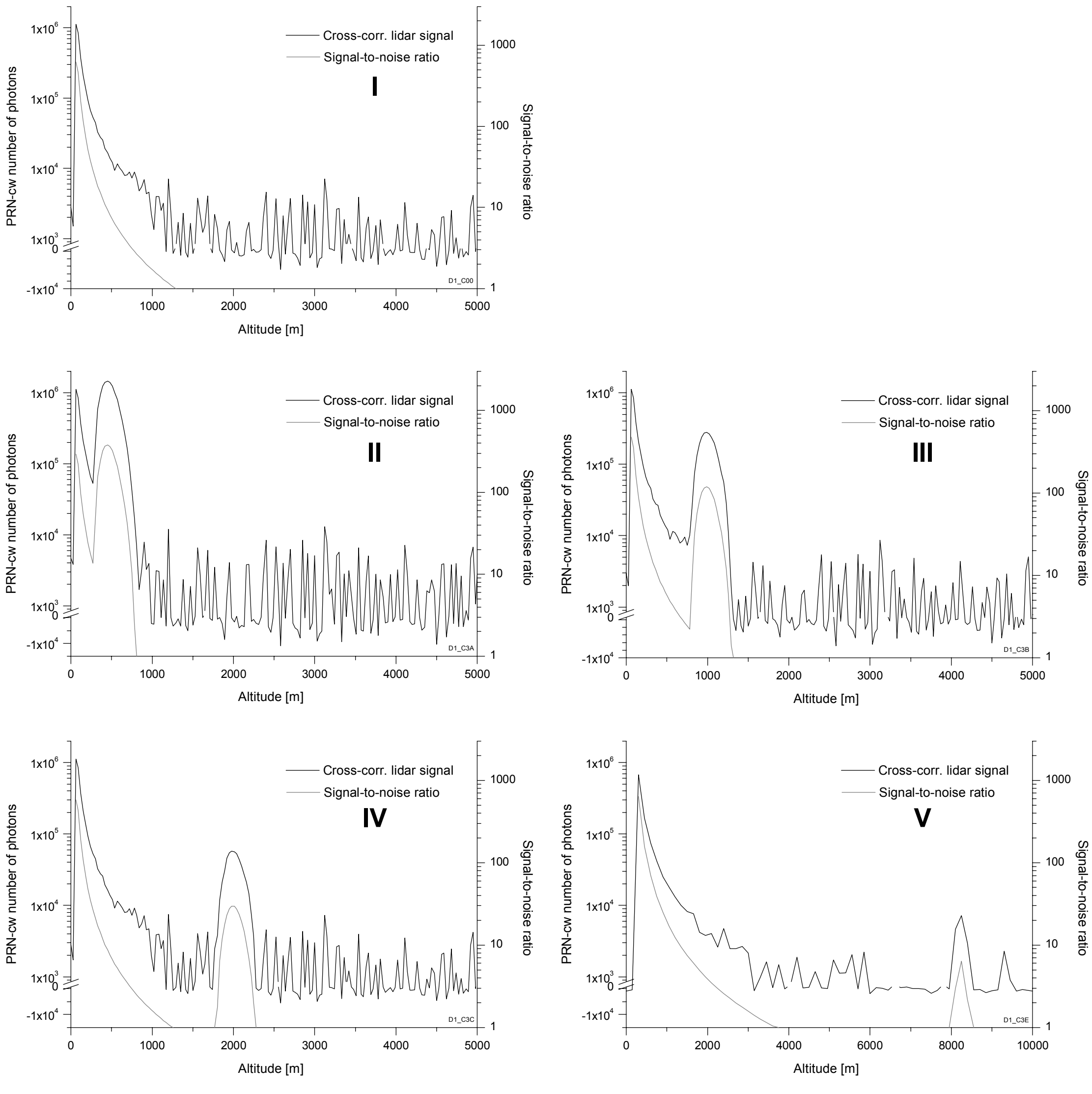

Figure 5.14. *Results from computer performance simulation of the proposed MLL in case of optically thinner dust layer. (I) is with no cloud layer, while (II-V) are with a cloud layer at higher and higher altitude. See Tables 5.1 and 5.2 for instrument and atmospheric layer parameters. (I-IV) are with 30 m range resolution and (V) with 150 m.*

distribution of the aerosol. The case in Figure 5.14-I is for optical density related to background dust aerosol conditions. The case in Figure 5.15-I is for dust storm related optical density. Figures 5.14-II to 5.14-IV demonstrate that ascent of layer of ice particles with reasonable optical density may be detected during the night. The case illustrates in Figure 5.14-V shows that a layer of clouds as high as 8 km may be detected over background dust aerosol, in this case with a reduced range resolution[*]. The results in Figures 5.15-II to 5.15-IV may be associated with fog layer accent again, but in conditions of dust storm. The maximum detection altitude in this case is 3 km, when again the resolution is decreased to 150 m in order to detect the backscatter signal from this layer.

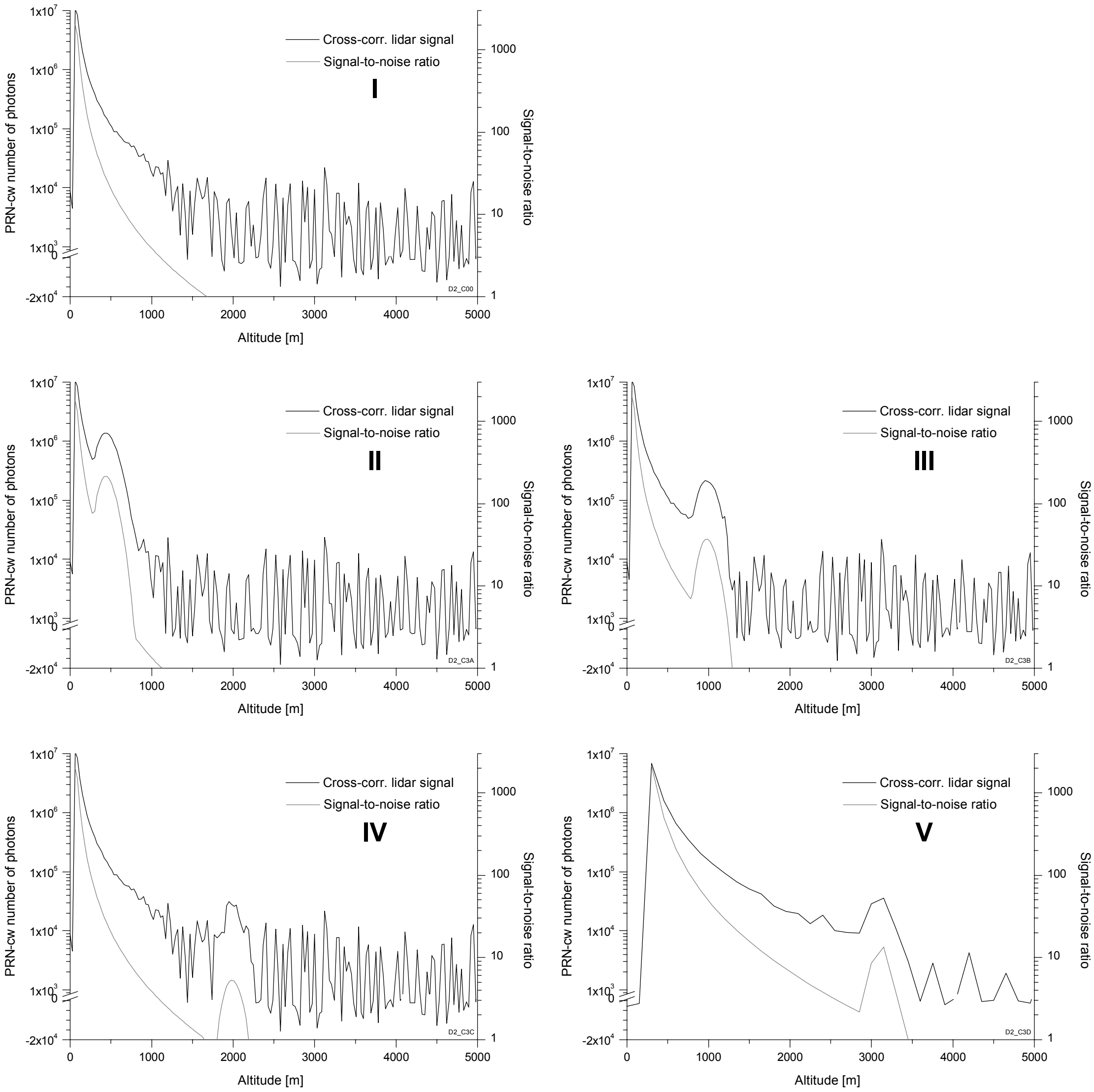

Figure 5.15. *Results from computer performance simulation of the proposed MLL in case of optically thicker dust layer. (I) is with no cloud layer, while (II-V) are with a cloud layer at higher and higher altitude. See Tables 5.1 and 5.2 for instrument and atmospheric layer parameters. (I-IV) are with 30 m range resolution and (V) with 150 m.*

[*] The modulation of the laser diode is fixed at 10 MHz and accordingly the duration of a single channel is 100 ns, fixed also. This provides an initial range resolution of 15 m. However, during data processing, the resolution may be lowered to increase the SNR. This is why simulation may have a range resolution different from 15 m.

5.2.5 Conclusion

A concept of PRN-cw lidar instrument to detect aerosols in the lower Martian atmosphere has been elaborated and presented here. It makes profit of one of the main advantages offered by the PRN-cw technique: the use of a cw-laser diode with high beam qualities. Coupled with an all-solid state detector and a simple photon-counting acquisition system, such a laser allows the construction of really compact, simple and reliable lidar instruments. These qualities place such instruments as serious candidates for specific space missions.

Numerical simulations of the detected signal with the computer model discussed in Chapter 2 and adapted for Martian atmosphere show that the foreseen instrument may detect with sufficient signal-to-noise ratio aerosol layers during night-time up to altitudes of several kilometres, when the signal is integrated on 1000 s. Substantial information on the altitude distribution of the aerosols might be then delivered.

At the time of this study, the possibilities offered by FADOF filters were not totally known and we did not consider this possibility. Such a filter might be included in a lidar for a space mission; the instrument would be more efficient. However, it will be heavier, larger and will also consume more power. Problems may also arise from the temperature level and the electromagnetic field necessary to make the filter working properly.

Chapter conclusion

In this chapter, we have demonstrated how to improve the performances of a PRN-cw lidar by using an ultra narrow-band filter and have presented a concept for a PRN-cw lidar space mission on planet Mars. This demonstration and this concept have in common that they want to make the maximal use of the advantages offered by the component around which the PRN-cw lidar technique is based and built, that is the laser diode. These advantages are the laser bandwidth, size, weight, reliability and efficiency. They also share the confidence that, despite the limitations of the PRN-cw technique, they may find domains of applications where pulsed instruments are less adapted, because of environmental requirements.

Here finishes the part of this work that was dedicated to the PRN-cw technique. The second part will present a compact elastic backscatter lidar instrument for airborne application. This time, the pulsed technique will be concerned: the laser beam source will no more be a cw-laser diode, but a pulsed hybrid laser diode and a passive Q-switched micro-chip laser.

Chapter 6

A compact automated airborne lidar

Introduction

Critical for the size of a lidar is the laser. We have seen that one of the advantage offered by the PRN-cw technique is the use of cw-laser diode. Such light source is usually of small dimensions. However, other small lasers exist like pulsed hybrid diode lasers or micro-chip lasers. In this Chapter, we describe the realisation of a compact depolarisation backscatter lidar that operates from a high-altitude research aircraft. A first version of this lidar was based on an infrared (IR) pulsed hybrid diode laser. Due to not reliable detectors and changes in the measurement planning of the campaign from night-time to day-time, the instrument could not adapt to the measurement. A second version has been developed around a "green" micro-chip laser. In Section 6.1 we explain why we built such an airborne lidar. Its operating platform, a Russian high-altitude aircraft, and the operational and environmental requirements are described. The IR version is presented in Section 6.2 and the "green" version in Section 6.3. A software allowing fast overview and quality control of the data measured during several hours is also presented (§ 6.4). Measurements obtained during airborne campaigns are not presented here but in Chapter 7, together with the campaign targets. Ground-based measurements performed with the "green" instrument during test periods are also not shown in this present chapter, but in the next one.

6.1 A compact airborne lidar: why and where

Among the instruments for aerosol studies the backscatter lidars are recognised as unique in their capability to detect the range-resolved profile of the aerosol backscatter coefficient, that is the aerosol particles range (altitude) distribution. The advantage of the airborne platform is that the area coverage leads to a substantial increase of the impact of the collected information.

Presently used backscatter airborne lidars (as well as DIAL) prove to be powerful tools for backscatter detection in a number of reported case studies, varying from PBL convection cells, gravity waves [Palm94, Palm96, Flam96], stratospheric aerosol measurements and DIAL ozone [Wirt94, Wirt96], mountain-wave induces PSC [Godi94], intercomparison experiment of lidar and in-situ instrument in the troposphere [Rede96], water vapour DIAL [Chyb96].

On the other hand, the routine operation of the presently employed airborne backscatter lidars suffers the limitation of very high running cost. This is because they are big instruments with all disadvantages implied: consuming high electric power and employing airborne platforms of large size and power sources, limiting the capabilities of the platform to accommodate other instruments for atmospheric measurements, etc. They are also not automated instruments and enough room is needed for the personnel as well.

There is a trend in the airborne missions for atmospheric studies to employ drones or aircraft with one-man crew. The latter may be either high-altitude aircraft or very light craft, or both [Lang97]. For such airborne platform, the requirements for the volume, mass and operational automation of the lidar are extremely stringent. Some approaches have already been explored [Kric96].

6.1.1 "Geophysica", a stratospheric airborne platform

A notably important event in this trend is the start of the co-operation of a group of scientists from a number of EU countries with Russia in the use of the high-altitude research aircraft named "Geophysica", based on a derivative of the Russian military aircraft Myasishchev M-55. Figure 6.1 is a view of the aircraft. "Geophysica" is an all-weather single-seat stratospheric aircraft capable of operating both day and night for about 5-6 hours up to an altitude of 21 km, even in critical environmental conditions (e.g. temperatures down

Figure 6.1. *The Russian M-55 "Geophysica" high-altitude aircraft. The dorsal bays were removed at the time of this view.*

to -80°C, strong cross-winds at take-off/landing). Its cruising velocity is about 700 km/h. These characteristics together with the possibility of housing a scientific payload up to 1'500 kg inside its bays (the main bay is over 5 m long and can accommodate bulky instruments) make "Geophysica" an ideal platform for research in the upper troposphere and lower stratosphere. "Geophysica" has undergone several transformations in order to house the scientific payload and to increase its efficiency and flexibility as scientific laboratory. With this perspective, the bays of the aircraft have been modified according to a modular criterion and have been equipped with standard interfaces for the instruments (attachment points, electrical connections, viewing windows, servicing hatches). In addition, a number of dorsal bays has been built to lodge instruments onto the fuselage of the aircraft.

At present the M55-Geophysica is, together with the U.S. aircraft ER-2 (a modified version of the U-2 reconnaissance aircraft, managed by NASA and used for scientific purposes), one of the two airborne platforms operating world-wide for stratospheric research. While the ER-2 has a longer flight endurance than the "Geophysica", the latter has superior characteristics with respect to scientific payload capacity, power supply, manoeuvrability, and less dependence on ground meteorological conditions.

6.1.2 "Geophysica" payload

The scientific payload on "Geophysica" contains a number of in situ and remote-sensing instruments from various European and Russian institutes. They aim at chemistry (trace

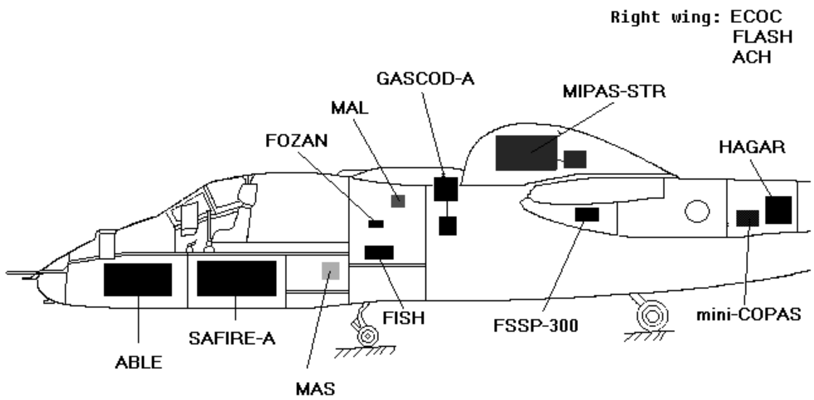

Figure 6.2. *Geophysica payload as initially defined for the APE-GAIA Antarctic polar campaign, austral Spring 1999.*

gases) and microphysics (aerosol particles) measurements. The payload is determined by the objectives assigned to a measurement campaign. As illustration, Figure 6.2 is a view of the payload for polar campaign.

In-situ chemistry instruments are of three categories. Water concentration is measured by several hygrometers, in liquid phase (ACH), in gas phase (FLASH) and as total content (FISH). Two ozone meters are also present (ECOC and FOZAN). Finally a gas chromatograph measures CFC's, N_2O, SF_6 (HAGAR). The remote -sensing devices for chemistry species are two Fourier-transform spectrometers operating in the far and medium infrared (SAFIRE-A and MIPAS-STR) and a UV-visible spectrometer (GASCOD-A). Their measurement products are profiles and vertical columns of atmospheric constituents. In-situ aerosol instruments that fly on board "Geophysica" are particles counters (FSSP-300 and COPAS), a multi-wavelength laser scattometer providing backscatter coefficient and depolarisation ratio (MAS) and two spectrometers for cloud element analysis (CVI).

Finally, two depolarisation elastic backscatter lidars are on board the aircraft for aerosol remote sensing. The first, ABLE, from University of Roma, is a long-range lidar able to sense either in the zenith or in the nadir direction*. It provides data from 2 km and further. It is a pulsed lidar built around a Nd-YAG laser with second (and possible third) harmonic generator(s). This laser operates at low repetition rate (20 Hz) for a total mean optical power of about 10 W. Its weight is 250 kg. The second lidar is MAL (Miniature Aerosol Lidar), instrument that we developed at the Observatory of Neuchâtel and present in this Chapter. In the set of complementary instruments transported by the aircraft, it has been assigned the task to detect clouds and aerosol layers in the troposphere and the low stratosphere, above the aircraft and in its vicinity, that is to say up to 2 km. Its purpose is to fill the gap between in-situ and far-remote measurements. It is called "miniature lidar" because it has to fit in a volume of 28 litres with dimensions 51x32x17 cm^3.

6.2 IR-MAL instrument

6.2.1 Objectives and requirements

The APE-POLECAT† campaign took place between mid-December 1996 and mid-January 1997. It comprised the inaugural mission of "Geophysica" and flights by the German DLR Falcon. Both aircrafts flew from Rovaniemi, Finland. They were involved in the study of the PSCs (polar stratospheric clouds).

For this campaign, MAL has been developed in co-operation by the Observatory of Neuchâtel and the Space Research Institute of the Russian Academy of Sciences (IKI). Due to the short time available before the campaign, it was derived from a system existing in IKI. The requirements addressed to MAL for the campaign are listed in Table 6.1. The instrument had to measure only night-time. Volume, weight and power consumption of the instrument were limited. It couldn't be installed in a pressurised box.

---

* The probing direction is chosen before each flight.

† APE-POLECAT was a joint campaign between the European international programme APE (Airborne Polar Experiment) using Geophysica as platform and the POLECAT campaign, which was part of the German Ozone Research Programme.

Requirement type	Objectives
Scientific task	Detection of PSCs in zenith direction, in the vicinity of the aircraft (up to 2 km), during night-time only.
Operation mode	Fully automated; no operation by the pilot during the flight.
	Power supply switched on by the Russian aircraft crew on ground before take-off and switched off on ground after landing.
Environment constrains	Limited dimension of 51x32x17 cm^3.
	Weight: max. 15 kg.
	Available power: 3 A under 27 V for the whole instrument, instrument heating included.
	Not pressurised instrument able to work at pressure down to 50 mb and external temperature down to –50°C.

Table 6.1. *Requirements to be fulfilled by MAL for the APE-POLECAT campaign.*

6.2.2 Instrument description

Laser

Due to the pressure constrain, the best choice for the laser source was an all-solid state laser. The lidar was designed and realised with a hybrid pulsed laser diode array of the type LHCVD 193-30 from the firm Laser Diode Products, Inc. The diode is a stack of three emitting layers with overall size of 256 μm x 152 μm. This laser emits at 837 nm in the near infrared (this is why this version of MAL is named IR-MAL). Its bandwidth is approximately 7 nm and it is linearly polarised. The laser is powered by a driver developed for that purpose. It is positioned on a card immediately next to the laser diode leads. The pulse repetition rate is set as high as possible to achieve maximum mean power. Considering that a laser pulse must be fully extincted before the next pulse is emitted – there shall be no response from the previous pulse once the next is emitted – a frequency of 17.5 kHz was chosen. The measured corresponding quasi-cw average power is 14 ± 2m W. Other information on the laser are found in Table 6.2 describing the parameters of the lidar subsystems.

Detection

For detection of the backscatter light at the two polarisations (parallel to the one of the transmitted beam (*p*) and perpendicular to it (*s*)) we used two pieces of single-photon avalanche photodiodes (SPAD). They were immediately available with their electronics circuits[*]. The SPADs operate at bias voltage above the threshold, so the reception of a single

[*] From Czech Technical University, Prague, Czech Republic, with whom IKI was collaborating that time.

photon causes a large amplitude output signal pulse. This provides a high sensitivity combined with resistance to high illumination damage, like direct sun light during airplane turns, etc. The disadvantage of this technical solution is the high numbers of the dark counts, as well as the possible dependence on the history of illumination. The bias on/off switching of the SPADs makes the recovery time also longer, about 30 μs.

Sub-system	Parameter	Specification
Diode laser	Type	LDI-LHCVD193-30
	Wavelength / bandwidth	837 nm / 7 nm
	Peak power	35 W
	Pulse duration	40 ns
	Pulse repetition rate	17.5vkHz
	Quasi-cw average power (@17.5 kHz)	14 + 2 mW
	Beam depolarisation	~2.2%
Receiver / transmitter	Telescope type	4x Galilean refractor
	Effective aperture	134 mm ∅
	Beam divergence	2.3 mrad full angle
	Receiver field of view	0.9 mrad full angle
Filter	Type, cut-off	glass, 780 nm
Detection	Detectors	2 single-photon APDs
	Effective area, specified / measured	100 mm / 83-85 mm ∅
	Dark noise (@ room temperature)	200 kHz
	Quantum efficiency	23%
Data acquisition system	Type	Single-photon counting
	Acquisition range resolution	30 m
	Number of gates (bins)	256
	Duration of a single measurement	3.4 s (65'280 laser shots)
Full instrument	Configuration and dimensions	single box; 51x32x17 cm^3
	Weight	12.7 kg
	Electric power / voltage	4 W / 27 V DC; 50 W for instrument heating

Table 6.2. *Parameters of IR-MAL lidar sub-systems.*

Transmitter / receiver optics

The transmitter and receiver optics have the same optical layout. An aspheric lens is collecting the laser diode emission (for the transmitter) or focusing the collected light on the SPADs' sensitive area (for the receiver). Aligned with the aspheric lenses, both for the transmitter and receiver, are 4x-beam expanders. The selection of the two polarisations (*p*) and (*s*) is done by a polarisation beamsplitter cube.

The spectral selection of the backscatter light is provided by a glass filter only with cut-off at 780 nm. The advantage is that in this case the temperature variations of the laser wavelength are of no importance and a system for laser diode temperature stabilisation is not required. The disadvantage is that the optical background noise prevents from lidar operation in full day-light.

The sensitive detection areas of the SPADs (82-85 μm) are serving as single pinhole aperture for the receiver. Therefore, the receiver field of view is smaller than the laser divergence, which leads to a decrease of the used laser power and complication in the lidar calibration and data evaluation.

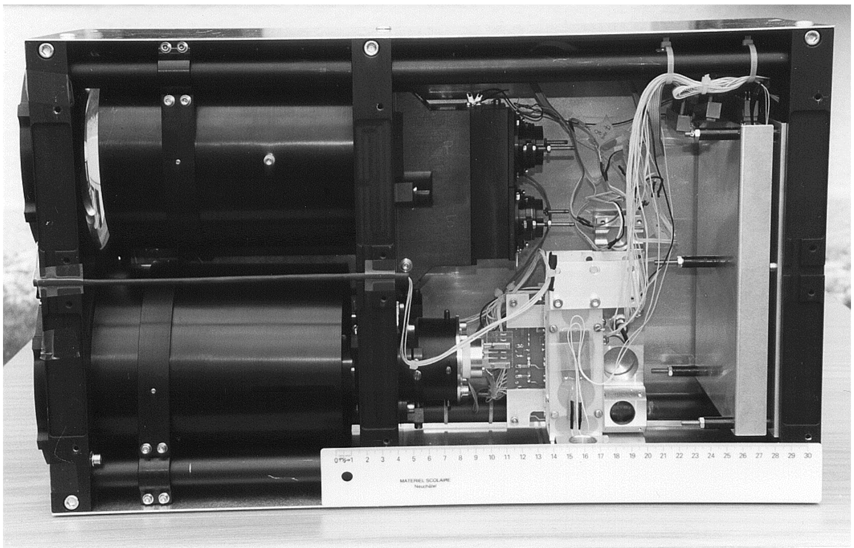

Figure 6.3. *Side view of IR-MAL without cover. The instrument is looking at horizontal direction left. The two cylindrical bodies are the baffles of the receiver (upper) and the transmitter (lower) telescopes. The Al cylinder on the right of the transmitter telescope is the laser diode. The polarisation beamsplitter is in the rectangular body on the right of the receiver telescope. The SPADs are removed and normally attached to this body. The data acquisition electronics is also not present and normally attached to the vertical Al plate on the right face. The ruler at the bottom of the instrument is 30 cm long.*

Mechanical support package

The mechanical support is arranged as a 3D optical bench of three plates, supported in their corners by four rods. The plates and the rods are machined from aluminium, what distributes properly the heat load inside the package. The adjustable holders for the laser, the two SPADs and the lenses are positioned firmly on the plates. Each holder has individually double blocking after the alignment. The electronic boards of the laser diode driver, SPAD bias sources and data acquisition, and the service systems are mounted between the plates on frames. This arrangement in "cage structure" allows secure positioning and holding of the components and compact packaging in a small volume.

All lidar sub-systems – transmitter and receiver optics, detection and acquisition electronics, interface and system supporting electronics – are mounted in a strong box with the required dimensions 51x32x17 cm^3. The box is not hermetically closed. The total weight of the box with the lidar is 12.7 kg, that is slightly less than the allowed limit. Thermal insulation is provided by layers of foam and thin aluminium sheets.

Data acquisition

The detection is performed in photon-counting mode with a resolution of 30 m and 256 range gates. With the optical performances of MAL and since the energy in a single laser pulse is weak, the probability of detecting a single photon from backscatters for one laser pulse is very small. As the deadtime of the SPAD detectors is relatively long (~30 μs; that is in the order of the duration of one sweep, 51 μs*), and the photon arrival frequency low, a simple data acquisition system was assembled.

The data acquisition is synchronised with the laser diode and SPAD switching. For each shot, it detects a single photon, recording its round-trip time. The SPAD starts to detect the backscatter light when it starts to arrive from the layer at 30 m from the instrument. The first 30 m are omitted because they contain laser light scattered from the optical components in the lidar and from the optical shield window. One measurement lasts about 3.4 s and consists of 65'280 laser pulses. This acquisition system is low-consumption, small, light and robust without critical component (this was important for the airborne experiment). Its design was already existing at IKI.

The IR-MAL instrument does not integrate its own computer. A microprocessor included in the acquisition system ensures the acquisition operation. It must be linked through serial line to an external computer. This external computer sends a command to the microprocessor to trigger the acquisition system. After the measurement is over, the microprocessor sends the measured data to the external computer who stores them. During the flight, the external computer is the central computer on board the aircraft. On ground, a laptop or a desktop is used.

Electronics services systems

There are two electronics service systems. The first one is the thermo-stabilisation system. It provides the active stabilisation of the mechanical at –18°C and switching-off of the operation if the temperature is below -30°C. The second one is the power supply board – itself powered by the aircraft electricity supply – that furnishes the necessary DC voltage to the laser diode driver, SPAD bias power supply, data acquisition electronics, and thermo-stabilisation system.

Data correction

As a large number of laser pulses is emitted during a single measurement, 65'280 pulses, a histogram of the round-trip times forms. It represents the range-resolved profile of the atmospheric backscatter with respect to the deadtime of the SPAD and acquisition system. As a first step of the data processing, it is important to correct for this deadtime. This cor-

* This implies that, when the lidar detects one count per laser pulse, the system is saturated.

rection means the transfer of the measured histogram with non-zero deadtime to a histogram with zero deadtime.

As demonstrated in [Bukh94], the expectation value for the elements of the zero deadtime histogram $N_{Z,i}$ (representative for the atmospheric backscatter profile) may be obtained from the measured nonzero deadtime histogram $N_{NZ,i}$, by the following equation:

$$N_{Z,i} = N_{NZ,i} \cdot \exp\left(\mu(1;i-1)\right), \tag{6-1}$$

where

$$\exp\left(-\mu(1;i-1)\right) = 1 - \left\{\sum_{j=1}^{i} \frac{N_{NZ,j}}{N_T}\right\}. \tag{6-2}$$

Here $i=1,2...k$, where k is the number of gates of the acquisition system; N_T is the number of the laser pulses during the measurement.

The application of the deadtime correction procedure is illustrated by Figure 6.4. It shows an example of night-time measurement during the ground-based test of the lidar. Both direct measured histogram, i.e. measured with non-zero deadtime, and its recovered histogram, with zero deadtime, are plotted. Represented are the atmospheric and target response. Both plots differ substantially what denotes how much the deadtime of an acquisition system may deform the real signal falling on a detector and the difficulty to interpret reasonably well the raw data in this case. In the corrected histogram, the signal after the hill response is the noise, mainly of the detector.

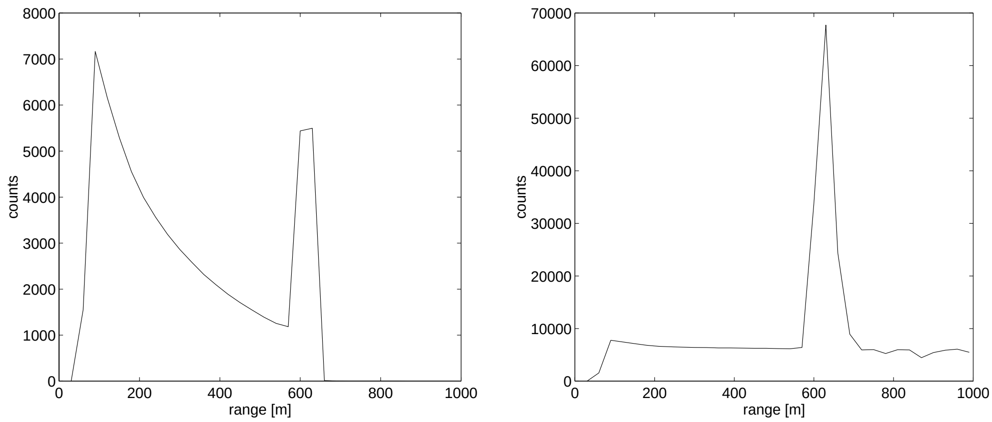

Figure 6.4. *Deadtime correction illustration. On the left is the measured histogram of the lidar backscatter signal from Mountain Chaumont – hill with trees –, while the right plot is the corresponding deadtime corrected histogram.*

6.2.3 Results from measurement campaign

During the test and the scientific APE campaign, IR-MAL showed an excellent reliability and stability of operation. The instrument was operational always when the on-board central computer was operational. This was unfortunately not always the case; the central computer suffered several times from malfunctioning. IR-MAL was aligned before the test campaign; when it came back from the scientific campaign, four months later, it was still aligned, although it had ever been readjusted in the meanwhile. That means both solid mechanical package and adequate vibration isolation of the on-board assembly. No electrical system failures were detected and no component needed to be replaced, even if the temperature of the instrument inside the insulation box went down to –18°C.

IR-MAL proved to be prone to dark count rate. SPAD detectors were much more noisy than expected, with a dark count rate depending on the temperature of the detector*. As consequence, the practical detectable measurement extend during the flight campaigns was limited to 350 m from the lidar. It made impossible to retrieve absolute values for the backscatter coefficient and depolarisation ratio. A shift in the flight campaign planning also increased the proportion of day-time flights, what was a further limitation for IR-MAL operation.

No presence of cloud base was detected in the operational range of IR-MAL. This is consistent with the PSC observations done with OLEX lidar on board the DLR Falcon aircraft, which flights were synchronised with Geophysica. OLEX measurements demonstrated that PSCs were observed around 25 km. This was out of the range of IR-MAL, as Geophysica flew at altitudes of 19-20 km. In-situ instruments too never detected that "Geophysica" flew through a PSC. The absence of PSCs close above to the M-55 flight altitudes determined the shift in the data processing procedure. IR-MAL data were processed for evidences of variation of the background aerosol layer. Practically this was achieved by summing the data of the successive range bins close to the aircraft. IR-MAL was so considered as a backscatter sonde. Removing of the noise component of the signal was partially successful.

Figure 6.5 presents the IR-MAL data in backscatter sonde mode† and comparison with data from FSSP-300 (Forward Scattering Spectrometer Probe, particle counter) for the second scientific flight, performed on 29 December 1996. That day, the aircraft dived from 19 km down to 9 km before ascending again up to 21 km. The upper plot contains the IR-MAL data; the darker curve is the polarised channel and the lighter one the depolarised channel. In the lower plot, the darker curve represents the particle total concentration as measured by FSSP-300 and the lighter one the aircraft altitude.

The dive is visible for both instruments. the For IR-MAL data, it may be seen that the downward trend related to the cooling-down of the detector is still present. This remaining component results from the noise complexity and the impossibility to remove it

* The dark count rate was 260 kHz at 15°C and 150 kHz at –10°.

† Data are corrected for deadtime, for noise (first approximation) and averaged on five successive data sets. A sliding average was finally applied.

totally. Concerning background aerosol, more than tendencies could not be indicated by IR-MAL.

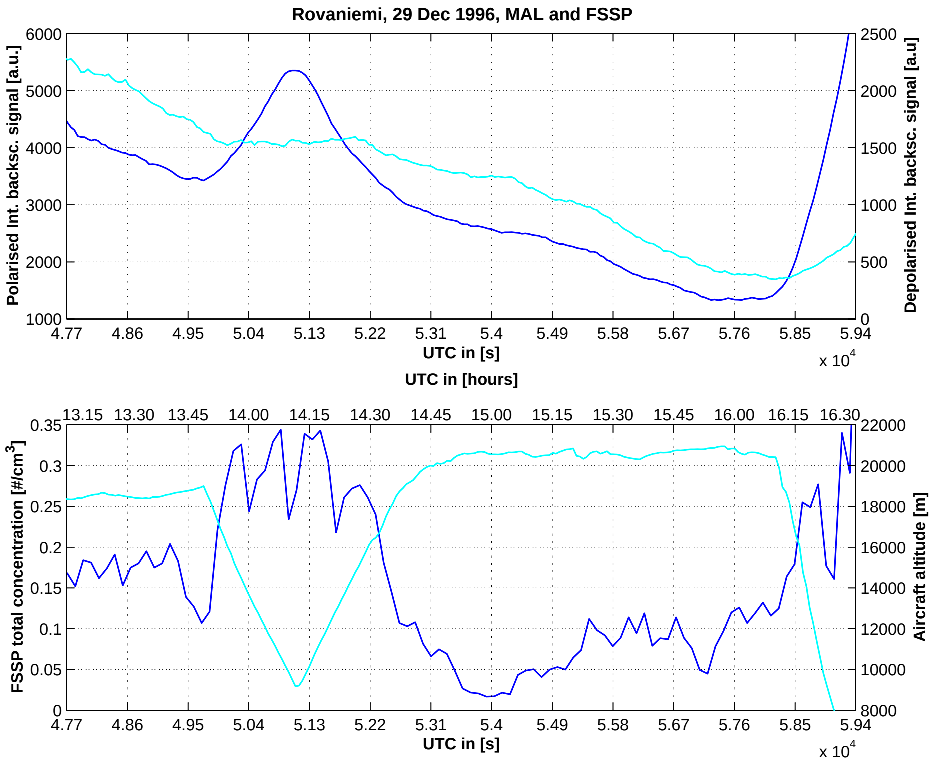

Figure 6.5. *Mission flight, 29 December 1996 in Rovaniemi. In the upper plot are represented the processed backscatter signals integrated over the interval [60, 210] meters. Darker, resp. lighter, curve is the polarised, resp. depolarised, channel. In the lower plot, the particle concentration as detected by FSSP-300 is in darker colour and the aircraft altitude in lighter colour. The dive is marked for both instrument.*

6.2.4 Conclusions for IR-MAL instrument

IR-MAL was the first airborne lidar developed at the Observatory of Neuchâtel. The scientific outputs from the campaign were scarce and object of disappointment. This situation resulted from the unexpected insufficient performances of the detectors and the impossibility of replacing them in time. The campaign was also initially mainly foreseen during night-time, and our optical filtering method chosen in consequence. At the end, the campaign was mostly during day-time, and the instrument not adapted to measure under these conditions. Dependence on an external computer which did not work properly contributed also to dissatisfaction.

Nevertheless, although working at ambient pressure and at low temperatures, IR-MAL showed quite good reliability and stability of mechanical and electrical operations. No parts were damaged. The instrument was also easy to install on board "Geophysica" and to disembark. In anticipation of future upgrade, the development of IR-MAL may be considered as a reasonable first step, contributing a valuable experience.

A non-negligible result of this first airborne mission is that it allowed to learn about the special environment conditions found at high altitudes and the requirements they imposed to stand-alone instrumentation.

6.3 GMAL instrument

6.3.1 Objectives and requirements

The two next campaigns planned for "Geophysica" aimed at studying first the exchanges between the high troposphere and the lower stratosphere in the Tropics and then the Antarctic polar atmosphere at early spring time, when the sun re-appears in this region. To participate to these campaigns, the IR-MAL instrument needed to be upgraded. The requirements addressed to the upgraded instrument are listed in Table 6.3. It shall now operate during day-time also. Its volume and power consumption remain the same. On the other hand, the instrument may be heavier and placed in a pressurised box if necessary.

Requirement type	Objectives
Scientific task	Detection of high-altitude clouds (cirrus, PSCs) and aerosol layers in zenith direction, in the vicinity of the aircraft (up to 2 km), during day- and night-time.
Operation mode	Fully automated; no operation by the pilot during the flight.
	Power supply switched on by the aircraft crew on ground before take-off and switched off on ground after landing.
Environment constrains	Limited dimensions of 51x32x17 cm^3.
	Weight: max. 30 kg.
	Available power: 3 A under 27 V for the whole instrument, instrument heating included.
	Capability to work at pressure down to 50mb and external temperature down to –50°C.

Table 6.3. *Requirements to be fulfilled by the upgraded MAL for post-APE-POLECAT missions.*

6.3.2 Consideration on upgraded instrument

The principle upgrade for IR-MAL is to make it able to measure during daytime. Considering the dependency of the SNR on sub-system parameters (cf. Equation 1-51), two complementary possibilities exist. The first is to use a more powerful laser diode. The used IR pulsed laser diode is already quite powerful for this type of laser. A more powerful one would be larger and have larger emitting area. As consequence, the transmitting optics would be more bulky. Remembering that the total volume should remain the same, this option shall be rejected.

The second possibility is to decrease the detected background radiation component. Two parameters influence directly this component: the filter bandwidth and the field of view of the receiving telescope. Both parameters are on their turn directly related to the laser beam quality: a laser with narrow bandwidth allows to use a narrow-band filter, and a laser with narrow divergence in both direction perpendicular to the laser beam propagation allows to decrease the field of view. Pulsed laser diodes usually show high divergence in one of the two directions. Reshaping the laser beam for narrow divergence complicates the optics and increases the risk of misalignment. Pulsed laser diodes shall so be rejected. On the other hand, they are very reliable, because of their all-solid state character.

All-solid state lasers with good beam quality exist and are even often used for aerosol backscatter lidars. They are diode-pumped Nd-YAG lasers. They are powerful lasers and would be for these reasons good candidate for MAL instrument. However, they show some disadvantages. They usually are of significant dimensions (i.e. much larger than laser diodes and in the order of IR-MAL volume including their driver); they require high current for the pumping diodes (IR-MAL does not have a lot of it at disposal). They traditionally also contain high-voltage parts necessary for the pulse emission (active Q-switch). Use of high voltage should be avoid for IR-MAL, because it is source of electromagnetic fields that may create serious noise problems to the aircraft equipment and to other instruments on board "Geophysica".

Fortunately, at the time we reflected how to upgrade IR-MAL – it was in 1997 –, started to appear on the market a new type of pulsed lasers from the Nd:YAG family, called micro-chip lasers. They are passive Q-switched, of small dimensions, may use low DC voltage and have reduced electrical power needs. Their divergence is of few milliradians. Their pulsed repetition rates are kHz or tens of kHz, and the energy of a single pulse in the order of microjoules (their active Q-switched "big brothers" emit pulses of some millijoules or even joules). A drawback is that their optical power and pulse repetition rate are sensitive to the ambient temperature. That is why some are temperature stabilised (in this case, they require more power and are slightly larger).

The choice of the laser and the other sub-system parameters for the upgrade of IR-MAL were defined after extensive numerical simulations for detection of high-troposphere/low-stratosphere clouds, in conditions of high-optical background. The simulations have been run both at the Observatory of Neuchâtel and at IROE-CNR, Florence. We finally opted for a micro-chip laser with second-harmonic conversion. Such laser allows the use of a narrow-band interference filter, reduction of the field of view and use of low-noise photon-counting PMTs.

As the characteristics of the micro-chip laser beam is quite different from the ones of a laser diode beam, we decided to build a fully new instrument to reach as optimal instrument configuration as possible and not to make changes on IR-MAL. This second generation of MAL instrument is named GMAL for "Green" MAL.

6.3.3 Instrument description

Next follows the detailed description of GMAL. The parameters of its sub-systems are resumed in Table 6.4. The block-diagram of GMAL is presented in Figure 6.6 and a view of the instrument is shown in Figure 6.7.

Mechanical support package

The IR-MAL "cage structure" gave entirely satisfaction both from stability and instrument assembly points of view. The same arrangement has been reproduced for GMAL.

Laser

GMAL is built around a passive Q-switched Nd-YAG micro-chip laser operating at 532 nm. This laser is based on diode-laser pumping with integrated second-harmonic conversion generator and beam expander. The emitted light is linearly polarised and does not need additional beam shaping. This laser has the advantages to be small – its head is a 120 mm long cylinder of 15 mm diameter –, and to have electrical power needs – 1.4 A under 3.3 V DC – compatible with the ones the aircraft may deliver. It is not temperature stabilised and its optical power has to be monitored for later signal normalisation during the data processing. This is done by inserting a piece of glass acting as beamsplitter – due to Fresnel reflections on its surfaces – along the path of the light. While the transmitted part is sent to the atmosphere, a fast dual-element photodiode collects the reflected part. One output signal from this detector triggers the acquisition system while the other is integrated to provide the mean value of the laser output.

Receiver optics

The receiver optics was also redesigned to reach optimal use of the transmitted optical power. The receiver telescope is a refractor consisting of a 50-mm f/4 achromat lens for a focal length of 20 cm. Large f/number is necessary for narrow field of view. The diameter of the receiving lens is limited by the predefined height of the instrument: larger diameter would mean larger focal length. But space shall be left for the detection unit coming after the focal point. A diaphragm placed at the focal plane limits the field of view.

Detection

After the diaphragm, a lens collimates the optical signal and a 0.2nm narrow-band interference filter rejects most of its background light component. The filter is thermally stabilised and isolated so it is not sensitive to temperature changes. The exact temperature has been

Sub-system	Parameter	Specification
Laser	Type	Nd-YAG micro-chip
	Wavelength	532 nm
	Output power	20 mW
	Polarisation, beam depolarisation	linear, <1%
	Beam divergence	0.3 mrad full angle
	Pulse duration	<50 ns
	Pulse repetition rate	11 kHz
Receiver	Telescope type	prime focus refractor
	Effective aperture	50 mm ∅
	Receiver field of view	1 mrad full angle
Filter	CWL, bandwidth	532 nm, 0.2 nm
Detection	Detectors	2 photon-counting PMT modules
	Photocathode effective area	4x20 mm^2
	Dark noise (@ room temperature)	35-160 cps
	Output logic and pulse width	TTL positive, 30 ns
	Counting rate sensitivity (@ 532 nm)	typ. $3x10^5$ cps/pW
Data acquisition system	Type	photon-counting
	Range resolution	10 m
	Number of gates (bins)	1024 (initially 256)
	Duration of a single measurement	6 s (65'280 laser shots)
Full instrument	Configuration and dimensions	single box, 51x32x17 cm^3
	Weight	27 kg
	Current / voltage	max. 3 A / 28 V DC; incl. instrument heating
	Switching mode	automatic through external pressure sensor
	Operation control	continuous house-keeping parameter record
	Safety	against depressurisation, overheating, overcooling

Table 6.4. *Parameters of GMAL lidar sub-systems.*

chosen so the central wavelength of the filter corresponds to the laser wavelength. A polarisation-beamsplitter cube divides the remaining optical signal into two lineary orthogonal polarisations – one is parallel to the laser polarisation (p-polarisation) and the second is perpendicular to it (s-polarisation). The detection is performed by two photon-counting modules. Each incorporates a PMT and high-speed amplifier-discriminator-high voltage power supply circuits in a housing. The modules require only 5 V DC source.

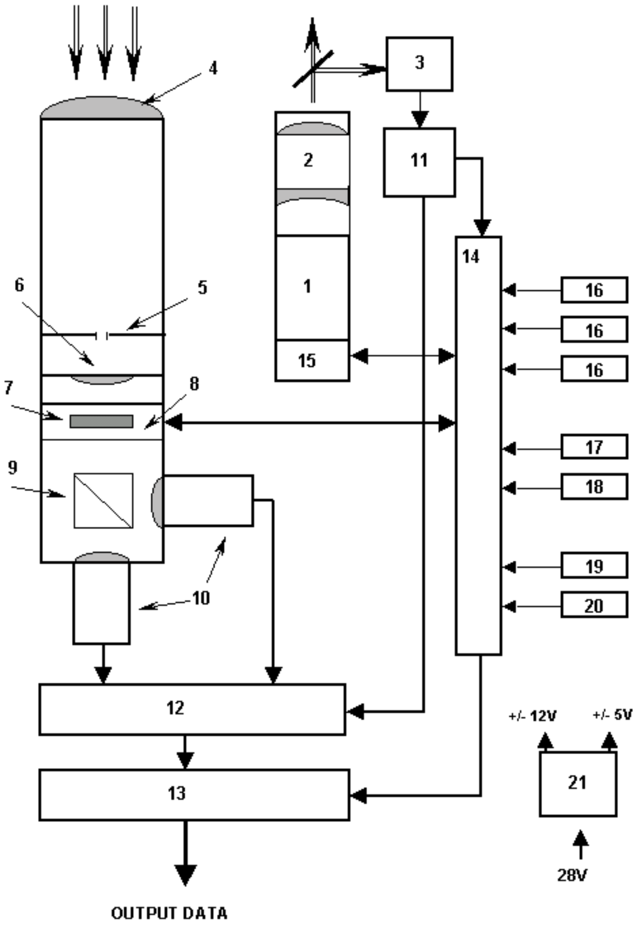

1. Nd:YAG laser with 2nd-harmonic conversion
2. Beam expander
3. Dual-element photodiode
4. Receiver lens
5. Receiver diaphragm
6. Collimating lens
7. Interference filter
8. Interference-filter housing
9. Polarisation beamsplitter
10. PMT photon-counting module with field lens
11. Synchronisation and power monitoring electronics
12. Acquisition electronics
13. Embedded PC
14. House keeping and safety-loop electronics
15. Laser temperature stabilisation
16. Temperature sensors
17. Sensor for pressure inside the pressurised box
18. Pressure switch outside the pressurised box
19. Input voltmeter
20. Consumed current meter
21. DC-DC converters

Figure 6.6. *GMAL block-diagram.*

Acquisition system

The acquisition system is of the same kind as for IR-MAL. It is managed by a microprocessor. Two multichannel-scaler chains count the TTL pulses coming from the detection units. The data acquisition was in a first step performed in 256 gates with a resolution of 10 m, what resulted in a 2.5 km useful range. In a second step, it was upgraded to 1'024 gates for a 10.2 km useful range. For each emitted laser pulse, each gate may count up to 1 event. Considering the optical configuration of the instrument, the bandwidth of the detecting heads, and the proposed scientific tasks at high altitude, this is sufficient. No dead-

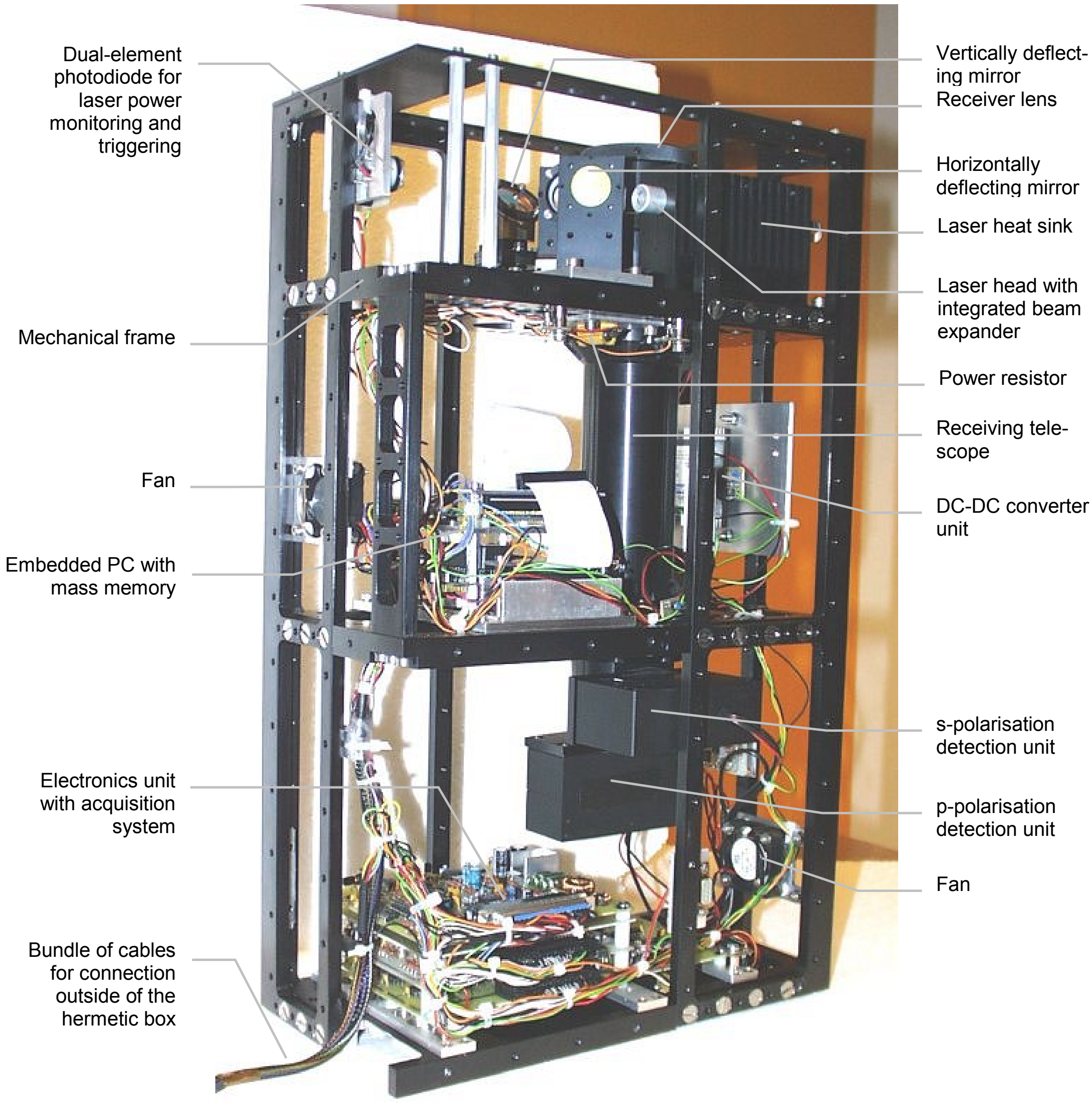

Figure 6.7. *A view of the instrument once assembled and before being placed in its hermetic container*

time correction is necessary as it was the case for IR-MAL, what improves the quality of the data. One measurement contains 65'280 laser pulses and lasts about 6 s. Once it is achieved, the data are downloaded through serial line by the micro-processor to an embedded PC. In turn the latter asks the former to proceed to a new measurement. Each measurement data – also called a "data set" – consists of 4 kBytes. They are in binary format.

Computer

In order GMAL to be fully stand-alone and not to be subject to possible problems that may affect the aircraft central computer as it occurred to IR-MAL, an embedded PC has been integrated in the instrument. It is a 66 MHz PC/104 running DOS and equipped with two 140 MB flash disks – one being as backup. This type of mass memory offer much more reliability under harsh conditions than normal hard disks. Such a memory mass makes the instrument stand-alone operational for more than 55 hours (in 1024-gate final configuration). For unattended computer operation, the watchdog timer feature is a must as well, as it prevents the system from a definitive blocking. The used embedded PC provides also the possibility to use a computer with screen and keyboard as terminal when they are linked through serial line.

Operation protections

In order to avoid low-pressure damages of sensitive components (the laser, the detection units, the embedded PC), the instrument is installed in a 27-litre thermally isolated hermetic aluminium box. This box offers also protection in the conditions of severe humidity and temperature differences. Three power resistors are placed on the mechanical structure of the instrument and act as heaters. Placed on the top of the box, the two windows for the emitted and backscattered radiation are surrounded by two heated baffles that protects them from condensation and freezing, as well as from the scattered ambient background.

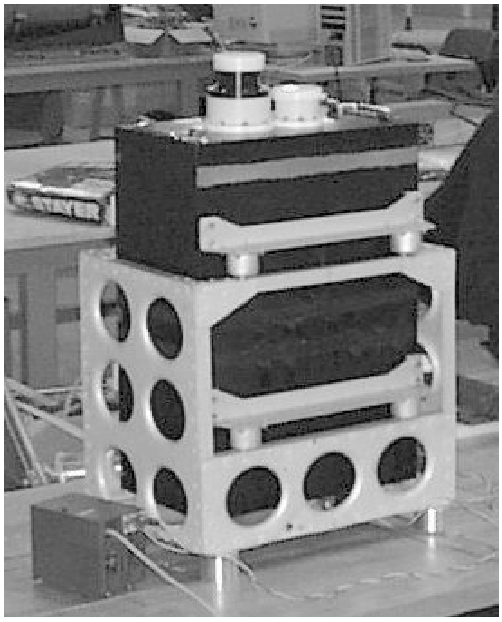

Figure 6.8. *GMAL lidar in its pressurised box and supporting frame for installation. The 24 V DC power supply for ground test is visible on the bottom left corner of the photo.*

Several safety loops have been implemented to avoid or limit damages. In case of overheating, GMAL is temporarily switched off – only basic housekeeping electronics is left operating – until the temperature drops down to an established value. In case of overcooling, only heating resistors are powered until the temperature reaches up again a suitable limit. In case the inner pressure drops below 0.2 atm because the box is no more hermetic, GMAL is also switched off.

When the instrument operates, a set of housekeeping parameters is continuously recorded and saved on the computer: pressure and temperature at various locations inside the box, total driving current, voltage sources. The safety loops do not use the data recorded by the computer, but the ones directly measured. This makes the electronics self-consistent and there is no risk of instrument malfunction due to bugs in a controlling software. We prefer the concept that each part is stand-alone and has a well-defined frame of work. Interactions between various sub-systems are sources of problems. It is better to limit them to the strict necessary.

Operation on board "Geophysica"

On board the aircraft, GMAL stands in a stage called "basket" and is attached to it by eight shock-absorber suspensions, as illustrated in Figure 6.8. The basket itself is attached to the structure of the aircraft, behind the cockpit, as shown in Figure 6.9. GMAL consumes no more than 3 A under 24-28 V DC. Once the power line is made available, usually before the take-off, the instrument switches on and operates automatically after the aircraft reaches a pre-selected altitude with pressure of 0.5 atm. If the aircraft descents again below this altitude, like before landing, GMAL switches off. As GMAL does not need special assistance or preparation before the flight, except the power line to be made available on

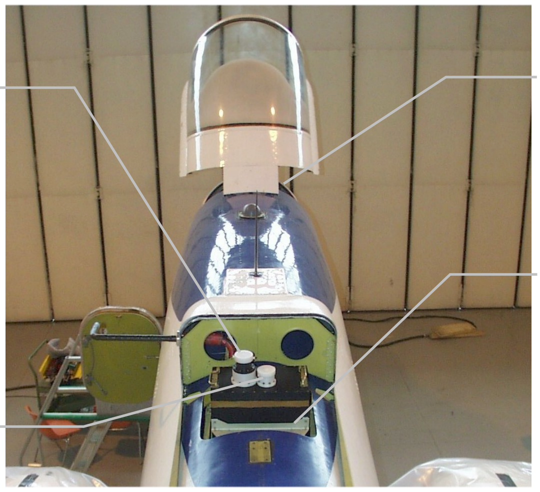

Figure 6.9. *GMAL instrument installed on board the "Geophysica" aircraft*

ground, it offers real autonomy for 55 hours. This automatic switch is also particularly convenient for the pilot who does not have to take care of the instrument when flying.

When the instrument switches on, the computer boots and automatically controls the data acquisition. Data sets are acquired indefinitely until the computer switches off, that is, under normal conditions, when the whole instrument switches off. In case the computer reboots by itself (watchdog function) the measurement process restarts automatically. In order not to loose data in case of computer problem or power supply interruption, data are written on the hard disk as soon as they are acquired and not stored in volatile memory. This process occurs after each single data set acquisition of 6-second measurement duration. Data are downloaded on ground through parallel line to a laptop PC. This laptop acts also as terminal for the embedded PC.

6.4 Quick data look and data quality control

As already mentioned, each 6s a data set is created. About 600 data sets are then recorded per measurement hour. In average, 3000 data sets are recorded during a single flight of five hours. It is not possible to check manually each single data set. For this reason a software for fast data overview and data quality control has been realised (MATLAB environment). The status of the instrument during flight is first analysed. Then measured data are successively averaged, corrected for background radiation and for the range. Their quality is further controlled. Noisy or doubtful data are rejected.

6.4.1 Housekeeping parameters

After a flight, before looking on the measured data, it is necessary to examine how the instrument worked and if problems have been encountered. Housekeeping parameters are automatically recorded for each data set. Figure 6.10 is an example of the evolution of the housekeeping parameters during a flight.

The laser power is recorded as it depends on the laser temperature. It is necessary for further data correction and comparison. The laser pulse repetition rate is monitored but is not of direct interest. The current is the current consumed by the whole instrument. It is a control for the filter temperature stabilisation and the heating of the instrument. The temperature is measured at four different places: at the three stages of the "cage structure" and in the vicinity of the electronics boards. The four DC voltages necessary for the different sub-systems of the instrument are also recorded. The measured pressure is the pressure inside the hermetic box. This allows a leakage leading to depressurisation to be recorded. Fortunately this has ever happened up to now. The relative time since the start of the

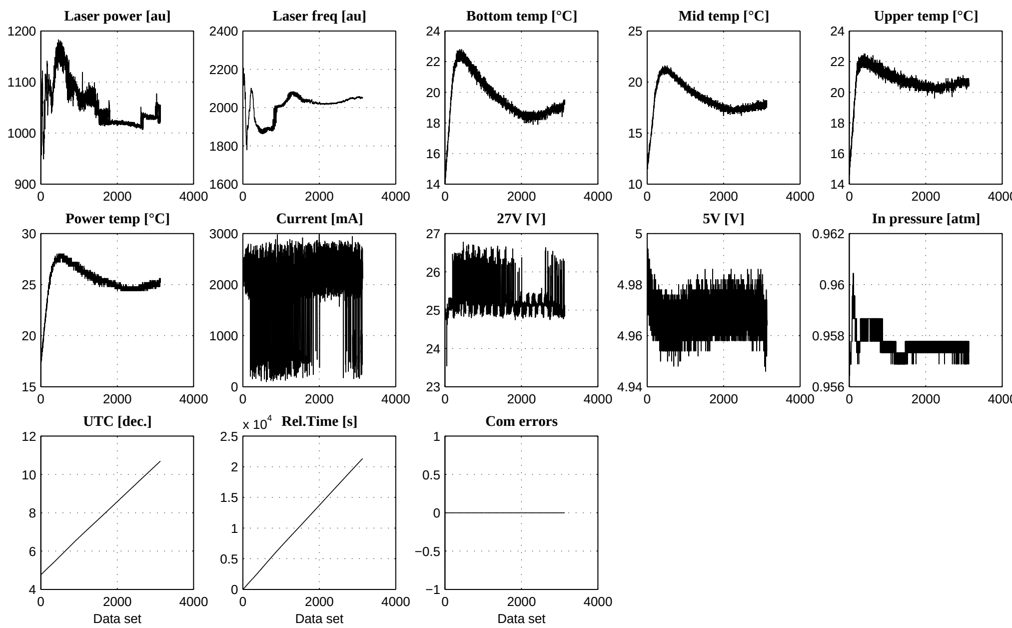

Figure 6.10. *Example of the housekeeping parameters as recorded during a flight*

measurement allows to check the duration of each data set. Each time the computer reboots, the time origin is set to zero. In such a way, the number of times the computer reboots is so directly determined. Before each flight, the clock of the computer is checked and readjusted if necessary. By convention, UTC time is used by all instruments on board "Geophysica". Comparisons between data measured by different instruments as correlations with the aircraft flight parameters are possible through this parameter. The number of communication errors during the data transfer from the acquisition system to the embedded computer is registered too.

6.4.2 Data average

Averaging several successive single profiles improves the quality of the data. Grouping the profiles by M means that profiles 1 to M are averaged together and result in one averaged profile; profiles $M+1$ to $2M$ result in another averaged profile; etc[*]. The same type of average may be performed on the bins (samples) of a profile ("binning" operation). If N is the number of bins to be averaged, the SNR improves by factor $\sqrt{M \cdot N}$ [†]. The price to pay is lower resolution for time evolution (if $M>1$) and lower range resolution (if $N>1$). Further we will refer to the factor $M \cdot N$ as "average order".

In the averaging process, the fluctuations of the noise diminish and the background noise may be better estimated. This is the reason why we prefer to bin- and profile-average before computing the noise offset. We also prefer to work with averaged data than summed data because direct comparison is easier. For instance, signals computed with different average orders can be compared with each other; two signals obtained during different flights may also be directly compared.

6.4.3 Background correction

As the acquisition is performed in photon-counting, the recorded signal consists in the backscattered signal, the quantum noise, and the background radiation component[‡]. As the duration of a sweep (response to a single laser pulse) is short, 68 µs, the background component may be considered as fluctuating around its mean value (also called simply "offset") during a single sweep. As consequence, it also fluctuates around its – integrated – mean

[*] "Sliding average" is another way to proceed. In this case, profiles 1 to M are averaged, then profiles 2 to $M+1$, and so on. By experience, this kind of average may be dangerous, because a single initial profile may contaminate several resulting profiles and create artificial signals. If, for instance, at a given altitude, there is a peak due to noise in one of the initial profiles, this peak will spread now in the M resulting profiles that use this initial profile to be computed. The broadened peak may be interpreted as a real signal of a given duration. What is actually wrong.

[†] Several couples of M and N are possible for a same factor. The choice of M and N depends on the type of resolution that shall be emphasised, temporal or spatial.

[‡] We omit the dark noise in order to simplify the explanations. In photon-counting mode, if a low noise detector is used, the background radiation component is much larger than the dark noise (apart for very dark night cases) and it may be neglected or considered as part of the background noise.

value for a single data set, which is obtained by summing the responses from 65'280 laser pulses. The offset may have a different value from one sweep to another (e.g. if the background radiation level changes); nevertheless it remains constant over the full profile. This offset shall be computed and removed from the raw profile in order to get only the backscattered signal profile and process further the data. The next correction to be operated on the signal is a multiplication by the square of the range (range-correction). The offset shall be carefully estimated, otherwise "parabolic-shape" feature will appear

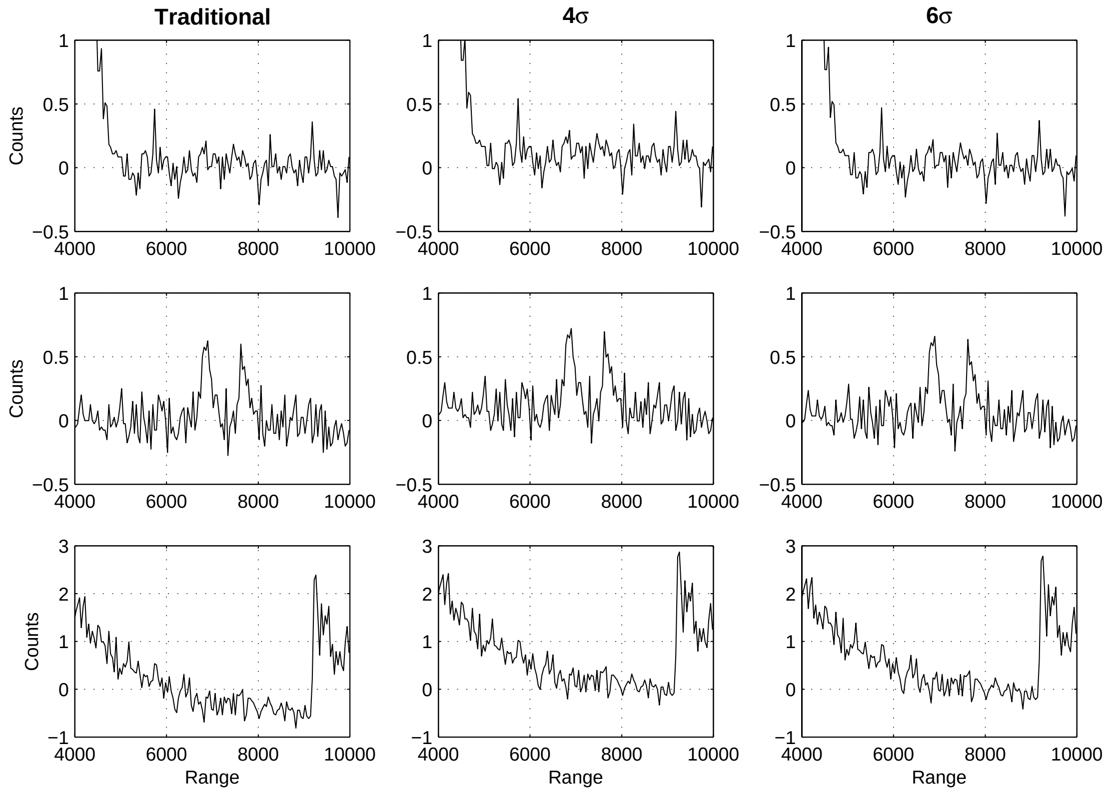

Figure 6.11. *Three types of background correction (columns) applied on three different profiles (rows).*

The sweep duration is usually chosen so that its last portion consists in only the background component. It corresponds to ranges far enough so the backscattered signal is about zero because the beam is totally extincted. On this portion, the mean value is then computed; it is equal to the mean background component. This offset value is further subtracted from the whole profile. As result, the final portion of the profile fluctuates around 0. This is the traditional method to calculate the mean background component.

Our acquisition system covers 10 km (more precisely 10.24 km). We choose the region from 7 to 10 km to compute the background noise (later simply called the "background region"). The results obtained by the traditional method applied to three different signals measured by GMAL are shown in the first graph column of Figure 6.11*. The first

* These profiles have been obtained by averaging 10 data sets and 4 samples. They represent thus one-minute measurements with a resolution of 40m.

4 km are not shown in order to emphasise the small signals of the profile tail. The upper profile was measured from the aircraft at high altitude. For ranges above 5.5 km there is only noise. The second profile was also measured from the aircraft. The signature of a two-layer cloud emerging from the noise is visible. The third profile is from a ground measurement. The negative exponential part of the signal is the signature of the molecular atmosphere, while the bump at the very end of the profile is due to a cirrus. In the first case, the fluctuations are symmetrically distributed around 0. In the second case, the part after the cloud layers is slightly distributed below 0. In the last case, it is obvious that the calculated offset is really over-estimated. For the two last case the offset is over-estimated, slightly for the second case, really too much in the third case. The reason is the presence of the clouds (and of the molecular atmosphere in a lesser extend), which increases the offset values.

We developed an algorithm to take into account the presence of cloud layers in the interval where the background offset is computed. We first find the three minimal points of the background region and compute the mean value of them. This mean value, B_0, represents the lower limit of the fluctuations of the background component. It is a first approximation of the mean background offset B. The fluctuations F due to B may be approximated by the fluctuations F_0 that B_0 would induce. As the background signal obeys Poisson distribution characteristics, the standard deviation $\sigma(F_0)$ of these fluctuations is equal to the square root of B_0 divided by the square root of the average order*:

$$\sigma(F) \approx \sigma(F_0) = \sqrt{B_0} \big/ \sqrt{M \cdot N} \ . \qquad (6\text{-}3)$$

For large statistic, Poisson distribution is approximated by Gaussian distribution. That is to say, the background fluctuations are Gaussian distributed. It results that the interval given by $[B_0\ , B_0+6\sigma(F_0)]$ contain about 99% of the background data†. All data not contained in this interval – they are so larger than $B_0+6\sigma(F_0)$ – are with very high probability not purely due to the background radiation but include also some backscattered signal. In second approximation B is computed as the mean value over all data contained only in the interval $[B_0\ , B_0+6\sigma(F_0)]$.

The results obtained by this algorithm are applied to the same previous profiles and are presented in Figure 6.11 in the third graph column. In the second column are reported the results obtained when considering 4σ instead of 6σ. Let's discussed the first profile. With 4σ, the offset is under-estimated. The reason is that larger noise fluctuations have not be taken into account in the calculation of the mean value. In the case of 6σ, we retrieve the save value as for the traditional method. This justifies the approximation of the background noise by Gaussian distribution. The same remark for 4σ is valid for the two-layer cloud. For 6σ, the offset value is slightly smaller, as the cloud does not contributes any more to the offset computation. The noise distribution on interval 8-10 km is now symmetrical. For the cirrus detected from the ground, 4σ gives a more realistic value for the

* The average order would not be present if we had worked with summed values instead of averaged values.

† This is not totally exact because the distribution of the fluctuations F_0 is slightly different from the one of F as B_0 is slightly different than B.

offset than 6σ . The reason is that $B_0+4\sigma$ is a better approximation for the upper limit of the noise fluctuations as the molecular atmosphere still contributes to the signal. However 6σ already improves sensitively the situation. From these discussions and results, we decided to process our data with 6σ.

The choice of taking three points to compute the minimal mean value at the beginning of the procedure is a question of balance. It allows to obtain a reasonable value which is not too singular: not too small and not too large.

6.4.4 Range-correction

In Chapter 1, we have seen that the lidar response function is inversely proportional to the square of the range. For a first analysis of the data and later to retrieve optical properties of the detected targets, the signal must be corrected for the range. This is done by multiplying the background-corrected signal by the square of the range. By this straightforward operation, the dynamics of the range-corrected signal is lower. Graphic visualisation of a measurement is this way also easier.

6.4.5 Data quality control on SNR criteria

A first selection of the data is operated on the criteria of the SNR. Once the background component B has been computed and the backscattered signal S obtained, it is possible to calculate the SNR of the signal for each data point. Data for which the SNR criteria is not fulfilled are discarded. The theoretical criteria is

$$\mathrm{SNR} = \sqrt{M \cdot N}\,\frac{S}{\sqrt{S+B}} > 1\,. \qquad (6\text{-}4)$$

In practice, we rather use an empirical criteria given by

$$\sqrt{M \cdot N}\,\frac{S}{\sqrt{S}+\sqrt{B}} > 1\,. \qquad (6\text{-}5)$$

The single fluctuations are considered instead of the fluctuations of the overall detected optical signal. As the sum of the former is larger than the latter, more weight is attributed to the noise.

Figure 6.12 shows a ground-based measurement on 22 December 1999. Data have been corrected for background noise*. The range is the distance from the instrument. Two layers of clouds seem visible, around 6 km and at 9-10 km. The layer above the instrument is the PBL. Data not submitted to the SNR criteria are plotted on the left, data submitted to the criteria on the right. In this case, data with SNR < 1 have been removed. From the

* They also have been range-corrected for clearer visualisation but this is of no important for the present purpose. When submitted to the SNR criteria, data have not yet been range-corrected.

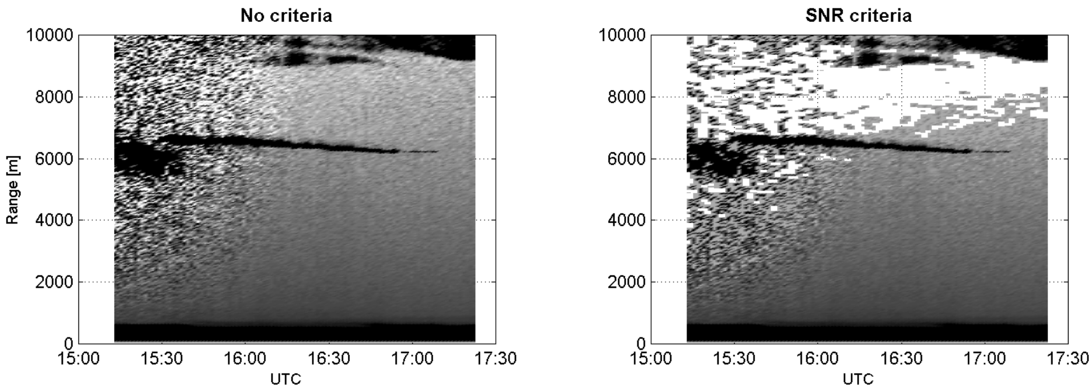

Figure 6.12. *Example of ground measurement. For the left plot, the SNR criteria has not been applied to the data, while it has been for data of the right plot.*

left plot, we may estimate that the sunset was at about 16:15 UTC; at high altitudes, the white-dark-grey "mosaic structure" changes to veiled grey. This "mosaic structure" is typical for a background noise level much larger than the backscattered signal (after sunset, it vanishes as there is almost no more background.); it reveals the fluctuations of the background noise. Even after application of the SNR criteria, this structure is still present, like for instance at altitudes below and above the lower cloud, around 15:30 UTC. It means that the SNR criteria is not sufficient. Among the remaining data, some are noise with sufficiently high value to fulfil the SNR criteria. It might have been possible to set a higher threshold for the SNR, like 2 instead of 1. Yet, we observed in this case that some valid signal disappeared.

6.4.6 Detection probability filter

Noise data that meet the SNR condition correspond to false detection. We developed a detection probability filter – called also "neighbour filter" – which algorithm evaluates if data have high probability to be real signal or low probability, in which case they are rejected. The principle is to analyse the immediate vicinity of each data. The data of a measurement may be thought as the element of a matrix; the columns are the single profiles, while the rows correspond to the bins, representative of a given altitude. Data have high probability of being real signals if the number of neighbouring data which meet the SNR criteria is large. On the contrary if a data is isolated, it is very likely noise. Neighbours of an element are the element on its left, the element on its right, above it and below it[*].

Data are filtered in three phases – more exactly the neighbour filter is applied three times successively. First they are rejected if they have two or more neighbours that did not satisfy the SNR criteria[†]. We speak of "neighbour threshold of order 2". Then, on the obtained data, the filter is applied again with neighbour threshold of order 3 (rejection if three

[*] This is valid for the elements in the centre of the matrix. The elements in the corners have two neighbours, those of the borders three.

[†] The situation is adapted for corner and border elements.

or more neighbours have already been rejected). Finally the filter is applied a third time with a neighbour threshold of order 4. The number of successive applications of the filter and the corresponding neighbour threshold orders have been determined empirically to get optimised results.

As example, the probability detection filter has been applied to the data of the previous example that met the SNR criteria. The results of the successive phases are shown in Figure 6.13. The upper left plot (N2) is obtained after application of phase 1 (2 neighbours). The upper right plot (N2+N3) results from phase 2 and the lower left plot (N2+N3+N4) from the last phase. The lower right plot is obtained by applying successively twice the filter with neighbour threshold of order 3 on the initial data (i.e. the data meeting the SNR criteria).

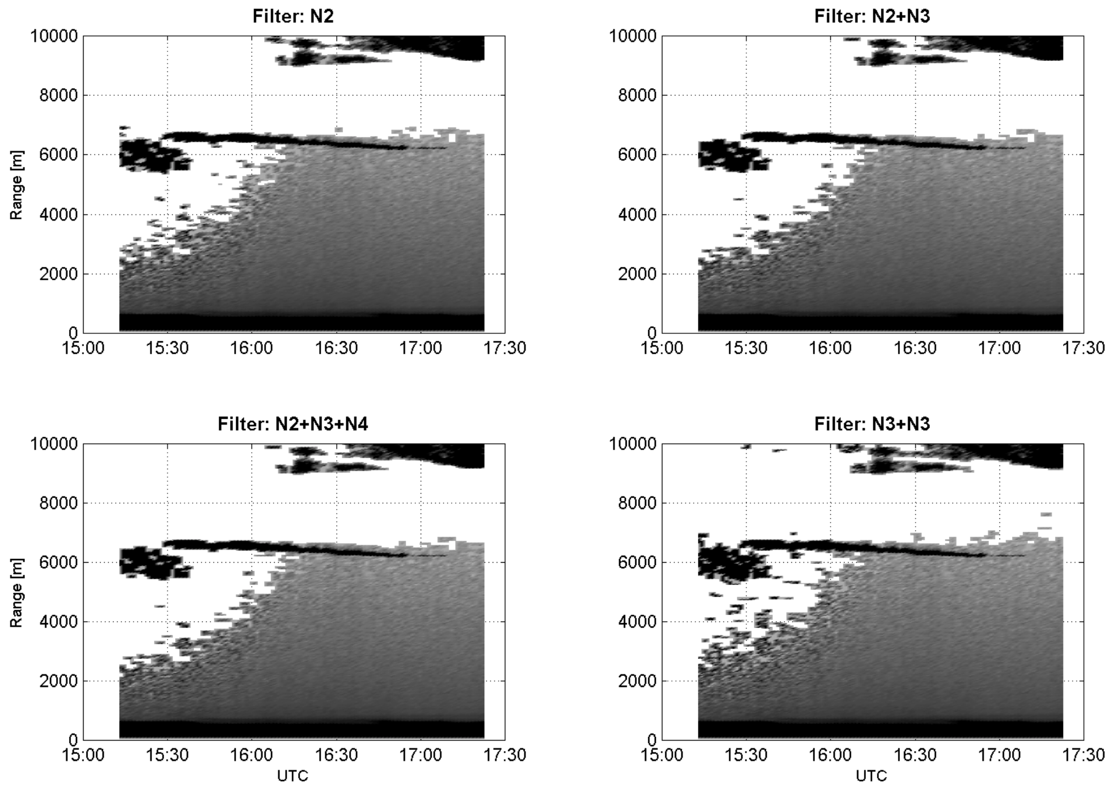

Figure 6.13. *Illustration of the application of the detection probability filter based on the analysis of the neighbouring data. Initial data are the data of the previous figure that meet the SNR criteria. N2, N2+N3, N2+N3+N4 are the results obtained from the three usual successive applications of the filter. The lower right plot is for comparison only. It is obtained by applying twice the filter with neighbour threshold of order 3 on the same initial data.*

It may be seen that a single application of the filter with neighbour threshold of order 2 dramatically improves the rejection of noisy data. The next application refines the rejection, while the last application has almost no effect. Our final result shown in the lower left plot is much more clear and easy to interpret. The "mosaic structure" is no more present, and the transitions from one data to another are no more sharp. This continuity is indirect evidence for better data quality. For instance, it is expected that, when the sun gradually disappears, the molecular atmosphere is detected from higher and higher altitude.

Initial application of the filter with a strong condition, neighbour threshold order of 2, might erase numerous valid data. This is not the case. All atmospheric features that could be guessed from the uncontrolled data (cf. Figure 6.12, left plot) are clearly present. For comparison, the result obtained from a weaker initial condition, threshold of order 3 repeated twice, is also shown in Figure 6.13 (lower right plot). Looking at the shape of the high-altitude cirrus, we see that some small details have been removed with threshold order 2, although they are likely real signals. However, starting with threshold of order 3 leaves more spots which are likely false detection (cf. data in presence of daylight). We prefer the situation with stronger initial threshold, because data are more secure.

SNR criteria and neighbour filter operations are tightly linked. They shall be considered as two successive step of a larger procedure called data quality control. We point out that during this procedure the data are not processed at all, in the sense that their value does not changed. We only sort the data out, selecting the "good" ones and removing the "bad" ones.

6.4.7 Depolarisation ratio

In order to computer the depolarisation ratio (cf. Chapter 1 Section 1.3.7), the relative sensitivity between the *p*- and *s*-polarised channels* shall be known. It has been measured that channel *p* is 1.40 times more sensitive than channel *s*. We determine the (volume) depolarisation ratio as the ratio between the noise-corrected *s*-signal and the noise-corrected total signal (i.e., the sum of *s*- and *p*-polarisation signals. Cf. Equation (1-68), with K_d=1.4). The aerosol depolarisation ratio may be also computed from the volume depolarisation ratio [Cair99].

6.4.8 Backscattering ratio computation

The next step in the data processing is the computation of the volume backscatter coefficient or volume backscatter ratio (cf. Chapters 1 and 2). For optically very thin layers, like aerosol in the stratosphere, the extinction of the laser beam may be neglected. The backscatter coefficient is then directly proportional to the range-corrected signal (cf. "lidar equation" in Chapter 1). It is however necessary to define the instrument calibration factor which links the atmospheric signal with the detected signal.

The temperature and pressure outside the aircraft are measured by the aircraft instrumentation and by other embarked scientific instruments. So, for each flight, the molecular atmosphere density profile along the flight path may be computed†. From the averaged, range-corrected lidar signal profile measured in the polarised channel, we select

* Further, the *p*-, resp. the *s*-polarised channel (parallel, resp. perpendicular, polarisation) will be called "polarised", resp. "depolarised" channel.

† Above the maximum altitude reached by the aircraft, the molecular atmosphere is extrapolated using an exponential function.

points during the flight where only pure molecular atmosphere is present. As the molecular profile is known, the profile calibration constant for the polarised channel may be retrieved. The sensitivity ratio between the p- and the s-channel being known, the profile calibration constant for the depolarised channel is also known. Once this correction is done, the *p*- and the *s*-signals are added and divided for each altitude by the corresponding molecular density. This way an approximation for the backscatter ratio profile is obtained (cf. Chapter 2, Section 2.1.3). The atmospheric extinction is assumed negligible, what is a reasonable approximation for those altitudes. There is also no correction for the Rayleigh depolarisation.

Conclusion

Building a compact automated airborne lidar is not a trivial task for at least three reasons. It shall be first compact because the volume at disposition of the instrument is limited. Then the instrument shall be installed and working on board an aircraft. It has so to work in demanding environment conditions: low pressure and temperature, shaking and vibrating platform. Finally it shall work unattended. The power line is made available on ground before the flight; then, all operations shall be automated.

A first version of a compact automated depolarisation elastic backscatter lidar was developed at the Observatory of Neuchâtel. It was built around an IR pulsed laser diode. It aimed at short range measurements (up to 2 km) of clouds and aerosol layers during nighttime only. This instrument was non pressurised. Its operational behaviour on board the high altitude research aircraft "Geophysica" was excellent. However, due to detectors of unexpected poor quality, measured data are of low scientific values.

Based on the experience acquired with this IR instrument and gained during a first measurement campaign, a second version was developed and built around a 532nm microchip laser. Its was designed using the simulation software presented in Chapter 3. It is installed inside a hermetic box and protected again potential damages resulting from malfunction by several safety loops. It replaces the previous instrument on board "Geophysica"; yet its objectives are the same, but for day-time also. The instrument participated with success to several airborne campaigns and shows capabilities for ground-based operation. Results will be presented in the next chapter.

During campaigns, it is highly recommended to have in hand a tool for fast evaluation of the measured data in order to react rapidly if necessary. A software for fast data look and quality control has been developed. The procedure for the quality control is executed in two steps. Data are first selected on the criteria of their SNR. They pass then through a probability detection filter which estimates the level of false detection.

Remark

We have been continuing the upgrading of IR-MAL instrument. The laser diode is now thermally stabilised and a 12 nm bandwidth interference filter with 65% transmission is used instead of the colour cut-off filter. Background noise rejection is thus higher. The laser pulse repetition rate has been diminished to increase the maximal range from 8.5 km to 13.5 km. The Czech SPADs have been replaced by TE cooled SPADs. The latter have physical area of 500 μm and sensitive area of 400 μm, with quantum efficiency of about 30% at the laser wavelength. Their dark count rate is of the order of 1'500 s^{-1}. Due to their larger sensitive area, the field of view of the telescope is now larger than the laser beam divergence. Consequently, the part of the atmosphere illuminated by the laser diode is fully visible to the detector and no more partially. Preliminary night-time measurements show that the overall instrument efficiency dramatically improved.

Chapter 7

Airborne campaigns and measurements from ground

Introduction

In the previous chapter, the lidar GMAL has been described in details. For the record, it is a compact, fully automated depolarisation elastic backscatter lidar. It detects the backscattered signal following two orthogonal linear polarisations, parallel and perpendicular in respect to the polarisation of the laser beam. It is deployed on the high-altitude research aircraft "Geophysica" and its purpose is to detect clouds and aerosol layers at close ranges above the aircraft.

GMAL participated recently to three campaigns. Section 7.1 is an overview on how the instrument operated. Results from the ETC test campaign carried in Italy are presented in Section 7.2. Section 7.3 is dedicated to a tropical mission in the Indian Ocean for the study of transport and clouds around the tropical tropopause (campaign APE-THESEO). The third campaign, APE-GAIA, took place during last austral spring-time; it was planned to investigate the Antarctic polar stratosphere. During this last campaign, a second instrument similar to GMAL, but nadir-looking, was installed for the first time on board "Geophysica". Results from the campaign are presented in Section 7.4. Finally, low troposphere measurements performed on ground by GMAL are reported (§ 7.5). They demonstrate that potentialities exist for ground-based operation with such compact instrument.

The results presented here are mostly background- and range-corrected signals. Some are more elaborated, and optical properties (volume backscattering coefficient and extinction coefficient, cf. Chapter 1) have been retrieved. We do not intend to discuss deeply their scientific contents. As these campaigns have been made recently, much more time is necessary for this task. Our purpose is to show that valuable and useful data may be obtained by GMAL both from airborne and ground-based measurements.

7.1 Overview of the airborne operations

The assembly of GMAL finished in October 1998. The instrument was aligned and tested in November 1998. Since December 1998 till October 1999, this lidar installed on board "Geophysica" participated to three campaigns in different parts of the world. They are listed in Table 7.1. In total, it performed 31 flights for a total of 125 hours. The duration of the flights varied between 2 hours and 5 hours 40 minutes. GMAL took part in all of them. It showed only one operational failure in one of the flights, due to a computer hardware problem. During the remaining 115 hours of flight time GMAL was switched on, it accumulated data during more than 107 hours, while it was overheated and therefore not acquiring for the few other hours. It was usually tested before each flight, but it was also left in stand-alone operation for several successive flights – up to four. No misalignment was observed during any of these campaigns. The instrument was re-aligned only once between the tropical and the Antarctic campaigns. GMAL was also used on ground for several tens of hours. No failure of any type was observed.

Campaign	Aims	Location	Period
Extensive test campaign (ETC)	Tests of "Geophysica" with payload and of the individual instruments	Forli (Italy)	Mid-December 1998 – mid-January 1999
APE-THESEO	Transport and clouds around the tropical tropopause	Mahe (Seychelles)	Mid-February 1999 – mid-March 1999
APE-GAIA*	Chemistry of the Antarctic stratosphere and air-mass exchanges	Ushuaia (Argentine)	September – October 1999

Table 7.1. *Airborne campaigns to which GMAL instrument participated.*

7.2 Test campaign ETC

During December 1998 and January 1999, in prevision of scientific missions, an Extensive Test Campaign (ETC) took place in Forli (Italy). "Geophysica" performed six flights. The goals of this campaign were the following: to test the status of the aircraft in flight and for different payloads; to check the performance of the instruments; to check the compatibility between them and with the aircraft. For this campaign, GMAL was in the 256-gate configuration. As the range-resolution is 10 m, the maximal range of the instrument was 2.56 km.

* A second GMAL, GMAL2, participated to this campaign. It is nadir-looking, not zenith like GMAL.

7.2.1 Cloud detection

Figure 7.1 is an example of how the signal measured by GMAL may develop during a flight, in this case the 1st ETC flight carried out on 16 December 1998. Each five raw data sets (profiles, single measurements) of the *s*-polarised* channel are plotted with 20 m resolution†. A data set is created each 6s, what is the result from 65'280 laser pulses. The range extends from the aircraft (the flight altitude is considered as "zero-altitude" for the lidar profile) toward the zenith. On that day, Geophysica almost constantly climbed up to 20 km

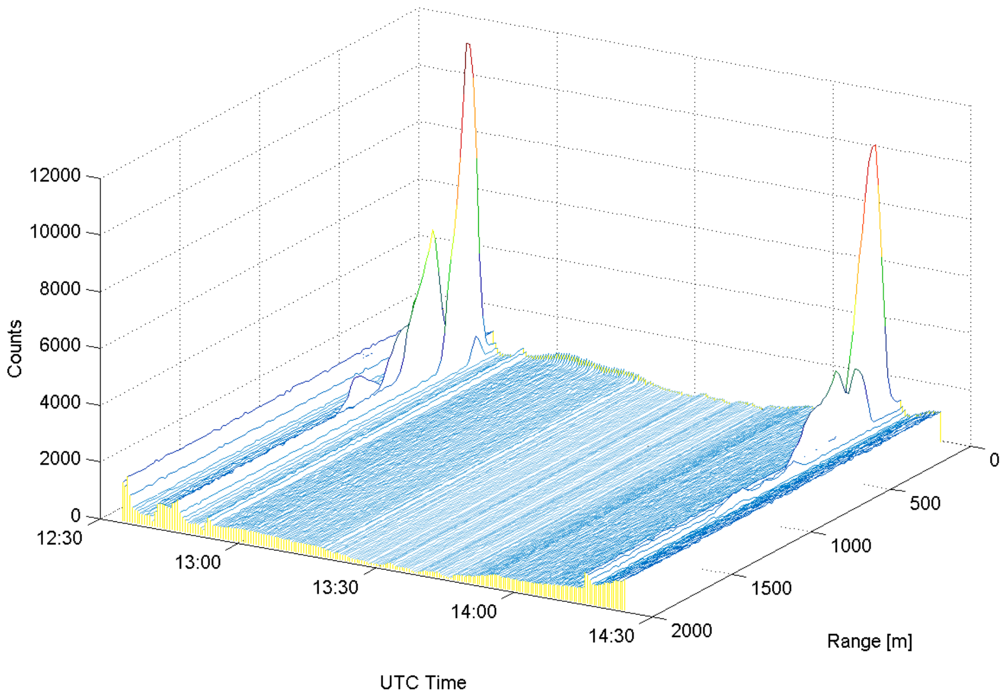

Figure 7.1. *Example of a all-flight development of the measured depolarised backscatter signal Forli, 1st ETC flight, 16 December 1998. Each five raw data set is plotted with 20-m resolution. Maximum reachable value per data set and per gate is 65'280.*

altitude and went down again. GMAL detected cirrus at 10-11km altitude during the ascent and descent of the aircraft. During the ascent, the cloud is detected closer and closer and then passed through while the reverse happens during the descent. As the sun is not high in the sky in Europe in December, the dependency of the background noise in function of the molecular density is clearly visible, as well as the increase of its value when flying below a cloud. Just after "Geophysica" penetrated and came out from the first cloud, a slight signal started to appear in the first gate. It disappeared half an hour later. Our interpretation is that the inner surface of the protecting aircraft window started to freeze and that this frost evaporated some time afterwards.

* Further, the p-, resp. the s-polarised channel will be called "polarised", resp. "depolarised" channel.

† This is the minimal range resolution actually used for GMAL. Even if 10 m is achievable, it has few meaning for the atmospheric observations the instrument shall record. Decreasing the range resolution allows to increase the SNR. As the aircraft flights at about 200 m/s, it is better to decrease the vertical range resolution than the time resolution (horizontal resolution).

Single profiles of the descent portion of the same 1st ETC flight are displayed in Figure 7.2. They are corrected for background. The integration time is again 6 s for the presented measurements. The profiles with lighter colour were recorded at 14:14:34 when the aircraft was in the cloud-free (i.e. molecular) atmosphere at 11.5km altitude. The profiles with darker colour were measured 90 s later at 10.4 km, i.e. when the aircraft was below the cloud. The signal from the cloud-free atmosphere is practically absent, what shall be expected from the Rayleigh (molecular) backscatter. The cloud response for the depolarised channel (*s*-signal) is very well pronounced, what indicates that this cloud contained ice-particles (cirrus). The depolarisation ratio for this cloud is 30-35%.

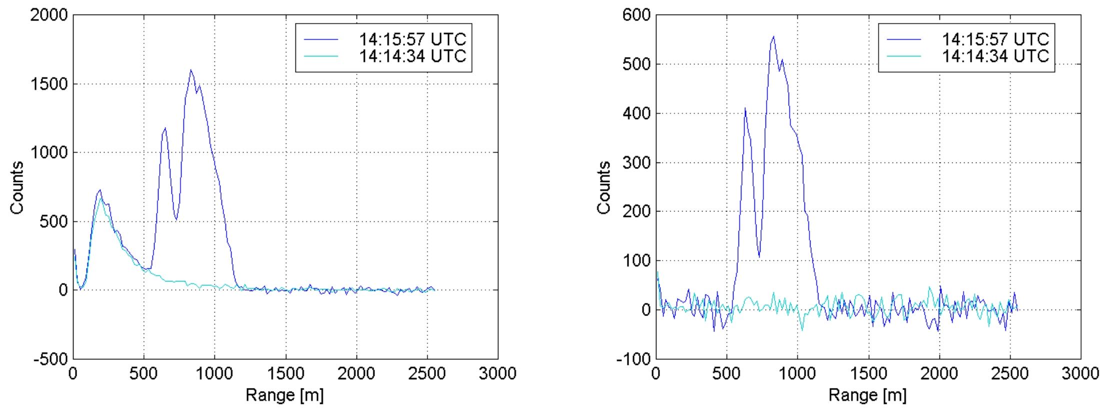

Figure 7.2. *Single raw profiles measured during the descent portion of the 1st ETC flight by the polarised, resp. depolarised, channel, and plotted in the left, resp. the right, pane. The lighter curves were measured in the cloud-free atmosphere; the darker ones, 90 s later, when the aircraft went down below a cloud.*

Another example of crossing a cloud during the ascent is given in Figure 7.3. This event occurred during the 6th ETC flight, on 3 January 1999. Here all single successive data sets of 6 s duration are reported for the polarised channel and the depolarisation ratio. The range resolution is 20 m. The two upper plots and the lower left plot are the same data visualised in different ways. The data have been corrected for background and range. In the upper left pane, the data are plotted versus time and range; they are not corrected for the flight altitude. The colour show the intensity of the corrected signal*. Yet they have been submitted to data quality control (SNR criteria and filter for probability detection). Data below 200 m range are not considered for the overlap function is not unity (i.e. the telescope does not see the whole area illuminated by the laser beam). In the upper right pane are plotted all range-corrected data. The quality control was not applied. Single profiles are visible in such a graphic way of visualisation. The colour scale is not the same as for the pane on the left. It was chosen to make the presence of the cloud more clear. The noise is here visible; negative values are due to the noise fluctuations that remain after subtraction of the mean background value. For the two lower plots, data underwent the quality control and were corrected for the flight altitude (black line). On the left is reported the *p*-polarised

* If low extinction through the cloud might be assumed, the range-corrected signal would then be proportional to the backscatter coefficient. In case of tropospheric clouds, such assumption is rough.

channel, on the right the depolarisation ratio. This ratio is constant for the cloud at about 35%. The density of the cloud particle is less homogeneous. In particular, there is a change at time 38'600 s, moment from where the cloud shows a stronger signal. Before, the cloud was detected at the same altitude; however, weaker; as if the cloud was more dissipated.

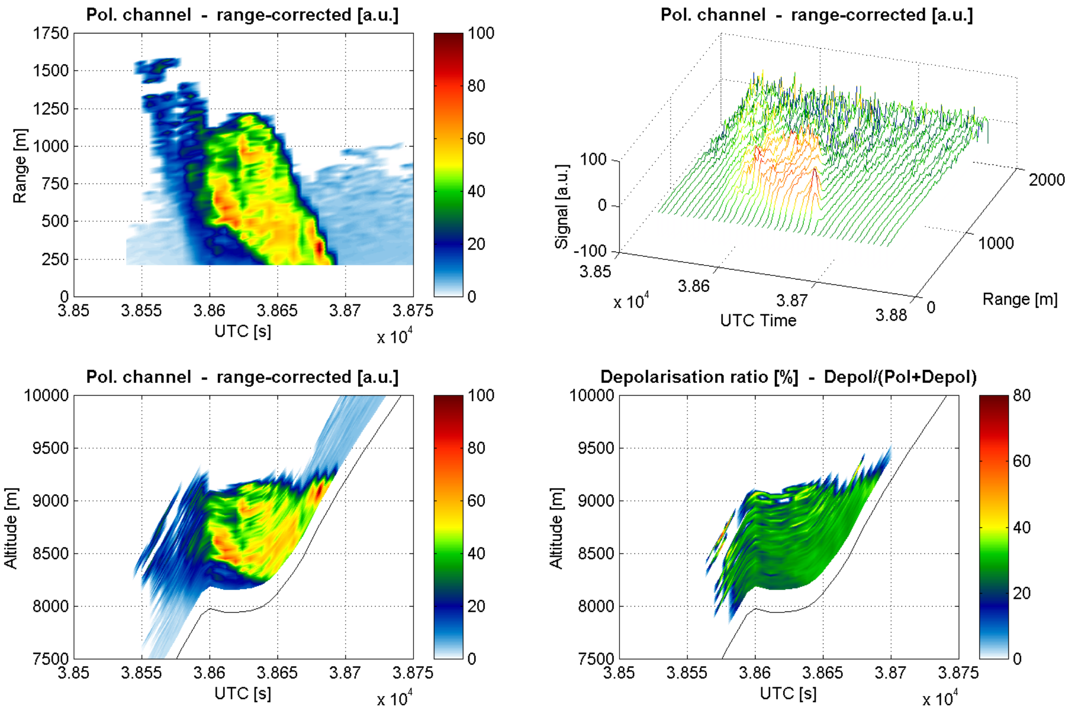

Figure 7.3. *Ascent portion of the 6th ETC flight on 3 January 1999. The minimal time resolution possible for the device, 6 s, is used. The range resolution is 20 m. The aircraft flew through a cirrus cloud (as given by the depolarisation of about 35 % in the lower right plot). The tree other plots show the cloud as measured by the polarised channel. The black line in the lower plots is the flight altitude.*

7.2.2 Thin aerosol layer detection

In case of very low optical density value, like for diffuse aerosol layer at high altitude, range-resolved profiles may be difficult to achieved, due to the low laser power of GMAL. However, it is possible to consider the device as a kind of "backscatter sonde", by integrating – or averaging – the signal of the near range over many samples. This technique was applied to the data collected during the 5th ETC flight, on 31 December 1998. For both channels, the time resolution has been decreased from 6 to 30 s, and the average value on the interval 200-400 m computed. The background noise has been subtracted and the result has been also corrected for the variation of the laser power. The result is shown in Figure 7.4. For a better representation of all curves, a value of 115 has been added to offset the real depolarised integrated backscatter signal. While the depolarised signal is constant with the altitude – apart from the noise fluctuations –, the polarised value variation shows clearly the presence of aerosol layers. This presence is not always anti-correlated with the aircraft altitude variations. Note particularly the increase of the integrated signal of polarised channel around 6:00. The increase at 6:45 may show that Geophysica "entered" a kind of diffuse aerosol layer at those altitudes. Using the procedure described in the previous chapter, we evaluated the scattering ratio between 1.15 and 1.35.

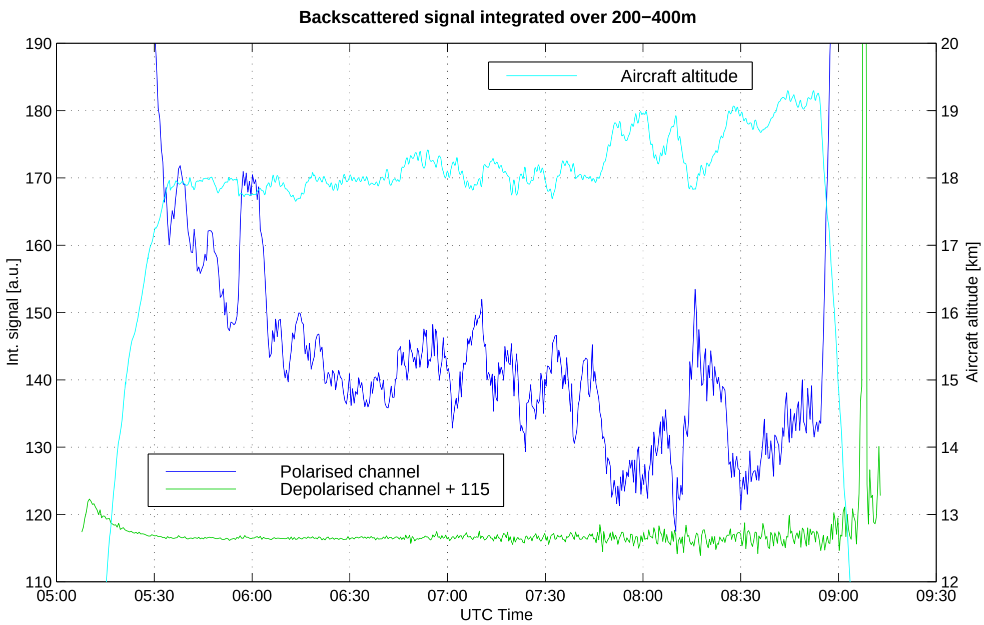

Figure 7.4. *Aerosol layers detected during the 5th ETC flight on 31 December 31 1998. The measured signals have been averaged on 30 s, corrected for background noise and laser power variation, and finally integrated over the interval 200 to 400 m.*

7.3 Tropical campaign APE-THESEO

7.3.1 Objectives and overview of the campaign

Tropospheric clouds and aerosols play a key role in the radiative transfer and by this in the budgets of the terrestrial and solar radiation, as well as to the atmospheric circulation and convection [Salb96, Mcil92]. A pronounced convection band takes place in the tropical region and is known as Inter Tropical Convergence Zone (ITCZ). This is a band of organised convection which, when taking place above the ocean regions, is oriented along the Equator. It is here where cumulonimbus clouds may go as high as 100 mb (approx. 16-17 km) and penetrate to the stratosphere. By this they play a role in the stratosphere-troposphere exchange [Holt95]. This high-column cumulonimbus clouds (or anvil, implicating to their shape) act as a pump, sucking maritime and continental air from PBL and lower troposphere to the high troposphere and the lower stratosphere, bringing water vapours, particles and trace gases. This transportation and exchange processes contribute to the chemical processes determining the stratosphere composition and, in particular, to the ozone balance.

An illustration of important changes in the particle microphysics is the transition from droplets to ice particles, which characterises the transition from the cumulonimbus to the expanded cirrus cloud fields around the anvil, with the possible correlation to the dehydration of the air. Recent studies indicated the potential of the high tropospheric cirrus clouds for chlorine activation and in this way, their potential role in the atmospheric chemistry [Borr96].

Those considerations show the importance of aerosol and cloud measurements in airborne campaigns dedicated to study the results of large tropical convections in high troposphere and lower stratosphere.

Beginning of February 1999, the APE-THESEO (Airborne Platform for Earth observation: the contribution to THESEO) campaign started and lasted for one month. It took place in the Indian Ocean, with the mission based in the Seychelles. It was dedicated to the study of the microphysical processes in tropical cirrus, the transport of tracers across the tropical tropopause and in the tropical lower stratosphere. For this study of the atmospheric transport and exchange processes around the ITCZ cloud systems, measurements of both the chemical composition of the air masses and measurements of the aerosol load in and around the studied air volume were foreseen, as an assessment of the particles microphysical properties. The DLR Falcon, equipped with an ozone/aerosol lidar (OLEX), acted as a pathfinder for “Geophysica” and provided information on ozone and aerosol. The pathfinding role was particularly important to detect sub-visible cirrus at the edge of tropical cumulonimbus clouds (hot towers) so that “Geophysica” could be directed there. “Geophysica” made seven flights.

The objectives of GMAL were the detection of clouds and aerosol layers in the vicinity of the aircraft and determination of their backscatter and depolarisation ratios. Operationally GMAL worked well. However, its performances were affected, sometimes strongly, by the freezing of the aircraft protecting window GMAL probes through. This may be explained by very high humidity level and high temperature on ground. After each flight, the inner walls of the aircraft and the surfaces of the instruments were completely covered with water droplets. On the contrary, this never happened or very few during the flights in Europe. A makeshift heating system improved the situation with the aircraft window freezing but did not remove totally the problem. For two flights the measurements were so degraded that they cannot provide useful scientific information and cannot be considered. The extreme conditions in the Tropics – high temperatures on ground, very cold temperatures in the stratosphere and high humidity on ground – were sources of problems to all instruments. They unfortunately were fatal to some of them and lead to damages or crash; fortunately for us, this did not happen to GMAL.

In the next section, Figures 7.5-7.7 have been prepared in IROE-CNR, Florence, Italy, based on GMAL data.

7.3.2 Detection of high-altitude cirrus clouds.

Figure 7.5 presents measurements of high-altitude cirrus clouds performed by GMAL during the APE-THESEO campaign. Depolarisation and backscatter ratios are shown. Cirrus clouds are clearly visible in the case of 24th February when the aircraft flew above a mesoscale convective region or in the case of 9th March when the "Geophysica" flew over the tropical cyclone "DAVINA". The presence of thin cirrus above 16 km has sometimes been detected as in the case of 24th, 27th February and 9th March, as shown here, or on 6th March. These layers at tropopause altitudes are under investigation; in some cases, they seem not to be connected with convective activity.

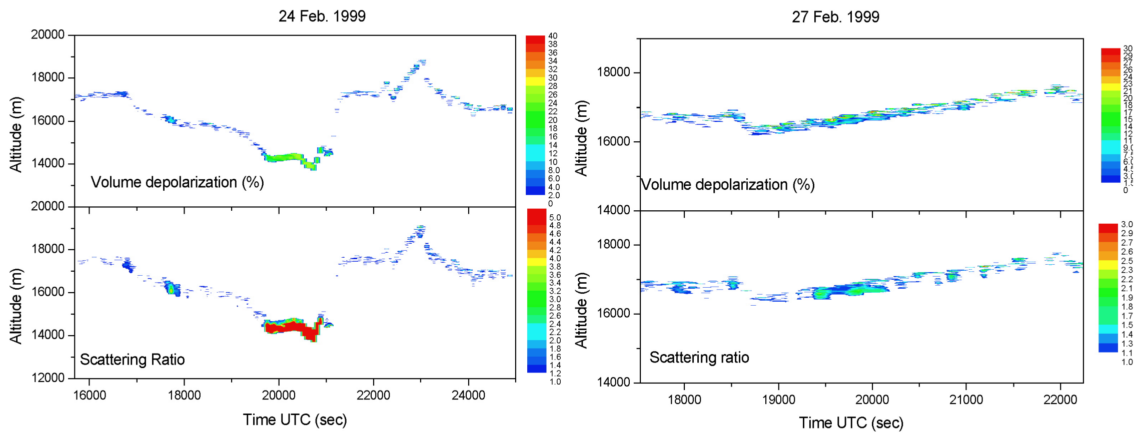

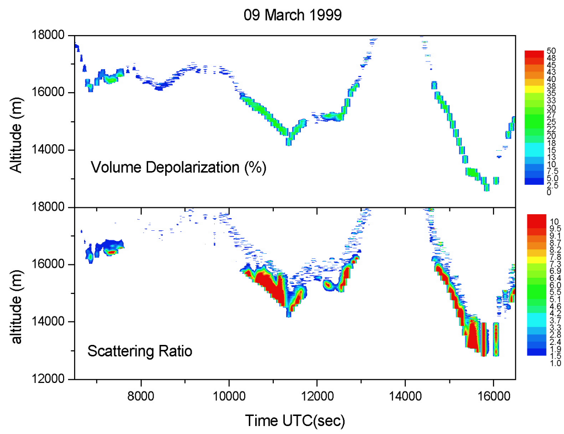

Figure 7.5. *High altitude cirrus as detected by GMAL for 3 flights during the APE-THESEO campaign. Clouds at the tropopause level (~16-17km) are very thin.*

In Figure 7.6 the depolarisation ratio versus backscatter ratio is reported for all the measurements performed during the APE-THESEO campaign for altitudes between 15 and 19 km with a step of 1 km. At low altitudes (around 15-16 km) for high values of the backscatter ratio, the depolarisation saturates around 25 % indicating the presence of cirrus clouds. At higher levels the backscatter ratio decreases, but up to 17 km, high values of the depolarisation are still detected. From 17 to 19 km, there is a sharp decrease of the backscatter and the depolarisation is mostly below 5 %.

In Figure 7.7, a direct comparison of GMAL measurement with MAS (Multiwavelength Aerosol Scattometer, [Adri99]) is reported for the case of the 27 February. A thin layer has been crossed by the aircraft during a climb. The event has been observed by the two instrument with a different timing. This is due to the fact that they are probing the atmosphere at different altitudes: MAS probes horizontally at the altitude of the aircraft and GMAL starts from 200 m above the platform. This means that when the aircraft is climbing approaching a layer (like the case reported in the figure) this is first seen by GMAL and then, only when the aircraft is at the same altitude of the layer, by MAS.

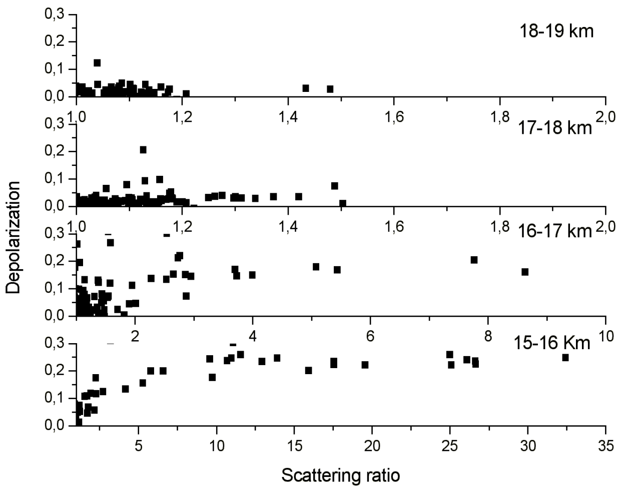

Figure 7.6. *Depolarisation versus backscatter ratio for different altitude ranges for the whole APE-THESEO campaign.*

Results of GMAL and of the in-situ instrument FSSP-300 (Forward Scattering Spectrometer Probe, [Baum92]) during the flight of 24th February are shown in Figure 7.8. The backscatter and volume depolarisation ratios as measured by GMAL are reported together with the total particle number density and the concentration of particles with

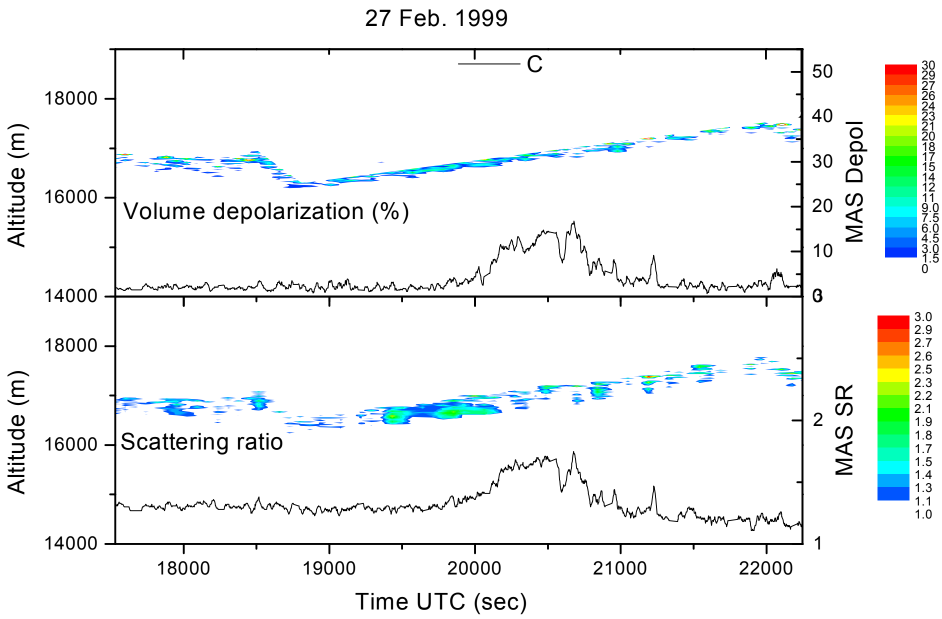

Figure 7.7. *Comparison between GMAL and MAS for 27th February flight. The cloud detected by MAS is shifted in accordance to the detection of GMAL because the measurements were performed during "Geophysica" shallow climb.*

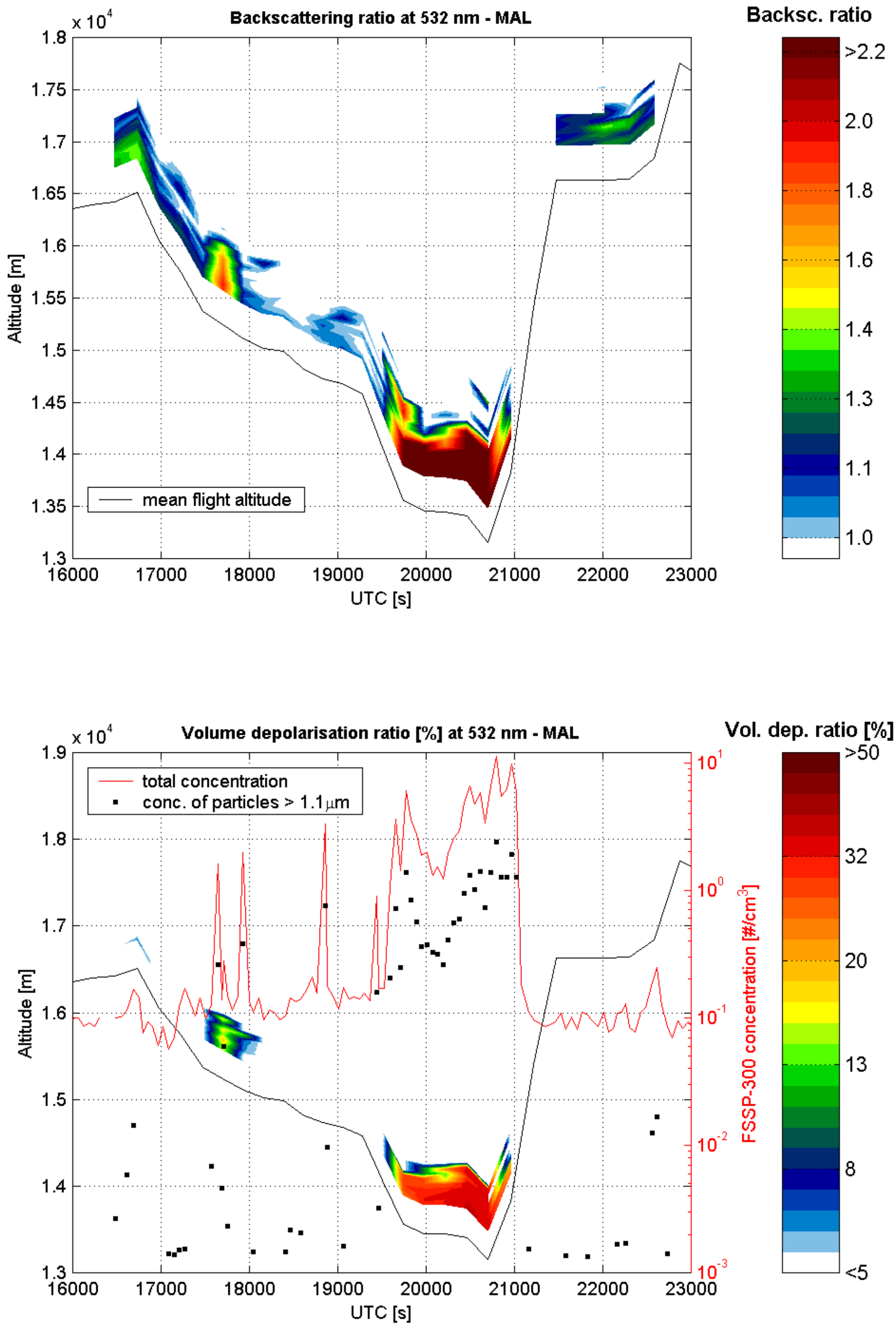

Figure 7.8. *Comparison between GMAL and FSSP-300 for 24th February flight.*

size > 1.1 μm as provided by FSSP-300 at the level of the aircraft. The results from both instruments are well correlated; the short periods of enhanced number densities shown in FSSP-300 data coincide with corresponding small increases in GMAL data. This agreement indicates a good cross-validation between GMAL and FSSP-300.

7.4 Antarctic campaign APE-GAIA

7.4.1 Objectives and overview of the campaign

A notable example of the aerosol role in the stratospheric processes is the ozone destruction in the polar regions [Crut86, Moli93, Solo98]. The destruction process includes a chain of reactions, initiated by a heterogeneous photo-chemical reaction for chlorine activation. This reaction (as well as a number of others in the chain that leads to the ozone loss) takes place on the surface of particles forming the polar stratospheric clouds (PSCs). These clouds are formed at altitudes of about 17-29 km at low temperature in the stratosphere, when the polar vortex is created during the winter. Their particles are composed mostly from frozen H_2O and/or mixture of HNO_3/H_2O. The role of the PSCs in the ozone destruction makes the study of their formation, transport (sedimentation), spatial expand, density, particles microphysical properties, particles destruction (evaporation), etc., an important part of the ozone problem studies.

Recent studies have shown the impact of the background stratospheric aerosol on the ozone chemistry, by acting as nuclei for the PSC formation in proper conditions [Zhan96]. The stratospheric background aerosol layer consists of droplets of H_2SO_4/H_2O in a mass ratio of about 3:1. The PSC particles and background aerosol formation, composition and microphysical parameters are dependable on the temperature and thermal history of the air masses, as well as the concentration of some critical trace gases. Their contribution to the subsequent chemical processes is also dependent on the concentration of chemical constituencies (H_2O, HNO_3, H_2SO_4, HCL, HBr, etc.).

These interconnections between the aerosol formation and the chemical processes in the stratosphere imply an adequate study of the aerosol load of the atmosphere, the expand of the aerosol (PSC) around the aircraft, the microphysical parameters of the particles, as well as their correlations to the chemical composition of the atmosphere.

The APE-GAIA (Airborne Polar Experiment – Geophysica Aircraft In Antarctica) mission took place in the period from 15th September to 15th October 1999 [Carl99]. Five scientific flights were performed from Ushuaia (Argentina, lat. 55°S, long. 68°W), the southernmost city of the world, with "Geophysica". Flying southward over the Antarctic Peninsula at latitudes up to 70°S and at altitudes from 14 to 20 km, allowed to investigate the main targets of the mission: the chemical composition of Antarctic lowermost stratosphere during the transition phase from the ozone depletion to the recovery phase, the mixing of mid-latitude and polar air masses, and the re-activation of chlorine over the Palmer peninsula.

The modelling activity provided, in forecast mode, accurate information about location of the boundaries of the polar vortex, as well as about occurrence of lee-waves and formation of filaments eroded from the vortex edge. Three flights aimed at entering as deep as possible inside the polar vortex and at performing dives inside, one of them reaching down to almost the tropopause. This type of flight was repeated more than once in order to study the chemistry of the polar air and the mixing between polar vortex and mid-latitude air at different times as a function of the season and with slightly different vertical coverage. One flight was performed inside a major event of lee-wave formation over the Antarctic Peninsula and one flight crossed twice a filament eroded from the vortex edge.

The objectives of GMAL participation in this campaign were the detection of PSCs and aerosol layers, as well as the determination of their backscatter and depolarisation ratios.

7.4.2 Nadir probing instrument and GMAL upgrading

For this campaign, GMAL acquisition system was upgraded from 256 gates to 1024, allowing a maximal range of 10.2 km. A second GMAL instrument – called GMAL2 – was built during summer 1999 and was also deployed on board "Geophysica" during the campaign. Its place is not behind the pilot cabin, but in the right wing boom. This instrument is not looking to zenith, but nadir, that means it points towards ground surface. It is similar to GMAL with one difference, the laser. The laser of GMAL is operating with a pulse repetition rate of 11 kHz. This ensures that a maximum range of 13.6 km may be recorded before the next pulse is emitted. As the aircraft flies at altitudes up to 20-21 km, the laser repetition rate is too high. A maximum value of 7 kHz shall be used. A 2.5 kHz laser similar to GMAL laser was purchased. Nevertheless the decrease in the pulse rate affected the mean optical power: it was only 3 mW while GMAL laser has 20 mW. We did not find a more powerful laser which could fit the volume/power consumption/voltage requirements for installation in GMAL2 as light source.

During the campaign, GMAL2 suffered from very cold temperatures. Its location may be as cold as –55°C while GMAL is in area where the temperature does not drop below –35°C. Such low temperatures where not expected for GMAL2. The instrument did not work for two flights because its internal temperature was too cold. After the instrument had been better isolated, it worked eventually.

The background noise is stronger for nadir-looking instruments flying at high altitude than for zenith-looking instruments (up to 20-50 times), due to the fact that ground and cloud surfaces reflect the sun light. More light is also diffused by the atmosphere below the aircraft than above the aircraft, as it is denser. In consequence, the laser power was too week for the signal to reach a significant SNR. We decided to change the laser with an exact copy of GMAL laser, despite the higher frequency. This way, results were obtained. However, during night-time, i.e. in absence of background radiation, we faced the double-echoes problem. As a long-range nadir-looking lidar was also present, comparison of both instruments result will help for data interpretation. This work has been performed for two of the flights. The Antarctic campaign for GMAL2 shall be seen in a perspective of instrument test, as was APE-POLECAT for IR-MAL/GMAL.

7.4.3 Large PSC event above Antarctic Peninsula

With an alert of about 36 hours, forecasts model predicted lee-wave formation over the Antarctic Peninsula for the 2nd of October 1999. A flight was accordingly planned with a flight route aiming at probing the temperature oscillations and observing the induced effects in the atmosphere. "Geophysica" flew from Ushuaia toward the Antarctic peninsula, following a three legs trajectory, with the second leg over the eastward branch of the

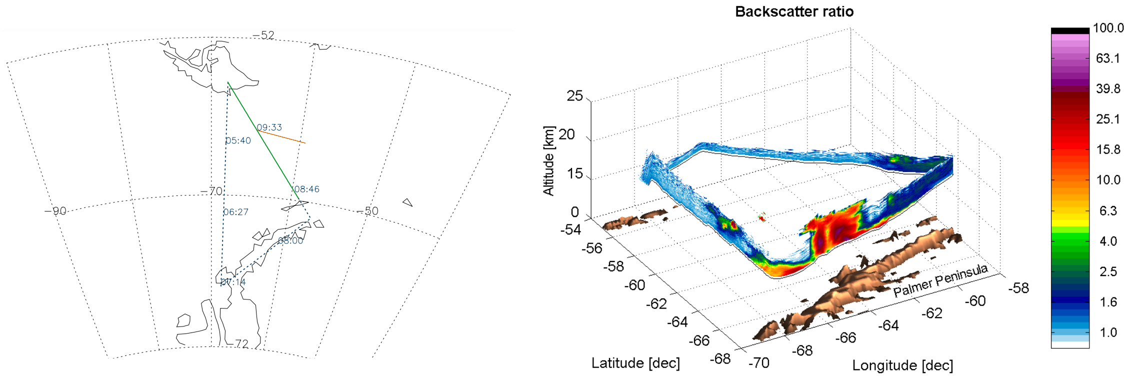

Figure 7.9. *On the left, planned and actually realised flight trajectory for 2nd October 1999 mission. The second leg is along the Palmer peninsula. On the right, backscatter ratio. For better presentation, the altitude slice between 5 and 15 km has been removed.. The line marks the position of the aircraft.*

Palmer peninsula, as depicted in Figure 7.9. That day, the vortex edge was almost parallel to the peninsula. Figure 7.9 also presents the backscatter ratio along the flight trajectory. A number of polar stratospheric clouds (PSCs) appear along – West and East – and across the peninsula with the maximum of the event approximately from 63° West to 65° West, where the flight trajectory is above the peninsula. The PSC event lasted for ~1h50min, i.e. for a horizontal range of 1'350 km. Note the cloud at altitude ~24 km at 65°South, before the aircraft turns from South to East. An individual measurement of this high-altitude cloud is presented in Figure 7.10.

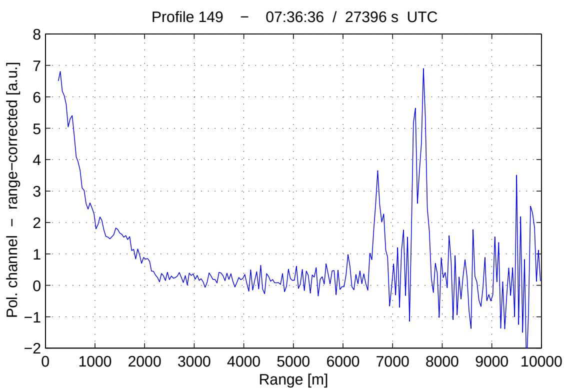

Figure 7.10. *Noise and range-corrected lidar signal (p-polarised) for the measurement of high-altitude cloud (27'400 s UTC). The range is considered from the aircraft flight altitude, which is ~17.6 km. Range resolution is 40 m by combining four successive range gates of acquired signal with no additional smoothing. The integration time is 60 s what means averaging along approximately 12 km of flight path.*

The altitude variation of the backscatter ratio and depolarisation ratio during the flight time is shown in Figure 7.11. In Figure 7.12 the depolarisation ratio is plotted versus the backscatter ratio. Several areas may be distinguished. A first area corresponds to the clouds Nos. 1 and 3 in Figure 7.11, with depolarisation ratios of 25-30%. In cloud 1, at time of about 25'500 s and altitude of 20 km, a stronger backscattering layer is found. It corresponds, in the left upper pane of Figure 7.12, to backscatter ratio of 40-75%. The rest of this subplot is then very similar to cloud 3 with backscatter ratio up to 20-25. Cloud 4 is

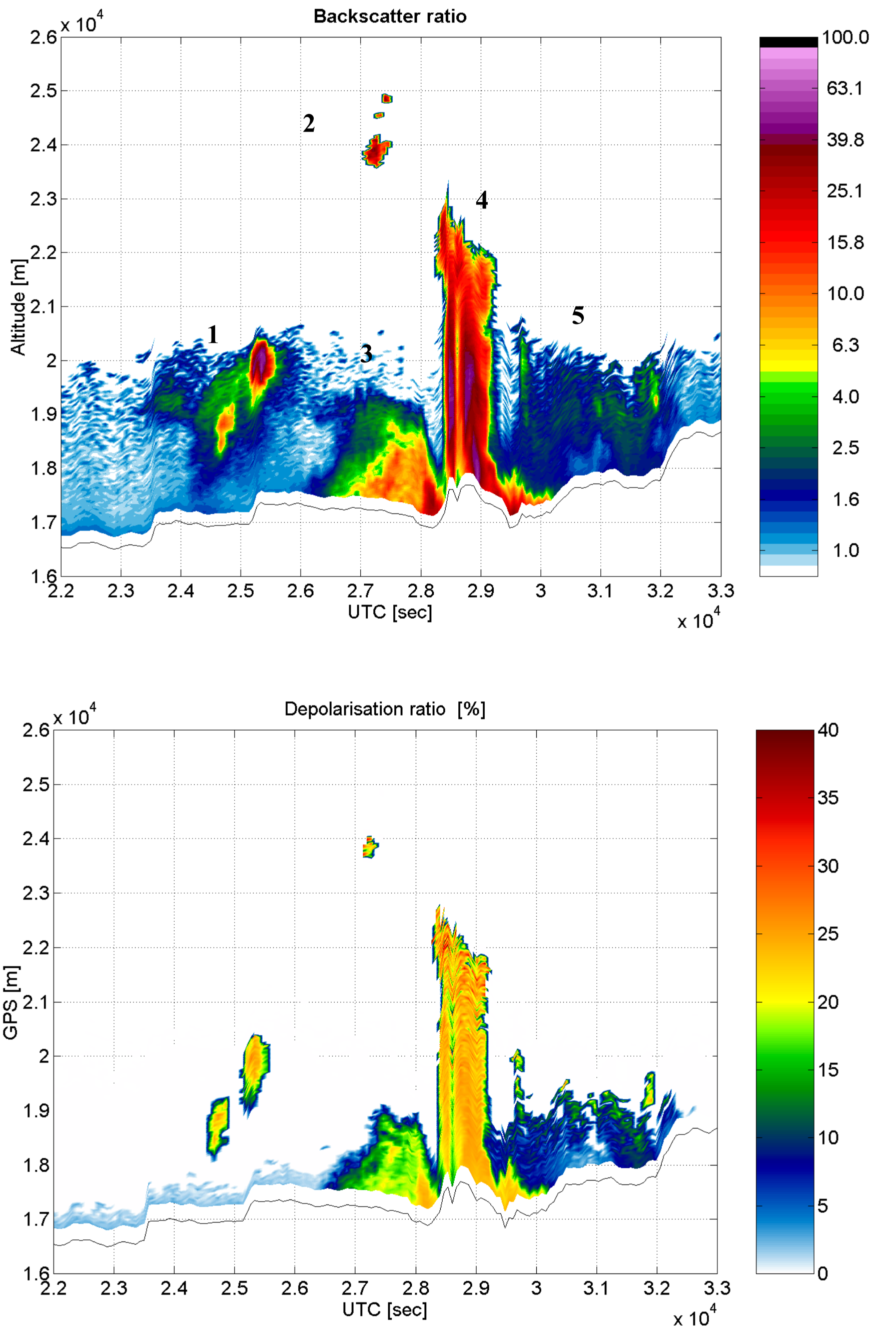

Figure 7.11. *Altitude variation of the backscatter ratio and the depolarisation ratio during the flight on 2nd October 1999. The lines show the altitude of the aircraft. The range resolution is 40 m and the time resolution is 60 s.*

another area. Its optical properties comprise the features of the previous clouds. Well distinct area is cloud 5. Here the backscatter ratio is much thinner with mean value around 2. The depolarisation ratio goes up to about 20%, with the main part comprised between 3 and 14%.

The main feature of this large PSC event is enlarged in the upper plot of Figure 7.13. For comparison, the temperature measured at the aircraft altitude is reported in the lower pane. In order to emphasise the temporal evolution, the time resolution is here 30 s, both for the lidar signal and the temperature. As the lidar range resolution is 80m, the SNR is the same as for the data reported in the upper plot of Figure 7.11. The dark line is the aircraft altitude. The very low temperature experienced by the aircraft caused a partial loss of the engine efficiency which made difficult for the aircraft to maintain a constant altitude. A "tower" consisting of two distinct parts and extending vertically for about 4 km is clearly visible. The central separation coincides with a local maximum of the temperature. It is not particle free but has different characteristics. From a preliminary analysis, it seems that it corresponds also to the moment the aircraft crossed the peninsula, from west to east, above a mountain chain. "Hot" lidar signals match well with local minimum temperatures. Deeper analyses are presently in progress to have a better understanding of this event. Comparison and correlation between the various on board instruments are being performed, as well as a model and numerical analysis of the vortex and lee-wave structure.

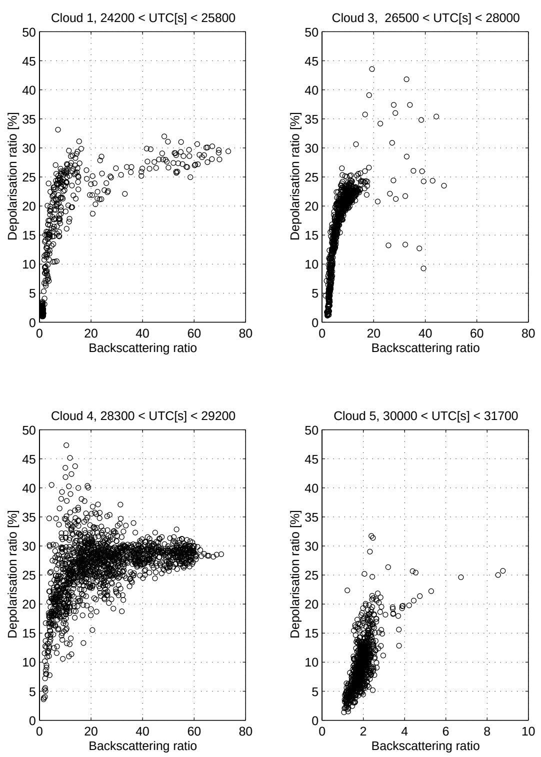

Figure 7.12. *Depolarisation ratio versus backscatter ratio for the observed PSC event at different moments of the flight.*

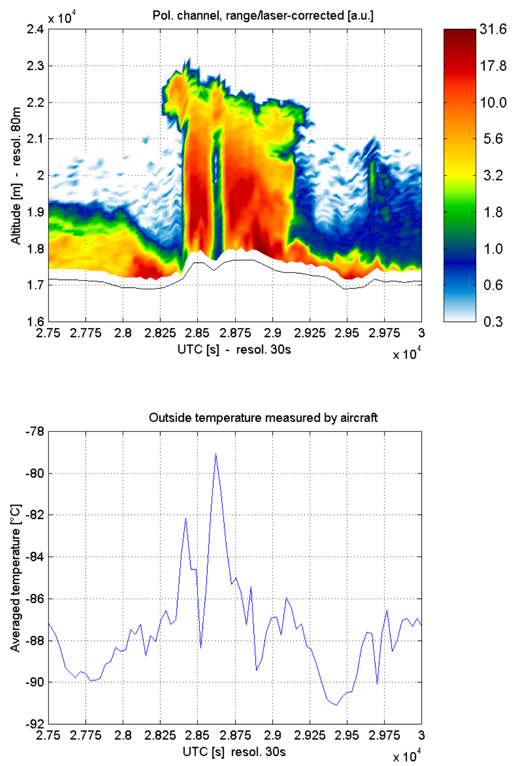

Figure 7.13. *Comparison of the range-corrected p-signal and the temperature measured at aircraft altitude as function of the time for the main event feature. The time resolution is 30 s.*

The results show that the observed clouds are consistent with predominantly PSCs of type II [Brow90; Toon90]. It is not typical to find so strong PSC events at those altitudes and so late in the season. The distribution of the cloud pattern with respect of Palmer (or Antarctic) Peninsula, indicates that most probably the "tower" clouds are caused by mountain wave activity [Cars98]. This measurement would not have been possible without precise forecasting of the orographic wave activity.

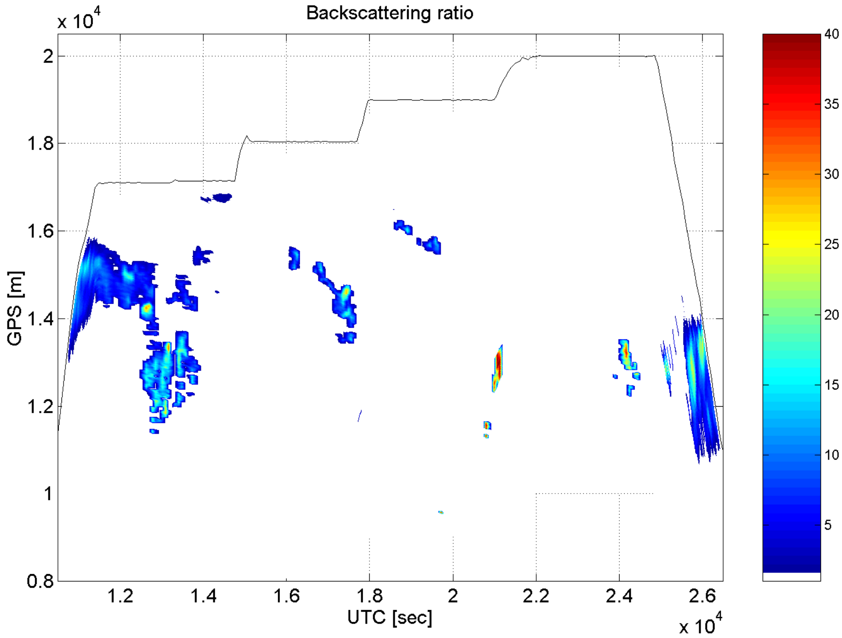

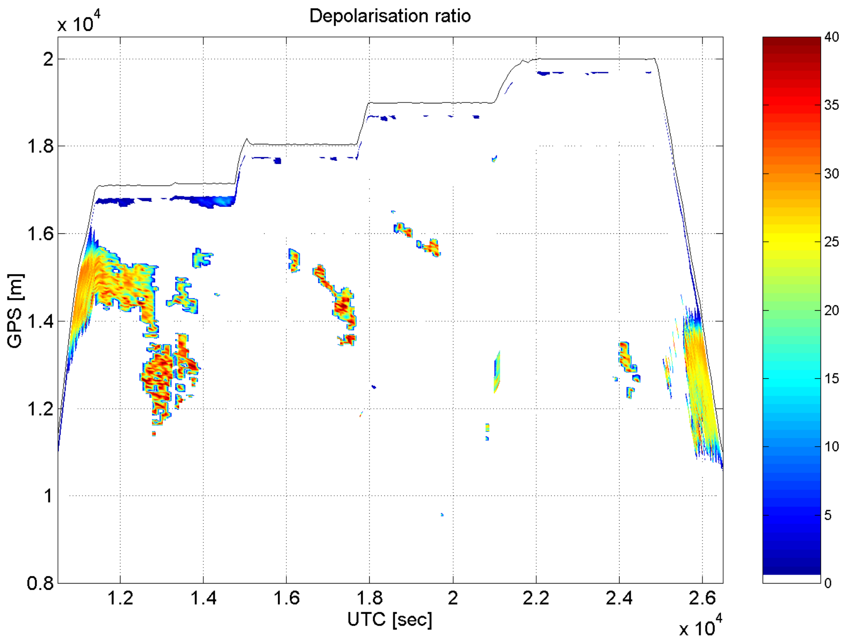

Figure 7.14. *Backscatter and depolarisation ratios during the third leg of the transfer flight, Recife (Brazil) – Isla do Sal (Cape Verde) over the Atlantic Ocean, 22 October 1999. The black lines show the altitude of the aircraft. The range resolution is 40 m and the time resolution is 60 s. Of attention are the clouds at altitudes 14-16 km and the small one at 17 km (~14'000 s UTC).*

7.4.4 Cirrus cloud field above Atlantic Ocean

A further opportunity offered by the APE-GAIA campaign was the possibility to carry out scientific observations during the return flight of "Geophysica" from South America to Europe. The possibility of performing scientific measurements at low latitudes during the transfer flight is of great scientific interest. This made possible to explore the upper troposphere and lower stratosphere over a wide range of latitudes, and to study the interactions between the polar and middle latitude stratosphere. The transfer flight consisted of four legs: Ushuaia – Porto Alegre (Uruguay), Porto Alegre – Recife (Brazil), Recife – Isla do Sal (Cape Verde), Isla do Sal – Seville.

During the third of the four legs, "Geophysica" crossed during night time the Atlantic Ocean. Figure 7.14 shows the backscatter and the depolarisation ratios obtained from GMAL2. We may notice the presence of clouds at high altitude, between 13 and 16 km. Their high depolarisation ratio indicates that they were of ice.

We mentioned in Section 7.4.2 that due to the too fast pulse repetition rate of the laser, GMAL2 may encounter problem of double echoes. The frequency of the laser is 11k Hz and corresponds in lidar range to about 13.5 km. It means that if the aircraft flights at 20 km altitude, a signal detected at 16.5 km could in reality indicate the presence of a layer 3 km above the ground. In case of double echo, the clouds detected at altitudes between 13.5-16 km would then be signatures from altitudes 0-2.5 km. As "Geophysica" was flying above the ocean, these signatures could be the ones of low tropospheric clouds. However, the depolarisation of such clouds could not be as high as 30%, because there are no solid particle clouds at such altitude. In consequence, these high-altitude clouds seem to be real. As confirmation we shall compare GMAL2 data with the data measured by the long-range lidar ABLE. For the time being the question where such clouds may stem from is under investigation.

The same depolarisation criteria has been used to clean up the whole set of data from the echo of the Ocean. All data showing a depolarisation ratio less than 5% have been removed. This number was chosen large enough to eliminate possible errors due to Rayleigh molecular depolarisation and some partial depolarisation from the Ocean surface.

7.5 Ground measurements

As for airborne operation, GMAL requires for ground tests only a 24V power supply and a computer to download the data – during the measurement, this computer is not necessary. In order to evaluate its present and actual possibilities for ground-based application, GMAL was left operating at various occasions during several hours.

Here follows three examples. Presented data are the range-corrected signal of the polarised channel and the volume depolarisation ratio. This ratio is given as previously by the depolarised signal divided by the total of the polarised and depolarised signals. Data have been corrected for the fluctuations of the laser power – even if it is not always specified. Data underwent quality control.

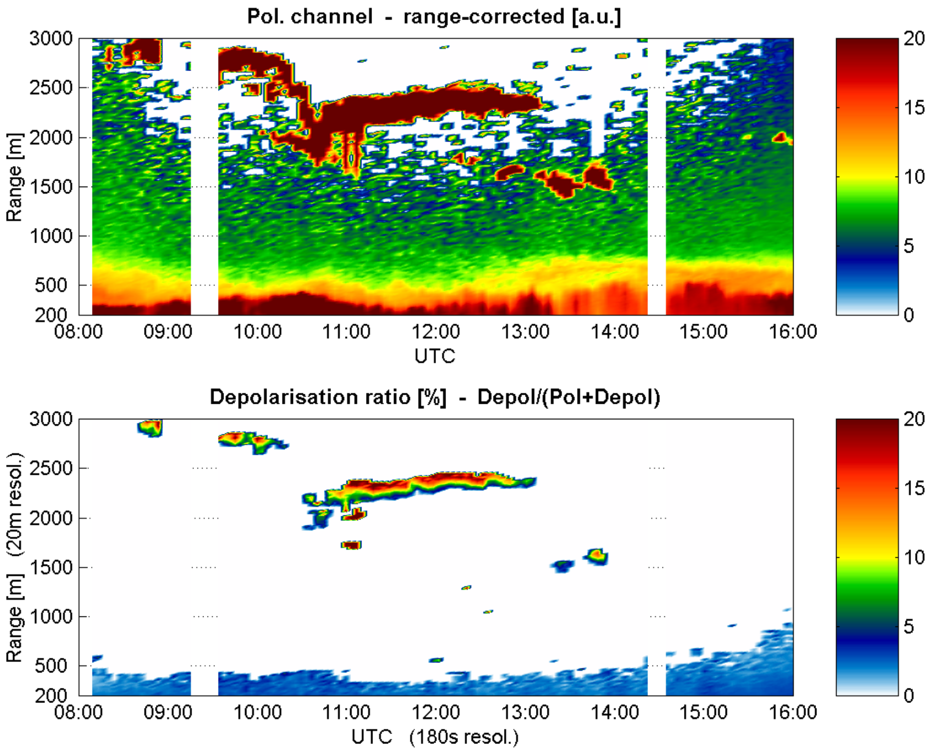

Figure 7.15. *Low-troposphere evolution on 6 December 1999. The range resolution is 20 m. Data have been averaged on 3 minutes. The blank stripes indicate when GMAL was not measuring.*

Figure 7.15 shows the evolution of the backscatter of the low atmosphere above the Observatory of Neuchâtel on 6 December 1999. The range-resolution is 20 m and data have been averaged for 3 minutes. Data below 200 m are not shown, because below this distance the overlap function is smaller than one. A cloud is present at 2-2.5 km altitude. Because the colour scale has been chosen to enhance the PBL development, the cloud inner part seems very homogeneous. A layer extending at maximum 900m above the instrument is clearly visible. It was in continual movement during the day. An interesting feature occurred between 12:30 and 14:00. Up to about 500 m there is a layer, then another very

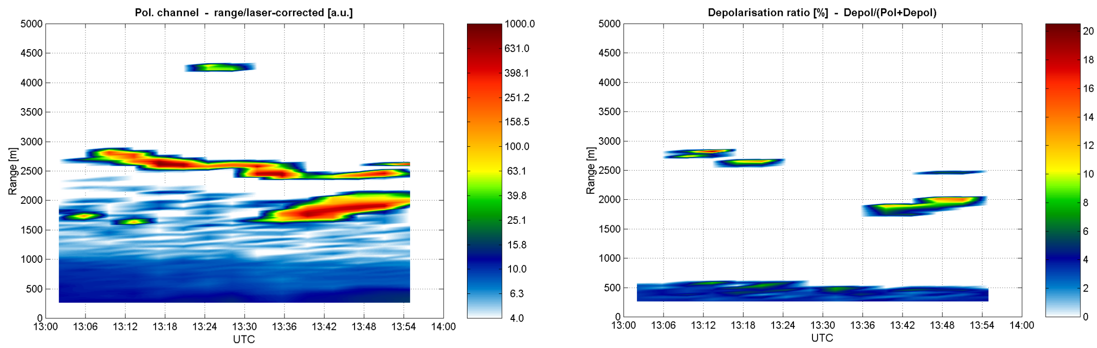

Figure 7.16. *Troposphere evolution on 8 March 2000. The range resolution is 40 m. Data have been averaged on 3 minutes. Low-altitude clouds are present. No structure in the PBL is visible.*

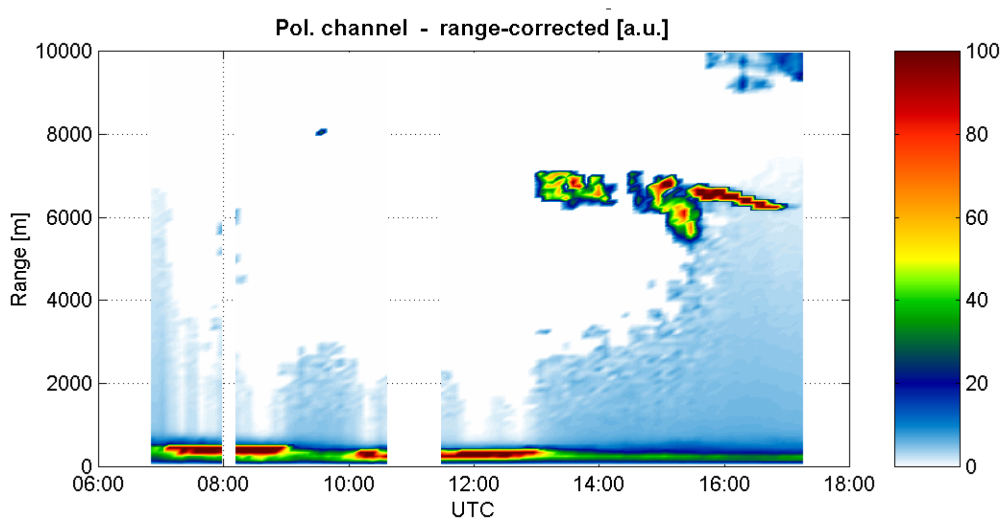

Figure 7.17. *Troposphere evolution on 22 December 1999. The range resolution is 100 m. Data have been averaged on 5 minutes. The blank stripes indicate when GMAL was not measuring. The light colour parabolic feature is due to the background radiation which decreases the SNR of the data.*

thin one, and above a more dense again. There is no depolarisation in the PBL. This is not the case for the cloud. We may notice that the upper part of the clouds seems to depolarise more than their base. The reason is likely due to multiple scattering.

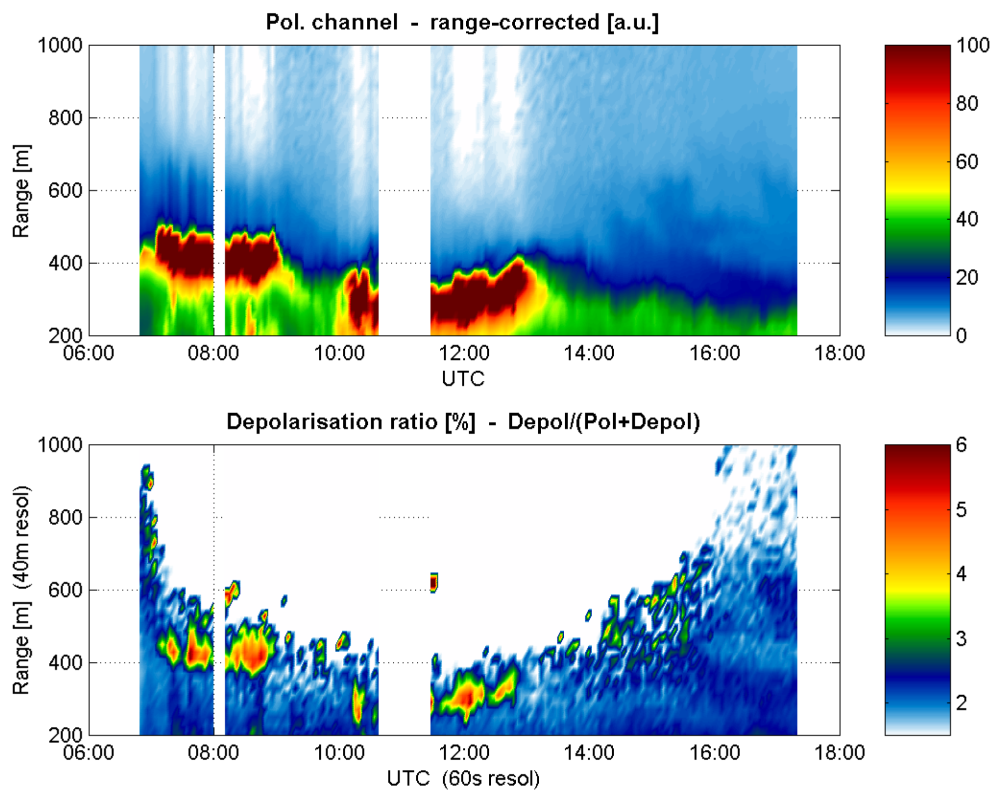

Figure 7.18. *Zoom on the PBL evolution on 22 December 1999. Here the range resolution is 40 m. Data have been averaged on 1 minute.*

Opposite to this case, is the measurement made on 8 March 2000. It is shown in Figure 7.16. It is only one hour long. But here, the PBL top is not well marked.

The third case is a measurement done on 22 December 1999. The range resolution is 40 m and data have been averaged on 1 minute. Figure 7.17 is only an overview of the full day. The range resolution is 100m, because this way, better SNR may be achieved and several very different phenomena may be seen in a first look. The PBL again presents a number of layers. In second part of the day, a first cloud at circa 6km altitude appears. Even later, a high cloud (cirrus) is visible. It might have been present before, but lost in the background noise. Figure 7.18 is a zoom of altitudes up to 1 km above GMAL. This layer varied quite much that day. Two denser pockets (likely fog) passed over the Observatory at different altitudes. After 13:00, the layer altitude goes down. A very thin structure appears between 300 and 600 m.

Figure 7.19 still concerns the measurement on 22 December 1999, but for the end of the day. Three different types of clouds were detected. The first, between 15:15 and 15:30 does not seem very dense, but has high depolarisation ratio (about 30%). The second, the long and thin one, is more dense and depolarises very few. Its upper part again has higher depolarisation ratio than the base. The last one, at 9-10 km altitude, is optically thin again with depolarisation ratio of about 40%. These characteristics are those of a cirrus.

These examples show that GMAL has potentialities to work on ground during daytime. Of course, in presence of the sun the data quality is degraded and only close ranges may be observed. For PBL observation this is however sufficient.

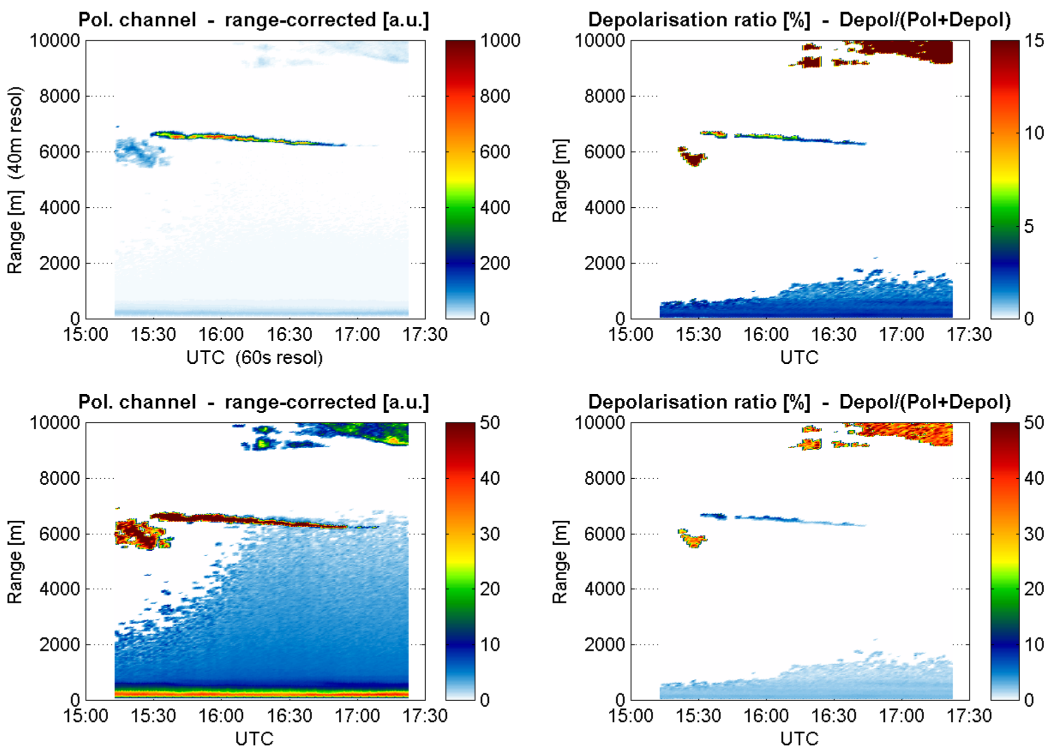

Figure 7.19. *Three different types of clouds were detected on 22 December 1999. They differ by the combination of intensity of their backscatter signal, their depolarisation ratio and their shape. The range resolution is 40m and data have been averaged on 1 minute.*

Conclusion

The results from the airborne operation of GMAL show that the lidar GMAL ensures detection of backscatter signal from subvisible clouds and aerosol layers in the range close to the aircraft. Two lidars of the same kind are finally installed on M-55 "Geophysica", one probing towards zenith, the second probing in nadir direction. The collected data are processed and evaluations of the backscatter and depolarisation ratios are obtained. The presented examples of measurements are for PSC, aerosol layers and high-altitude cirrus clouds. Although the SNR is much higher during night-time, a detection during day time is possible even in the tropics with high sun elevation angles. The operation of the lidars is reliable, no malfunction or misalignment has been indicated, apart from the cases when the overheating or undercooling resulted in temporary switch-off until the lidar housekeeping system managed to restore the proper conditions. We plan to keep this lidar configuration for the follow-on M-55 campaigns, with possible technical upgrading of the instruments.

The airborne operation during the three campaigns with GMAL provided also valuable lessons concerning lidar operation on such platform: extreme temperature changes of the environment, aircraft bay windows prone to condensation and freezing, more user friendliness for spare parts replacement, necessity for fast data downloading. All this will be implemented for the next campaigns.

Ground-based tests of the lidar GMAL showed performances for elastic backscatter measurements in the PBL and lower troposphere. This, combined with the automated and trouble-free operation and the compact size of the instrument, gives possibility to plan its participation in campaigns and in routine measurements. Coverage of seasonal and diurnal variations, as well as observation of special events may be done in a cost-efficient basis. To take full advantage of these features of GMAL, we have to develop a new system for remote control and data downloading and the necessary environmental protection. The increased data flow will also require a faster data-processing software.

Conclusion

Two ways to realise compact elastic backscatter lidars have been presented. Both ways led to the realisation of compact lidars with capability for practical applications.

The two realised compact backscatter lidars are instruments for detection of the altitude-resolved profile of clouds or aerosol load in near range of the atmosphere. Both instruments are capable for long-term unattended operation. They may provide valuable information where compactness and possibility for unattended operation are strongly required: routine, long-term monitoring of PBL top and aerosol layers in the lower troposphere, monitoring of the base of opaque cloud layer, aerosol and cloud studies from a high-altitude aircraft.

The natural question at the end of the thesis is if some of these lidars proves to be better. The answer is that there can not be a unique lidar solution for all possible cases. This is seen by the comparison between these two approaches.

The micro-pulsed lidar realised around a high-repetition rate micro-chip laser shows excellent performance for its size and weight. It demonstrated fully automated operation on a high-altitude research aircraft. The results from the ground-based test show that it may be used with success as research instrument for long-term monitoring of aerosol load in PBL and lower troposphere. On the other side the eye-safety requirements still have to be considered. A trouble-free operation of the micro-chip laser and the PMT requires better protection from the environment and temperature control.

The PRN-cw lidar is inferior compared to the pulsed lidar in term of SNR. Its SNR is also more affected by the background noise. Detection of aerosol features giving lower backscatter signal is affected by aerosol features giving higher backscatter signal. This is the reason why, in its compact version, the PRN-cw lidar is more convenient for detection of clouds (ceilometer) and targets (laser radar or range-finder). On the other hand, the PRN-cw lidar may be realised using cw-laser diode. This is the most efficient and the most economical laser source. It is also the most compact laser, with still good beam quality. Lidars which are extremely small and robust, stable and with long endurance may be realised. This provides options for lidar aerosol measurements in scenarios which can not be covered by other kind of lidar. One example is mission to a planet, where the aerosol component of the atmosphere is of importance (Mars is well-known as such). Another advantage of the diode laser application is that it allows the use of an ultra narrow-band filter (FADOF), what gives possibility to cancel the effect of the background noise on the SNR. Applications where very narrow bandwidth are required might be based on PRN-cw technique. A separate advantage of the use of a cw-laser diode comes from eye-safety considerations. This reserves for a PRN-cw lidar areas where the human activity imposes eye-safety requirements which can not be answered by pulsed lidar or pulsed laser range-finder: ceilometer at airports, laser altimeter on a low-flying aircraft and helicopter in rescue missions, range-finding for collision avoidance. For these kinds of applications where the linearity is not of highest importance, a hardware cross-correlator offers the advantage of real-time measurements (no digital processing at all).

The perspectives for future technological improvements in compact lidars are function of the technology development as for every class of instruments. In our case the future technology will bring even smaller and more powerful lasers, both diode and microchip; more sensitive, compact and lower noise detectors, etc. Anyway, the technological improvements in laser, detectors, etc., are obvious, but they are not the only necessary. The future lidars will operate more and more in situations where the limit to the measurements will be imposed by the cost of the operation, storage capacity or the possibility for remote control. The longer the lidar operates, more data are collected. If they are collected in automatic mode, more time has to be spent in their quality selection, processing and evaluation. This requires development of more efficient and automated software for data quality control and data processing.

One trend for improvements shall be mentioned separately since it is not for instrument only. When the near range of the atmosphere - from aircraft platform or from ground - is the subject of the study, a (compact) lidar operates more and more as part of a group of various instruments. This synergy imposes more requirements to the mission planning as well as to the planning of the operation of the individual instruments, lidar included.

Bibliography

[Absh92] Abshire J.B., Rall J.A..R., Manizade S.S., "Altimetry and lidar using AlGaAs laser modulated with pseudo-random codes", 16th International Laser Radar Conference, *Nasa Conference Publication*, Vol. 3158, part 2, p.441, Boston, 1992.

[Absh93] Abshire J.B., Rall J.A..R., "AlGaAs lidar-theory and measurement", in "Optical remote sensing of the atmosphere technical digest", Vol. 5, *Optical Society of America*, Washington D.C., 1993.

[Absh94] Abshire J.B., Rall J.A..R., Spinhirne J.D, Sasses K., "MESUR lidar - Lidar from the Mars surface for atmospheric studies", Mars surveyor science objectives and measurement requirements workshop, JPL Technical Report Number D12017, pp. 20-21, 1994.

[Adri99] Adriani A., et al., "Multiwavelength aerosol scattometer for airborne experiments to study the stratospheric particle optical properties", *J. Atmos. Oc. Tech.*, Vol. 16, pp. 1329-1336, 1999.

[Afrl] MODTRAN, HIGHTRAN, FASTCOD data bases and codes: AFRL/VSBM, Air Force Research Laboratories, 29 Randolph Road, Hanscom AFB, MA 01731-3010. Http://www-vsbm.plh.af.mil.

[Araz88] Arazi B., "A common-sense approach to the theory of error correcting codes", *MIT Press*, 1988.

[Baum92] Baumgardner, D., J. E. Dye, B. W. Gandrud, and R.G. Knollenberg, "Interpretation of measurements made by the Forward Scattering Spectrometer Probe (FSSP-300) during the Airborne Arctic Stratospheric Expedition", *J.Geophys. Res.*, 97, 8035-8046, 1992.

[Blam91] Blamont J.E. et al., "Vertical profiles of dust and ozone in the Martian atmosphere deduced from solar occultation measurements", *Planet. Space Sci.*, Vol. 39, No. 1-2, pp. 175-187, 1991.

[Borr96] Borrmann S., Solomon S., Dye J.E., Luo B., "The potential of cirrus clouds for heterogeneous chlorine activation", *Geophys. Res. Lett.*, Vol. 23, pp. 2133-2136, 1996.

[Brig77] Briggs G.A., Baum W.A. and Barnes J., "Viking orbiter imaging observations of dust in the Martian atmosphere", *J. Geophys. Res.*, Vol. 84, No. 28, 1977.

[Brow90] Browell E., Butler C., Ismail S., Robinette P., Carter A., Higdon N., Toon O., Schoeberl M., Tuck A., "Airborne lidar observations in the wintertime arctic stratosphere: 1st polar stratospheric clouds", *Geophys. Res. Let.*, Vol. 17, pp.385-388, 1990.

[Bukh94] Bukharin A.V., Pershin S.M., "Theoretical analysis of an eye-safe lidar", *Atmospheric and Oceanic Optics*, Vol. **7**, pp. 521-537, 1994. In Russian.

[Bukh98] Bukharin A.V., Linkin V.M., Lipatov A.N., Liyash A.N., Makarov V.S., Pershin S.M., Turin A.V., "Russian compact lidar for NASA Mars surveyor program 98", in 19th International Laser Radar Conference, July 1998 – Annapolis, USA. *NASA*, proceedings part 1, pp. 241-244, 1998.

[Cair99] Cairo F., Di Donfrancesco G. Adriani A., Pulverenti L. and Fierli F., "Comparison of various lidar depolarisation parameters measured by lidar", *Appl. Opt.*, Vol. 38, No 21, pp. 4425-4432, 1999.

[Carl99] Carli B., Cortesi U., DeRossi G., "Airborne Polar Experiment Geophysica Aircraft In Antarctica (APE-GAIA): A remote sensing chemistry mission", proceeding of the Fourth International Airborne Remote Sensing Conference, 21st Canadian Symposium on Remote Sensing, Ottawa, Canada, 21 – 24 June 1999.

[Cars98] Carslaw K. S., Wirt M., Tsias A., Luo B. P., Doernbrack A., Leutbecher M., Volkert H., Renger W., Bacmeister J. T., Reimer E., Peter T., "Increased stratospheric ozone depletion due to mountain-induced atmospheric waves", *Nature*, Vol. 391, pp. 675-678, 1998.

[Chen93] Chen H., She C.Y., Korevaar E., "Na Vapour dispersive Faraday filter", *Optics Letters*, July 1993.

[Chen94] Chen L., Alvarez L.S., Yin B., and Shay T.M., "High-sensitivity direct detection optical communication system that operates in sunlight", *SPIE*, Vol. 2123, pp.448-454, 1994.

[Chen96] Chen H., White M., Krueger D.A., She C.Y., "Daytime mesopause temperature measurements with a sodium-vapour dispersive Faraday filter in a lidar receiver", *Optics Letters*, Vol. 21, No. 15, pp. 1093-1095, 1996.

[Chyb96] Chyba T., et al, "Advanced airborne water vapour DIAL development and measurements", *Springer-Verlag*, Advances of Atmospheric Remote Sensing with Lidar - Selected papers of the 18th ILRC, Berlin, pp.301-304, 1996.

[Colb89] Colburn D.S., Pollack J.B. and Haberle R.M., "Diurnal variations in optical depth at Mars", *Icarus*, Vol. 79, pp. 159-189, 1989.

[Crai94] Craig R., Li B. and Chan B., "Laser qualification for the SILEX program", Free-Space Laser Communication VI, *SPIE*, Proceedings Vol. 2123, pp. 238-242, 1994.

[Cruz86] Crutzen P.J., Arnold F., "Nitric acid cloud formation in the cold Antarctic stratosphere - A major cause for the springtime 'ozone hole'", *Nature*, No. 324, pp. 651-655, 1986.

[Desh94] Deshler T., "In situ measurements of Pinatubo aerosol over Kiruna on four days between 18 January and 13 February 1992", *Geophys. Res. Lett.*, Vol. 21, pp. 1323-1326, 1994.

[Dick91] Dick D.J., and Shay T.M., "Ultrahigh-noise rejection optical filter", *Optics Letters*, Vol. 16, No. 11, pp. 867-869, June 1991.

[Eggc97] EG&G product catalogue, 1997.

[Este91] Atmospheric model, Annex 2 to *ESTEC report XA91/265/MH*, likely 1991.

[Este92] Pelon J., Stefanutti L., "Evaluation of possible modifications of the cloud parameters in the ATLID atmosphere model", *ESTEC internal report*, 1992 or later.

[Flas76] Flasar F.M., Goody M., "Diurnal behaviour of water on Mars", *Planet. Space Sci.*, Vol. 24, pp. 161-181, 1976.

[Flam96] Flamant C, Pelon J., "Atmospheric boundary layer structure over the Mediterranean during a Tramontane event: evidence of gravity waves influence", *Springer-Verlag*, Advances of Atmospheric Remote Sensing with Lidar - Selected papers of the 18th ILRC, Berlin, pp. 31-34., 1996.

[Gate66] Gates D., *Science*, Vol. 151, pp 523 –529, 1966.

[Godi94] Godin S. et al, "Airborne lidar observation of mountain wave induced polar stratospheric clouds during EASOE", *Geophys. Res. Lett*, Vol. 21, pp. 1335-1338, 1994.

[Golo64] Golomb S.W., Ed., "Digital Communications with Space Applications", *Prentice-Hall*, Englewood Cliffs, N.J., 1964.

[Golo67] Golomb S.W., "Shift register sequences", *Holden-day*, San-Francisco, 1967.

[Hech87] Hecht E., Zajac A., "Optics", 2nd Edition, *Addison-Wesley*, 1987.

[Holm82] Holmes J.K., "Coherent spread spectrum systems", *Wiley-Interscience Publication*, 1982.

[Holt95] Holton J. et al., "Stratosphere-Troposphere exchange", *Rev. Geophys.*, Vol. 33, pp. 403-439, 1995.

[Hunt79] Hunt G.E., "Thermal infrared properties of the Martian atmosphere 4. Prediction of the presence of dust and ice-clouds from Viking IRTM spectral measurements", *J. Geophys. Res.*, Vol. 84, No. B6, pp. 2865-2874, 1979.

[Iecs93] International Electrotechnical Commission, Http://www.iec.ch.

[Isma89] Ismail S., Browell E., *Applied Optics*, Vol. 28 No. 17, pp. 3603-3615, 1989.

[Jame90] James P.B., ”he role of water ice clouds in Martian hydrologic cycle”, *J. Geophys. Res.*, Vol. 92, No. B2, pp. 1439-1445, 1990.

[Jela92] Jelalian A.V., “Laser Radar Systems”, *Artech House*, London-Boston, 1991.

[Kahn84] Kahn R.A., “The spatial and seasonal distribution of Martian clouds, and some meteorological implications”, *J. Geophys. Res.*, 89, pp. 6671-6688, 1984.

[Kief92] Kieffer H.H., Jakosky B.C, Snyder C.W., Matthews M.S, Editors, “Mars”, *University of Arizona Press*, 1992.

[Kore96] Korevaar E., Hofmeister R. et al., “Design of satellite terminal for BMDO lasercom technology demonstration”, *SPIE*, Vol. 2381, Free-space laser communication technologies VII, pp. 38-49, 1997.

[Kore97] Korevaar E., Schuster J., et al., “Description of STRV-2 lasercom flight hardware”, *SPIE*, Vol. 2990, Free-space laser communication technologies IX, pp. 38-49, 1997.

[Lang97] Langford J., “Robotic aircraft for atmospheric research», *Spring*, EUROTRAC Newsletter, No. 18, pp. 14-15, 1997.

[Leco00] Lecomte S., Fretel E., Mileti G., Thomann P., “A self-aligned extended-cavity diode laser stabilized by Zeeman effect on Cesium D2 line”, *Applied Optics*, Vol. 39, No. 9, 2000.

[Kirc96] Krichbaumer W., “Airborne cloud measurements with the DLR Microlidar during the CLEOPATRA Campaign”, *Journal of Atm. and Oceanic. Technology*, Vol. 13, pp. 54-57, 1996.

[Marq96] Marquardt J.H., Cruz F.C., et al, “Grating-tuned semiconductor MOPA lasers for precision spectroscopy”, *SPIE* Vol. 2834, pp. 34-40, 1996.

[Mcil92] McIlveen R., “Fundamentals of Weather and Climate”, *Chapman&Hall*, 1992.

[Meas84] Measures R.M., “Laser remote sensing, fundamentals and applications”, *John Wiley*&*Sons*, 1984.

[Mend91] Menders J., Benson K., Bloom S.H., Liu C.S., and Korevaar E., “Ultranarrow line filtering using a Cs Faraday filter at 852 nm”, *Optics Letters*, Vol. 16, No. 11, June 1991.

[Mile95] Mileti G., Thomann P., “The impact of laser optical pumping on the physics and on the performance of Rb frequency standards”, *World Scientific*, Proceedings of 5th Symposium on frequency standards and metrology, p. 392, Woods Hole (MA), 1995.

[Mink92] Minkoff J., “Signal, noise and active sensors”, *John Wiley*&*Sons*, 1992.

[Moli93] Molina M.J. et al, "Physical chemistry of the $H_2SO_4/HNO_3/H_2O$ system: Implications for polar stratospheric clouds", *Science*, No 261, pp. 1418-1423, 1993.

[Moro91] Moroz V.I., Kerzhanovich V.V., Krasnopolsky V.A., "Mars 94 project: engineering model of the Mars atmosphere (MA-90)", *Russian Journal of Space Research (Kosmicheskie Issledovania)*, Vol. 29, pp. 3-84, 1991. In Russian.

[Murp93] Murphy J.R., Haberle R.M., Toon O.B., Pollack J.B., "Martian global dust storms: zonally symmetric numerical simulations including size dependent particle transport", *J. Geophys. Res.*, Vol. 98, No. E2, pp. 3197-3220, 1993.

[Norm88] Norman D.M, Gardner C.S., "Satellite laser ranging using pseudonoise code modulated laser diodes", *Applied Optics*, Vol. 27, 3650, 1988.

[Obne94] Observatory of Neuchâtel, in collaboration with Institute of Microtechnics of University of Neuchâtel, et al., "Interferomètre industriel à diode laser stabilisé en fréquence pour mesures de haute précision", CERS projects No. 2457.1 and 2996.1, 1992-1994.

[Over95] Overbeck J.A.., M.S. Salisbury, M.B. Mark, E.A.Watson, "Required energy for a laser radar system incorporating a fiber amplifier or an avalanche photodiode", *Applied Optics*, Vol. 34 No. 33, pp. 7724-7730, 1995.

[Palm94] Palm S.P., Melfi S.H., Carter D.L., "New airborne scanning lidar system: application for atmospheric remote sensing", *Appl. Opt.*, Vol. 33, pp. 5674-5681, 1999.

[Palm96] Palm S.P., Hagan D., Schwemmer G., Melfi S.H., "Interference of atmospheric boundary layer water vapor and temperature profiles over the ocean using airborne lidar data», *Springer-Verlag*, Advances of atmospheric remote sensing with lidar - Selected papers of the 18th ILRC, Berlin, pp. 39-42, 1996.

[Poll77] Pollack J.B. et al., "Properties of aerosol in the Martian atmosphere as inferred from Viking lander imaging data", *J. Geophys. Research.*, Vol. 84, No. 28, pp. 4479-4495, 1977.

[Poll95] Pollack J.B., Ockert-Bell M.E., Shepard M.K., "Viking Lander image analysis of Martian atmospheric dust", *J. Geophys. Res.*, Vol. 100, No. E3, pp. 5235-5250, 1995.

[Rede96] Redemann J., Turco R.P., Pueschel R.F., Browell E.V.,. Grant W.B, "Comparison of aerosol measurements by lidar and in situ methods in the Pacific Basin troposphere", *Springer-Verlag*, Advances in Atmospheric Remote Sensing with Lidar, Selected Papers of the 18th ILRC, Berlin, 55-58, 1996.

[Rose83] Rosen J.M., Hofmann D.J., "Unususal behaviour in the condensation nuclei concentration", *J. Geophys. Res.*, Vol. 88, pp. 3725-3731, 1983.

[Salb96] Salby M.L., "Fundamentals of Atmospheric Physics", *Academic Press*, 1996.

[Sale91] Saleh B.E.A, Teich M.C., "Fundamentals of photonics", *John Wiley*&*Sons*, 1991.

[Sdlc96] Spectra Diode Labs product catalogue 1996/1997.

[Sdlc97] Spectra Diode Labs product catalogue 1997/1998.

[Skol90] Skolnik M.I., "Radar handbook", *McGrowHill Publishing Company*, 2nd edition, 1990.

[Smit97] Smith P.H., et al, "Results from the Mars Pathfinder camera", *Science*, No. 278, pp. 1758-1765, 1997.

[Solo88] Solomon S., "The mystery of the Antarctic ozone 'hole'", *Rev. Geophys.*, No 26, pp. 131-148, 1988.

[Take83] Takeuchi N. et al., "Random modulation cw lidar", *Applied. Optics.*, Vol. 22 No. 9, pp. 1382-1386, 1983.

[Take86] Takeuchi N. et al., "Diode-laser random-modulation cw lidar", *Applied. Optics.*, Vol. 25, No. 1, pp. 63-67, 1986.

[Thom87] Thomas L., Jenkins D.B., Wareing D.P., Vaughan G., Farrington M., "Lidar observation of stratospheric aerosols associated with the El Chichon eruption", *Annales Geophysicae*, Vol. 5A-1, pp. 47-56, 1987.

[Thor77] Thorpe T.E., "Viking orbiter observations of atmospheric opacity during July-November 1976", *J. Geophys. Res.*, Vol. 82, pp. 4151-4159, 1977.

[Toon90] Toon O., Browell E., Kinne S., Jordan J., "An analysis of lidar observations of polar stratospheric clouds", *Geophys. Res. Let.*, Vol. 17, p.393-396, 1990.

[Usst76] US Standard Atmosphere 1976, *Handbook of Chemistry and Physics*, 64th Edition, pp. F155-F157.

[Vaug94] Vaughan G., Wareing D.P., Jones, S.B. Thomas L., Larsen N., "Lidar measurements of Mt. Pinatubo aerosols at Aberystwyth from August 1991 through March 1992", *Geophys. Res. Lett.*, Vol. 21, pp. 1315-1318, 1994.

[Wald93] Waldman G. and Wootton J., "Electro-optical systems performance modeling", *Artec House*, 1993.

[Wang92] Wang Q., Chen R., Peng Y., Zheng L., «Frequency-tracking and locking of diode laser using transmission spectrum of a Faraday anomalous dispersion optical filter», *SPIE* Vol. 1979, pp. 380-387, 1992.

[Wann92] Wanninger P., Valdez E.C., and Shay T.M., "Diode laser frequency stabilization based on the resonant Faraday effect», *IEEE Photonics Technology Letters*, 4, pp. 94-96, 1992.

[Wede97] Wedekind C. “Lidar-Untersuchunge von Bildung und Dynamik polarer Stratosphärenwolken in der Arktis”, PhD Thesis at Freie Universität Berlin, 1997.

[Wirt94] Wirt M., Ehret G., Mörl P., Renger W., “Two dimensional stratospheric distribution during EASOE”, *Geophys. Res. Lett*, Vol. 21, pp. 1287-1290, 1994.

[Wirt96] Wirt M.,. Renger W, “Airborne lidar observation of ozone in the Arctic winter 1994/95”»,. *Springer-Verlag*, Advances of Atmospheric Remote Sensing with Lidar - Selected papers of the 18th ILRC, Berlin, pp. 517-520, 1996.

[Yari91] Yariv A., “Optical electronics”, 4th edition, *Saunders College Publishing*, 1991.

[Yehp82] Yeh P., “Dispersive magnetooptic filters”, *Applied Optics*, Vol. 21, No. 11, pp. 2069-2075, June 1982.

[Yinb92] Yin B., Shay T.M., “A potassium anomalous dispersion optical filter”, *SPIE* Vol. 1635, Free-space laser communication technologies IV, pp. 128-134, 1992.

[Yinb94] Yin B., Alvarez L.S., Shay T.M., “The Rb 780-nanometer Faraday anomalous dispersion optical filter: theory and experiment”, TDA Progress Report 42-116, *J.H. Yuen Editor*, NASA/JPL, pp. 71-85, Feb. 15, 1994.

[Zure92] Zurek R.W., et al, “Dynamics of the atmosphere of Mars”, 835-933, in “Mars”, *University of Arizona Press*, pp.835-933, 1992.

List of publications

Publications related to the subject of this work

1. Matthey R., Mitev V, "Computer model study of pseudo-random noise modulation, continuous-wave (PRN-cw) backscatter lidar", *SPIE*, Vol. 2505, pp. 140-149, 1995.
2. Mitev V., Matthey R., Reusser D., "Development of a pseudo-random noise modulation, continuous-wave (PRN-cw) total backscatter lidar", *SPIE*, Vol. 2505, pp. 150-160, 1995.
3. Matthey R., Mitev V., Weibel P., "PRN-cw backscatter measurements with a powerful narrowband diode laser", *Springer-Verlag*, Advances of Atmospheric Remote Sensing with Lidar - Selected papers of the 18th ILRC, Berlin, pp. 115-118, 1996.
4. Mitev V., Bukharin A., Matthey R., Pershin S., de Schoulepnikoff L., "Comparative test of a PRN-cw and a μ-joule pulsed total backscatter lidars", *Springer-Verlag*, Advances of Atmospheric Remote Sensing with Lidar - Selected papers of the 18th ILRC, Berlin, pp. 119-122, 1996.
5. Matthey R., Mitev V., Makarov V., Bukharin A., Turin A., "Stratospheric depolarisation/backscatter estimation with miniature airborne lidar MAL during APE campaign", Proceedings of the 4th European ozone symposium, Schliersee, Germany, pp. 704-707, 1997.
6. Matthey R., Mitev V., "PRN-cw lidar with broadband powerful diode laser for cloud and target detection", in 19th International Laser Radar Conference, July 1998 – Annapolis, USA. *NASA*, proceedings part 2, pp. 883-886, 1998.
7. Mileti G., Matthey R., Mitev V., "Day-time PRN-cw backscatter lidar demonstration with narrow-band diode laser MOPA and FADOF", in 19th International Laser Radar Conference, July 1998 – Annapolis, USA. *NASA*, proceedings part 2, pp. 867-870, 1998.
8. Santacesaria V., Morandi M., Stefanutti L., Mitev V., Matthey R., Makarov V., Adriani A., Cairo F., Di Donfrancesco G., "Microjoule lidar observations of aerosol and cloud during the APE-THESEO mission around the tropical tropopause", to be published in proceedings of 5th European ozone symposium, Saint-Jean-de-Luze, France, 1999.
9. Matthey R., Mitev V., Mileti G., Makarov V., Turin A., Morandi M., Santacesaria V., "Miniature aerosol lidar for automated airborne application", *SPIE* , Vol. 4035, Laser Radar Technology and Applications V, 2000.

Publications not related to the subject of this work

10. Del Guasta M., Morandi M., Stefanutti L., Stein B., Kolenda J., Rairoux P., Wolf J.-P., Matthey R., Kyrö E., "Multiwavelength lidar observation of thin cirrus at the base of the Pinatubo stratospheric layer during the EASOE Campaign", *Geophysical Research Letters*, Vol. 21, No. 13, pp. 1339-1342, 1994.

11. Wedekind C., Immer F, Mielke B., Rairoux P., Stein B., Wöste L., Del Guasta M., Morandi M., Stefanutti L., Masci F., Rizi V., Matthey R., Mitev V., Douard M., Wolf J.-P., Kyrö E., "Polar stratospheric cloud measurements by multispectral lidar at Sodankylä in winter 1994/95", *Springer-Verlag*, Advances of Atmospheric Remote Sensing with Lidar - Selected papers of the 18th ILRC, Berlin, pp. 513-516, 1996.

12. Matthey R., Mitev V., Lazzarotto B., Calpini B., Morandi M., Castagnoli F., Agostini P., Antonelli A., Stein B., Wedekind C., "Depolarisation/backscatter lidar for stratospheric studies" *SPIE*, Vol. 3104, Lidar Atmospheric Monitoring, pp. 2-11, 1997.

13. Guzzi D., Morandi M., Santacesaria V., Stefanutti L., Kyrö E., Matthey R., Mitev V., Adriani A., Di Donfrancesco G., Agostini P., Cuzzola V., Antonelli A., Stein B., Wedekind C., "Stratospheric aerosol observation during SAONAS", Proceedings of the 4th European ozone symposium, Schliersee, Germany, pp. 131-134, 1997.

14. Kivi R., Kyrö E., Wedekind C., Rontu L., Dörnbrack A., Stein B., Wille H., Mitev V., Matthey R., Rosen J., Kjome N., Rizi V., Redaelli G., Lazzarotto B., Calpini B., Del Guasta M., Morandi M., Stefanutti L., Agostini P., Antonelli A., Rummukainen M., Turrunen T., Karhu J., "SAONAS activities at Sodankylä in winter 1996/7", Proceedings of the 4th European ozone symposium, Schliersee, Germany, pp. 135-138, 1997.

15. Del Guasta M., Morandi M., Stefanutti L., Balestri S., Kyrö E., Rummukainen M., Kivi R., Rizi V., Stein B., Wedekind C., Milke B., Matthey R., Mitev V., Douard M., "Lidar observation of spherical particles in a -65° cold cirrus observed above Sodankylä (Finland) during SESAME", *J. Aerosol Sci.*, Vol. 29, pp. 357-374, 1998.

16. Rizi V., Redaelli G., Visconti G., Masci F., Wedekind C., Stein B., Immler F., Mielke B., Rairoux P., Woste L., Del Guasta M., Morandi M., Castagnoli F., Balestri S., Stefanutti L., Matthey R., Mitev V., Douard M., Wolf J.-P., Kyro E., Rummukainen M., Kivi R., "Trajectory studies of polar stratospheric cloud lidar observations at Sodankylä (Finland) during SESAME: comparison with box model results of particle evolution", *Journal of Atmospheric Chemistry*, Vol. 32, pp. 165-181, 1999.

17. Frioud M., Mitev V., Matthey R., "Determination of the critical system and data processing parameters for Raman-DIAL O_3 and H_2O measurements: numerical simulation", *SPIE*, Vol. 3821, pp. 35-45, 1999.

18. Mitev M., Matthey R., Grigorov I., Kivi R., Kyrö E., Morandi M., Castagnoli F., Del Guasta M., Stein B., Wedekind C., Rizi V., Agostini P., "Rayleigh backscatter lidar measurement of stratospheric temperature above Sodankylä – Finland", to be published in proceedings of 5th European ozone symposium, Saint-Jean-de-Luze, France, 1999.

19. Kivi R., Kyrö E., Dörnbrack A., Müller M., Wille H., Stein B., Mitev V., Matthey R., Rosen J., Rizi V., Stefanutti L., Del Guasta M., "Observations of stratospheric temperatures, ozone and aerosols over northern Finland in the winter of 1998/1999", to be published in proceedings of 5th European ozone symposium, Saint-Jean-de-Luze, France, 1999.

20. Stein B., Wedekind C., Wille H., Immer F., Müller M., Wöste L., Del Guasta M., Morandi M., Stefanutti L., Antonelli A., Agostini P., Rizi V., Readelli G., Mitev V., Matthey R., Kivi R., Kyrö E., "Optical classification, existence temperatures and coexistence of different PSC types", *J. Geophys. Res.*, Vol. 104, pp. 23983-23993, 1999.

Presentations related to the subject of this work and accepted in near future conferences

21. Matthey R., Mitev V., Mileti G., Bastiano M., Makarov V., "Observation of polar stratospheric clouds by automated airborne backscatter lidar during APE-GAIA campaign", 20th International Laser Radar Conference, 10-14 July, 2000, Vichy, France.

22. Santacesaria V., Stefanutti L., Adriani A., Cairo F., Di Donfranceso G., Matthey R., Mitev V., "Microjoule airborne lidar observations of aerosol and cloud around the tropical tropopause", 20th International Laser Radar Conference, 10-14 July, 2000, Vichy, France.

23. Cairo F., Adriani A., Pulvirenti L., Viterbini M., Di Donfrancesco G., Mitev V., Matthey R., Bastiano M., Redaelli G., Dragani R., Ferretti R., Paolucci T.,"A large event of polar stratospheric cloud observed over the Antarctic peninsula with the airborne backscattersonde MAS and the lidar MAL, in comparison with synoptic and mesoscale modeling", Quadriennal Ozone Symposium, 3-8 August 2000, Sapporo, Hokkaido, Japan.

24. Cairo F., Adriani A., Pulvirenti L., Viterbini M., Di Donfrancesco G., Mitev V., Matthey R., Bastiano M., Redaelli G., Dragani R., Ferretti R., Bernardini L., "Presence of a stratospheric thin laminar structure of aerosol observed by backscattersonde MAS and the lidar MAL in the APE GAIA campaign", Quadriennal Ozone Symposium, 3-8 August 2000, Sapporo, Hokkaido, Japan.

Presentations not related to the subject of this work and accepted in near future conferences

25. Frioud M., Mitev M., Matthey R., "Backscatter lidar study of PBL structure in Rhine Valley during MAP-FORM", 20th International Laser Radar Conference, 10-14 July, 2000, Vichy, France.

26. Mitev V., Matthey R., Grigorov I., Kyrö E., Kivi R., Morandi M.., Rizi V., Müller M., Stein B., "Rayleigh lidar observations of wintertime stratospheric temperature perturbations above Sodankylä - Finland: correlation with PSC events and stratospheric warming", 20th International Laser Radar Conference, 10-14 July, 2000, Vichy, France.

27. Guzzi D., Morandi M., David C., Liley B., Mitev V., Matthey R., Cuzzola V., "Evolution in aerosol loading and related optical properties at mid-latitudes", 20th International Laser Radar Conference, 10-14 July, 2000, Vichy, France.

Curriculum vitae

Renaud Matthey is born in La Chaux-de-Fonds, Switzerland, in 1965. He graduated from the Department of Physics in the Swiss Federal Institute of Technology, Zürich in 1990. In 1991 he joined the Observatory of Neuchâtel. During 1991-1993 he was as a visiting fellow in the Lidar Group in IROE/CNR, Florence. Since 1993 he has been working in the Lidar group in the Observatory of Neuchâtel.